HYBRID INORGANIC–ORGANIC MATERIALS:
Novel Poly(propylene oxide) Based Ceramers, Abrasion Resistant Sol–Gel Coatings for Metals, and Epoxy–Clay Nanocomposites

with an additional chapter on:

Metallocene Catalyzed Linear Polyethylene

Kurt Jordens

Dissertation submitted to the faculty of the
Virginia Polytechnic Institute and State University
in partial fulfillment of the requirements for the degree of

DOCTOR OF PHILOSOPHY
in CHEMICAL ENGINEERING

Garth Wilkes, Chairman
Richey Davis
Eva Marand
John Dillard
Allan R. Shultz

August 3, 1999
Blacksburg, Virginia

KEYWORDS: Ceramer; sol–gel; abrasion resistant coatings; polyethylene; HDPE; linear PE; polymer–clay nanocomposites; montmorillonite.

HYBRID INORGANIC–ORGANIC MATERIALS:

Novel Poly(propylene oxide) Based Ceramers, Abrasion Resistant Sol–Gel Coatings for Metals, and Epoxy–Clay Nanocomposites

with an additional chapter on:
Metallocene Catalyzed Linear Polyethylenes

Kurt Jordens

(ABSTRACT)

The sol-gel process has been employed to generate hybrid inorganic-organic network materials. Unique *ceramers* were prepared based on an alkoxysilane functionalized soft organic oligomer, poly(propylene oxide) (PPO), and tetramethoxysilane (TMOS). Despite the formation of covalent bonds between the inorganic and organic constituents, the resulting network materials were phase separated, composed of a silicate rich phase embedded in a matrix of the organic oligomer chains. The behavior of such materials was similar to elastomers containing a reinforcing filler. The study focused on the influence of initial oligomer molecular weight, functionality, and tetramethoxysilane, water, and acid catalyst content on the final structure, mechanical and thermal properties. The sol-gel approach has also been exploited to generate thin, transparent, abrasion resistant coatings for metal substrates. These systems were based on alkoxysilane functionalized diethylenetriamine (DETA) with TMOS, which generated hybrid networks with very high crosslink densities. These materials were applied with great success as abrasion resistant coatings to aluminum, copper, brass, and stainless steel.

In another study, intercalated polymer–clay nanocomposites were prepared based on various epoxy networks montmorillonite clay. This work explored the influence of incorporated clay on the adhesive properties of the epoxies. The lap shear strength *decreased* with increasing clay content. This was due to a reduction in the toughness of

the epoxy. Also, the *delaminated* (or *exfoliated*) nanocomposite structure could not be generated. Instead, all nanocomposite systems possessed an *intercalated* structure.

The final project involved the characterization of a series of metallocene catalyzed linear polyethylenes, produced at Phillips Petroleum. Polyolefins synthesized with such new catalyst systems are becoming widely available. The influence of molecular weight and thermal treatment on the mechanical, rheological, and thermal behavior was probed. Although the behavior of this series of metallocene polyethylenes was not unlike that of traditionally catalyzed materials, this work is one of the first comprehensive studies of these new linear polyethylenes. The main distinction between the metallocene and traditional Ziegler–Natta catalyzed polyethylenes is the narrow molecular weight distributions produced by the former (for this series of materials, $2.3 < \overline{M}_w / \overline{M}_n < 3.6$).

DEDICATION:

For my family

Acknowledgements

First and foremost I want to thank my loving family for their undying support throughout my life.

I would like to thank the members of my advisory committee for their contributions to my development as a student. Firstly, Prof. Wilkes, one of the most knowledgeable polymer scientists and best teachers I have ever known; Prof. Davis, with whom I've had many stimulating conversations with, whether it were about polymer science or astronomy; Prof. Marand, for her encouraging remarks about my work and writing; Prof. Dillard, whom I first met ten years ago as a freshman studying general chemistry in his class; and Prof. Riffle who introduced me to polymer research as an undergraduate, along with her student at the time Andy Brink, who remains a friend mine today.

I am thankful to have Sandy Simpkins working in chemical engineering. She is one of the very best.

I would like to thank the Center for Adhesive and Sealant Science (along with the Adhesive and Sealant Council Education Foundation), the finest student–funding organization on campus. Also, the support staff, who were extremely helpful and caring throughout the years, especially Linda Haney, Katy Hatfield, Tammy Jo Hiner, and Kim Mills.

Although I've had many acquaintances throughout my graduate career, I also formed a few true and lasting friendships. Among them, Slade and Tara Gardner, Rob and Janice Greer, Chris and Jennifer Robertson, David Shelby, and Watson Srinivas.

I am thankful for my friendship with Slade, who helped me with the art of motorcycle maintenance, brewing, and situations that appeared to be certain DOOM. Not to forget the stimulating conversations during lab coffee breaks. He and Tara have been extremely generous to me over the course of our friendship, which I hope will endure despite the distance between us.

Similarly, Rob was a fine brewing, cooking, camping, basketball, fragging, and shooting companion. I am lucky to know him and his wife who are amongst the most hospitable people I have known, and exceptional parents of Hattie Grace and Zachary.

And Chris, whom I met many years ago as an undergraduate, but did not form a friendship with until graduate school. I've enjoyed our time together sharpening our cooking and pool skills, and the many coffee breaks in the lab and elsewhere.

Dave Shelby, my original companion at the Pub on Friday nights, who shares my enjoyment of chili and honey mustard. He is one of the brightest people I've known, and I appreciated his helpful discussions concerning our homework problems for physical chemistry of polymers, and other polymer related issues, and helping me land a job. I'm looking forward to his housewarming party.

And Watson, whose lab guidance and helpful discussions are well appreciated. And I'll never forget our coffee breaks in the lab, the times we smoked avantis, and sipped fine Canadian spirits.

Also many of my other labmates offered good advice and wisdom over the years. These include Don Loveday, Jim Dounis, Don Brandom, Brian Risch, Ta-hua Yu, Varun Ratta, Bryan Kaushiva, Jianye Wen (Lo Wen), Dave Godshall, Matt O'Sickey, and Matt Johnson.

This dissertation would not be complete without the help of Steve McCartney, who not only is the finest microscopist I have ever met, but has become a fine friend over the years, particularly at the Pub in days of old.

"... No way of thinking or doing, however ancient, can be trusted without proof. What everybody echoes or in silence passes by as true today may turn out to be falsehood tomorrow, mere smoke of opinion, which some had trusted for a cloud that would sprinkle fertilizing rain on their fields...."
– from Economy, the first chapter of "Walden", by Henry David Thoreau

"…Death closes all: but something ere the end,
Some work of noble note may yet be done,…"
– from "Ulysses", by Alfred Lord Tennyson

"To go into solitude, a man needs to retire as much from his chamber as from society."
– from "Nature", by Ralph Waldo Emerson

"O while I live to be the ruler of life, not a slave,…"
– from "A Song of Joys", by Walt Whitman

"Every tree sends its fibres forth in search of the Wild."
– from "Walking", by Henry David Thoreau

"…I will drink life to the lees. …"
– from "Ulysses", by Alfred Lord Tennyson

Table of Contents

Abbreviations and Parameter Definitions

2220N	ACCLAIM™ hydroxyl terminated polyether polyol oligomer, composed of primarily propylene oxide with some (≈ 25%) ethylene oxide comonomer, of ≈ 2200 g / mol.
a	Yasuda constant from the Carreau-Yasuda equation; describes the transition zone between the newtonian plateau and the shear thinning region for viscosity versus shear rate data
APS	γ–aminopropyltriethoxysilane
Cp	cyclopentadienyl ring
CP / MAS NMR	cross polarization magic angle spinning nuclear magnetic resonance spectroscopy
CR–39	a diallyl diglycol carbonate resin (lightly crosslinked)
D2000	JEFFAMINE® amine terminated poly(propylene oxide) oligomer of ≈ 2000 g / mol (Huntsman Corporation)
D230	JEFFAMINE® amine terminated poly(propylene oxide) oligomer of ≈ 230 g / mol (Huntsman Corporation)
D400	JEFFAMINE® amine terminated poly(propylene oxide) oligomer of ≈ 400 g / mol (Huntsman Corporation)
d	long period or long spacing derived from SAXS (same as *L*)
DDS	diaminodiphenylsulfone
DETA	diethylenetriamine
d_f	the fractal dimension
DMF	dimethylformamide
DMS	dynamic mechanical spectroscopy (DMA, DMTA)
DSC	differential scanning calorimetry
E	Young's modulus or equilibrium Young's modulus
E'	dynamic storage modulus (tensile)
E"	dynamic loss modulus
E_a	melt flow activation energy; describes the temperature sensitivity of viscosity for a material
EAcAc	ethylacetoacetate
EO	ethylene oxide
f-2220N	alkoxysilane functionalized 2220N
f-D2000	alkoxysilane functionalized D2000
f-D230	alkoxysilane functionalized D230
f-D400	alkoxysilane functionalized D400
f-DETA	alkoxysilane functionalized diethylenetriamine
G	equilibrium shear modulus or relaxation modulus
G_N^0	plateau modulus
GPC	gel permeation chromatography (same as SEC)

$I(\boldsymbol{s})$	scattered x-ray intensity as a function of the scattering vector
ICPTES	3-isocyanatopropyltriethoxysilane
IMPA	imino bis propylamine
IPA	isopropanol or 2-propanol
k	Boltzmann's constant
L	long period or long spacing (same as d)
ℓ_{am}	amorphous layer thickness
ℓ_c	lamellar thickness
LCB	long chain branching; the convention chosen in this dissertation is that such a branch has a length in excess of the entanglement molecular weight for the polymer. Hence the branch is considered long only if it is *rheologically significant*
ℓ_g^*	average initial lamellar thickness derived in the Lauritzen-Hoffman model of crystal growth for flexible polymer chains
LLDPE	linear low density polyethylene; a copolymer produced from ethylene and a small amount of an α–olefin, traditionally 1-butene, 1-hexene, 1-octene, or 4-methyl 1-pentene
MAO	methylaluminoxane
M_c	molecular weight between crosslinks for a network material or the critical entanglement molecular weight (weight average if polymer has a non–uniform molecular weight distribution) for a linear polymer where there is a transition from $h_0 \propto \overline{M}_w$ behavior to $h_0 \propto \overline{M}_w^{3.4}$
MD	machine direction
M_e	entanglement spacing molecular weight; weight average for a non-uniform molecular weight distribution
$\overline{M}_n$	number average molecular weight
$\overline{M}_v$	viscosity average molecular weight
$\overline{M}_w$	weight average molecular weight
$\overline{M}_w / \overline{M}_n$	breadth index or polydispersity ratio
MTS	mica type layered silicate clay
n	exponent in the Carreau-Yasuda equation related to the slope of the viscosity-shear rate curve in the power law region
N_v	number of crosslinks per unit volume for a network polymer
Od_2Me_2AmBr	dioctadecyldimethyl ammonium bromide
PC	bisphenol–A polycarbonate (LEXAN®, for example)
PDMS	poly(dimethyl siloxane)
PE	polyethylene
PEI	poly(ethylene imine)
PEK	poly(ether ketone)

PEPO	poly(arylene ether phosphine oxide)
PMMA	poly(methyl methacrylate)
PPO	poly(propylene oxide)
PS	polystyrene
PSF	polysulfone
PSS	poly(styrene sulphonate)
PTMO	poly(tetramethylene oxide)
PVAc	poly(vinyl acetate)
Q_s	the invariant (SAXS)
R	the universal gas constant
$\bar{r}^2$ and $\sqrt{\bar{r}^2}$	the mean square and root mean square end–to–end distance of a linear polymer chain
RF	radio frequency
$\bar{r}_{G,z}$	the electronic radius of gyration (also the z-average radius of gyration)
s	magnitude of the scattering vector, equal to $\frac{2}{l}\sin q$
SAXS	small–angle x-ray scattering
SCB	short chain branching; in LLDPE such a branch *usually* contains 2-6 carbons from copolymerization with α–olefins. However, a SCB can be any length that is shorter than the entanglement molecular weight of the polymer, and as such is not *very* significant to the rheological behavior
SEC	size exclusion chromatography (same as GPC)
SEM	scanning electron microscopy
tan$d$	loss tangent from DMS; equal to *E"/E'*. *d* is the phase angle between the imposed sinusoidal strain function and the responding stress function. δ=0° implies a perfectly elastic solid, δ=90° implies a purely viscous liquid
TD	transverse direction
TEM	transmission electron microscopy
TEOS	tetraethoxysilane or tetraethylorthosilicate
T_c	crystallization temperature
T_g	glass transition temperature
TG	thermogravimetry (same as TGA)
TGA	thermogravimetric analysis
THF	tetrahydrofuran
T_m	melting temperature
TMOS	tetramethoxysilane
WAXS	wide angle x-ray scattering
w_c	crystalline phase mass fraction (i.e. percent crystallinity divided by 100%)
XPS	x-ray photoelectron spectroscopy
XRD	x-ray diffraction

$\langle \Delta r^2 \rangle$	mean square electron density fluctuation or scattering power (from x-ray)
ΔT	undercooling or supercooling = $T_m - T_c$
ε	tensile strain
ε_b	strain at break
ε_y	strain at yield
f_{am}	amorphous phase volume fraction
f_c	crystalline phase volume fraction
f_{PPO}	volume fraction of PPO–rich phase in a ceramer
f_{sil}	volume fraction of silicate or polysiloxane–rich phase in a ceramer
$\dot{\gamma}$	shear rate
l	wavelength of illuminating radiation
$\eta(\dot{\gamma})$	shear rate dependent viscosity
η^*	complex or dynamic viscosity
η_0	zero–shear viscosity
η_∞	infinite shear-rate viscosity
q	one half of the radial scattering angle in an x-ray scattering experiment
r	density
r_{am}	density (or electron density if x-ray related) of amorphous phase
r_c	density (or electron density if x-ray related) of crystalline phase
r_{PPO}	electron density of PPO phase in a ceramer (x-ray)
r_{sil}	electron density of silicate or polysiloxane–like phase in a ceramer (x-ray)
σ_o	tensile engineering stress
σ_b	(engineering) stress at break
σ_y	(engineering) stress at yield
τ_η	characteristic viscous relaxation time (Carreau–Yasuda equation)
ω	frequency of oscillation in rad / s (rheology)

Chapter 1

Introduction

This dissertation is somewhat unconventional in its content. Instead of one, large dissertation project, five distinct, smaller–scale projects are included.

Chapter 2 contains a review of the literature that is relevant to ceramer materials and polymer–clay nanocomposites. Projects in these areas are included in chapters 3 through 6, and fall under the guise of inorganic–organic hybrid materials. The project reported on in Chapter 3 concerns the structure–property relationships for novel ceramer materials based on JEFFAMINE® poly(propylene oxide) oligomers (terminated with amine groups) and tetramethoxysilane. These materials are "nanocomposites" since they posses a nano-scale combination of the organic oligomer chains with a polysiloxane or silicate structure. The behavior of these materials is similar to that of an elastomer containing a reinforcing filler. Chapter 4 encompasses a similar project of ceramer materials made from an ACCLAIM™ poly(propylene oxide) oligomer (terminated with hydroxyl groups) and tetramethoxysilane. The ACCLAIM™ oligomer has a higher functionality than the JEFFAMINE® oligomers (a "cleaner" chemistry), which led to an interesting comparison of ceramers made from both sources. However, the synthetic pathways were slightly different for the different oligomers. The generation of JEFFAMINE® ceramers involved urea chemistry, which occurs readily at room temperature. The synthesis of ACCLAIM™ based ceramers

required urethane chemistry, which was facilitated by using a catalyst in an inert environment at elevated temperature.

Chapter 5 deals with different ceramer materials employed as transparent, abrasion resistant coatings for metal substrates. These ceramers were based on a low molecular weight organic material (diethylenetriamine) rather than an oligomer. When this material was functionalized with *nine* alkoxysilane groups per initial diethylenetriamine molecule (assuming complete functionalization), a very high crosslink density was achieved after the sol–gel reaction. This created hard, transparent, abrasion resistant coatings which provided excellent protection to a number of metal substrates, including aluminum, stainless steel, copper, and brass.

Chapter 6 addresses the effect of incorporating montmorillonite clay into epoxy adhesives, mainly focusing on the adhesive bonding properties. It was anticipated that incorporating clay into the epoxy could provide a barrier to diffusion, particularly to water. Since water degrades adhesive bonds, it was anticipated that the incorporation of clay into the adhesive would improve the durability of the bond in the presence of water. The widely popular Epon828 epoxy resin (Shell) was chosen for study with three curing agents: Huntsman Corporation's JEFFAMINE® D400 and D2000, and Shell's Epicure 3140. These generated cured epoxy networks with varied glass transition temperatures of ≈ –37, 45, and 105 °C. Unfortunately, incorporating the clay into the epoxy led to a decrease in the single lap shear strength of the epoxy formulations. Some of the other results of the present work are in contrast to reports in the literature. Some of these points are initially raised in the critical review of the polymer–clay nanocomposites literature covered in chapter 2. Some other work reported in chapter 6 includes polymer–clay nanocomposites based on montmorillonite clay with various thermoplastics such as poly(vinyl acetate), polystyrene, and Estane™, a thermoplastic polyurethane.

In chapters 7 and 8, a systematic study of the influence of molecular weight and thermal treatment on the properties of metallocene catalyzed linear polyethylenes is reported. Although these new catalysts generate whole polymers of narrow molecular

weight distribution, their behavior is not unlike narrow fractions of the broad distribution polymers produced by the more conventional Ziegler–Natta and chromium oxide catalysts.

Chapter 9 is a brief discourse on suggestions for future work in the five areas covered by this dissertation.

Preceding this introductory chapter is a list of abbreviations and variable definitions which are used extensively throughout this dissertation. The reader is referred to this list when reviewing the remainder of this document.

Chapter 2

Review of CERAMER and Polymer–Clay Nanocomposites Literature

Part I. Ceramer Literature

2.1 Introduction

The term *ceramer* is a combination of "ceramic" and "polymer". Its original definition described a type of hybrid network system generated from metal alkoxides and functionalized polymers or oligomers by the sol-gel reaction. More recently the term has been utilized to describe a network material generated by the sol–gel reaction of alkoxysilane functionalized organics. The evolution of research from Professor Garth Wilkes' laboratory in the *ceramer* area has ranged from novel hybrid materials to high refractive index glasses, and finally to abrasion resistant coatings. Scrupulous selection of sol-gel reactants can lead to a wide variety of final material properties. Since an understanding of sol-gel chemistry is so important to making materials of this kind, a brief discourse on the nature of the sol-gel reaction will first be given. After investigating the synthetic aspects, various hybrid material systems produced by this route will be critically reviewed. A large portion of the existing published literature in the ceramer area originates from the laboratory of Professor Garth Wilkes. Hence the

reader is made aware that this part of the chapter will appear to focus a great deal on the work of this lab; however other researchers have contributed to the area as well and will certainly be acknowledged and discussed.

Two of the ceramer projects in this dissertation deal with novel sol–gel materials based on poly(propylene oxide) and tetramethoxysilane (Chapters 3 and 4), and another deals with abrasion resistant coatings for metal substrates (Chapter 5).

2.2 The Sol-Gel Reaction

2.2-A. Introductory comments

Firstly it may be beneficial to dissect the very term "sol-gel". The term *sol* itself implies a liquid or soluble fraction. *Gel* generally describes that part of a reacted system that has reached the gel point, or percolation threshold which implies extensive connectivity on a molecular level. The gel point occurs at a critical extent of (a network) reaction when there exists at least one large molecule* of macroscopic dimensions and "infinite" molecular weight.[1] Further reaction may occur beyond the gel point in which crosslink density may increase and molecules present in the sol fraction may react into the network structure. Some general characteristics of the gel include insolubility and infusibility.

Many inorganic oxide glasses (e.g. soda-lime glass, borosilicate glass, fused quartz, etc.) are infinite networks. Before the discovery of the sol-gel process, production of these materials could only be accomplished by melting mixtures of e.g. sand, sodium carbonate (or sulfate) and limestone which requires extremely high temperatures, in excess of 1000 °C. After bubbles of gas have been expelled from this melt, the amorphous liquid is rapidly vitrified to prevent crystallization.[2] Hence it is in the form of a supercooled liquid, or glass. Similar, but purer types of glasses can be synthesized by the sol-gel reaction involving (generally liquid) metal alkoxides, water, and often a

* *Note the coexistence of a sol fraction which contains many smaller molecules that are distinct from the network structure.*

catalyst. The polycondensation reaction (the formation of the network) can take place in this liquid mixture at much lower temperatures[3] than conventional melt processing. The sol-gel route does have some limitations. The most obvious of these is that for pure sol-gel systems in general, only thin films can be produced, rather than large monoliths. This is due to the excessive shrinkage upon curing (because of evaporation of by-products) which leads to cracking of larger bulk samples. This problem can be overcome in some situations, and in fact monolithic samples can be generated by slow controlled drying over the course of weeks or even months.[4] One advantage of the sol-gel route over melt processing is that high purity glasses can be made rather easily as is dictated by the reactant purities. Since the reactants of the sol-gel reaction tend to be liquids, they can be distilled to high purity. Many impurities may exist in melt formed glasses, an obstacle which is extremely difficult to overcome by this process.

2.2-B. Details of sol-gel chemistry

The sol-gel reaction is said to have occurred when a metal alkoxide reacts with water to form a metal hydroxide which condenses into a metal—oxygen—metal sequence, with the liberation of water and alcohol. The metal may be aluminum, tin, cesium, the transition elements titanium, zirconium, the metalloid silicon, etc.[5] Silicon alkoxides have a more controlled and lower reactivity than the other metal alkoxides (details to follow) and hence the majority of the understanding of the sol-gel reaction is derived from materials created from silicon based alkoxides.

Sol-gel chemistry involves two reaction steps. The first step, named the *hydrolysis* step, is illustrated in reaction [A] below for a generalized silane as the metal alkoxide:

$$Si(OR)_4 + 4\,HOH \rightarrow Si(OH)_4 + 4\,ROH \qquad \text{Reaction [A]}$$

The R group represents an alkyl chain such as methyl, ethyl, isopropyl, *tert*-butyl, etc., and the nature of this group plays a role in the rate of the hydrolysis reaction (i.e. inductive and steric factors). In general, the smaller such groups are, the faster the reaction so that tetramethoxysilane, (TMOS, where R = methyl), undergoes hydrolysis faster than tetraethoxysilane, (TEOS, R = ethyl), other conditions being the same. The R

group is also important to the shrinkage during curing as losing more volume (with larger ROH molecules) causes greater shrinkage. The mechanism of reaction [A] proceeds in three stages. First, the "metal" atom of the metal alkoxide (in this case the metalloid silicon) undergoes nucleophilic attack by the oxygen atom in a water molecule. While the silicon atom is in this penta-coordinated state, a proton is transferred from the water molecule to an OR group on the same silicon atom. Finally, the ROH molecule is released from the silicon atom.[6]

The second step in the sol-gel process is the *polycondensation* step which can take place by either of the two sub-reactions in [B] below:

$$\equiv Si—\mathbf{OH} + \mathbf{HO}—Si\equiv \rightarrow \equiv Si—O—Si\equiv + HOH$$

$$\equiv Si—\mathbf{OR} + \mathbf{HO}—Si\equiv \rightarrow \equiv Si—O—Si\equiv + ROH$$

Reaction [B]

The existence of the second sub-reaction implies that the hydrolysis step shown in reaction [A] need not be complete for polycondensation to begin. Both sub-reactions in [B] lead to the same ≡Si—O—Si≡ bridge. Note that the reactant silanes in reaction(s) [B] have three other reactive sites that are not shown (recall the original silane structure from reaction [A]) which may participate in network development. All three reactions in [A] and [B] are reversible.

Although not universally accepted, many scientists believe that two moles of water are required for every one mole of tetrafunctional alkoxide in the sol-gel reaction. This was alluded to before upon pointing out that the hydrolysis step need not be complete for condensation to begin. If this is the case, a net loss of four moles of alcohol would occur upon complete conversion of one mole of tetrafunctional silicon alkoxide to the amorphous silicon dioxide network.

2.2-C. Reactivity of various metal alkoxides

For the example given above involving a tetrafunctional silicon metal alkoxide, it was said that during the sol-gel process the silicon atom becomes penta-coordinated. This implies that the reactivity of a metal alkoxide may be influenced by its ability to increase its coordination number, *n*, in the network oxide. If *z* is the oxidation state of

the metal atom in the alkoxide, then one can define the degree of unsaturation of the metal atom as *n-z*. Hence increasing the quantity *n-z* denotes increasing the coordination number of the metal atom when going from the alkoxide to the network oxide state. For example, the tetra-coordinated alkoxide titanium (IV) butoxide forms a network of TiO_2 in which the titanium is hexa-coordinated. This yields a value of *n-z* of two (six minus four). Metal alkoxide reactivity is also dependent upon the strength of the nucleophile (i.e. water, silanol, etc.) and the electronegativity of the metal atom. Electronegativity is defined as the power of attraction for the electrons in a covalent bond,[2] and hence varies from atom to atom. As a general (but not perfect) rule of thumb for alkoxides, electronegativity and reactivity are inversely related, i.e., as the electronegativity of metal atoms increases, the chemical reactivity of the corresponding metal alkoxides decreases.[5] Data for electronegativity, coordination number in the network oxide (*n*), and degree of unsaturation (*n-z*) are given in Table 1 for isopropoxides of various metal atoms. The elements cesium and fluorine are included as a reference since they have the lowest and highest electronegativities of all elements, respectively. Since silicon has a high electronegativity and a low degree of unsaturation (relatively), sol-gel reactions involving silicon alkoxides are slow. For the same R group, reactivities of metal alkoxides follow the order:[5]

$$Ce(OR)_4 > Zr(OR)_4 > Ti(OR)_4 \; ; \qquad Sn(OR)_4 >> Si(OR)_4$$

Tin has a higher electronegativity than silicon but its alkoxide is much more reactive than the corresponding silicon alkoxide implying that the degree of unsaturation also plays a role in metal alkoxide reactivity. In fact this has been suggested as the main driving force for the reactivity of non-silicate metal alkoxides towards nucleophilic attack.[7] All non-silicate metal alkoxides react quickly and hence generally require chemical additives to slow the reaction. This can be accomplished by the addition of inorganic acids, β-diketones, carboxylic acids, or other ligands.[8]

The use of complexing ligands is a popular way of stabilizing non-silicate metal alkoxides. Ethylacetoacetate (EAcAc), for example, complexes with metal alkoxides by forming metal—AcAc bonds which are much less susceptible to hydrolysis than

metal—OR bonds. This inhibition is likely related to steric factors and the strength of the metal—AcAc bond (i.e. the strength of the ligand). An important point that must be considered when using complexing ligands is that they remain in the resulting material and hence may affect final properties. Complexing ligands can also serve as surface altering agents for nanoparticles in a reacting sol. The effect of this is to prevent the particles from agglomeration or promote chemical stability (by retarding reactivity).

2.2-D. Influence of catalyst

Sol-gel reactions involving silicon alkoxides generally require a catalyst to increase the reaction rate. This can be either a base or an acid. Each influences the sol-gel reaction in a different manner. Acids tend to increase the rate of the hydrolysis step, by promoting the protonation of the alkoxo group (OR), while having little effect on the polycondensation step.[5] Bases, on the other hand, increase both the hydrolysis and the polycondensation step.[5,9,10] This occurs due to the presence of OH^- and $Si–O^-$ species which are better nucleophiles than water and silanol, promoting the rapid attack of silicon.[5] Under such conditions, hydrolysis and condensation occur simultaneously. This promotes a different structure than that formed from the same reactants under acid catalysis. The end result of base catalyzed reactions is generally a highly branched, dense particulate species (reaction-limited, Eden cluster). Under acid catalyzed conditions, the end result is more of a linear species usually referred to as a diffusion-limited aggregate (DLA). These structures possess self similarity at different length scales, an attribute known as fractal character.* Such behavior can be identified by a power law shape of the small angle x-ray scattering (SAXS) data in the Porod (tail) region. In this region, the scattered intensity, *I(s)* is related to the scattering vector *s* as:[11]

$$I(s) \propto s^{-d_f}; \qquad s = \frac{2\sin q}{l} \tag{1}$$

* *Another term having the same meaning as self-similarity and fractal behavior is dilation symmetry. These all refer to the characteristic of some materials whose structure at different size scales (i.e. nanometer, hundreds of nanometers, etc.,) resemble each other.*

where q is one-half of the radial scattering angle (the Bragg angle), l is the incident beam wavelength,[12] and d_f is the fractal dimension, which is an index of the "openness" of the molecular structure.[13] A mass fractal has the characteristic that its mass M scales as a power of its length or size, i.e. $M \propto (length)^{d_f}$. Mass fractal dimensions are always less than the dimension of space in which they occupy and hence d_f is always between one and three for a mass fractal.[14] A uniform, three dimensional solid has a fractal dimension of 3. The lesser the fractal dimension is compared to the dimension of space it occupies, the more open the structure. Surface fractals have the attribute of their surface area scaling with a non-integer power of length between three and four. It has been suggested that for a material to truly display fractal behavior it must maintain a constant slope in the Porod region over at least one decade of s,[15] although some have proposed that trends can be discerned for slopes extending over only one half decade.[11] A SAXS plot of *log I(s)* vs. *log s* in the Porod region is linear with slope $-d_f$ between –1 and –3 if a mass fractal is present, or a slope of (d_f-6) between –3 and –4 if a surface fractal is present.[11,*]

Different acid catalysts lead to varied hydrolysis and condensation reaction mechanisms. This is evidenced by the fact that the hydrogen ion concentration alone (i.e. pH) does not dictate the reaction rate. Gel times for TEOS have been observed for different acid catalysts all of the same concentration (0.05 moles of acid per mole of TEOS) as illustrated in Table 2. Note that the initial solution pH is not an indicator of gelation time. Hence the effect of catalyst structure on the mechanism of the sol-gel reaction is complex. Note also in this table that the gel time for this silicon alkoxide, when no catalyst is employed, is approximately an order of magnitude longer than the gel times in the presence of the various catalysts listed.

---

[*] *The relationship between the Porod slope and the fractal dimension given above are for pin-hole collimated (point source) x-rays. For slit–collimated instruments (i.e. the Kratky type) the slope can be corrected to that given by a point source by substracting 1 from the smeared value.*

2.2-E. Influence of water

Since water is a reactant in the sol-gel process, its presence plays a role in the reaction kinetics and final structure of the material. In as early as 1951 it had been observed that the hydrolysis reaction rate was first order with respect to the water concentration under acid catalysis and independent of water concentration under basic catalysis.[16] As for the effects on gel structure, adding insufficient amounts of water tends to promote a linear structure.[17] Increasing the amount of water in the reaction tends to densify the structure as evidenced by an increase in the fractal dimension observed by Nogami and Nagasaki.[18] Their systems, involving mixed zirconium and silicon alkoxides, displayed a range of the Porod slope (slit smeared data) of –0.5 (lowest water content) to –1.5 (highest) implying that all structures are still relatively linear, although a densification trend is certainly evident.

A convenient way to express the amount of water employed in the sol-gel reaction is through the hydrolysis ratio, *h*, defined as the ratio of moles of water per mole of metal alkoxide.[5] For *h* less than two, the alcohol liberating polycondensation reaction is preferred, but for *h* greater than two, the water forming condensation is favored[6] (recall reaction [B]).

2.2-F. Influence of solvent

By varying the solvent in the sol-gel reaction, one varies the types of interactions present. This results in changing the overall reaction rate, and in a very general sense, the effect of solvent on rate can be ranked by the following:[19]

- *Promoting fastest rates*, non–polar, aprotic solvents (i.e. dioxane),
- *Promoting intermediate rates*, polar, aprotic solvents (i.e. DMF, acetonitrile),
- *Promoting slowest rates*, polar, protic solvents (i.e. methanol, formamide).

Polar, protic solvents with strong dipole moments tend to deactivate the reactants by stabilizing their charges and solvating the metal alkoxide, hence slowing down the reaction rate. Also hydrogen bonding may take place between a polar solvent (i.e.

formamide) and the silicon species thereby slowing the reaction by way of steric hindrance.[20] These effects lessen as the opposite extreme is reached, non–polar, aprotic solvents, where essentially only dilution of reactants is achieved.

2.3 Hybrid Materials by the Sol-Gel Process

2.3-A. Introductory comments

The sol-gel technique has been exploited in the past to produce both crystalline and non-crystalline ceramic oxides. Realizing the flexibility of this technique, organic components have been incorporated into the crosslinked sol-gel network to produce hybrid organic-inorganic materials. There are three known ways to accomplish this;[21] firstly, due to the porous nature of the oxide gels created from the sol-gel approach, organics can be impregnated into these voids thereby forming the hybrid. There are no covalent connections between the organic and inorganic components by this route. An example of this type of hybrid was prepared by Pope and Mackenzie[22] and Abramoff and Klein[23] involving the impregnation of the pores of silica gel with liquid methylmethacrylate which is subsequently polymerized to yield a transparent hybrid film. In the second route, the organic can be added to the sol-gel reaction before gelation when the mixture is still in a liquid state. Gelation of the inorganic oxide then traps the organic component within the three dimensional network. Hybrids prepared in this way also do not possess covalent links between the two phases. Oxide gels have been impregnated by this route with organic materials such as dyes,[24] poly(methyl methacrylate), polycarbonate (PC), poly(vinyl acetate), [25] poly(acrylonitrile), poly(2-pyridine),[26] poly(vinyl alcohol),[27] and poly(ethyloxazoline)[28] to name a few. The third route to make sol-gel hybrids involves reacting appropriately functionalized organic molecules directly into the inorganic network. In doing so, covalent bonds exist between the organic and inorganic components. Hybrids made by this technique involving *low molecular weight organics* were coined *ormocers* and *ormosils*,[29,30] ("organically modified ceramics" or "silicates"). A similar sol-gel approach involving metal alkoxides and functionalized *polymers* or *oligomers* led to materials created at

nearly the same time* coined *ceramers*[31-33] (recall the combined word of "ceramics" and "polymers"). The term *ceramer* has dominated the literature in this area,[34] and these materials were first produced in 1985 in the laboratory of Professor Garth Wilkes.[31] Since then this research group has published much in the area.[35-60]

The following literature review will track the chronological order in which the research was published. Novel structural materials were the first type of ceramers to be produced and will be the first discussed. Next came high refractive index materials which will then be reviewed with a final strong emphasis on abrasion resistant coatings.

2.3-B. Early CERAMERS as novel materials

The incorporation of oligomeric PDMS ($\overline{M}_n$ = 1700 g/mol) into a sol-gel reaction to produce a transparent film was first accomplished by Wilkes et. al.[32] The silanol termini on the PDMS chains participated in the sol-gel reaction of TEOS. Hence an amorphous network (evidence from wide angle x-ray scattering[33]) was formed from the co-condensation of PDMS and TEOS in the presence of an acid catalyst (HCl). The chemistry for network formation (the co-condensation step) is shown below:

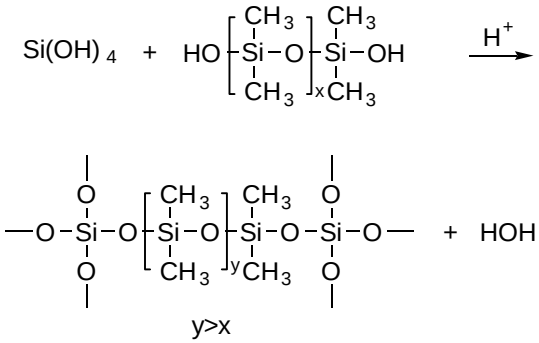

Reaction [C]

The step involving hydrolysis of TEOS is not shown since it is exactly the same as reaction [A].

---

* *The first* ceramers *synthesized were not hybrid organic-inorganic materials, being made from tetraethoxysilane and PDMS both of which are considered inorganic.*

The preparation method was as follows. Both TEOS and PDMS were simultaneously charged to a reaction flask and acid was subsequently added. Since the TEOS must hydrolyze to some extent before it can condense, the PDMS oligomers may chain extend (i.e. self-react) by reaction through their terminal silanols. This was believed to occur to some extent, but increasing the acid content lessened this event. Increasing the acid content accelerates the hydrolysis rate of TEOS, thereby permitting condensation of TEOS to begin sooner. This reduces the time allowed for the chain extending reaction of PDMS. Dynamic mechanical spectroscopy (DMS) was employed as a characterization tool for the TEOS-PDMS systems. For a system containing 48 wt.% TEOS, the tan*d* data showed two peaks, one at –106 °C and one at –10 °C. The lower temperature peak was assigned to phase separated, chain extended PDMS regions, while the higher temperature peak was assigned to oligomeric PDMS chains incorporated into the polysiloxane structure. The glass transition temperature for pure PDMS is –120 °C.[61] The shifting of the tan*d* peak upwards to –106 °C was attributed to the constraints on the ends of the phase separated PDMS chains imposed by the direct bonding to the glassy matrix. The larger shift to –10 °C is attributed to the greater confinement of the oligomeric chains in the glassy matrix. It was also observed that increasing the acid content in the reaction medium decreased the magnitude of the –106 °C peak and increased the magnitude of the –10 °C peak. This behavior was attributed to the acid effect on the hydrolysis reaction rate mentioned above. At higher acid concentrations, the hydrolysis rate of TEOS is faster and hence there is less time for PDMS chain extension and ensuing phase separation. Another phenomenon potentially caused by the higher acid concentration is the “scrambling” of PDMS chains. This corresponds to a broadening of the molecular weight distribution of the PDMS oligomers.

Tensile stress-strain experiments indicated that the materials were quite flexible, unlike inorganic glasses. Elongation at break for some samples approached 20%, evidence that the rubbery PDMS formed a continuous phase in the overall material. This suggests therefore that at least some of the PDMS chains have become

incorporated into the inorganic network. Again higher acid content yielded, in general, more flexible materials (which possessed lower Young's moduli) credited to better dispersion of the rubbery polymer into the inorganic matrix. SAXS was also employed as a tool for determining the relative amount of dispersion of the rubbery component into the glassy matrix by way of monitoring the mean–square electron density fluctuations, $\langle \Delta r^2 \rangle$ in the samples. The quantity $\langle \Delta r^2 \rangle$ is a relative index of homogeneity when used to compare samples of similar formulation; the lower its value the more homogeneous the system.[62] The trend observed was decreasing $\langle \Delta r^2 \rangle$ with increasing acid content in agreement with the DMS results. Homogeneity could also be improved by utilizing lower molecular weight PDMS chains. This is evidenced by comparing the DMS data of ceramers made with 550 or 1700 g/mol oligomers. The ceramers made from the lower molecular weight PDMS displayed a much broader tan*d* curve and a much lower magnitude low temperature peak associated with phase separated, chain extended PDMS.

Increasing the TEOS content was expected to produce a more brittle, glassy material. This was not precisely the case as the 60 wt.% TEOS samples behaved similarly to the 48 wt.% TEOS materials. The authors indicated that two different effects could be balancing each other; greater TEOS may lead to more glass-like behavior but may also lead to better dispersion of the rubbery components.[32] They did witness a general (but small) increase in the storage moduli with increasing TEOS content, when comparing 48, 60, and 70 wt.% TEOS materials.[33]

Mackenzie et. al. have synthesized analogous TEOS-PDMS hybrids and examined the effect of catalyst on microstructure.[21] They found that increasing the concentration of HCl in the sol-gel reaction led to more highly porous final products.

With the success of PDMS incorporation into TEOS networks, later work involved assembling hybrid networks from TEOS or TMOS and oligomeric chains of the crystallizable homopolymer poly(tetramethylene oxide) (PTMO).[35] The short hydroxyl–terminated PTMO chains ($\overline{M}_n$ of 650, 1000, 2000, and 2900 g/mol) were first end-functionalized with triethoxysilane groups (Reaction [D])

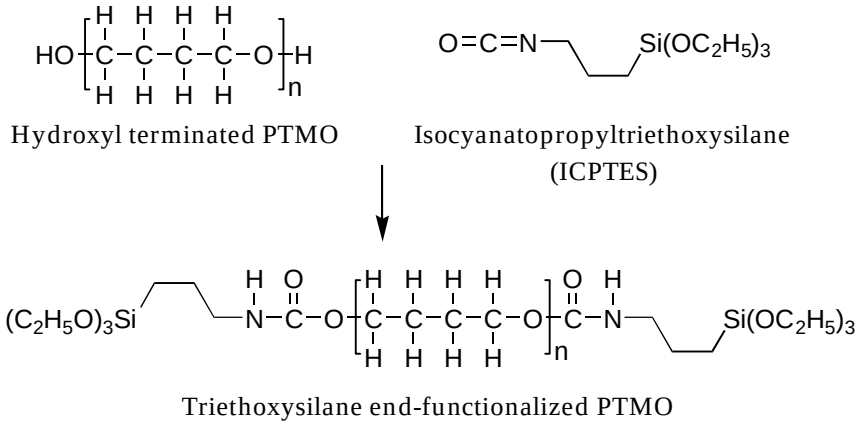

Reaction [D]

which later become active in the sol-gel reaction. To achieve this, hydroxyl terminated PTMO is reacted with the isocyanate group of isocyanatopropyltri-ethoxysilane (ICPTES) (in the ratio of 1 mole PTMO to 2 moles ICPTES) forming two urethane linkages. The triethoxysilane moieties then act as the reactive sites in the sol-gel reaction. The effect of these end–groups is to increase the functionality of the PTMO (from two for hydroxyl terminated PTMO to six for each triethoxysilane end–capped linear chain). This would result in better compatibility between the inorganic and PTMO components in the network structure and improved mechanical properties through higher potential crosslink densities.

Pure PTMO homopolymer can crystallize at room temperature. In fact the two higher molecular weight (functionalized) oligomers used in this study had to be heated above room temperature to melt the crystalline phase before addition to the reaction medium. However, after the sol-gel reaction was complete, a photographic WAXS pattern showed no evidence of crystalline reflections, only an amorphous halo. Supporting (and stronger) evidence was found from DMS and DSC during a temperature sweep from –100 °C to 150 °C where no melting processes were observed. A sample was also strained to 50% elongation in an attempt to strain induce crystallize any phase separated PTMO chains but the WAXS photograph showed no sign of crystalline reflections. This was evidence of good PTMO incorporation into the network structure.

However, a ceramer made from triethoxysilane end–functionalized PTMO oligomers (2000 g/mol) without additional metal alkoxide does display crystallizability.[63] The original film was amorphous, however, while heating the sample through the crystallization window during a dynamic mechanical experiment, a sudden increase in the storage modulus *E'* occurs at ≈ –70 °C. Complete melting is observed just above 0 °C, as evidenced by a corresponding sharp decrease in *E'*. But in general, the PTMO based ceramers containing a significant amount of TEOS or TMOS are not crystallizable, implying that the oligomeric chains are well dispersed in the inorganic matrix.

A hypothesized morphological model of these hybrid materials is shown in Figure 1. This model suggests the existence of condensed TMOS clusters in a matrix rich in PTMO. SAXS experiments show a peak assigned to the average distance between clusters. This peak becomes sharper and shifts to lower values of the scattering vector ***s*** for increasing PTMO molecular weight. This behavior corresponds to sharper phase separation of the inorganic and organic components and larger distances between inorganic clusters. Incorporating lower molecular weight PTMO chains leads to more uniform dispersion and smaller electron density fluctuations.

The authors have suggested that the correlation distances obtained from SAXS may reflect the end-to-end distance of the oligomeric PTMO chains since these chains are the linking structures between the glassy silicate domains. As a first approximation they have employed the Flory-Fox equation for the r.m.s. (root mean square) end-to-end distance for a linear Gaussian chain.* A plot of their data comparing the calculated $\sqrt{\bar{r}_0^2}$ to the experimentally determined correlation distance is given in Figure 2.

In comparison to the PDMS-TEOS hybrids, the PTMO containing materials display much improved tensile properties, such as a higher elongation at break, proving that

---

* *Wilkes et. al.[35] utilized the approximation of the unperturbed r.m.s end-to-end distance for a linear statistical chain by the equation* $\sqrt{\bar{r}_0^2} = 0.093\sqrt{\bar{M}_v}$ *which is for a dilute solution of PTMO chains in isopropanol at 46°C (theta conditions). The authors acknowledge that at these low molecular weights, the chains are not likely to behave completely Gaussian.*

these newer systems are more flexible. From the DMS data for both of these materials, the PTMO hybrids appear to have slightly higher storage moduli in the plateau region than the PDMS containing systems.[32,35] A titanium based metal alkoxide was co-reacted into the PTMO–TEOS hybrid.[36,38] However, due to the much more rapid reaction of the titanium based alkoxide (compared to the silicon based alkoxide), a chemically controlled condensation method[64] was employed to synthesize these ceramers.[36] The result of titanium incorporation into the hybrid was higher Young's modulus and ultimate strength but lower elongation at break.[36] This was attributed to the catalytic effect of titanium on TEOS condensation causing a "tighter" network structure. SAXS evidence has shown that the structure of hybrids with and without titanium are qualitatively the same but titanium systems have larger electron density fluctuations, leading to greater integrated intensities (and greater values of the invariant).

To improve the integration of PTMO into the hybrid network a series of altered PTMO oligomers were synthesized.[39] The new 5800 g/mol oligomers contained one, two, or three triethoxysilane groups along the backbone in addition to the two at the chain ends. This greatly increases the functionality of the PTMO in the sol-gel reaction and hence the extent of incorporation into the inorganic framework is increased. The resulting materials had higher moduli and lower elongation at break than materials produced from end-functionalized, 5800 g/mol PTMO. Increasing the TEOS content has a similar effect although once an initial amount of 70 wt.% TEOS is reached a phase inversion likely occurs (leading to a continuous glassy phase) since the elongation at break suddenly drops.

Successful employment of a polymeric acid catalyst, poly(styrene sulfonic acid) (PSS), has shown improvements in the mechanical properties of such ceramers.[53] The polymeric acid catalyzed material showed a higher Young's modulus, higher plateau storage modulus, and less loss dispersion behavior than the same respective HCl catalyzed ceramer. SAXS response was the same for both systems, but the PSS

catalyzed system showed a weight loss by thermogravimetry (TG*,[65]) of ≈ 16% at low temperatures (between 100 and 160 °C) where the HCl catalyzed material was stable. This was tentatively assigned to entrapped solvent. However, the final char yields for both the HCl and PSS catalyzed ceramers were nearly the same, with the PSS catalyzed materials having a slightly larger but reproducible amount of residue.

Closer examination of the structure of PTMO–TEOS ceramer materials by Rodrigues and Wilkes using SAXS led to a better understanding of the nature of the growth of the inorganic phase within the hybrids and the characteristics of the microphase separation.[11] More specifically, these investigators explored the structure of various ceramer systems through fractal analysis. Two important regions of the SAXS profiles were investigated, the Porod region (tail), where fractal dimensions can be determined, and the Guinier region, where the electronic radius of gyration can be resolved.

The influence of gelation time on the SAXS profiles (intensity versus *s*) of a 20 wt.% PTMO–TEOS hybrid [henceforth denoted PTMO(80) TEOS(20)] was quite significant. Increasing cure times of 30 minutes, 2 hours, 12 hours and 2 weeks showed an increase in the absolute intensity at the peak position and a small decrease in the corresponding long spacing. The increased intensity is due to further network reaction, densification of the inorganic phase, and sharper phase separation between the inorganic phase and the PTMO oligomer chains. The decrease in the long spacing is a result of evaporation of solvent causing the PTMO chains to contract. The same data plotted as *log I(s)* vs. *log s* provides information on the fractal character and plotted as *log I(s)* vs. s^2 supplies (more conveniently) the electronic radius of gyration (henceforth denoted $\bar{r}_{G,z}$). The results of their experiments are presented in Table 3. For the 30 minute cure time, the Porod slope had a value of –1.28 (d_f = 1.28) implying that the mass of the scattering entity scales nearly linearly with its length. The radius of gyration associated with these scattering entities is 6 Å, which suggests that the scattering particles are just a few

---

* *The International Confederation for Thermal Analysis (ICTA) has abandoned the old terminology of thermogravimetric analysis, TGA.*[65] *The use of the abbreviation TG for thermogravimetry should not be confused with that of the glass transition temperature, T_g.*

repeat units in length. After a 2 hour cure time, the fractal dimension increases to 1.59 and therefore the structure is becoming more compact. The scattering particles are also becoming larger as evidenced by the increase in the radius of gyration to 10 Å. At both 12 hours and 2 weeks, this trend continues, but there is a break in the slope within the Porod region yielding an additional slope at larger angles. The decrease in the low–angle slope from –2.4 (12 hours) to –2.69 (2 weeks) indicates that the network reaction is still proceeding at the "primary" silicate particles located at the PTMO chain ends. Also, the decrease in the higher angle slope from –1.54 (12 hours) to –2.0 (2 weeks) suggests that some "secondary" particles are physically trapped within the network, providing a more mixed state. The process of nucleation and growth is typified by such increase in primary particle size at the expense of secondary particles. Most likely, the PTMO chain ends are the nucleation sites for the silicate particles. Upon nuclei formation, phase separation ensues and the silicate particles grow. Secondary particles diffuse towards nucleation sites, reacting with available TEOS during this process causing growth and convolution. The development of two slopes also insinuates that monomer-cluster type growth is occurring. For this type of growth, monomers are continually reacting into the network, as opposed to cluster–cluster growth where larger structures are developed early on followed by connection between clusters. For materials synthesized with a large PTMO content (many chain ends and hence nucleation sites), later stages of growth appear to be more cluster–cluster like due to transport limitations.

Varying the amounts of TEOS and PTMO in the hybrids changes the general structure of the final products. Increasing the relative amount of PTMO increases the amount of chain ends and hence nucleation sites. This leads to a system with a larger number of smaller silicate particles, which was witnessed in the SAXS profiles. One final point regarding SAXS characterization of these ceramer systems is that solvent plays a significant role in their ultimate structure. For the co–solvent system of N,N' dimethylformamide (DMF) and isopropanol (IPA) the inorganic and organic domains

are well phase separated in contrast to the co–solvent system of tetrahydrofuran (THF) and IPA where a greater degree of phase mixing is present.

Surivet and coworkers[66] synthesized ceramers based on PDMS oligomers, without additional metal alkoxide. One of their synthetic pathways involved a polyurethane prepolymer process. This technique generated an isocyanate–terminated polyurethane prepolymer (with oligomeric PDMS as the soft segment), which was later reacted with 3-aminopropyltriethoxysilane to form an alkoxysilane–functionalized polyurethane prepolymer. After employing this material in the sol–gel reaction, the resulting ceramer was essentially a hybrid of a segmented polyurethane–urea crosslinked through alkoxysilane endgroups. These materials showed two distinct glass transitions by DMS, one corresponding to the phase separated soft segment (PDMS), and one corresponding to the softening of the phase separated hard segments. SAXS investigations led the authors to propose a similar structural model as Wilkes (recall the model shown in Figure 1). Since these authors did not employ metal alkoxides in their ceramer formulations, the silicate phase is smaller than that depicted in Wilkes' model (i.e., only due to endgroup crosslinking). Similar ceramers were prepared in this same work based on hydrogenated 1,2 polybutadiene oligomers.

Aging in a controlled pH environment has been observed by Brennan and Miller to change the morphological features of ceramers.[67] Soaking a PTMO(60) TEOS(40) ceramer in a 70% ethylamine / water solution (basic) for 25 hours promotes sharper phase separation of inorganic and organic components. This is evidenced from DMS and SAXS fractal analysis. Sharpening of the tan*d* peaks and lowering of the glass transition temperature (approaching that of PTMO homopolymer) illustrated the phase demixing. The structure also changed from a mass fractal (smeared Porod slope –1.42, fractal dimension 2.42) to a surface fractal (smeared Porod slope –2.1, fractal dimension 2.9). Similar results were obtained by Betrabet and Wilkes upon soaking PTMO(50) TEOS(50) films in 1 M NaOH.[56] DMS experiments showed better chain mobility in the PTMO domains (again shifting of T_g to lower values) attributed to sharper phase separation. The amorphous silicon dioxide network is soluble in the basic NaOH

solution and thermogravimetry showed a lower char yield of the treated ceramers due to dissolution of some of the SiO_2. Identical soaking treatment of a titanium isopropoxide containing ceramer [PTMO(50) TiOPr(50)] resulted in little change in the properties of this hybrid, a result of the lower solubility of titanium dioxide in basic media.

Other pioneering research in the sol-gel hybrid network area originated in Germany in the laboratory of Helmut Schmidt. A particular focus of Schmidt was on generating materials for use in contact lenses.[29] For this application there are several material property requirements:

- Sufficient flexibility, high hardness and scratch resistance,
- refractive index at the sodium D line, $n_D > 1.43$, transmission > 98%,
- less than 10 wt.% water uptake, little interaction with lachrymal fluid of the eye, no toxic materials in the sol–fraction,
- good wettability with water (contact angle < 30° in the hydrated state),
- sufficient oxygen permeability to supply the cornea (permeability coefficient > 1E-11 ml O_2 cm^2 ml^{-1} s^{-1} $mmHg^{-1}$).

The material thus synthesized (termed ormosils, and later generalized to ormocers) which best met these demands was made from a titanium alkoxide (i.e. TiOPr), an epoxysilane, and a methacryloxysilane in the molar ratio 5:90:5, respectively. Monomeric methacrylates were utilized as linear crosslinking agents and were initiated with peroxide. The chemical structures of the epoxysilane and methacrylates employed are illustrated in Figure 3. The monolithic samples generated from these reactants possessed a tensile strength of ≈ 5 MPa, Young's modulus of ≈ 0.34 MPa, Mohs' hardness of 3, refractive index, n_D, of ≈ 1.5, contact angle with water of 25 ± 5°, and an oxygen permeability coefficient of ≈ 1.3E-10 ml O_2 cm^2 ml^{-1} s^{-1} $mmHg^{-1}$, thus meeting all of the criteria.

Another sector of polymer science benefiting from sol-gel chemistry is toughened elastomers. In general, many polymeric elastomers contain reinforcing fillers to

improve the mechanical properties. This is traditionally accomplished with carbon black or silica particles. The processing involved can be rather tedious, and Mark and his coworkers have alternatively generated *in-situ* precipitated silica particles in a crosslinked PDMS network using sol–gel chemistry.[68-80] One possible method involves swelling a preformed PDMS network in liquid TEOS (to a rubber volume fraction of 0.3). Addition of e.g. glacial acetic acid initiates hydrolysis and condensation of TEOS, which may self–react but also can link to the PDMS network through silanol termini within the network elastomer.[69] The growth of the inorganic phase leads to spherical SiO_2 particles (with narrow diameter distribution near 200 Å)[73] which act to stiffen and toughen the matrix material. Acidic catalysts produced less well defined particles than basic catalysts, and high catalyst concentration led to small particles. Synthesizing these types of materials can also be accomplished by simultaneous curing and filling making the process a "one pot" approach.[72] Other metal alkoxides such as n-propyl titanate,[81,*] aluminum tri-*sec* butoxide,[82] and zirconium (IV) n-propoxide[83] have been utilized to generate *in-situ* TiO_2, Al_2O_3, and ZrO_2 particles, respectively. All materials produced as such showed parallel behavior to *in-situ* silica filled PDMS. Mark et. al.[84] have even polymerized styrene within PDMS networks to toughen the material. Stretching of this system above the glass transition temperature of polystyrene (PS) followed by cooling in the stretched state (to below T_g) led to elliptical PS particles. Full recovery from the strained state was not achieved due to relaxation of the PS particles when above T_g. The axes of the elliptical particles oriented parallel to the stretch direction. Young's modulus measured at room temperature in the machine direction (MD) was higher than that of a similar isotropic material. The modulus of the stretched material measured in the transverse direction (TD) was lower than the isotropic modulus. Other organic polymer-inorganic glass composites made by Mark et. al. include incorporated aramid[85] and polyimide.[86,87]

---

[*] *n-propyl titanate is also known by the name titanium (IV) n-propoxide.*

2.3-C. High refractive index hybrid ceramer systems

The next direction pursued in the ceramer area by Wilkes' group involved the generation of high refractive index, optically transparent materials. For this purpose, oligomers of high performance polymers (glass transition temperatures in excess of 120 °C) were employed as the organic component. Poly(arylene ether) ketone (PEK),[43,47] poly(arylene ether sulfone) (PSF),[47] and poly(arylene ether phosphine oxide) (PEPO)[52] with amine termini allowed for end-functionalization with isocyanatopropyltriethoxysilane analogous to the process shown in Reaction [D].

PEK-TEOS glasses were made by blending the desired amounts of PEK and TEOS with a calculated amount of water and HCl catalyst in a solvent. Curing was accomplished at either 25, 100, or 200 °C. The final products were translucent glasses which varied from yellow to auburn. At high TEOS loadings, some turbidity is observed and is likely due to phase separation of large silicate particles. Soxhlet extraction indicated that the glasses cured at 25 °C did not reach a high extent of network reaction. This was credited to a time-temperature-transformation (tTT) effect.[88] That is, as the reacting sol grows in molecular weight, the T_g of the mixture increases until finally it reaches the reaction temperature and vitrification freezes the reaction. Differential scanning calorimetry (DSC) provided supporting data for the vitrification claim. For a 100% functionalized PEK glass, stepwise DSC scans of the same sample to higher and higher limit temperatures showed a systematic increase in the T_g. As a result of this vitrification, glasses cured at 25 °C displayed poor mechanical properties. Glasses cured at 100 °C possessed sufficient crosslink density to promote good mechanical properties (i.e. high toughness). Curing at 200 °C generated brittle materials due to very high crosslink densities. A generalized morphological model was proposed for these hybrids which loosely resembles that in Figure 1, however with considerably sharper phase separation between inorganic and organic domains. SAXS profiles of selected glasses generally showed a correlation distance associated with distances between inorganic clusters.

Functionalized PEK, PSF,[47] and PEPO[52] were incorporated into transparent hybrid glasses along with titanium isopropoxide. Curing above the glass transition temperature of the homopolymer was deemed necessary for sufficient network development. Increasing the weight fraction of titanium alkoxide in the material led to a linear increase in the index of refraction at the sodium D line (n_D, where the wavelength is 589 nm) for all three functionalized organic precursors. The PEK based ceramers showed an increase in n_D from ≈ 1.60 to 1.74 when the initial titanium alkoxide content was varied from 0 to 70 wt.%. Similarly, the PSF based ceramers showed a variation in n_D from ≈ 1.61 to 1.76 for a variation of titanium content from 0 to 75 wt.%. PEPO based ceramers prepared with 95 wt.% titanium alkoxide yielded a value of n_D as high as 1.80.[52] However, the dependence of refractive index on wavelength of the above ceramers (quantified by the Abbe number, $v_D = (n_D - 1)/(n_F - n_C)$, where F and C correspond to light of wavelengths 486 and 656 nm, respectively) is rather high but lies between that of organic polymers and inorganic glasses.[47]

2.3-D. Abrasion resistant coatings

Inorganic glasses are typically hard, abrasion resistant materials. Glass forming organic polymers (e.g. polycarbonate (PC), PMMA, PS, etc.) are typically "soft" and sensitive to scratching. The main advantage of organic glasses over inorganic glasses is their lower density; however a trade-off in scratch resistance is evident. Since organic glasses are replacing inorganic glasses in many applications due to weight reduction, a driving force exists for generating thin, optically transparent abrasion resistant coatings for these soft substrates.

Transparent hybrid coating materials can be synthesized from silane functionalized *low molecular weight* organic molecules. In 1990 Schmidt and Wolter prepared hard coatings for PC (MAKROLON®).[89] The authors used aluminum tri-*sec* butoxide, a trimethoxyepoxysilane, and a triethoxypropylsilane in the molar ratio 2:5:3 to create 5 micron coatings by dip coating and curing between 90 and 130 °C. Abrasion tests were

performed on a Taber Abraser instrument which utilizes aluminum oxide particles to wear the sample surface. Abrasion resistance was then determined by measuring haze after wearing the sample. A significant improvement in abrasion resistance over the uncoated control was observed.

Wilkes' group also generated abrasion resistant coatings for soft polymeric glasses. For this purpose, functionalized melamine and tris(*m*-aminophenyl) phosphine oxide[54] were incorporated into the sol-gel process by way of compatibilizing solvents (DMF, THF, IPA). Shortly after adding aqueous HCl the solution was spin coated onto PC sheet (LEXAN® bisphenol-A type) and allowed to dry in a 60 °C oven until the coating was no longer tacky. Thermal curing at temperatures near 130 °C (always remaining below the glass transition temperature of polycarbonate, to avoid substrate warping) for 12 hours led to the final products. Coating thickness ranged from 1 to 3 microns, as observed by scanning electron microscopy (SEM). After abrasion, light transmittance (420 nm wavelength) was measured through the abraded area. For applications such as eyeglass lenses, it is important for the PC to maintain transparency to visible light. Low wavelength light (420 nm) was chosen since shorter wavelengths tend to scatter the most (i.e. Rayleigh scattering intensity is proportional to λ^{-4}). Scratches on the surface of PC lead to this diffuse scattering of light which results in a reduction in the transmitted intensity. This test then serves as an index of the abrasive resistance of transparent materials. The abrasion resistive behavior of both the melamine and tris(*m*-aminophenyl)phosphine oxide based coatings was similar in the transmittance test, which was well improved over the uncoated control. The phosphine oxide coating appeared to perform better at a lower number of abrading cycles; however transmittance at 500 cycles was the same for both (~ 96%).* SEM observations led to the conclusions that the uncoated PC is abraded by a ductile plowing process while the two coatings undergo a tearing mechanism. The majority of the surfaces of coated, abraded

* *The human eye can generally detect haziness at as high as » 98% transmittance.*

samples showed little to no wear and the scratches were few and far between. Similar coatings based on bis and trismaleimides performed comparably in the abrasion test.[54]

Much improved abrasion resistant coatings consisted of functionalized 4,4'-diaminodiphenylsulfone (DDS) and also from diethylenetriamine (DETA).[55] Both DDS and DETA were triethoxysilane–functionalized by reaction with a stoichiometric amount of ICPTES. Titanium (IV) isopropoxide and zirconium (IV) n-propoxide were the first metal alkoxides used in conjunction with these functionalized organics. Aqueous HCl served as a catalyst for the network reaction and spin coating was employed to generate samples. A qualitative index of coating adhesion to the PC substrate was accomplished by a standardized Scotch tape test (ASTM D3359), and more quantitatively by a 180° peel test. Adhesion was seen to improve with increasing cure temperature for a given chemistry. Pretreatment of the PC substrate with an oxygen plasma slightly enhanced the adhesive strength between the coatings and their substrates. The oxygen plasma generates polar (—OH, —COOH, etc.) groups on the surface of PC thereby promoting adhesion of the coating by intermolecular mechanisms (H-bonding, covalent bonding into the network structure, etc.). As for abrasion resistance, of the systems studied the best performing was DETA(50) Zr(50) cured at 145 °C. Increasing the amount of zirconium alkoxide in the initial reaction produced more abrasion resistant coatings as determined by the light transmittance test. The same effect is observed for increasing the cure temperature, since a more highly reacted network is likely to be harder and more abrasion resistant. Titanium based coatings did not perform as well as their zirconium counterparts; however, they did exceed the performance of the uncoated control.

Great expansion of PC coating chemistries was latter achieved by Wen and Wilkes.[57,58] The organic components that were functionalized with ICPTES include DETA, glycerol, ethylene glycol, 1,4 butanediol, 1,6 hexanediol, resorcinol, iminobispropylamine (IMPA), and poly(ethyleneimine) (PEI). Among the metal alkoxides were TMOS, TEOS, titanium (IV) butoxide (Ti), zirconium (IV) n-propoxide (Zr), and aluminum tri-*sec* butoxide (Al). For all non-silicate metal alkoxides (with the

exception of titanium (IV) butoxide) a complexing ligand was used (ethylacetoacetate, EAcAc) in the ratio of 0.5 moles of ligand per mole alkoxide. The PC substrates were sometimes pretreated with either an oxygen plasma or primer solution (0.5 wt.% γ-aminopropyltriethoxysilane, APS in IPA) in an attempt to improve the adhesion between coatings and substrates. A Taber Abraser was used with CS-10 wheels and 250 or 500 grams of loading to induce wear in the samples. A simple "direct pull–off method" was utilized to detach the coatings from their substrates and hence quantify the coating adhesive strength. Coatings composed of neat DETA, DETA(62)Ti(38), DETA(62) Zr(38), and DETA(62)Al(38) all illustrate similar abrasion resistant behavior and comparable adhesion strengths. However, coatings that have TMOS incorporated into them show distinctly improved abrasion resistance. For both glycerol and DETA based systems, increasing the amount of TMOS in the coating formulation improves the abrasion resistance; however, an upper limit in TMOS incorporation exists. This is due to the large amount of coating shrinkage (leading to cracking) associated with reacting TMOS and the limiting amount is ≈ 70 wt.% for DETA based and 40-50% for glycerol based coatings. The sole contribution that TMOS gives to the network structure is SiO_2, thus producing a harder, more highly crosslinked and thus abrasion resistant material. All coatings with a significant amount of TMOS in them displayed poor adhesion to the PC substrate, which is likely due to the incompatibility of the inorganic with the organic PC. The two surface pretreatment methods, oxygen plasma exposure and primer solution application, were employed to combat this adhesion problem. X-ray photoelectron spectroscopy (XPS) showed that oxygen plasma treatment of the PC substrate for two minutes increased the surface concentration of hydroxyl and carboxylic acid groups by seven and two times, respectively. This addition of polarity to the PC surface would allow more intermolecular interactions between the coating and substrate and also may permit the coating to covalently bond to the substrate by reaction through surface hydroxyls. Both of these phenomena would increase the adhesive strength between the coating and substrate which was observed in the direct pull–off adhesion tests. The much simpler application of a primer solution also

enhanced the adhesion for TMOS based coatings, and in general showed greater enhancement than plasma treatment. The primer molecule is thought to provide a bridge between the coating and substrate, which will be examined in further detail later.

The effect of extreme "hot-wet" conditions was probed for various systems. Most coatings remained intact after 24 hour exposure to boiling deionized water; however, the abrasion resistance after this treatment suffered in most cases. Analogously, significant drops in the adhesive strength were observed. The exception was the DETA-Zr formulation which was seemingly unaffected by the treatment (from the data it appears that the abrasion resistance may actually increase slightly after the hot-wet exposure).

Attempts have been made in the past to correlate abrasion resistance to coating hardness, with some success. The abrasion rate of a material is inversely proportional to the surface hardness.[90] With less naiveté, the abrasion rate of a substance is dependent on other parameters such as surface roughness, friction coefficient, and fracture toughness as well (a more detailed discussion of abrasion and wear in general will be given in the next section). Realizing this, microhardness tests were employed to see if a correlation existed between the hardness and abrasion resistance of the coatings. An increase in the hardness for the series of neat coatings (no additional metal alkoxide used in the formulation) of hexandiol, butanediol, ethylene glycol, and glycerol was observed which corresponded to an improvement in the abrasion resistance in that same order.[58] However, the coating based on resorcinol was harder than all the coatings in the above series yet displayed less transmittance after 250 cycles on the Taber Abraser than all the coatings in this entire series. Also, coatings with incorporated TMOS revealed no correlation between the measured hardness and the abrasion resistance. Therefore, caution was suggested in using hardness as an index of abrasion resistive character for these ceramer materials.

A diallyl diglycol carbonate resin (CR-39) was also employed as a substrate for abrasion resistant coatings.[58] This material is lightly crosslinked, and in general has

better wear characteristics compared to the bisphenol–A type of polycarbonate. For this substrate a primer solution of 5.0 wt.% APS improved the adhesive strength between the coatings and substrates more than a 0.5 wt.% solution. Much improved abrasion resistance over the uncoated control was noted.

A molecular dynamics simulation of PC chains and an APS primer molecule demonstrated that it was possible to form H–bonds between the PC substrate and primer molecule. The simulation showed that preferential orientation of the primer molecule would occur so that the amine group of APS interacts with the PC chain and the triethoxysilane moiety reaches out and away from the PC.[58] The triethoxysilane can then participate in the sol-gel reaction with the applied coating formulation, thereby forming a bridge between the coating and substrate, enhancing adhesion. However, more recently Li and Wilkes[91] have shown that the APS primer molecule actually reacts with the polycarbonate surface. The amine group of APS reacts with the carbonate to form a urethane linkage, thereby covalently linking the primer molecule to the substrate surface. This then allows the pendant alkoxysilane groups to participate in the sol–gel reaction, once the coating formulation is applied to the primed substrate. Hence the true bonds between the primed PC surface and the ceramer coatings are covalent, rather than secondary.

Other transparent, abrasion resistant sol-gel coatings for polymers have recently been prepared by Schmidt and Kasemann.[92] Their approach was to create a hybrid coating with an imbedded hard inorganic phase with dimensions less than 50 nm (to prevent light scattering and hence turbidity) and an organic component to lend flexibility. The matrix material was an epoxysilane (identical to the structure in Figure 3), with additional TEOS, and the inorganic particles (11 wt.% of the total coating formulation) were provided from a boehmite sol with diameters ≈ 50 nm. This system was either spin or dip coated onto the PC substrates and thermally cured at 100 °C (the cure time was not reported). The authors claim that this coating on PC shows the same Δ% haze value (similar to % transmittance) as float glass after 100 Taber cycles, but no quantitative data were provided.

Similar coating formulations were also applied to aluminum substrates.[92,93] Since aluminum surfaces generally contain hydroxyls (reactive sites in the sol-gel process), direct linking of such coatings to the aluminum surface seems likely. Introduction of a diol in the epoxysilane and propyltrimethoxysilane coating provides additional flexibility, and salt spray results show coated samples are considerably less affected than the control aluminum.

A recent publication in the literature has shown a process of depositing an abrasion resistant coating on PMMA by a plasma process.[94] This process involves three steps, surface activation, polymerization, and post-treatment. After cleansing the PMMA surface, it is exposed to an RF plasma generated in an inert gas. This step is said to provide crosslinking of PMMA at the surface, thereby reducing the amount of low molecular weight species there which would discourage adhesion. The inert gas plasma treatment is claimed to produce a more wettable surface. Various monomers were initiated by a generator operating in continuous mode for 40 minutes producing 0.5 micron films. The density of the films is controlled by the input power of the generator, and in general this power was between 20 and 60 watts. Post-treatment involved subjecting the sample to an argon plasma at high power loadings for a few minutes, increasing the crosslink density at the coating surface.

Of the monomers used, the only two which formed polymerized coatings were vinyldimethylethoxysilane and vinyltrimethoxysilane. Both showed sporadic adhesion and good durability. Argon/water vapor surface activation plasmas showed the greatest improvements in adhesion and durability of the resulting coatings. The abrasion resistance of these coated systems was determined by a method involving drawing a stylus repeatedly over the substrate under pressure, producing scratches. Visual inspection served as the characterization tool. Adhesion behavior was ascertained through a scotch tape test. Both of these techniques are qualitative. With this consideration in mind, a boiling water treatment of argon/water vapor plasma treated polymerized coatings for 10 minutes showed no effect in these tests. The

plasma post-treatment was deemed unnecessary since no improvement in the coating properties could be observed with this process.

The area of abrasion resistant coatings for polymeric substrates has also seen activity in the patent literature.[95-99] In as early as 1967 an inorganic-organic hybrid abrasion resistant coating was patented.[95] This coating was comprised of SiO_2 particles (generated from acid catalyzed TEOS) within an organic polymer matrix. Another is composed of a colloidal dispersion of a water insoluble dispersant in an alcoholic solution of the partial condensate of a silanol.[96] Abrasion resistance can also be afforded by elastomeric materials, such as polyesterurethane type coatings (5 mils thick, or 127 microns) patented in 1988.[97] Mixtures of tri and difunctional organoalkoxysilanes can be reacted in the presence of polyvinylpyrrolidone to generate abrasion resistant coatings for acrylics and PC.[98]

Ceramer formulations have also been employed as a primer layer themselves.[100,101] Linseed and sunflower oil (typical "drying oils" used as binders in paints) combined with various metal alkoxides served as a protective primer layer for metal substrates. By incorporating metal alkoxides along with the drying oils, the adhesion of this primer layer to the metal substrates was improved. The protective coating layer also prevented corrosion of base metal, mostly from incorporation of zinc acetate dihydrate into the formulation.

This concludes the review of sol-gel generated hybrid network materials. The following section discusses the subject of wear of materials as it applies to abrasion resistant coatings.

2.4 Wear

2.4-A. Introductory comments

A precise and all inclusive definition of wear is difficult to formulate, although everyone has a basic understanding of the term. Wear occurs when the surfaces of two materials interact with each other with a relative motion. There are four major classifications of wear, namely:[102,103]

- adhesive wear
- abrasive wear
- corrosive wear
- surface fatigue and brittle fracture wear

There are also other, minor types of wear including fretting, erosion, cavitation, and impact chipping.

2.4-B. Adhesive wear

Adhesive wear occurs when two smooth bodies slide over each other and fragments are pulled off one surface and adhere to the other. Although these two interacting surfaces can be smooth on a macroscopic scale, on an atomic level they are quite rough. Hence contact between the two materials occurs only at isolated "asperities", a term commonly used in the wear field referring to the "hills" of the surfaces. When an asperity from one surface comes into contact with an asperity on the other surface, local stress levels become extremely high compared to the overall applied load, and yielding and plastic deformation can occur. Hence the transfer of a fragment, or the formation of a loose particle, can easily take place in the process of adhesive wear.

2.4-C. Abrasive wear

Abrasive wear occurs when a rough, hard material plows out a groove in a softer material. Fragments which are plowed out of the softer material generally form loose wear particles. Abrasive wear can be the result of either a rough hard surface sliding against a softer one or loose hard particles sliding between two rubbing surfaces. The first process is known as two-body wear, whereas the second case is called three-body wear. It should be noted however that contradictory definitions of two and three-body wear exist in the literature and no formal agreement exists among scientists.[104] Two-body abrasive wear does not occur in cases where the two surfaces are smooth, and likewise, three-body wear does not occur if the abrasive particles are softer than both of the rubbing surfaces.

Abrasion resistance is often quantified through an abrasive wear rate or its inverse which is called wear resistance. The first of these two parameters is equivalent to the material volume swept out per distance of abrasive travel on the surface. A number of physical properties are related to wear resistance. The most commonly discussed such parameter is indentation hardness, which is determined by pressing a hard indenter into a flat surface and noting the area of indentation per unit load. The indentation hardness is then defined as the load per area. The abrasive wear rate for a large number of pure metals is inversely proportional to the indentation hardness.[105,106] Hence a common generalization encountered in the wear field states that harder materials are more abrasion resistant.

For the case of abrasion by particles, the wear rate increases with increasing particle size, up to a critical size above which the rate remains fairly constant.[107] It has been hypothesized that the true factor is particle roughness, which can be a function of particle size, and hence the previous relationship holds. It has also been noted that very small abrasive particles may lead to low wear rates due to a “clogging” of wear tracks by the small abrasive grains, which would prevent abrasive action. Rabinowicz has argued that under abrasive wear by small particles, large wear particles are formed from the *adhesive* wear process (which is occurring simultaneously) which causes clogging and prevents the abrasive from contacting the surface.[102] One final point concerning abrasive particle size is that for systems with a distribution of grain sizes, the largest particle size, rather than the average size, is the most important.

Polishing is a sub-category of abrasive wear. It involves very small abrasive particles, generally less than 5 microns. Since wear rates are very slow for such a condition, it is customary to utilize very high sliding speeds. Due to the large amount of heating upon fast sliding, it is more important that the abrasive grains have a higher melting point than the material surface, rather than be harder at room temperature. Under low load and high speed conditions, wear particles generally do not form, and material is moved from high to low spots on the polished material.

Other important factors which can influence the wear process, and hence the abrasive wear rate, are humidity and lubrication. Humidity can actually lead to an increase in the experimentally measured wear rate due to the flushing of wear debris by condensed water which increases the potency of the abrasion process. Lubricants are primarily employed to reduce the friction force between contacting surfaces and hence reduce the amount of wear.

2.4-D. Corrosive wear

If corrosion can occur on the surface of a material being abraded due to the right environmental conditions, the corrosion products can wear off the surface. This process is known a corrosive wear, and is rather complex. It consists of two stages, the first of which involves the corrosion reaction. In the second stage the sliding of the two surfaces causes wearing away of the corroded layer. In most cases, corrosion products are more brittle than the original surface.

2.4-E. Surface fatigue wear

Surface fatigue wear is a type of fracture wear. It occurs during repeated sliding or progressive cycling through a track. The repeated loading and unloading can generate surface and sub-surface cracks which may eventually lead to fracture (observed as the formation of large fragments), leaving behind large pits in the original surface. Usually the loading and unloading have little influence on the appearance of the surface up to a critical number of cycles, at which suddenly deterioration is rapid. The fragments which are formed by the surface fatigue type of wear are large on a relative basis (≈ 1000 microns, compared to ≈ 30 microns for adhesive wear). Lubricants tend to have a detrimental effect on the useful life of a material under surface fatigue wear. Also, the time to failure of a material is markedly dependent on the load and generally follows the relation $t \propto load^{-3}$.

2.4-F. Brittle fracture wear

Like surface fatigue wear, brittle fracture wear is also a form of fracture wear. It generally occurs in brittle materials such as ceramics and glasses. During sliding contact, cracks are formed in the surface and eventually fragments are produced as a result of surface breakup. Wear rates in general are quite high compared to the other wear mechanisms. Brittle fracture wear is highest for a material whose tensile strength is less than one third its compressive strength. This implies that very brittle materials have poor wear behavior.

Part II. Polymer–Clay Nanocomposites Literature

2.5 Introductory comments

The polymer–clay nanocomposites area has received significant attention in the recent years. However, work on layered clays has gone on for quite some time as it is of great importance to researchers studying soils. It was not until more recently that scientists have seen the applicability of such clays in materials science.

A novel idea of generating materials with a "superstructure" similar to olefins (i.e. stacked lamellar) was published in 1983.[108] The concept presented in that document was to synthesize materials with lamellar structures connected with tie molecules as found in polyethylene, polypropylene, etc. This was accomplished with a completely unrelated molecularly structured material, an inorganic clay. The authors used vermiculite, a layered clay mineral, and "tied" the lamellae together with organic cations. The resulting film showed flexibility in a stress–strain experiment "superior" to a poly(ethylene terephthalate) (PET) film (higher modulus and energy to break), however the new material lacked the recoverability that PET can display at low extensions.[109] This is most likely due to the nature of the clay–cation interaction being ionic (easier to break) versus the covalent bonding between the tie molecules and lamellae in semicrystalline polymers.

Early work from Toyota researchers in Japan involved generating nylon 6–montmorillonite clay hybrids.[110,111] These materials have found application in the automotive industry due to their "under the hood"* temperature stability.[112] The nylon 6–clay hybrids display physical properties that are much improved over the neat polymer. For example, the clay hybrid displayed increased heat distortion

* *For a short time the timing belt cover in the Toyota Camry was made from a nylon 6–clay hybrid material.*

temperature, higher modulus and tensile strength, greater impact strength, less water adsorption, lower permeability, and lower thermal expansion coefficient than nylon 6. The research in the polymer–clay nanocomposite area has expanded to include such polymers as polypropylene,[113,114] poly(ε-caprolactone),[115,116] poly(ethylene oxide),[117,118] poly(methyl methacrylate),[119] polystyrene (PS),[120–122] PDMS,[123] polyimides,[124,125] polyesters[126] and epoxy networks,[127–131] to name a few. It is the interesting structure of montmorillonite clay that allows nanocomposite formation with polymeric species, as will be discussed in the next section.

2.6 The Structure of Montmorillonite Clay

Montmorillonite belongs to a family of clays known as the 2:1 layered silicates (also called mica-type silicates or swelling silicates). The clay can be found all over the world in soils and has been (and still is) a major area of research for soil scientists. It has long been employed as a catalyst for isomerization reactions, converting linear (normal) hydrocarbons to branched hydrocarbons. It is composed of crystalline sheets, measuring ca. $1000 \times 1000 \times 10$ Å. The clay sheets stack upon each other much like a deck of cards, and for talc (molecular structure approximately $Mg_3Si_4O_{10}(OH)_2$), also a 2:1 layered silicate, the crystalline sheets are of neutral charge and the regions between crystal sheets (generally referred to as the galleries) are empty.[132] Thus the crystalline layers of talc are loosely superimposed on one another and slide over each other readily, giving rise to the softness and soapy feel of talc.[132] Mica, with structure approximately $KAl_3Si_3O_{10}(OH)_2$, carries negative charge in the crystalline layers, and electric neutrality is accomplished by alkali cations (mostly potassium) which are present in the gallery regions. This material can be split into very thin sheets which are used for windows in stoves and furnaces, and electrical insulation.[132] Similarly montmorillonite (structure approximately $AlSi_2O_5(OH)\cdot xH_2O$), has excess negative charge within the crystalline sheets (structure to be addressed shortly). Hence, to counterbalance this negative charge, alkali cations must reside in the gallery regions in the naturally occurring clay. These ions are Ca^{2+}, Mg^{2+}, K^+, Na^+, etc., with the

abundance of each ion following the order of listing.[133] Four such sheets are illustrated in Figure 4.

A single crystalline sheet in montmorillonite is made up of two tetrahedral silicon dioxide layers sandwiching an edge-shared octahedral layer. In the crystalline layers, isomorphous substitution of silicon atoms by aluminum atoms is what generates the excess negative charge.[135] Figure 5 depicts the structure of montmorillonite at a smaller size scale than Figure 4, showing the layered building blocks of the sheets. The open circles represent oxygen atoms, the filled circles hydroxyl groups, and in the center of the tetrahedra lie (mostly) silicon atoms. The combined length represented by one 2:1 layered sheet (≈ 9.6 Å) and one gallery region can be observed as a correlation length (or long spacing or long period) from x-ray scattering (labeled "*L*" in Figure 4).

2.7 Organically modified montmorillonite

Naturally occurring montmorillonite is hydrophilic,* and as a result it is generally incompatible with most organic materials (e.g. organic polymers). However, the alkali cations can be exchanged out of the clay and be replaced with virtually any other cation. Various cation exchange reactions of montmorillonite clay have been explained elsewhere in detail.[110,111] The process generally involves dispersing the clay in hot water in very low concentrations, typically ≈ 1 wt.%. To this is added a second solution which has dissolved in it the proper (calculated) amount of cation for exchange. This proper amount of cation is calculated based on the cation exchange capacity (CEC) of the clay. This number is often supplied by the clay manufacturer, but there are methods for determining the CEC when it is unkown.[133,134]

Popular molecules chosen as organic cations for exchange with montmorillonite are alkylammonium ions ("onium" ions). These molecules generally have one or more alkyl chains of 3-18 carbon members. The cationic ammonium moiety associates with the negative charges of the clay sheets, and the "greasy" chains extend away from the

* *Therefore, mud exists.*

clay layers, generally leading to an increased gallery thickness. For this reason, clays exchanged with alkyl ammonium ions have long spacings that are larger than the naturally occurring clay, and the long spacings increase with increasing alkyl chain length. For reference, Table 4 includes the long spacings (measured by x-ray diffraction) for montmorillonite clay exchanged with a series of alkyl ammonium ions. These alkylammonium exchanged forms of montmorillonite are in general organophilic, instigating compatibility with organic materials.

Three common methods have been developed for generating polymer–clay nanocomposites. Firstly, an organically modified montmorillonite can be combined with a polymer by a solution process. Or, it is also possible to combine a molten polymer with a modified clay without solvent; however, the kinetics are generally slower, especially if the polymer molecular weight is large. The last procedure entails blending monomer with the clay (which is in general organically modified), followed by subsequent polymerization of the monomer within the clay galleries. The nature of all such nanocomposites will be addressed in the next section.

2.8 Polymer–clay nanocomposites

2.8–A. Nanocomposite Structures

Polymer–clay nanocomposites generally have two sub–groupings, *intercalated* or *delaminated* (exfoliated) as demonstrated in Figure 6. The intercalated type of polymer–clay hybrid has been touted[135] to have highly extended single chains confined between the clay sheets, within the gallery regions. The clay sheets retain a well ordered, periodic, stacked structure. The intercalation process can be monitored by tracking the increasing long spacing from x-ray scattering, since the galleries must expand to accommodate larger molecules.

The delaminated or exfoliated structure ideally has well dispersed and randomized (in orientation) clay sheets within a matrix of the “coil-like” polymer chains. In this case the sheets have lost their stacked orientation, and if the structure is truly random then no distinct long spacing should be observable by x-ray scattering. However,

literature in the field has a less strict definition of a delaminated hybrid. In most cases in the literature involving delaminated hybrids the clay sheets maintain a considerable amount of order as they tend to remain in a "stacked" structure. Hence it is difficult to distinguish between intercalated and delaminated nanocomposites. In some cases in the literature the only factor which allows distinction between the intercalated and delaminated structure is the spacing between clay sheets (or long period), as both possess stacked–layer structures. In general, the literature defines a polymer *intercalated* montmorillonite as having a long spacing less than ≈ 60 Å, whereas *delaminated* hybrids have spacings greater than ≈ 60 Å. As one might anticipate, these numbers are not absolute dividing lines between the two types of hybrids, and there is a lack of agreement in the literature. In the author's opinion there is a blatant misuse of the term delaminated (exfoliated) when it is employed to describe a hybrid that displays a clear x-ray peak corresponding to the long spacing of an ordered material. Some researchers improperly utilize wide angle x-ray scattering to monitor the nanocomposite formation, and what they conclude as a disappearance of a correlation peak (evidence of delamination) is really just a convergence of the peak with the main beam. The proper tool to employ, in the author's opinion, is small angle x-ray scattering. As will be seen in chapter 6, this has proven to be an excellent tool to monitor the structure of nanocomposites formed between montmorillonite and epoxies, polystyrene, polyvinyl acetate, and a polyurethane TPE. However, this is an uncommon tool in the literature in the nanocomposites area. Most literature studies accompany their wide angle x-ray data with transmission electron microscopy, which in all cases observed by this author, possess this stacked–layer structure even though the term *delaminated* is employed. These clay sheets remain stacked for several layers (≈ 5 to 10) and hence are not completely delaminated and randomized in their orientation within the nanocomposite. Several TEM images scanned from the literature are shown in Figure 7 through Figure 11 for these so–called "delaminated" nanocomposites. Note that in all cases, the clay layers remain stacked upon one another. Hence the reader is forewarned that in the literature review to follow, the term "delaminated" is meant to

reflect this non–ideal, stacked layer nanocomposite, and not the well dispersed, randomized case.

2.8–B. Nylon 6–Clay Nanocomposites

Some polymer-clay nanocomposites have been synthesized by first intercalating monomer into the clay interlayers and subsequently polymerizing it which can lead to "delamination" upon chain growth. For example, organically modified montmorillonite clay will ingest ε–caprolactam forming an intercalated hybrid (modified montmorillonite can be swollen with large amounts of molten ε–caprolactam at 200 °C).[136] Increasing the temperature to 260 °C for six hours under nitrogen in the presence of an accelerator (6-aminocaproic acid) polymerizes the ε–caprolactam forming a nylon 6–clay hybrid. The polymerization process causes delamination of the silicate layers leading to a fairly well dispersed system as seen by transmission electron microscopy[111] (TEM), as shown in Figure 7. The stacked clay layers are evident in these materials, however. The Toyota workers have also developed a synthesis route for the hybrid in "one pot".[137] Annealing nylon 6–clay hybrids at elevated pressures produced a phase of high melting temperature (observed by DSC), corresponding to a different unit cell.[138] Nylon 6 has two crystal forms, α and γ. After annealing the hybrid under elevated pressure, the amount of the γ form decreased, while a high melting α phase emerged. This same phenomenon was observed upon high pressure injection molding of the hybrid.[139]

2.8–C. Polyimide–Clay Nanocomposites

The Toyota group has also designed a polyimide–clay hybrid.[140] The preparation method was somewhat unique. Many alkylammonium ions were employed to cation exchange the montmorillonite, among them were a dodecylammonium salt, n-decyltrimethyl ammonium chloride, and 12-aminododecanoic acid. To perform the cation exchange reaction, the naturally hydrophilic montmorillonite clay was first dispersed in deionized water at 80 °C. This was added to a solution of intercalating agent in water with a small amount of acid (HCl), and allowed to stir for one hour. The

exchanged clay was then recovered by filtration and washed several times to remove any excess intercalating agent. Once clean and dry, the organoclay was dispersed in dimethylacetamide (DMAc) to a solids content of ≈ 3 wt.%. This solution was blended with a DMAc solution containing poly(amic acid). A film was then cast followed by heating to high temperatures where the amic acid can imidize forming the polyimide–clay hybrid. Of nine different intercalating agents employed, only one was judged to allow dispersion of the organoclay in DMAc. The intercalating agents varied mostly on the basis of carbon chain length attached as side groups. Increasing the aliphatic chain length produces an organoclay with decreased hydrophilicity. The cation that successfully afforded dispersion in DMAc contained a 12 membered carbon chain.

TEM investigations into the structure of this hybrid showed that the silicate layers were all oriented in a parallel orientation. This can produce a tortuous path for any potential penetrant molecules if the clay layers are well dispersed in the polymer matrix. For this reason the permeability coefficient of water vapor into the hybrid drops almost an order of magnitude at 8 wt.% clay loading. The same order of magnitude decrease is noted for the oxygen permeability coefficient at ≈ 5 wt.% clay. An almost identical polyimide–clay hybrid was synthesized by Pinnavaia and coworkers.[124] These scientists noted an order of magnitude drop in the permeability of CO_2 into the hybrid at 8 vol.% clay loading in excellent agreement with the Toyota researchers.

2.8–D. Epoxy–Clay Nanocomposites

Pinnavaia and his coworkers have also generated epoxy–clay hybrids. Acidic forms of exchanged montmorillonite permit the epoxy resin to enter the clay.[141] Intercalating agents such as aminocarboxylic acids and primary amines can react directly with the epoxy resin, so no curing agent was added. Due to the fact that only a small amount of intercalating agent is available for reaction (not stoichiometric), the effect is more of a catalytic one. Identical DSC scans for neat epoxy and an organoclay–epoxy blends clearly display this effect. The neat epoxy shows a large reaction exotherm starting at ≈ 384 °C, but the clay blended epoxy shows an exotherm at 229 °C. The associated heats

of reaction were within ≈ 7% of each other. A reference scan of neat organoclay was run to establish that no such exotherm exists in the clay alone. These nanocomposite materials are in a powder form not conducive of mechanical testing. TEM micrographs did show the existence of a (non-ideal) delaminated structure, i.e. an intercalated structure (in the author's opinion). Other epoxy–clay work by this same group included an epoxy system identical to one of the formulations used in the research of chapter 6 of this dissertation. This formulation was Epon828 and JEFFAMINE® D2000. This system produced a rubbery material when cured, due to the large amount of D2000 required to stoichiometrically cure Epon828. Not surprisingly, this rubbery epoxy formulation had improved mechanical properties when the clay was incorporated.[127] Increases in Young's modulus and tensile strength were observed with increasing clay content in the range of 0 to 23 wt.% clay. Improvements in the modulus and stress at break were dependent on the number of carbon atoms in the alkylammonium ions of the organoclay. Longer carbon chains (greater initial gallery size) tended to promote increased mechanical properties, in the range of 4 to 16 carbon atoms.[128] Other related studies by this group showed that the nature of the alkylammonium ions could influence the final structure of the nanocomposite. They showed that tertiary and quaternary amines were the least favorable, and that protonated primary and secondary amines were prefered.[130] They concluded that this was due to the fact that the primary amine is the most reactive with the epoxy resin, and the quaternary amine is the least reactive. Hence the organoclay has a "catalytic" effect on the epoxy reaction within the gallery regions.

Epoxy–clay nanocomposites were also synthesized by Giannelis and coworkers.[131] Ten weight percent or less of an alkyl ammonium chloride exchanged clay was blended with the epoxy resin (at 90 °C) and sonicated for ≈ 2 minutes. After the sonication step, a massive increase in the viscosity of the mixture was noted, attributed to a "house of cards" structure formed by the silicate sheets. Wide angle x–ray scattering led to the conclusion that intercalation of the epoxy occurred, but not delamination. For this reason a curing agent had to be chosen which could react with the epoxy resin but also

cause delamination of the crystalline sheets. Two such curing agents were found, nadic methyl anhydride, and benzyldimethylamine. Wide angle x–ray scattering of these nanocomposites after curing show no reflections corresponding to a correlation length between silicate sheets.* TEM provided support for the presence of (literature–defined) delamination, but again a stacked structure was clear. DMS of the epoxy–clay nanocomposite shows less drop in the storage modulus across the glass transition (Table 5) than the cured epoxy without the 4 vol.% clay.† Also, the inflection in the storage modulus *E'* at glass transition (i.e., the mechanical glass transition temperature) of the clay loaded material is slightly higher by roughly 5 K. The most significant change in the mechanical behavior is *E'* in the rubbery region, where it is significantly higher for the clay containing material. This is due to the clay behaving as a reinforcing filler for the rubbery epoxy.[142–144] The increase in the glassy region is much less pronounced.

2.8–E. Polystyrene–Clay Nanocomposites

Giannelis' research group has also published findings of direct polymer melt intercalation into an organoclay.[145] Ion exchange of montmorillonite clay with dioctadecyldimethyl ammonium bromide (Od_2Me_2AmBr) renders the clay organophilic. Twenty five wt.% polystyrene powder, $\overline{M}_w = 35\ kg/mol$,‡ was mixed with 75 wt.% organoclay and pressed into a pellet. The pellet was then subjected to 165 °C in a vacuum oven, and x-ray diffraction experiments were performed as a function of time. Over the course of 25 hours in this condition, the x-ray data show a disappearance of the peak associated with the Od_2Me_2AmBr exchanged clay at the

---

* *The x-ray scattering instrument used in this study could not resolve scattered radiation below 2q»1°, which corresponds to roughly 80 Å (*Cu*Ka radiation).*

† *Giannelis has a habit of reporting the clay content in vol.% rather than wt.%. Unfortunately, the vol.% is calculated based on the density of the unit cell of the clay, which does not include the gallery region. This makes the clay contents appear very small, when in fact on a weight basis, they are not.*

‡ *The critical entanglement molecular weight for polystyrene is 35 kg/mol.[146–148] Hence the material employed in the above study may not behave like high polymer, and should have been avoided.*

expense of a new peak corresponding to the PS–intercalated clay (increase in the long spacing from 25.2 Å to 32.0 Å). Another PS of 400 kg / mol was claimed to intercalated but at a slower rate. No statement on how long this process takes was offered, nor were any supporting x-ray data given. In a separate communication, the kinetics of PS melt intercalation are examined.[149] The rate of intercalation of PS into the organoclay shows an extreme dependence on molecular weight from their data. For instance, 152 kg / mol chains annealed with the clay (in pellet form in a vacuum oven as before) take 3.5 hours to become 60% intercalated at 180 °C (determined from x-ray peak intensity analysis). The authors claim that utilizing an extruder with a four minute residence time was sufficient to generate hybrids of Styron 685 (≈ 300 kg / mol) and clay; however, no supporting data were given.

2.9 Summary of Polymer–Clay Nanocomposites

To summarize, the present author wishes to state his strong opinion that the reports in the literature (addressed in this chapter and chapter 6) of delaminated or exfoliated polymer–clay structures are incorrect. The complete separation and randomization of orientation of the clay sheets has not been shown unequivocally for any material in all of this literature. Most researchers in this field employ (to date at least) insufficient tools for proving their conclusions. Such tools include TEM, whose images show a localized structure (and still all such images show a stacked structure of clay sheets). Also, wide angle x-ray scattering is employed instead of the more appropriate small angle x-ray scattering, which will be shown in the next chapter to be very useful in tracking the long spacings in the 20 to 60 Å range (and much larger is certainly obtainable by SAXS, up to ≈ 1000 Å). The true, ideal delaminated structure is the “holy grail” of the field, and likely the death of King Arthur will be observed before the completion of the quest.

Table 1. Electronegativity of atoms, coordination number in the network oxide (*n*), and degree of unsaturation (*n-z*) of various metal alkoxides. (Adapted from Sanchez and Ribot[5] and Pauling[2]).

Alkoxide	Electronegativity	n	n-z
$Si(OPr^{iso})_4$	1.74	4	0
$Sn(OPr^{iso})_4$	1.89	6	2
$Al(OPr^{iso})_3$	1.61	6	3
$Ti(OPr^{iso})_4$	1.32	6	2
$Zr(OPr^{iso})_4$	1.29	7	3
$Ce(OPr^{iso})_4$	1.17	8	4
Cs	0.7	-	-
F	4.0	-	-

Table 2. Gel time and solution pH for different acid catalysts of the sol-gel reaction of TEOS (adapted from Pope and Mackenzie[150]).

Catalyst	Initial solution pH	Gel time in hours
HF	1.9	12
HCl	≈ 0.05	92
HNO_3	≈ 0.05	100
H_2SO_4	≈ 0.05	106
CH_3COOH	3.7	72
None	5.0	1000

Table 3. Influence of cure time on the Porod slopes and electronic radii of gyration of PTMO(80) TEOS(20) ceramers (data collected by Rodrigues and Wilkes[11]).

Cure time	Porod slope*	$\bar{r}_{G,z}$ in Å
30 minutes	–1.28	6
2 hours	–1.59	10
12 hours	–2.4 –1.54	12
2 weeks	–2.69 –2.0	12

* *Corrected for a point source (pin-hole collimation), and hence* $d_f = -(\text{slope})$

Table 4. Long spacings ("basal spacings") for various alkylammonium exchanged montmorillonite clays.[127130]

Cation	Long spacing, Å	Gallery thickness* (Å)
$CH_3(CH_2)_3NH_3^+$	13.5	3.9
$CH_3(CH_2)_7NH_3^+$	13.8	4.2
$CH_3(CH_2)_9NH_3^+$	13.8	4.2
$CH_3(CH_2)_{11}NH_3^+$	15.6	6
$CH_3(CH_2)_{15}NH_3^+$	17.6	8
$CH_3(CH_2)_{17}NH_3^+$	18.0	8.4

* *gallery thickness = (long spacing – 9.6 Å), where 9.6 Å is the thickness of one 2:1 layered montmorillonite sheet.*

Table 5. DMS data at 110 Hz for neat cured epoxy and epoxy–clay hybrid. (Data derived from Giannelis et. al.[131])

Material	T_g (°C)	E'_{glass}, (GPa)	E'_{rubber}, (GPa)	$\Delta E'_{glass\text{-}rubber}$, (decades)
DGEBA-BDMA*	115	1.58	0.10	1.48
DGEBA-BDMA-Clay	120	2.51	0.50	2.01

* *DGEBA stands for the diglycidyl ether of bisphenol-A and BDMA stands for benzyldimethylamine.*

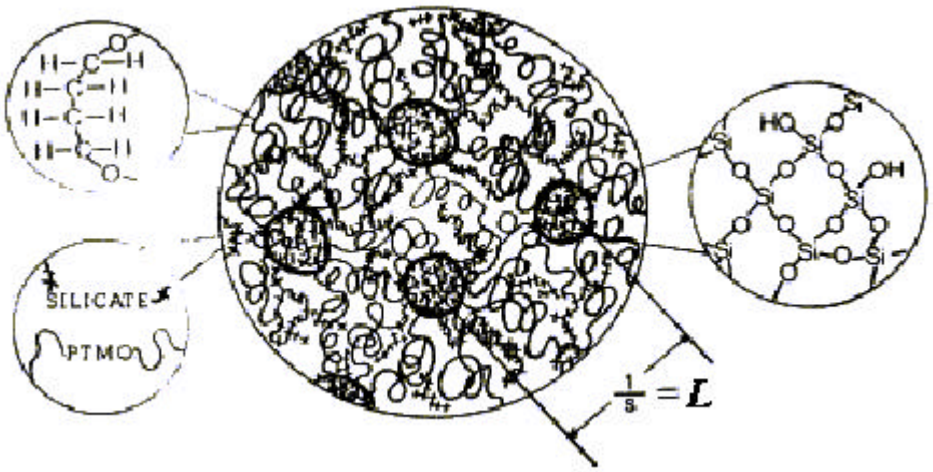

Figure 1. Hypothesized structure for the PTMO-TMOS hybrid network.[11] The correlation distance (between silicate clusters) is represented by the quantity $\frac{1}{s}$ from SAXS. A similar model was also proposed by Mackenzie for TEOS-PDMS hybrids.[21]

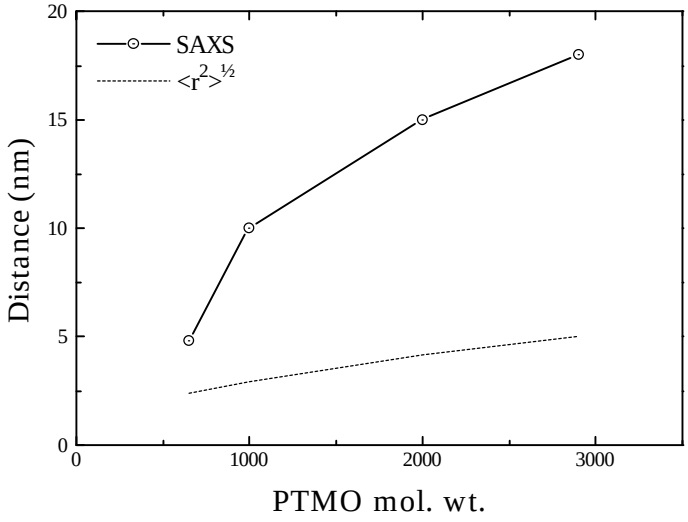

Figure 2. Comparison of SAXS correlation distances in PTMO-TMOS hybrids and calculated $\sqrt{\bar{r}_0^2}$ for oligomeric PTMO chains of varied molecular weights. (Adapted from Wilkes et. al.[35])

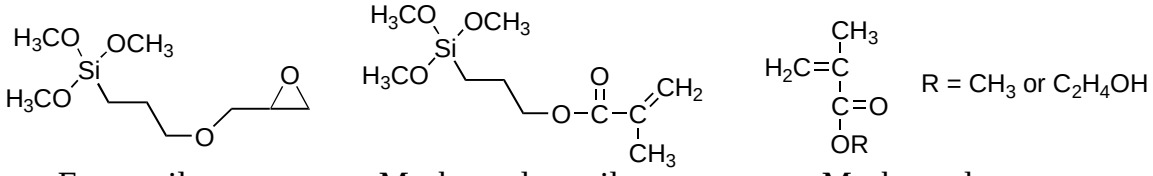

Epoxysilane Methacryloxysilane Methacrylates

Figure 3. Chemical structures of some reactants used by Phillip and Schmidt[29] in the sol-gel reaction to create contact lens materials.

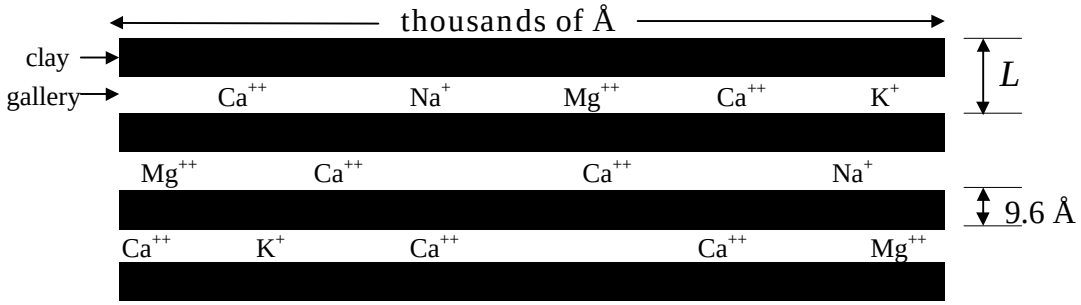

Figure 4. Drawing of the structure of four crystalline sheets of montmorillonite clay. Dimensions are approximate, and may vary.

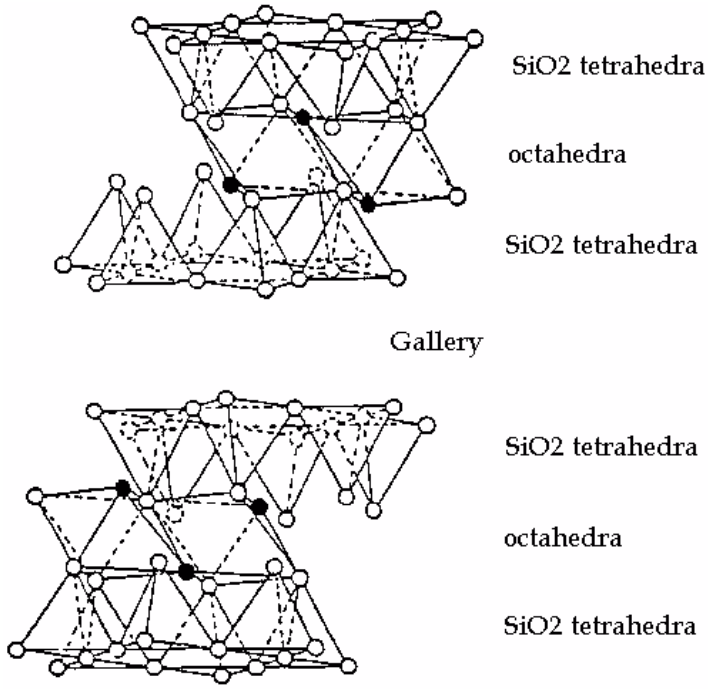

Figure 5. Idealized structure of montmorillonite clay showing the 2:1 layered arrangement of a small section of two crystalline sheets of the material. The galleries of naturally occurring montmorillonite would house alkali cations. (Adapted from Giannelis[135])

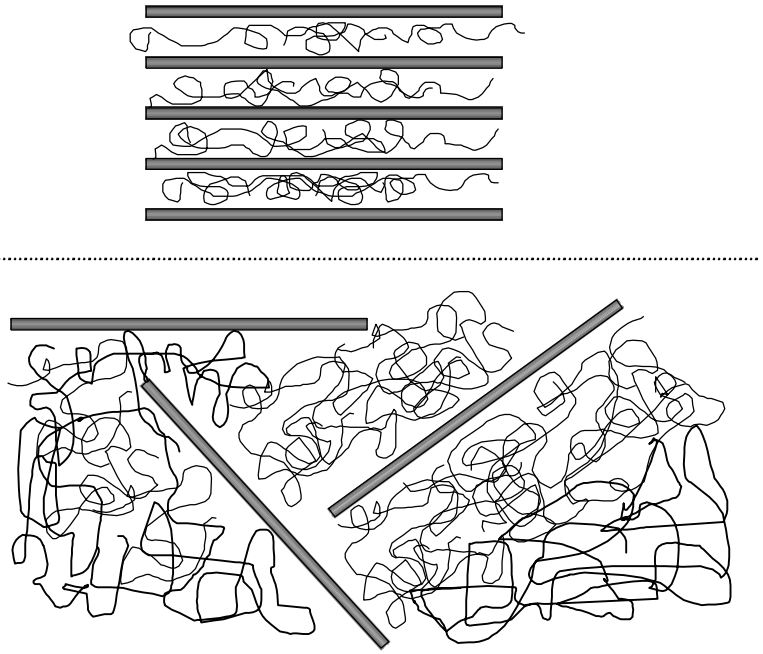

Figure 6. Drawing showing the differences between the structure of intercalated (top) and *idealized* delaminated (bottom) polymer–clay hybrids. "Delaminated" hybrids in the literature appear to be more like the structure shown in the top drawing.

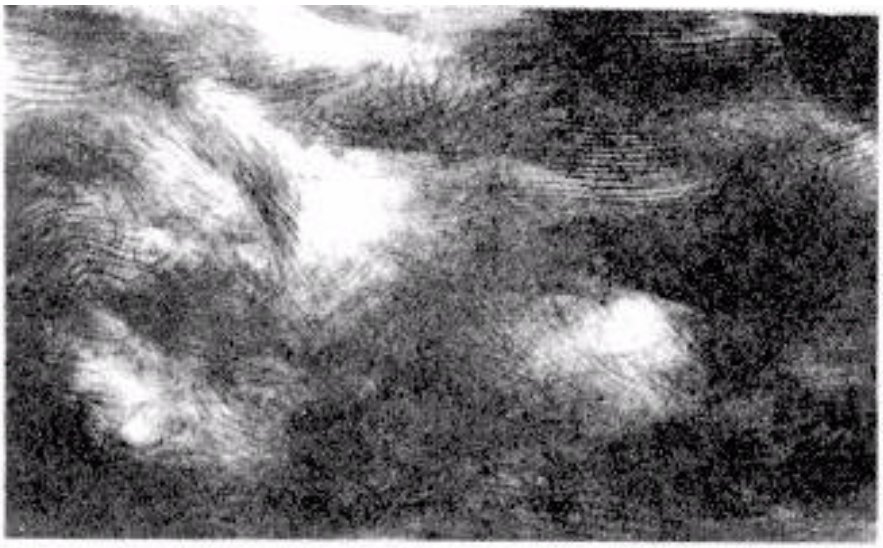

Figure 7. TEM image of a delaminated nylon 6–clay nanocomposite prepared by Usuki et. al.[111]

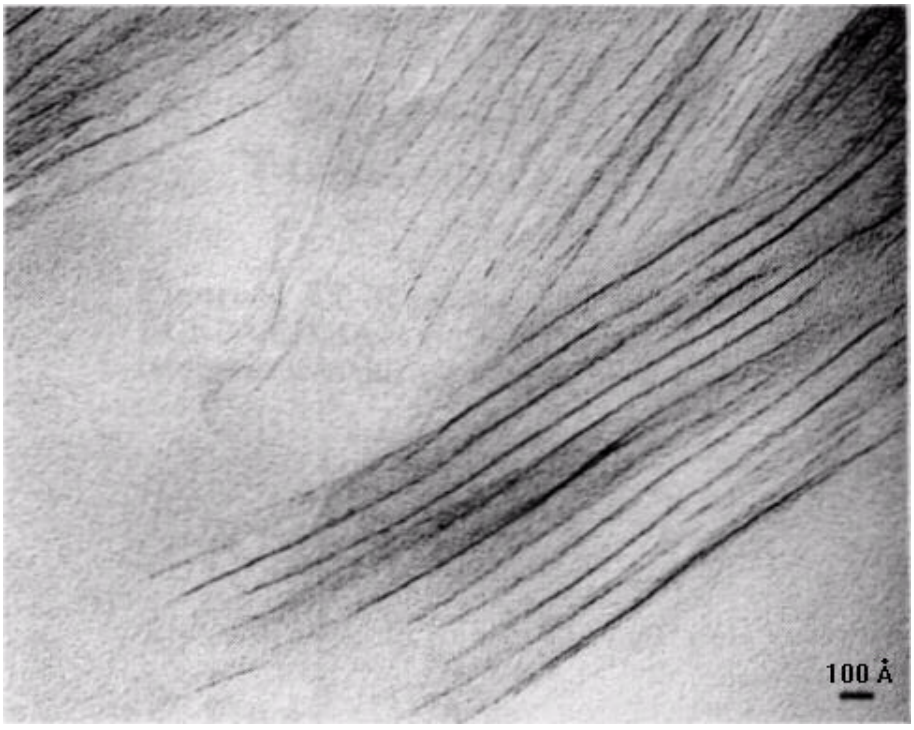

Figure 8. TEM image of a delaminated epoxy–clay nanocomposite prepared by Giannelis et. al.[131]

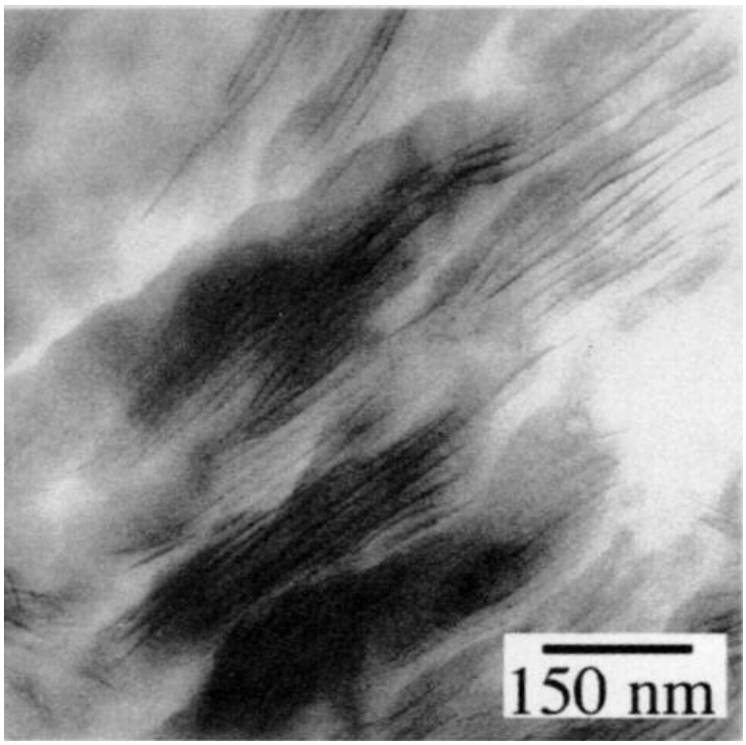

Figure 9. TEM image of a delaminated epoxy–clay nanocomposite prepared by Giannelis et. al.[151]

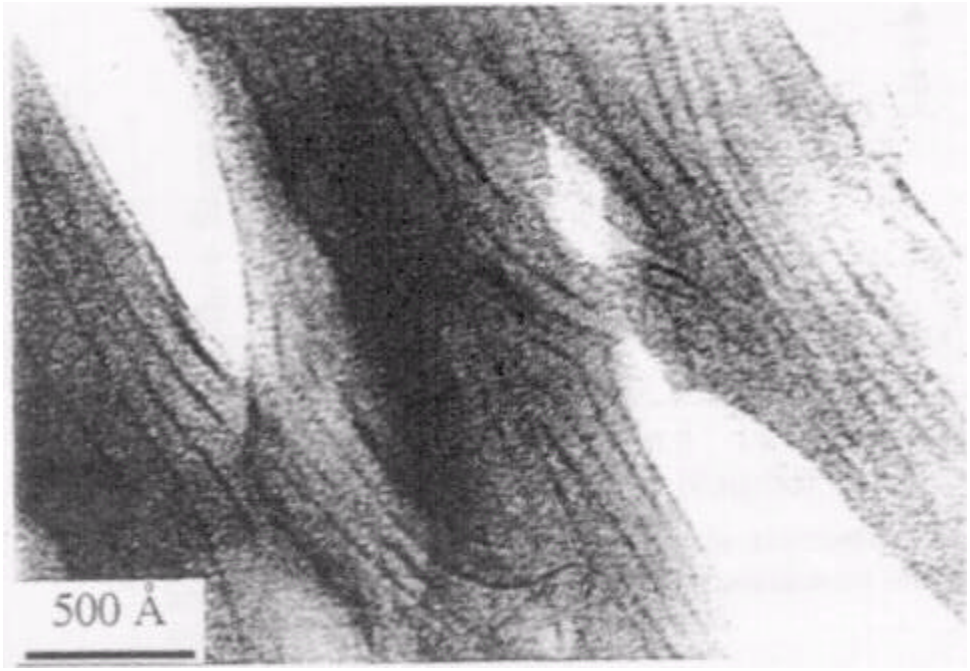

Figure 10. TEM image of a delaminated epoxy–clay nanocomposite prepared by Pinnavaia et. al.[130]

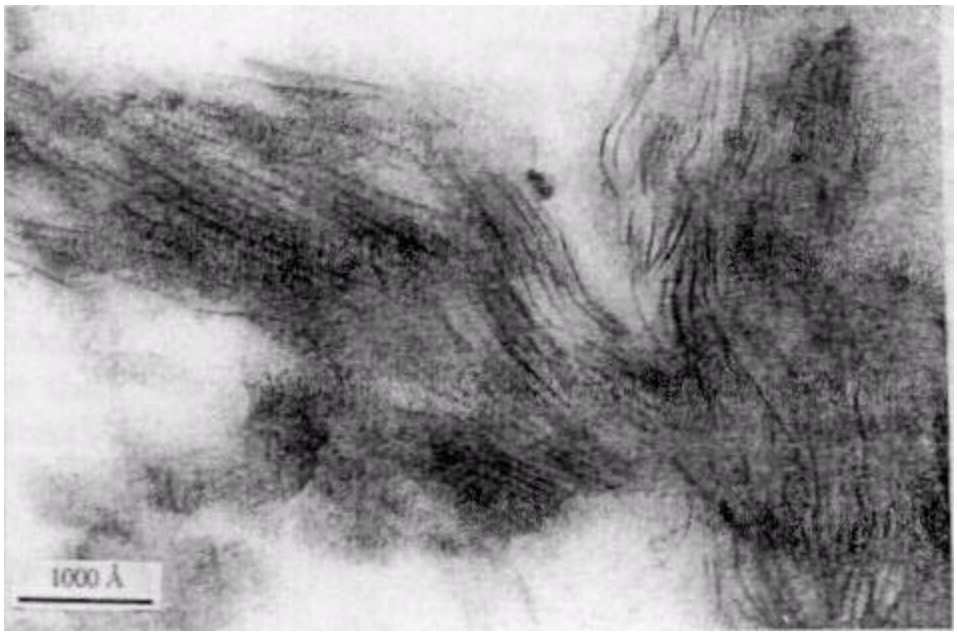

Figure 11. TEM image of a delaminated epoxy–clay nanocomposite prepared by Pinnavaia et. al.[127]

2.10 References

1 Paul J. Flory. Principles of Polymer Chemistry. Cornell University Press, copyright 1953, p. 347.

2 Linus Pauling. General Chemistry. Dover Publications, Inc., New York, copyright 1947, 1950, 1970.

3 V. Gottardi. *J. Non-Cryst. Solids*, **48**, 1, (1982).

4 B. M. Novak. *Adv. Mater.*, **5(6)**, 422, (1993).

5 C. Sanchez and F. Ribot. *New J. Chem.*, **18**, 1007, (1994).

6 J. Livage, M. Henry, and C. Sanchez. *Progress in Solid State Chemistry*, **18**, 259, (1988).

7 C. Sanchez and F. Ribot. Inorganic and Organometallic Polymers with Special Properties. R. M. Laine, ed., Nato ASI Series, vol 206, Kluwer Publishing, New York, (1992).

8 R. C. Mehrota, R. Bohra, and D. P. Gaur. Metal β-diketonates and Allied Derivatives. Academic Press, London, copyright 1978.

9 C. J. Brinker and G. W. Scherer. Sol-Gel Science, The Physics and Chemistry of Sol-Gel Processing. Academic Press, San Diego, copyright 1990.

10 C. J. Brinker, K. D. Keefer, D. W. Schaefer, and Ashley. *J. Non-Cryst. Solids*, **48**, 47, (1982).

11 D. E. Rodrigues and G. L. Wilkes. *J. Inorg. Organomet. Polym.*, **3(3)**, (1993).

12 Leroy E. Alexander. X-Ray Diffraction Methods in Polymer Science. Robert E. Krieger Publishing Company, Inc., Malabar, Florida, copyright 1969, p. 283.

13 G. L. Wilkes. *Personal communication (class notes, CHE 5114)*, (30 Jan 1995).

14 K. D. Keefer in Better Ceramics Through Chemistry. C. J. Brinker, D. E. Clark, and D. R. Ulrich, eds., North-Holland, New York, (1984).

15 J. E. Martin and A. J. Hurd. *J. Appl. Cryst.*, **20**, 61, (1987).

16 R. Aelion, A. Loebel, and F. Eirich. *J. Am. Chem. Soc.*, **72**, 5705 (1951).

17 S. Sakka and K. Kiamiya. *J. Non-Cryst. Solids*, **48**, 31, (1982).

18 K. Nogami and N. Nagasaki. *J. Non-Cryst. Solids*, **109**, 79, (1989).

19 A. Artaki, H. Zerda, and J. Jonas. *J. Non-Cryst. Solids*, **81**, 381, (1986).

20 I. Artaki, M. Bradley, T. W. Zerda, amd J. Jonas. *J. Phys. Chem.*, **89**, 4399, (1985).

21 J. D. Mackenzie, Y. J. Chung, and Y. Hu. *J. Non-Cryst. Solids*, **147&148**, 271, (1992).

22 E. J. A. Pope and J. D. Mackenzie. *Mater. Res. Soc. Bull.*, **12**, 29, (1987).

23 B. Abramoff and L. C. Klein in Sol–Gel Optics I. J. D. Mackenzie, D. R. Ulrich, ed., *Proc. SPIE*, **1328**, 241, (1990).

24 D. Avnir, D. Levy, and R. Reisfield. *J. Phys. Chem.*, **88**, 5954, (1984).

25 C. J. T. Landry nad B. K. Coltrain. *Am. Chem. Soc. Div. Polym. Chem. (Polymer Preprtints)*, **32**, 514, (1991).

26 B. M. Novak, N. Ellsworth, T. I. Wallow, and C. Davies. *Am. Chem. Soc. Div. Polym. Chem. (Polymer Preprtints)*, **31**, 698, (1990).

27 F. Suzuki and K. Onozato, *J. Appl. Polym. Sci.*, **39**, 371, (1990).

28 I. A. David and G. W. Scherer. *Am. Chem. Soc. Div. Polym. Chem. (Polymer Preprtints)*, **32**, 530, (1991).

29 G. Phillip and H. Schmidt. *J. Non-Cryst. Solids*, **63**, 283, (1984).

30 H. Schmidt. *Mater. Res. Soc. Symp. Proc.*, **32**, 327, (1984).

31 G. L. Wilkes, B. Orler, and H. Huang. *Am. Chem. Soc. Div. Polym. Chem. (Polymer Preprtints)*, **26(2)**, 300, (1985).

32 H. Huang, B. Orler, and G. Wilkes. *Polym. Bull.*, **14**, 557, (1985).

33 H. Huang, B. Orler, and G. Wilkes. *Macromolecules*, **20**, 1322, (1987).

34 L. Mascia. *Trends in Polym. Sci.*, **3(2)**, 61, (1995).

35 H. Huang and G. L. Wilkes. *Polym. Bull.*, **18**, 455, (1987).

36 R. H. Glaser and G. L. Wilkes. *Polym. Bull.*, **19**, 51, (1988).

37 R. H. Glaser, G. L. Wilkes, and C. E. Bronnimann. *J. Non-Cryst. Solids*, **113**, 73, (1989).

38 H. Huang, R. H. Glaser, and G. L. Wilkes in Inorganic and Organometallic Polymers. American Chemical Society Symposium Series 360, copyright 1988, Chapter 29, p. 354.

39 H. Huang, G. L. Wilkes, and J. G. Carlson. *Polymer*, **30**, 2001, (1989).

40 A. B. Brennan, H. Huang, and G. L. Wilkes. *Am. Chem. Soc. Div. Polym. Chem. (Polymer Preprtints)*, **30(2)**, 105, (1989).

41 D. E. Rodrigues and G. L. Wilkes. *Am. Chem. Soc. Div. Polym. Chem. (Polymer Preprtints)*, **30(2)**, 227, (1989).

42 B. Wang, H. Huang, A. B. Brennan, and G. L. Wilkes. *Am. Chem. Soc. Div. Polym. Chem. (Polymer Preprtints)*, **30(2)**, 746, (1989).

43 J. Noell, G. L. Wilkes, D. Mohanty, and J. E. McGrath. *J. Appl. Polym. Sci.*, **40**, 1177, (1990).

44 G. L. Wilkes, A. B. Brennan, H. Huang, D. Rodrigues, and B. Wang. *Mat. Res. Soc. Symp. Proc.*, **171**, 15, (1990).

45 B. Wang, A. Brennan, H. Huang, and G. L. Wilkes. *J. Macromol. Sci.-Chem.*, **A27(12)**, 1447, (1990).

46 M. Spinu, A. Brennan, J. Rancourt, G. L. Wilkes, and J. E. McGrath. *Mat. Res. Soc. Symp. Proc.*, **175**, 179, (1990).

47 B. Wang, G. L. Wilkes, J. C. Hedrick, S. C. Liptak, and J. E. McGrath. *Macromolecules (Notes)*, **24**, 3449, (1991).

48 A. B. Brennan, B. Wang, D. E. Rodrigues, and G. L. Wilkes. *J. Inorg. Organomet. Polym.*, **1(2)**, (1991).

49 B. Wang, A. Gungor, A. B. Brennan, D. E. Rodrigues, G. L. Wilkes, and J. E. McGrath. *Am. Chem. Soc. Div. Polym. Chem. (Polymer Preprints)*, **32(3)**, 521, (1991).

50 D. E. Rodrigues, A. B. Brennan, C. Betrabet, B. Wang, and G. L. Wilkes. *Am. Chem. Soc. Div. Polym. Chem. (Polymer Preprtints)*, **32(3)**, 525, (1991).

51 B. Wang and G. L. Wilkes, *J. Poym. Sci.: Part A, Polym. Chem.*, **29**, 905, (1991).

52 B. Wang, G. L. Wilkes, C. D. Smith, and J. E. McGrath. *Polymer Commun.*, **32(13)**, 400, (1991).

53 A. B. Brennan and G. L. Wilkes. *Polymer*, **32(4)**, 733, (1991).

54 B. Tanami, C. Betrabet and G. L. Wilkes. *Polym. Bull.*, **30**, 39, (1993).

55 B. Wang and G. L. Wilkes. *J.M.S.-Pure Appl. Chem.*, **A31(2)**, 249, (1994).

56 C. S. Betrabet and G. L. Wilkes. *Chem. Mater.*, **7**, 535, (1995).

57 J. Wen and G. L. Wilkes. *J. Inorg. Organomet. Polym.*, **5**, (1995).

58 J. Wen, V. Vasudevan, and G. Wilkes. *J. Sol-Gel Sci. Technol.*, **5**, 115, (1995).

59 K. Jordens and G. Wilkes. *Proc. Amer. Chem. Soc., Div. Polym. Mater. Sci. Engr. (PMSE Preprints)*, **73**, 290 (1995).

60 J. Wen, B. Dhandapani, S. T. Oyama, and G. L. Wilkes. *Chem. Mater.*, **9(9)**, 1968, (1997).

61 Stephen L. Rosen. Fundamental Principles of Polymeric Materials. John Wiley and Sons, Inc., New York, copyright 1982.

62 G. L. Wilkes. *Personal communication (class notes, CHE 5124)*, (4 May 1994).

63 T. M. Miller, L. Zhao, and A. B. Brennan. *J. Appl. Polym. Sci.*, **68**, 947, (1998).

64 H. Schmidt. *Mater. Res. Soc. Symp. Proc.*, **32**, 327, (1984).

65 Bernhard Wunderlich. Thermal Analysis. Academic Press, Inc., San Diego, copyright 1990, p. 373.

66 F. Surivet, T. M. Lam, J. Pascault, and C. Mai. *Macromolecules*, **25(21)**, 5742, (1992).

67 A. B. Brennan and T. M. Miller. *Chem. Mater.*, **6**, 262, (1994).

68 D. W. McCarthy, J. E. Mark, D. W. Schaefer. *J. Polym. Sci. Part B: Polym. Phys.*, **36**, 1167, (1998).

69 J. E. Mark and S. -J. Pan. *Makromol. Chem., Rapid Commun.*, **3**, 681, (1982).

70 J. E. Mark and Y. Ning. *Polym. Bull.*, **12**, 407, (1984).

71 Y. -P. Ning, M. -Y. Tang, C. -Y. Jiang, and J. E. Mark. *J. Appl. Polym. Sci.*, **29**, 3209, (1984).

72 J. E. Mark, C. Jiang, and M. Tang. *Macromolecules*, **17**, 2613, (1984).

73 J. E. Mark, Y. Ning, C. Jiang, and M. Tang, and W. C. Roth. *Polymer*, **26**, 2069, (1985).

74 M. Tang and J. E. Mark. *Polym. Engr. Sci.*, **25(1)**, 29, (1985).

75 Y. Ning and J. E. Mark. *Polym. Engr. Sci.*, **26(2)**, 167, (1986).

76 J. E. Mark and C. Sun. *Polym. Bull.*, **18**, 259, (1987).

77 D. Schaeffer, J. E. Mark, D. McCarthy, L. Jian, C. Sun, and B. Farago. *Mat. Res. Soc. Symp. Proc.*, **171**, 57, (1990).

78 P. Xu, S. Wang, and J. E. Mark. *Mat. Res. Soc. Symp. Proc.*, **180**, 445, (1990).

79 S. Wang, P. Xu and J. E. Mark. *Rubber Chem. Technol.*, **64(5)**, 746, (1991).

80 G. B. Sohoni and J. E. Mark. *J. Appl. Polym. Sci.*, **45**, 1763, (1992).

81 S. Wang and J. E. Mark. *Polymm. Bull.*, **17**, 271, (1987).

82 J. E. Mark and S. Wang. *Polym. Bull.*, **20**, 443, (1988).

83 S. Wang and J. E. Mark. *Macromol. Reports*, **A28(suppl. 3)**, 185, (1991).

84 S. Wang and J. E. Mark. *Macromolecules*, **23(19)**, 4288, (1990).

85 S. Wang, Z. Ahmad, and J. E. Mark. *Polym. Bull.*, **31**, 323, (1993).

86 S. Wang, Z. Ahmad, and J. E. Mark. *Macromol. Reports*, **A31(suppls 3&4)**, 411, (1994).

87 S. Wang, Z. Ahmad, and J. E. Mark. *Chem. Mater.*, **6**, 943, (1994).

88 J. K. Gilliam. *Polym. Engr. and Sci.*, **16**, 353, (1976).

89 H. Schmidt and H. Wolter. *J. Non-Cryst. Solids*, **121**, 428, (1990).

90 H. K. Pulker. Coatings on Glass. Elsevier Scientific Publishing, Inc., New York, (1984).

91 C. Li and G. L. Wilkes. *J. Inorg. Organomet. Polym.*, **7(4)**, 203, (1997).

92 R. Kasemann and H. Schmidt. *New J. Chem.*, **18**, 1117, (1994).

93 H. Schmidt, R. Kasemann, T. Burkhart, G. Wagner, and E. Arpac. *Amer. Chem. Soc. Div. Polym. Mater. Sci. Engr. (PMSE Preprints)*, **70**, 347, (1993).

94 U. Hayat. *J.M.S.-Pure Appl. Chem.*, **A31(6)**, 665, (1994).

95 A. A. Marks, M. M. Marks, C. Lee Wilson, and B. L. Orofino. *U.S. Patent 3,324,005*, (1967).

96 L. T. Ashlock, H. Mukamal, and W. H. White. *U.S. Patent 4,571,365*, (1986).

97 C. R. Coleman. *U.S. Patent 4,731,289*, (1988).

98 J. D. Basil, C. Lin, and R. M. Hunia. *U.S. Patent 5,115,023*, (1992).

99 G. A. Patel. *U.S. Patent 5,409,778*, (1995).

100 S. J. Tuman and M. D. Soucek. *J. Coat. Tech.*, **68(854)**, 73, (1996).

101 C. R. Wold and M. D. Soucek. *J. Coat. Tech.*, **70(882)**, 43, (1998).

102 Ernest Rabinowicz. Friction and Wear of Materials. John Wiley and Sons, New York, (1965).

103 J. Holling, ed. Principles of Tribology. The Macmillan Press Ltd., London, (1975, 1978).

104 J. D. Gates. *Wear*, **214**, 139, (1998).

105 M. M. Kruschov. *Proc. Conf. Lubrication and Wear*, 655, (1957).

106 E. Rabinowicz, L. A. Dunn, and P. G. Russell. *Wear*, **4**, 345, (1961).

107 B. W. E. Avient, J. Goddard, and M. Wilman. *Proc. Roy. Soc.*, **A258**, 159, (1960).

108 D. G. H. Ballard and G. R. Rideal. *J. Mater. Sci.*, **18**, 545, (1983).

109 D. G. H. Ballard in History of Polyolefins. R. B. Seymour and T. Cheng, eds., D. Reidel Publishing Co., Dordrecht, Holland. pp. 9. (1983).

110 A. Usuki, Y. Kojima, M. Kawasumi, A. Okada, Y. Fukushima, T. Kurauchi, and O. Kamigaito. *J. Mater. Res.*, **8**, 1174, (1993).

111 A. Usuki, Y. Kojima, M. Kawasumi, A. Okada, T. Kurauchi, and O. Kamigaito. *J. Mater. Res.*, **8(5)**, 1179, (1993).

112 A. Okada and A. Usuki. *Mater. Sci. Eng.*, **C3**, 109, (1995).

113 A. Usuki, M. Kato, A. Okada, and T. Kurauchi. *J. Appl. Polym. Sci.*, **63**, 137, (1997).

114 N. Hasegawa, M. Kawasumi, M. Kato, A. Usuki, and A. Okada. *J. Appl. Polym. Sci.*, **67**, 87, (1998).

115 P. B. Messersmith and E. P. Giannelis. *Chem. Mater.*, **5**, 1064, (1993).

116 R. Krishnamoorti and E. P Giannelis. *Macromolecules*, **30(14)**, 4097, (1997).

117 R. A. Vaia, B. B. Sauer, O. K. Tse, and E. P. Giannelis. *J. Polym. Sci. B: Polym. Phys.*, **35**, 59, (1997).

118 P. Aranda, Galván, B. Casal, and E. Ruiz–Hitzky. *Key Engineering Materials*, **61** and **62**, 469, (1991).

119 D. C. Lee and L. W. Jang. *J. Appl. Polym. Sci.*, **61**, 1117, (1996).

120 R. A. Vaia, H. Ishii, and E. P. Giannelis. *Chem. Mater.*, **5**, 1694, (1993).

121 R. A. Vaia and E. P. Giannelis. *Macromolecules*, **30(25)**, 8000, (1997).

122 R. A. Vaia, K. D. Jandt, E. J. Kramer, and E. P. Giannelis. *Chem. Mater.*, **8(11)**, 2628, (1996).

123 S. D. Burnside and E. P. Giannelis. *Chem. Mater.*, **7(9)**, 1597, (1995).

124 T. Lan, P. D. Kaviratna, and T. J. Pinnavaia. *Chem. Mater.*, **6**, 573, (1994).

125 A. K. Cheetham, C. J. Brinker, M. L. Mecartney, and C. Sanchez, eds., Better Ceramics Through Chemistry VI. *Mater Res. Soc. Symp. Proc.*, **346**, 81, (1994).

126 X. Kornmann, L. A. Berglund, J. Sterte, and E. P. Giannelis. *Polym. Eng. Sci.*, **38(8)**, 1351, (1998).

127 T. Lan and T. J. Pinnavaia. *Chem. Mater.*, **6(12)**, 2216, (1994).

128 T. J. Pinnavaia, T. Lan, Z. Wang, H. Shi, and P. D. Kaviratna. Chapter 17 of *ACS Symp. Ser., Nanotechnology*, **662**, 250, (1996).

129 H. Shi, T. Lan, and T. Pinnavaia. *Chem. Mater.*, **8(8)**, 1584, (1996).

130 T. Lan, P. D. Kaviratna, and T. J. Pinnavaia. *Chem. Mater.*, **7**, 2144, (1995).

131 P. B. Messersmith and E. P. Giannelis. *Chem. Mater.*, **6(10)**, 1719, (1994).

132 Linus Pauling. General Chemistry. Dover Publications, Inc., New York, p. 643, (1947, 1950, 1970).

133 G. W. Thomas in Methods of Soil Analysis Part 2–Chemical and Microbiological Properties. 2nd ed. number 9 (part 2) in the Agronomy series, A. L. Page, R. H. Miller, and D. R. Keeney, eds., American Society of Agronomy, Inc., and Soil Science of America, Inc., publisher. Madison, WI, pp. 159 (1982).

134 G. Rytwo, C. Serban, S. Nir, and L. Margulies. *Clays & Clay Minerals*, **39(5)**, 551, (1991).

135 E. P. Giannelis. *JOM (Journal of Minerals, Metals and Materials Society)*, **44(3)**, 28, (1992).

136 A. Usuki, Y. Kojima, M. Kawasumi, A. Okada, T. Kurauchi, and O. Kamigaito. *J. Polym. Sci.: A. Polym. Chem.*, **31**, 983, (1993).

137 A. Usuki, Y. Kojima, M. Kawasumi, A. Okada, Y. Fukushima, T. Kurauchi, and O. Kamigaito. *J. Polym. Sci. A., Polym Chem.*, **31**, 1755, (1993).

138 Y. Kojima, T. Matsuoka, H. Takahashi, and T. Kurauchi. *J. Appl. Polym. Sci.*, **51**, 683, (1994).

139 Y. Kojima, T. Matsuoka, H. Takahashi, T. Kurauchi. *J. Mater. Sci. Lett.*, **12(21)**, 1714, (1993).

140 Yano, A. Usuki, A. Okada, T. Kurauchi, and O. Kamigaito. *J. Polym. Sci.: A, Polym. Chem.*, **31**, 2493, (1993).

141 M. S. Wang and T. J. Pinnavaia. *Chem. Mater.*, **6**, 468, (1994).

142 Lawrence E. Nielsen. Mechanical Properties of Polymers and Composites Volume 2. Marcel Decker, Inc., NY, 1974.

143 F. R. Schwarzl, H. W. Bree, C. J. Nederveen, G. A. Schwippert, L. C. E. Struik, and C. W. Van der Wal. *Rheol. Acta*, **5**, 270, (1966).

144 R. F. Landel and T. L. Smith. *ARS J. (American Rocket Society Journal)*, **31**, 599, (1961).

145 R. A. Vaia, H. Ishii, and E. P. Giannelis. *Chem. Mater.*, **5**, 1694, (1993).

146 Y. Zang and P. J. Carreau. *J. Appl. Polym. Sci.*, **42**, 1965, (1991).

147 W. W. Graessley and S. F. Edwards. *Polymer*, **22**, 1329, (1981).

148 R. S. Porter and J. F. Johnson. *Chem. Rev.*, **66**, 1, (1966).

149 R. A. Vaia, K. D. Jandt, E. J. Kramer, and E. P. Giannelis. *Macromolecules*, **28(24)**, 8080, (1995).

150 E. J. A. Pope and J. D. Mackenzie. *J. Non-Cryst. Solids*, **87**, 185, (1986).

151 R. Krishnamoorti, R. A. Vaia, and E. P. Giannelis. *Chem. Mater.*, **8(8)**, 1728, (1996).

Chapter 3

Novel Ceramer Materials Based on JEFFAMINE® Poly(propylene oxide) Oligomers and Tetramethoxysilane

Abstract

Novel hybrid organic–inorganic network materials have been generated based on poly(propylene oxide) and tetramethoxysilane. The poly(propylene oxide) (PPO) source chosen for this study was the family of JEFFAMINE®s often employed as epoxy curing agents. These materials were end–functionalized with trialkoxysilane groups which later were exploited in the sol–gel reaction. The sol–gel variables of water and acid catalyst concentration had little influence on the final properties of the resulting network materials for the ranges probed. Increasing the tetramethoxysilane content, however, generated a structure that was increasingly more mass fractal in character. This same variable also had a distinct effect on the mechanical properties of the hybrids; the tetramethoxysilane reacts to form a silicate material which behaved as a reinforcing filler for the rubbery PPO component by increasing and broadening the glass transition. Decreasing the PPO molecular weight had a similar effect on mechanical properties, since the silicate content increases with decreasing PPO molecular weight. This is due to the increasing concentration of alkoxysilane end–groups and also the decreasing of the average molecular weight between crosslinks

with decreasing PPO molecular weight. For non–TMOS containing materials, small angle x-ray scattering revealed a correlation length associated with the silicate crosslinking phase separated by PPO chains, which increased with PPO molecular weight, as expected.

3.1 Introduction

In 1985, the first *ceramer*, composed of poly(dimethyl siloxane) (PDMS) and tetraethoxysilane (TEOS), was reported.[1] The relationship between the ceramer structure and properties was studied in detail.[2,3] However, one of the complications with synthesizing ceramers of this type is that the acid catalyst employed in the sol-gel reaction can cause the PDMS chains to undergo chain scission and recombination ("scrambling"), thereby lowering the molecular weight and broadening the molecular weight distribution of the oligomeric PDMS. Another well studied system which avoids this problem is that based on poly(tetramethylene oxide) (PTMO) with tetramethoxysilane (TMOS).[4–9] In these materials, however, the PTMO component of the ceramer may crystallize under the proper conditions. The focus of the present work is a new ceramer made from poly(propylene oxide) (PPO) and tetramethoxysilane (TMOS). The PPO oligomers used in this study are not stereospecific (atactic), and as such are not crystallizable. The glass transition temperature of high molecular weight PTMO (–84 °C)[10] is very close to that of high molecular weight PPO (–78 to –73 °C),[11–14] so ceramers made from each with similar formulations are readily comparable. It should be noted, however, that PTMO has a smaller mass per backbone bond than PPO (14.4 versus 19.3 g / mol), so a PTMO chain would have distinctly longer contour length than a corresponding PPO chain of equivalent molecular weight. For the PPO based ceramers of this work, there is no evidence of scrambling of the PPO chains by the acid for the concentrations used in this work. The PPO materials employed in this study are among the class of JEFFAMINE® polyoxyalkyleneamines available from the Huntsman Corporation. One of the disadvantages of these materials is that they are imperfect in their chemistry; they have less than the ideal functionality of two. Recently Lyondell

has brought to the marketplace PPO oligomers (ACCLAIM™ polyether polyols) which have very narrow molecular weight distribution and low monol content (and hence nearly ideal functionality). This has lead to an interesting comparison of ceramers made from both the JEFFAMINE® and ACCLAIM™ sources, and will be the subject of the next chapter. The focus of the present chapter is the influence of the sol–gel variables of water, acid, and TMOS content, as well as the molecular weight of the oligomeric PPO on the final properties of JEFFAMINE® based ceramers.

3.2 Experimental Approach

3.2–A. Materials and Synthesis

As stated above, the poly(propylene oxide) (PPO) starting materials employed in this study are among the class of JEFFAMINE®s made by the Huntsman Corporation. They are oligomeric forms of linear PPO with *ideally* one primary amine group at the termini of each molecule, that is, they are diamines. Although the JEFFAMINE®s are primarily used as curing agents for epoxies, the reactive amine end–groups may be exploited in many other reactions.

The structure of the JEFFAMINE® materials is shown in Figure 1. The three JEFFAMINE®s employed in this study had the average number of propylene oxide repeat units, n = 2.6, 5.6, and 33.1. They are referred to as D230, D400, and D2000, respectively, the numbers approximately representing the number average molecular weight of the oligomer, and the "D" meaning diamine (ideally). However, the actual functionality of these oligomers is less than 2. The functionality can be calculated based on the primary amine content and average molecular weight provided by the manufacturer, and is listed in Table 1 for the three JEFFAMINE®s used in this study. Since the functionality of these materials is strictly less than 2, the final network structure of the ceramers is certain to have imperfections such as dangling ends and a notable sol–fraction. Also, the actual number and weight average molecular weights, as well as the breadth indexes, are included in Table 1. These data were graciously

provided by the manufacturer, and were measured by gel permeation chromatography (GPC or SEC) in tetrahydrofuran.

Other chemicals used in this study include tetramethoxysilane (TMOS, 99+%, obtained from Gelest), isocyanatopropyltriethoxysilane (ICPTES, 95%, also from Gelest), isopropanol (IPA, ACS specifications, obtained from EM Science), and 1 M aqueous HCl solution (Aldrich Chemical).

To prepare the PPO oligomers for the sol-gel reaction, they were end-functionalized with alkoxysilane groups through the reaction outlined in Figure 1. The isocyanate moiety on the ICPTES molecule reacts with the amine group(s) on the PPO oligomer to form urea linkage(s). The reaction was carried out at room temperature in a 70 wt.% solution of IPA, with the isocyanate material (in three mole percent excess of stoichiometry) added dropwise over the course of 15 minutes. Following this addition, the reaction flask was sealed and continuously stirred for eight hours. This forms a new molecular species which can participate in the sol-gel reaction through hydrolysis and condensation of the alkoxysilane end–groups in the presence of water.

The silane functionalized JEFFAMINE®s can undergo the sol–gel reaction with the addition of water and acid catalyst, or may co–react with a metal alkoxide (TMOS in the present case) to form a hybrid network as outlined in Figure 2. The sol–gel reaction was carried out by adding to the functionalized JEFFAMINE® (and TMOS if desired) a calculated amount of water and allowing the mixture to stir for ca. one minute. If this reacting liquid was cloudy due to immiscibility of PPO with water, enough IPA was added to clarify the solution and form a homogeneous sol (homogeneous on the scale of the wavelength of visible light). This was followed by addition of aqueous 1M HCl slowly and dropwise to the briskly stirred beaker. The reaction media was then poured into clean polystyrene petri dishes, degassed in a vacuum chamber, and allowed to cure at room temperature. All samples were aged at laboratory conditions for at least one week prior to testing. The last one or two days of aging was performed under vacuum to remove most of the solvent, by-product alcohol, and water. The small angle x-ray scattering profiles of these ceramer materials remained constant after this aging

period, indicating that the reaction reached an equilibrium extent at these curing conditions. The thickness of the final ceramer films was on the order of 0.5 mm.

3.2–B. Characterization

All small angle x-ray scattering (SAXS) experiments were performed with nickel filtered, slit collimated Cu*Ka* radiation (1.542 Å)[15] produced by a Philips generator, model PW1729. A Kratky camera and a one–dimensional M. Braun position–sensitive detector were used to collect the scattered radiation. Absolute intensities were calibrated through the use of a polyethylene (Lupolen) working standard.[15] The raw data were analyzed to yield correlation distances and fractal dimensions where appropriate.

The differential scanning calorimetry (DSC) experiments were performed on a Seiko DSC 220C with nitrogen purge gas. A heating rate of 20 K / min was employed for all scans, and samples weighed between 5 and 10 mg.

Thermogravimetry (TG) was accomplished with a Seiko TG / DTA under air purge. A heating rate of 10 K / min was used and samples weighed between 5 and 10 mg.

A Seiko DMS 210 was utilized for dynamic mechanical spectroscopy (DMS) experiments. Rectangular samples had a gauge length of 10 mm, and were cut such that their cross–sectional area was between 2 and 7 mm^2. Scans were started at room temperature, and cooled slowly (1.5–2 K / min) with liquid nitrogen to ≈ –150 °C while collecting data. After this cooling scan, the sample was allowed to equilibrate to room temperature, and a heating scan was then started under nitrogen purge gas with a heating rate of 1.5–2 K / min. The data from the heating and cooling scans were then combined to give the thermomechanical spectrum for each sample. All DMS data shown in this chapter were measured at an oscillation frequency of 1 Hz.

Samples were extracted with acetone in an extraction thimble until the resulting values of the sol fraction did not change with time. The extraction thimble is a glass vial with a porous frit. It is placed in a beaker of solvent, enough to entirely submerge the sample but not the vial. The porous frit allows solvent and extracted material to pass, while retaining the network film. Complete extraction generally took one week,

while removing old acetone and adding fresh every few days. The measurement process involved weighing the sample and extraction vial before the experiment. After exposure to the extracting solvent, the vials and extracted samples were dried in a vacuum chamber for several days before weighing. All steps in the extraction process were performed at laboratory temperature.

3.2–C. Nomenclature

Due to the numerous variables explored in this work, a simplified system of nomenclature has been employed so that samples can be easily differentiated. This will be illustrated by the following example:

f-D2000(50) TMOS(50) 4/1/0.02

The f-D2000(50) represents alkoxysilane end–functionalized JEFFAMINE® D2000 which is 50 weight percent of the initial reaction mixture (relative to TMOS content). The TMOS(50) represents 50 wt.% tetramethoxysilane, and the 4/1/0.02 represents the molar ratio of water/alkoxysilane/HCl employed during the sol–gel reaction. The moles of alkoxysilane used in this calculation are derived from both the TMOS (—OCH_3) and functionalized JEFFAMINE® species (—OCH_2CH_3). Also, the combined weight percent of the functionalized JEFFAMINE® and the TMOS adds up to 100 wt.% for all formulations.

3.3 Results and Discussion

For reference, a few of the basic properties of various ceramers of the 4/1/0.04 formulation have been archived in Table 2. These include glass transition temperatures, silicate contents, sol fractions, correlation lengths, and fractal dimensions. All of these properties will be examined in further detail with respect to each formulation variable.

3.3–A. Influence of water content

f-D2000(100) ceramers

A strong peak is observed in the SAXS data for all ceramers of the f-D2000(100) family (Figure 3 which shows both the varied water and acid content). This peak corresponds to a microphase separated structure, where the oligomeric PPO chains form the continuous phase, segregated from the dispersed silicate phase, which provides significant contrast in electron density on the scale of the x-ray wavelength. For the three SAXS curves of varied water content labeled 4/1/0.02, 2/1/0.02, and 1/1/0.02, all have the same correlation length (Bragg spacing) near 45 Å. Hence water does not significantly influence the phase separated structure of the final networks for the range probed. This is reinforced by the DSC data of Figure 4. Across the same variation in water content, all DSC scans show a clear glass transition at –56 °C, corresponding to the glass transition of the phase separated PPO chains. Pure, high molecular weight PPO homopolymer has a reported[11–14] dilatometric glass transition temperature in the range of –78 to –73 °C. The presence of endothermic "bumps" in the range of 40 to 120 °C of Figure 4 is likely due to the release of water, solvent, and by-product alcohols. This has been confirmed by the absence of such bumps in a second heating scan of the same sample. There is no clear trend in the appearance of these bumps as a function of water content. There is a very slight weight loss (0.4 %) in this temperature range in the thermogravimetry data of Figure 5. This TG data for the series of varied water content also show no significant deviation in behavior.

The dynamic mechanical data similarly show that the water content plays a relatively insignificant role in the final properties as seen in Figure 6 (varied water and acid content included in this plot). For the three water contents probed here, all materials have an identical glass transition (≈ –57 °C), and the thermomechanical spectra essentially coincide. Hence the mechanical behavior is also unaffected by the water content for the range probed here.

For these f-D2000(100) materials, the storage modulus in the glassy state is ≈ 6 GPa, and drops roughly three orders of magnitude across the glass transition into the rubbery state. This behavior is also characteristic of isotropic, amorphous, organic polymers, as well as unfilled, *lightly* crosslinked organic networks.

The storage modulus for these materials in the temperature range of 25 to 200 °C (rubbery plateau) displays a slight increase with temperature. This may be due to further reaction above room temperature (which was the original cure temperature), thereby increasing the crosslink density and hence the modulus. Another explanation would be the rubber elastic effect. From ideal rubber elasticity it can be shown that:[16]

$$G = N_v kT = \frac{rRT}{M_c} = \frac{1}{3}E \quad . \tag{1}$$

G is the shear modulus and E is Young's modulus, both of which are determined from *equilibrium* experiments, not dynamic oscillatory measurements (which the storage modulus, E' is determined from in Figure 6). Regardless of the dynamic mechanical data being non-equilibrium data, such experiments provide results which are compliant with equilibrium swelling measurements for similar hybrid systems based on PTMO and TEOS.[17] Continuing the discussion of equation (1), N_v is the number of crosslinks per unit volume, k is Boltzmann's constant, T is the absolute temperature, r is the bulk density, R is the universal gas constant, and M_c is the number average molecular weight between crosslinks. Although equation (1) is for the equilibrium modulus of ideal networks with crosslink junctions of functionality four, the dynamic storage modulus is still expected to have the similar dependence on temperature in the rubbery state, i.e., $E \propto E' \propto T$ (this proportionality to temperature is considered the rubber elastic effect). It then follows that, for a material that obeys ideal rubber elasticity, knowledge of the modulus E_1 at a given temperature T_1 can be used to calculate the modulus of that material E_2 at temperature T_2 (assuming the density change from T_1 to T_2 is negligible) by the following:

$$E_2 = E_1 \frac{T_2}{T_1} \ . \qquad (2)$$

This is analogous to using the perfect gas law for calculating the pressure P_2 of a gas at some temperature T_2 given the knowledge of the pressure P_1 at T_1 for an isochoric process. Applying this approach to the data in Figure 6 within the rubbery plateau, the modulus values thus predicted by rubber elasticity are lower than the measured values. Hence the increase in storage modulus with temperature in the range of 50 to 200 °C is believed to be due to a combination of the rubber elastic effect (T increasing in equation (1)) and the increasing crosslink density due to further reaction above room temperature (N_v increasing or M_c decreasing in equation (1)). This can be confirmed by annealing a sample at an elevated temperature and afterward measuring the thermomechanical spectrum in the rubbery region. This has been achieved in Figure 7 where a sample of f-D2000(100) 4/1/0.04 was heated from room temperature to 150 °C, annealed there for 60 minutes, cooled to room temperature, and reheated to 150 °C, collecting data along the way for each step. During the first heating, the storage modulus is curved upward as temperature is increased (just as the data in Figure 6), and annealing at 150 °C causes a continued increase. However, the data from the subsequent cooling and heating steps all coincide. The line which has been drawn in the figure, which closely follows the subsequent cooling and heating data at the lower temperatures (15 to 70 °C), represents the proper shape for ideal rubber elasticity (calculated by equation (2)). The experimental data lie below the rubber elasticity line at higher temperatures, which is likely due to the presence of loose chains (sol–fraction). From Table 2 it can be seen that this ceramer has a sizable sol–fraction in the amount of 5.6 wt.% of the total sample. Hence Figure 7 confirms that upon the initial heating step of the DMS experiment, further curing occurs leading to an increased crosslink density. This generates higher storage modulus values during the first heating scan than are to be expected purely from the rubber elastic effect.

Interestingly, a small shoulder is observed in the tan*d* data just above the main glass transition in Figure 6. This relaxation process will be addressed in the section concerning the influence of TMOS content.

f-D2000(50) TMOS(50) ceramers

The influence of water concentration on the thermal and mechanical properties of TMOS containing ceramers is likewise trivial. However, there is a noticeable difference in the SAXS curves for f-D2000(50) TMOS(50) ceramers of varied water content, as shown in Figure 8. The material with the least water content, the 1/1/0.02 ceramer, has a distinct peak at 59 Å. Doubling the water concentration (the formulation of 2/1/0.02) leads to a slightly increased spacing of 61 Å. This may not be a significant difference. The sample of 4/1/0.02 formulation, however, shows a clearly different SAXS pattern, as a shoulder rather than a peak is observed. This shoulder appears at a lower angle than that corresponding to 61 Å.

The plot on the right in Figure 8 is a double log presentation of the data on the left. In this presentation, the mass fractal character of the ceramer materials can be discerned. This is evidenced by the linear shape in the tail portion (Porod region) of the $\log I(s)$ *vs.* $\log s$ plot. For a material to be truly fractal, it has been suggested[9] that this linear region should be maintained over at least one decade of *s*, which is not accomplished here. However, if the data could be collected to wider angles than the current instrument allowed, this linear behavior might have continued. Nevertheless, it has been suggested that trends can certainly be recognized using data which covers less than one decade.[9] The slope within the Porod region is related to the fractal dimension. The relationship depends on the type of fractal (mass or surface) and the form of x-ray beam collimation. All of the fractal ceramers studied here were mass fractals. For such materials, the mass (*M*) of the object scales with the characteristic length to the power of the fractal dimension (d_f): $M \propto (length)^{d_f}$. Since slit collimation was employed throughout this work, the relationship between the Porod slope (*m*) and the fractal dimension is $d_f = 1 - m$. For pin–hole collimation, $d_f = -m$;

other details concerning fractals have been discussed elsewhere.[9,18–20] The two ceramers with the lower water content (1/1/0.02 and 2/1/0.02) both possess a peak on the $\log I(s)$ *vs.* $\log s$ plot (as they did in Figure 8), followed by a linear region indicative of fractal behavior.

It should be noted that in the ceramer materials which possess a clear correlation peak, the Porod region may contain a contribution to the scattered intensity from a second order of the main correlation peak. This would influence the slope in the Porod region and hence the value of the fractal dimension may be incorrectly measured. This point is duly noted, and such data are analyzed for trends only.

The highest water content ceramer (4/1/0.02) has no distinct peak, but the fractal character is easily seen. The approximated fractal dimension for all three materials is roughly the same, ≈ 2.5. This means that the mass of these ceramers scales with its length to the power of 2.5. A solid, three–dimensional object of uniform density would have fractal dimension d_f = 3. Hence the molecular structure here is somewhat more "open", or less space filling, than a uniform solid. Although the fractal dimension appears to be independent of water concentration for this series of f-D2000(50) TMOS(50) ceramers, the scattering curves are quite different when plotted on a linear scale as discussed above.

The thermomechanical spectra of these TMOS containing ceramers show no significant effect of water content as shown in Figure 9. The three spectra in this plot coincide. The glass transition is broader (onset ≈ –60 °C, end point ≈ 70 °C) and at a higher temperature (≈ 10 °C) than the corresponding materials made without TMOS. The extreme broadness of the glass transition is due to a widely varied environment which the PPO chains inhabit. Some regions exist which are predominantly rich in PPO chains, and this would correspond to the lower temperature portion of the transition region. With 50 wt.% TMOS available during the sol-gel reaction, some regions likely exist where the PPO chains are highly constrained by an abundance of dense silicate structure. This would correspond to the higher temperature portion of the glass transition region. In between these two extremes, a distribution of structures

exists which would lead to the observed broadness of the glass transition. A more detailed discussion is to follow in the section concerning the influence of TMOS content.

Also, the tan*d* data of the 4/1/0.02 formulation show a small shoulder at the low temperature end of the glass transition, near –50 °C. This is due to the PPO chains which are most sharply phase separated and free of excessive constraints by the silicate material. This shoulder is less noticeable in the 2/1/0.02 material and is not present in the 1/1/0.02 formulation. It is hypothesized that this shoulder is due to the low miscibility of the D2000 material in water. Hence, even though the reacting sol appears homogeneous (on the scale of the wavelength of visible light), this high water content formulation is likely to lead to a sharper phase separation of a portion of the PPO chains in the final network, when compared to a formulation with less relative water content (and more relative IPA). This sharper phase separation would lead to higher contrast in electron density (this contrast is a necessary component of the scattering power of a material). This is in agreement with the observation in the SAXS data of Figure 8 that the integrated intensities increase with increasing water content (and hence the materials are increasing in scattering power due to sharper phase separation).

One last consideration of the dynamic mechanical data is that the storage modulus in the glassy state for these materials is roughly 10 GPa, and drops only 2 orders of magnitude across the glass transition into the rubbery state. This behavior is characteristic of a filler–reinforced elastomer and also a more highly crosslinked network. This issue will be discussed in more detail in the section on the influence of TMOS content.

The DSC scans for these three TMOS containing ceramers similarly show a very broad glass transition temperature, centered around ≈ –25 °C (not shown for brevity). The onset temperature appears to be near –60 °C, and the endpoint near 15 °C. Admittedly, the glass transition temperatures are difficult to discern by DSC; the DMS technique is much more sensitive for this purpose. The low sensitivity of the DSC technique is primarily due to the relatively low mass fraction of PPO in these ceramers.

Some endothermic bumps are present in the DSC scans at elevated temperatures (≈ 100 °C and above) which, as stated earlier, are believed to be due to the release of water, solvent, and by–product alcohols.

The thermogravimetry data for the f-D2000(50) TMOS(50) ceramers of varied water content are shown in Figure 10. The curves for this series of materials have the same characteristic shape, and the char yield for all three samples is ≈ 36 wt.%.

3.3–B. Influence of acid content

Since acid is a catalyst for the sol-gel reaction, increasing its concentration is expected to increase the sol-gel reaction rate, and hence reduce the gel time for a given formulation.

f-D2000(100) ceramers

As with the series of varied water content, the SAXS curves for the family of f-D2000(100) ceramers of varied acid content all possess a peak at ≈ 45 Å, shown in Figure 3. The five curves of varied acid and water content essentially coincide, implying that the acid content also has no influence on the final structure observed by SAXS. This is supported by the dynamic mechanical spectra of Figure 6. Again the five spectra corresponding to varied acid and water content coincide. DSC provides supporting evidence (not shown) that acid content has no effect on the final properties of the f-D2000(100) ceramers within the range probed. All three scans show a clear glass transition at ≈ –56 °C, just as the materials in Figure 4. The thermogravimetry data for these three samples, shown in Figure 11, also coincide well.

f-D2000(50) TMOS(50) ceramers

The SAXS profiles for the f-D2000(50) TMOS(50) materials do exhibit a dependence on acid content, as shown in Figure 12. The lowest acid content ceramer (4/1/0.01) shows a small peak at ≈ 76 Å. Increasing the acid content leads to a transition of the peak into a shoulder. The highest acid content material (4/1/0.04) shows a very slight shoulder, with no distinct correlation length in Figure 12. Plotting the SAXS data on a

double–log scale in the graph on the right again brings out the fractal character of these ceramers. The fractal dimension for these three materials are all in the range of 2.4 to 2.6, with no obvious trend with acid concentration.

There is also a noticeable difference in the thermomechanical spectra for this series, as shown in Figure 13. The peak observed in the tan*d* data for the lowest acid content material (4/1/0.01) occurs over the broadest temperature window. The extreme broadness of the glass transition is due to the widely varied environments that the PPO chains inhabit. The peak of the "main" relaxation for this material occurs at ≈ 10 °C, and a small shoulder is present at ≈ –50 °C. There also appears to be a small shoulder in the higher temperature near 90 °C.

The 4/1/0.02 formulation has a slightly less broad glass transition, and the peak of the main relaxation appears at a slightly lower temperature (≈ 0 °C) than the lowest acid content formulation. However, an equivalent low temperature shoulder is present at ≈ –50 °C. The high acid content ceramer (4/1/0.04) displays the lowest temperature main relaxation, at ≈ –15 °C. The low temperature shoulder is present for this material as well. A second shoulder is apparent for this material above the main glass transition, near 100 °C.

For this series of materials the DSC proves to be a much less sensitive probe than DMS (not shown). All three samples appear to have similar glass transition temperatures, near ≈ –30 °C by this method, and are very broad and their location is difficult to pinpoint.

The thermogravimetry data for these three samples, shown in Figure 14, are very similar in appearance. They all have the same characteristic shape and final char yield of ≈ 36 wt.%.

3.3–C. Influence of TMOS content

Addition of TMOS to the PPO based ceramers leads to a drastic change in morphological structure. This is easily seen in the SAXS data of Figure 15 which shows the scattering curves for f-D2000(100), f-D2000(75) TMOS(25), and f-D2000(50)

TMOS(50), all of the formulation 4/1/0.04. The sample with no added TMOS, the f-D2000(100) ceramer, has a distinct peak as noted before at 45 Å. However the sample with only 25 weight percent TMOS has a shoulder with no distinct peak. Incorporation of 50 weight percent TMOS leads to a very broad shoulder. The integrated intensity also increases with increasing TMOS content (in this range of 0—50 weight percent), or rather, the *invariant* increases with TMOS content. To describe this observation, a brief discussion of the scattering power and the invariant will be necessary. The invariant Q_s can be expressed as:[15]

$$Q_s = \int_0^\infty s \cdot I(s)\, ds \tag{3}$$

for slit–smeared absolute intensity $I(s)$. The invariant is related to the mean square fluctuation in electron density $\langle \Delta r^2 \rangle$ (or scattering power) which, for a two phase system displaying sharp phase separation, where each phase is of uniform electron density, the following simplified mathematical relationship holds:

$$\langle \Delta r^2 \rangle = f_{PPO} \cdot f_{sil} \cdot (r_{PPO} - r_{sil})^2 \propto Q_s \tag{4}$$

By employing this equation it is assumed that the ceramers are two phase systems, composed of a PPO phase of volume fraction f_{PPO} and electron density r_{PPO}, and a separate silicate phase of volume fraction f_{sil} =1–f_{PPO}, and electron density r_{sil}. With the value of $r_{PPO} - r_{sil}$ remaining constant, $\langle \Delta r^2 \rangle$ reaches a maximum at f_{PPO} = f_{sil} = 0.5. Hence the trend of increasing integrated intensity with increasing TMOS content (approaching 0.5 volume percent) of Figure 15 is certainly expected. Note that the infinite integral of equation (3) has not actually been evaluated for the data here. However, one can visually rank the area under the SAXS curves, since the data for each sample do not crossover at any point for the range of s measured in this study (measurements went to s=0.08 although the plot displays only up to s=0.05).

As can be seen in the double–log plot of this SAXS data on the right in Figure 15, adding TMOS to the f-D2000 ceramer formulation leads to a more mass fractal material. That is to say, the linearity in the Porod region extends over a larger range of *s* as the TMOS content is increased up to 50 wt.%

There is also a drastic difference in the dynamic mechanical behavior of the varied TMOS containing ceramers, as shown in Figure 16. Although all three samples show virtually the same storage modulus in the glassy region, at and above the glass transition, the material behaviors diverge. The glass transition, as ascertained from the storage modulus data, increases and broadens with increasing TMOS content. The f-D2000(100) ceramer behaves similarly to an amorphous, lightly crosslinked organic network in that there is a three order of magnitude decline in the storage modulus across the glass transition. However, the presence of the silicate phase derived from TMOS in the other two materials greatly increases the storage modulus in the rubbery region. Similar behavior has been noted in elastomers which contain a reinforcing filler;[21] in some cases an increase and broadening in the glass transition has been observed.[22,23] Here the reinforcing filler is the silicate phase. More interesting information can be uncovered by examining the tan*d* data, to be addressed next.

For the f-D2000(100) ceramer, the PPO chains are crosslinked by the silicate solely at the two ends of each linear molecule. Therefore, between each silicate crosslink junction is a ≈ 2000 g/mol PPO chain (along with the urea and n-propyl groups). This can be envisaged as a long rope held rigidly at both ends, where the rope has a coil–like conformation in between. PPO segments which are farthest from both crosslinked silicate ends are the most mobile, (like the bulk of the rope far from the held ends) and hence have the lowest glass transition near that of homopolymeric PPO. This is the relaxation which is observed in the tan*d* data in Figure 16 at –55 °C. Segments near the silicate ends are highly *constrained on this end,* but are much more free in the opposite direction which consists of other PPO segments (this is like the region of the rope near a grasped end). These *partially constrained* segments are one possible source of the small peak occurring at –10 °C, just above the main relaxation. The magnitude of the

relaxation of these partially constrained segments is considerably smaller than the magnitude of the major glass transition at –55 °C due to their lower concentration when compared to the more mobile, homopolymeric–like PPO segments. Although the subject of the next chapter, ceramers made from the ACCLAIM™ polyether polyol of a similar formulation also possess a small relaxation above the main glass transition. For these ACCLAIM™ ceramer materials, this relaxation appears as a shoulder to the main relaxation rather than a distinct peak as seen for the JEFFAMINE® systems. Such a shoulder has been observed (although not discussed) for other ceramer systems such as ones based on hydrogenated polybutadiene (Figure 12 of reference 24). This sort of post–T_g relaxation process is also likely due to segments at or very near the interface between the silicate phase and the PPO phase. This is often referred to as an *interphase*, which for the various ceramer materials addressed above, likely contains the linking urea or urethane groups. In all three of the above cases, the soft phase (PPO or polybutadiene) is connected to the silicate through urethane or urea bonds along with an n-propyl group. Hence these urea and n-propyl groups would be among the atoms in the interface region. The urea groups in the ceramers may act similarly to the "hard segments" in segmented copolymers such as polyurethanes and polyureas. Such segmented copolymers typically show a low glass transition, associated with the "soft" phase (the chemistry of which is often PPO, PTMO or PDMS, etc.) and a higher transition associated with the "hard phase" (typically derived from the isocyanate used to synthesize the polymer). Figure 10 of reference 25 shows DMS results of a PDMS-urea segmented copolymer. In this case, the PDMS is the soft phase, and the hard phase, which contains the urea groups, is derived from the methyldiphenyldiisocyante (MDI). A distinct transition is observed for each phase in these segmented copolymers as manifested in dual peaks in the tan*d* data.

Also relevant to the current discussion is an observation from the block copolymer literature. For an immiscible triblock copolymer (namely a styrene–butadiene–styrene triblock copolymer called Thermoelastic® 125 from Shell Chemical), which shows two distinct glass transitions by DMS (one from the styrene phase and one from the

separate butadiene phase), casting from a suitable solvent leads to the formation of an intermediate, mixed phase. This phase exhibits a glass transition at a temperature between the other two.[26] Then similarly, the observed relaxation above the main glass transition in Figure 16 can be due to the relaxation of an intermediate, mixed PPO and silicate phase. Again, for the materials in this study, this intermediate phase would be located between the silicate and the soft PPO phase.

When 25 wt.% TMOS is added to the formulation, the resulting silicate phase can interact with the PPO segments at locations other than just the PPO chain ends. Therefore, the rope analogy becomes too simplistic to describe the types of environment in which the PPO chains may inhabit. Expectedly then, the magnitude of the relaxation of the mobile, homopolymeric–like PPO segments (at –55 °C) decreases in Figure 16 for the 25 wt.% TMOS sample,[4] compared to the f-D2000(100) sample. This is accompanied by the appearance of a distribution of relaxation processes at higher temperatures (centered around –25 °C), resulting from these other silicate–PPO interactions. These relaxation processes can correspond again to the segments at the chain ends, near the silicate phase, and also other PPO segments at any location along the chain where some condensed silicate material (from TMOS) may impose constraints upon it. There is also a very small shoulder at 70 °C, likely corresponding to a population of more *highly constrained* segments. These can be segments which are moderately encapsulated, or at least more highly constrained by silicate leading to a higher temperature associated with this relaxation. Similarly, three distinct environments have been suggested for PTMO chains in a ceramer made with TMOS.[4]

When 50 wt.% TMOS is incorporated, the low temperature, homopolymeric–like PPO relaxation becomes a small shoulder rather than a peak (Figure 16). Hence the concentration of unconstrained PPO segments in this f-D2000(50) TMOS(50) ceramer is very small. Similar to the 25 wt.% TMOS sample, a distribution of higher temperature relaxation processes exists in this material. The tan*d* peak for the 50 wt.% TMOS ceramer reaches a higher temperature than the 25 wt.% TMOS material, due to the increased constraints imposed by the greater amount of silicate in this sample. The

relaxation of the partially constrained PPO segments appears to be the "major" active relaxation process for this material, as this is the region where the tan*d* data contains a maximum. There is a second shoulder, at ≈ 100 °C, again corresponding to a highly constrained population of PPO segments.

A critical point to mention is the poor tensile stress–strain properties of these JEFFAMINE® based ceramers. The sample–to–sample variation was rather great, and these materials failed at very low values of strain ($\varepsilon_b < 0.15$), shown in Figure 17 [f-D2000(75) TMOS(25) and f-D2000(50) TMOS(50) only, as the f-D2000(100) material was far too soft and tacky to perform tensile tests]. The shape of the σ_0–ε curves was linear, like that of a Hookean spring. This behavior of low strain at break and Hookean shape was observed for similar ceramers based on poly(dimethyl siloxane) and TEOS.[2,3] This is in contrast to the superior tensile behavior of similarly formulated ceramers based on the ACCLAIM™ poly(propylene oxide) oligomer, which is the subject of the next chapter. The tensile behavior of the ACCLAIM™ ceramers is similar to that of previously studied[4–7] PTMO–TEOS and TMOS ceramers.

The differential scanning calorimetry data for this series of materials are shown in Figure 18. It can be seen from this figure that increasing the TMOS content leads to a higher and broader glass transition, which directly supports the DMS data. The f-D2000(100) material has the largest change in heat capacity across the glass transition, ΔC_P, which is expected in light of the relative weight fraction of PPO in this material is the highest of the three samples.

The thermogravimetry data of Figure 19 were employed to estimate the weight fraction of silicate in the ceramer (values listed in Table 2). Assuming that the remaining material at the end of the scan ("char yield") is only the inorganic silicate component and all of the organic material was pyrolyzed, the char yield can be utilized as a rough estimate of the silicate content in the original ceramer. The silicate component for the f-D2000(100) material is generated solely from the alkoxysilane groups at the chain ends of the f-D2000 material as no metal alkoxide was added to this formulation. A simple calculation shows that the alkoxysilane end–groups of the f-

D2000 represent 13 % of the total molecular weight of the f-D2000 molecule (before the sol-gel reaction). However, in the network ceramer it is expected that a large portion of the alkoxysilane groups would be condensed, liberating water and alcohol; if the alkoxysilane groups were completely condensed, these end–groups (—SiO_3≡) would correspond to 7 % of the total weight of one "fully condensed f-D2000 molecule". The char yield then is expected to lie between 7 and 13 wt.% for the f-D2000(100) ceramer. A small amount of the measured char yield (13 %) may be due to carbonized organic material left behind and trapped inside the network oxide. As anticipated, adding TMOS to the formulation leads to an increase in the char yield (and hence silicate content) of the final material; f-D2000(75) TMOS(25) has 22 wt.% char yield and f-D2000(50) TMOS(50) has 36 wt.% char yield. Note that TMOS ejects a large portion of its mass upon hydrolysis and condensation (lost as methanol and water), and therefore the silicate content in the TMOS containing ceramers is lower (for the range probed here) than the weight fraction of TMOS added to the sol-gel reaction.

3.3–D. Influence of PPO molecular weight

The molecular weight of the PPO chains also plays a major role in the behavior of these ceramer materials. This variable will be discussed for non–TMOS containing samples only. The variation in the morphological structure can be seen in the SAXS profiles of Figure 20 (not absolute intensity). All three samples possess a correlation length, which increases with molecular weight. Increasing the molecular weight increases the average end–to–end distance of the PPO chains, and hence the correlation distance increases accordingly.[8] If the PPO chains behaved in a Gaussian manner, that is to say, if their unperturbed, mean square end–to–end distance $\bar{r}_0^2$ was related to the oligomer molecular weight M (or number of chain segments n) as:[27]

$$\bar{r}_0^2 \propto n \propto M \tag{5}$$

then a double–log plot of the correlation length versus the oligomer molecular weight should have a slope of ½. It is duly noted, however, that low molecular weight species

often do not behave in a Gaussian manner. Caution is thus suggested particularly for the D230 and D400 materials which have ≈ 2.6 and ≈ 5.6 propylene oxide repeat units each. Even the D2000 material has ≈ 33.1 repeat units, which still may be too small to expect Gaussian behavior. This aside, if the slope has a value of greater than ½, then the chains are more "expanded" than the unperturbed Gaussian state. This condition is often found when polymer chains are in low concentration in a good solvent. If the slope were less than ½, the chains are more "compressed", which would be the case for chains in a poor solvent. However, polymer chains typically will not take on a highly compressed conformation in solution, since they would rather precipitate into a separate phase. Hence values of the slope are seldom found much less than ½, but are often found greater than ½. The plot of correlation length versus molecular weight displays an unexpectedly low slope, namely 0.255 (Figure 21). Although only three data points are represented, the correlation coefficient for the linear fit of the data is R^2=0.99998. This suggests high confidence in the correlation, although a physical interpretation of this value of the slope is not readily apparent. It should be noted however, that the correlation length obtained from SAXS corresponds to the structure of both the PPO chains *and* the silicate phase (i.e. the distance between the centers of the silicate regions), and therefore the slope in Figure 21 is not a property of the PPO chain conformations only.

The sharpness of the SAXS correlation peaks also increases with molecular weight. This is due to the sharper phase separation of the higher molecular weight PPO chains, or conversely the improved incorporation and compatibility of the lower molecular weight PPO chains with the silicate component. This has been observed for PDMS–TEOS ceramers[3] as well as PTMO–TEOS ceramers[8] and is supported by the following dynamic mechanical data.

Figure 22 shows the influence of PPO molecular weight on the thermomechanical spectra of this series of samples. Decreasing the PPO molecular weight leads to an increased and broadened glass transition. The two lower molecular weight PPO oligomers (f-D400 and f-D230) do not exhibit a relaxation corresponding to the

homopolymeric–like PPO segments which the f-D2000 ceramer has. Since these shorter PPO chains have on average 5.6 and 2.6 propylene oxide repeat units respectively, the lack of a homopolymeric–like relaxation is expected. Hence the short chains are highly constrained at both ends, without a free, coil–like structure in between. With the shorter PPO chains, the relative amount of silicate is greater due to the increased concentration of alkoxysilane end–groups. This is confirmed by the thermogravimetry data of Figure 23, the results of which are included in Table 2. Hence decreasing the JEFFAMINE® molecular weight has a similar effect of increasing the TMOS content. Not surprisingly then, the relaxation processes observed in f-D400(100) and f-D230(100) of Figure 22 are broadened compared to the f-D2000(100) ceramer due to this large amount of silicate present, which can easily constrain the motions of the PPO segments. Broadening is likely aided by the presence of dangling ends, which are mostly a result of the imperfect functionality (<2) of the starting JEFFAMINE® materials. The dangling ends would relax at a lower temperature since they are only constrained at one chain end. Also broadening would be enhanced by the distribution of molecular weight of the starting JEFFAMINE® materials, as the D230 has the broadest molecular weight distribution and the D2000 has the narrowest (Table 1).

Lastly, the DSC curves for this series of ceramers are shown in Figure 24. Again these data support the DMS results. As the PPO molecular weight decreases, the glass transition increases and broadens, for reasons discussed above, and ΔC_P decreases due to the reduction in the relative weight fraction of PPO in the ceramer.

3.4 Conclusions

For the novel ceramers synthesized in this study based on JEFFAMINE® poly(propylene oxide) oligomers and tetramethoxysilane, the following conclusions can be made:

- Both the water and acid concentration have little influence on the final properties of these ceramers for the ranges probed in this study. However, increasing the water content for f-D2000(50) TMOS(50) ceramers lead to somewhat sharper phase

separation (by SAXS) of the PPO chains from the silicate due to the immiscibility of PPO with water.

- Increasing the TMOS content has a similar effect as decreasing the PPO molecular weight; both lead to an increased and broadened glass transition. This is due to an increase in the relative amount of silicate material which behaves like a reinforcing filler. Furthermore, decreasing the PPO molecular weight decreases the average molecular weight between crosslinks. This phenomenon also has the effect of increasing the glass transition temperature.
- Increasing the TMOS content tends to promote a more mass fractal structure for the f-D2000 based ceramers of 4/1/0.04 formulation.
- Increasing the PPO molecular weight increases the correlation length for non–TMOS containing ceramers observed by SAXS. This is expected since increasing the PPO chain length expands the average distance between the crosslinking silicate end–groups.
- Increasing PPO molecular weight also leads to a sharper phase separated structure due to the general decrease in miscibility with increasing molecular weight.
- DMS has proven to be a very sensitive instrument to probe the structure and thermal transition behavior of these ceramers, whereas DSC was rather insensitive.

3.5 Acknowledgments

The author wishes to thank the Huntsman Corporation for generously supplying the JEFFAMINE® polyoxyalkyleneamines for this study. Also, he would like to thank specifically Debra Direnfeld of the Huntsman Corporation for providing the molecular weight data for the JEFFAMINE®s employed in this study.

Table 1. Molecular weight, breadth index, and the average functionality of the JEFFAMINE® materials.

JEFFAMINE®	n*	$\overline{M}_n$	$\overline{M}_w$	$\overline{M}_w/\overline{M}_n$	f†
D230	≈ 2.6	195	240	1.23	1.89
D400	≈ 5.6	447	494	1.10	1.72
D2000	≈ 33.1	1577	1656	1.05	1.94

* *Average number of propylene oxide repeat units.*

† *Average functionality, i.e. the average number of primary amine groups per molecule (calculated).*

Table 2. Glass transition, silicate content, sol fraction, correlation length, and fractal dimension data for various ceramers of the 4/1/0.04 formulation.

Sample	T_g* (°C)	silicate content† (wt.%)	sol fraction (wt.%)	correlation length (Å)‡	fractal dimension‡
f-D2000(100)	–57	13	5.6	45	–
f-D2000(75) TMOS(25)	–46	22	2.9	–	2.7
f-D2000(50) TMOS(50)	–23	36	0.8	–	2.5
f-D400(100)	17	31	1.3	29	–
f-D230(100)	36	34	–§	25	–

* *Determined from DMS data as the midpoint of the drop in storage modulus across the glass transition.*

† *Estimated from char yield measured by thermogravimetry.*

‡ *Slit–smeared SAXS result.*

§ *Not measured.*

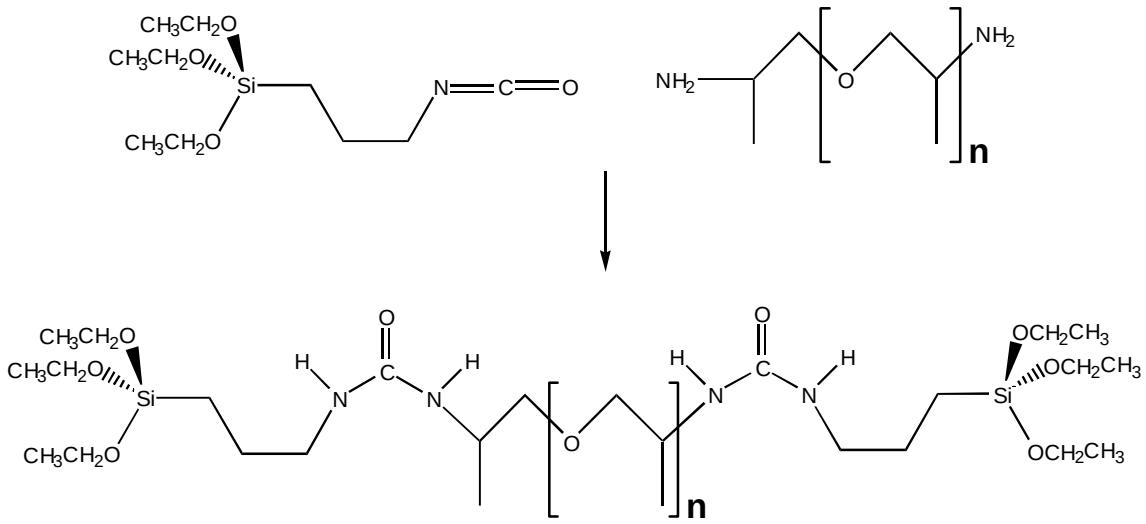

Figure 1. Schematic of the alkoxysilane functionalization of JEFFAMINE® poly(propylene oxide) oligomers.

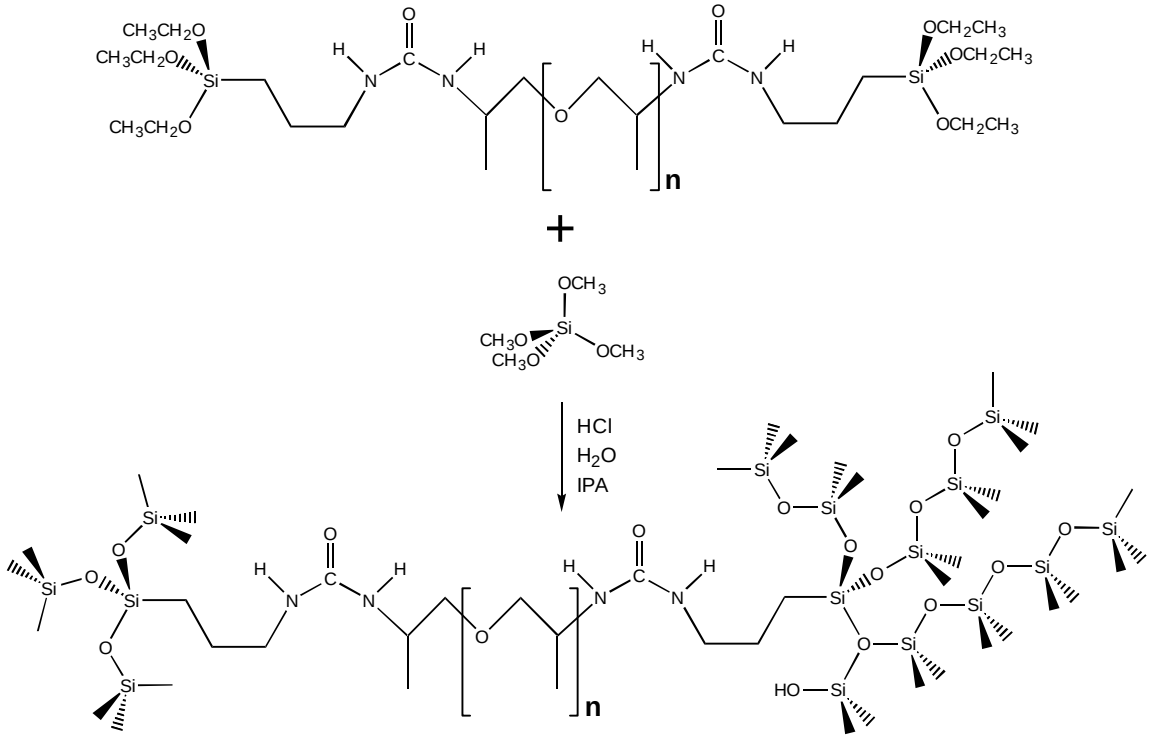

Figure 2. Schematic of the sol–gel reaction of functionalized a JEFFAMINE® PPO oligomer with tetramethoxysilane.

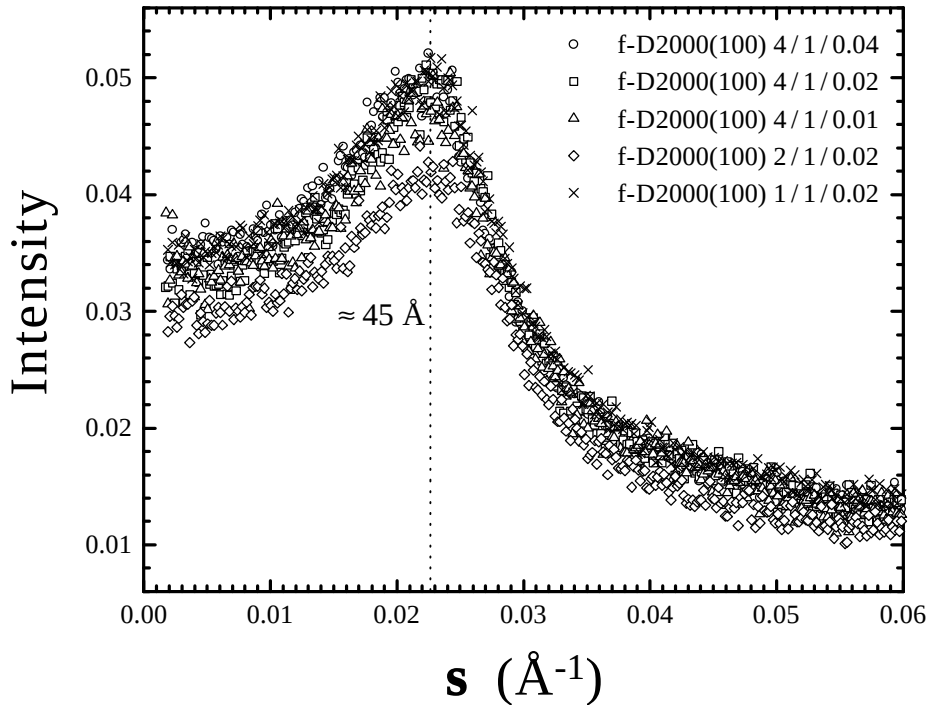

Figure 3. The influence of water and acid content on the SAXS behavior of f-D2000(100) ceramers.

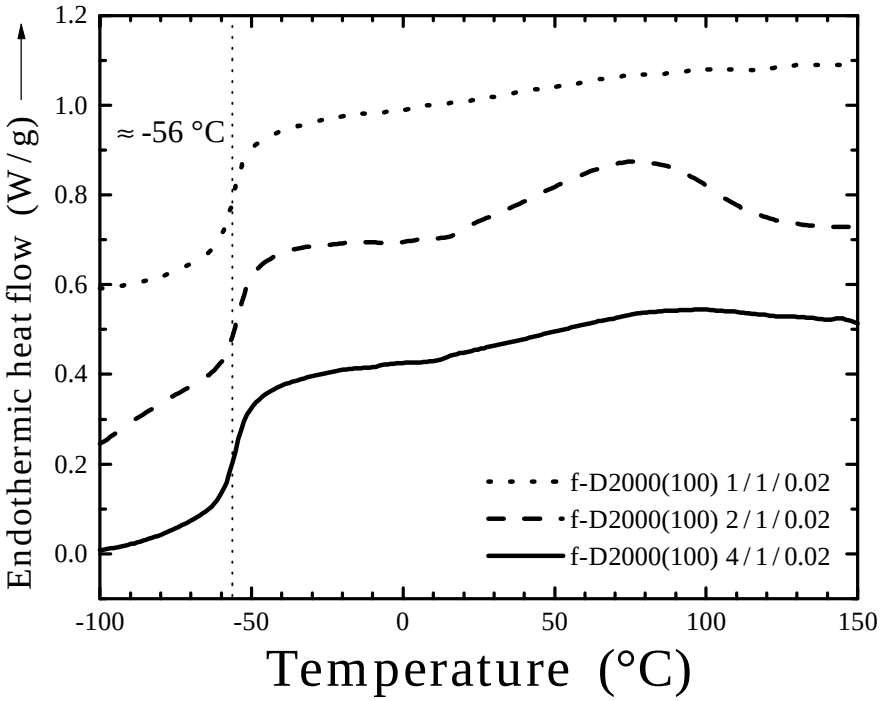

Figure 4. The influence of water content on the DSC scans of f-D2000(100) ceramers. Scans displaced vertically for clarity.

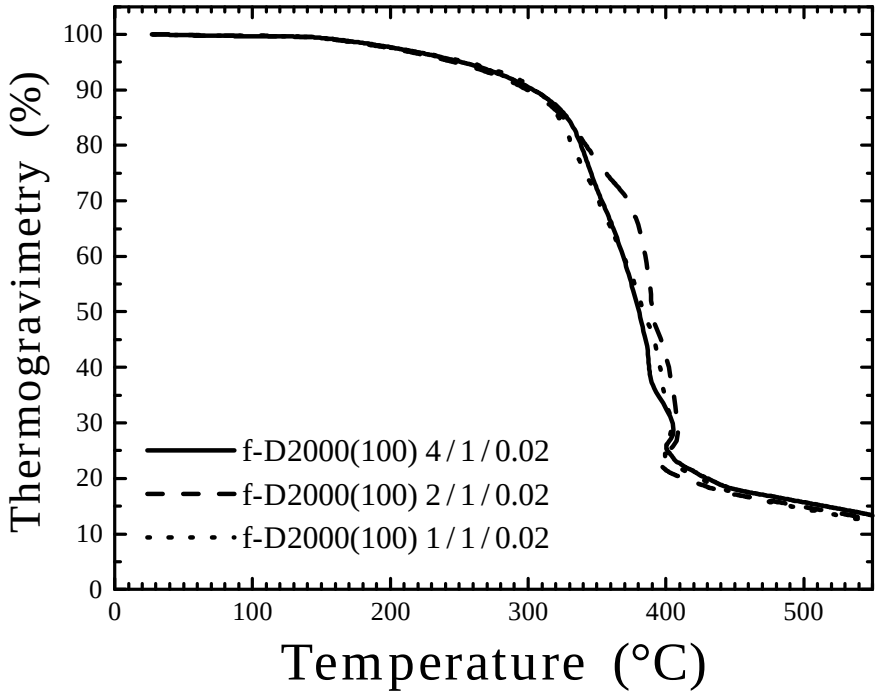

Figure 5. The influence of water content on the thermogravimetry of f-D2000(100) ceramers.

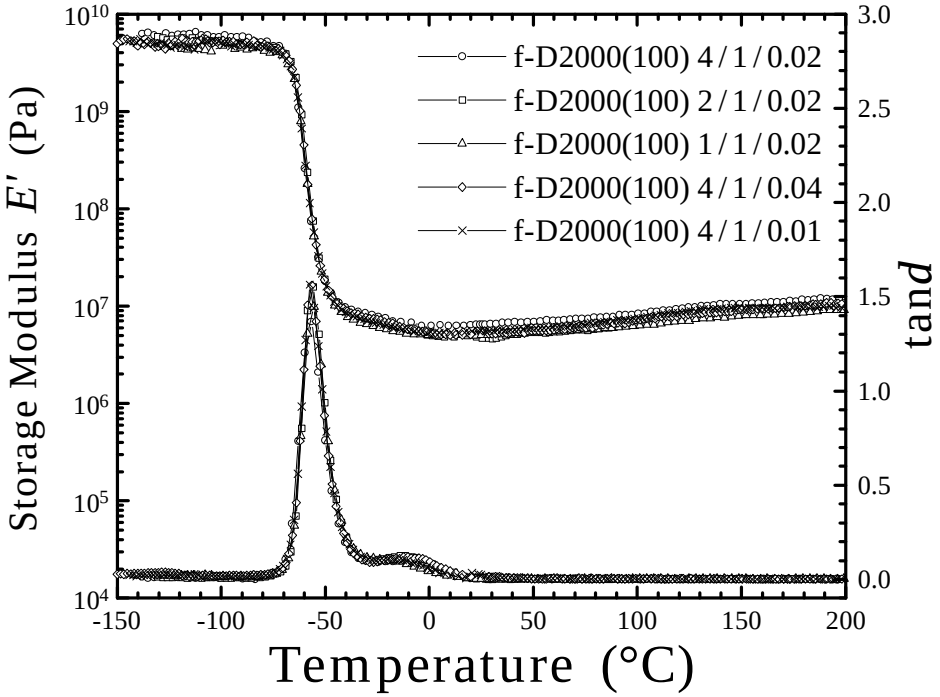

Figure 6. The influence of water and acid content on the thermomechanical spectrum of f-D2000(100) ceramers.

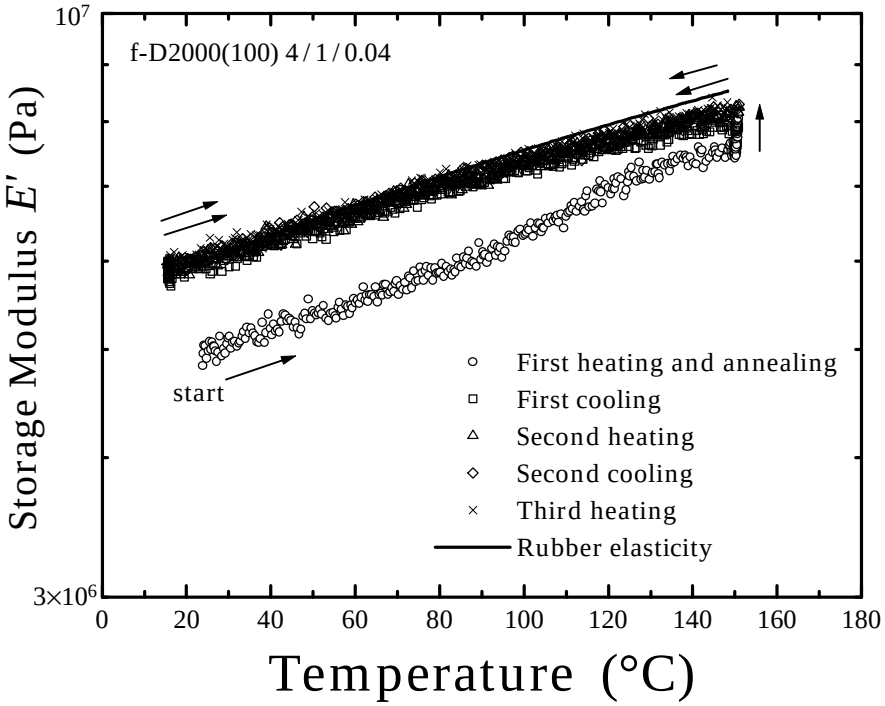

Figure 7. A cyclic dynamic mechanical experiment in the rubbery region of f-D2000(100) 4 / 1 / 0.04.

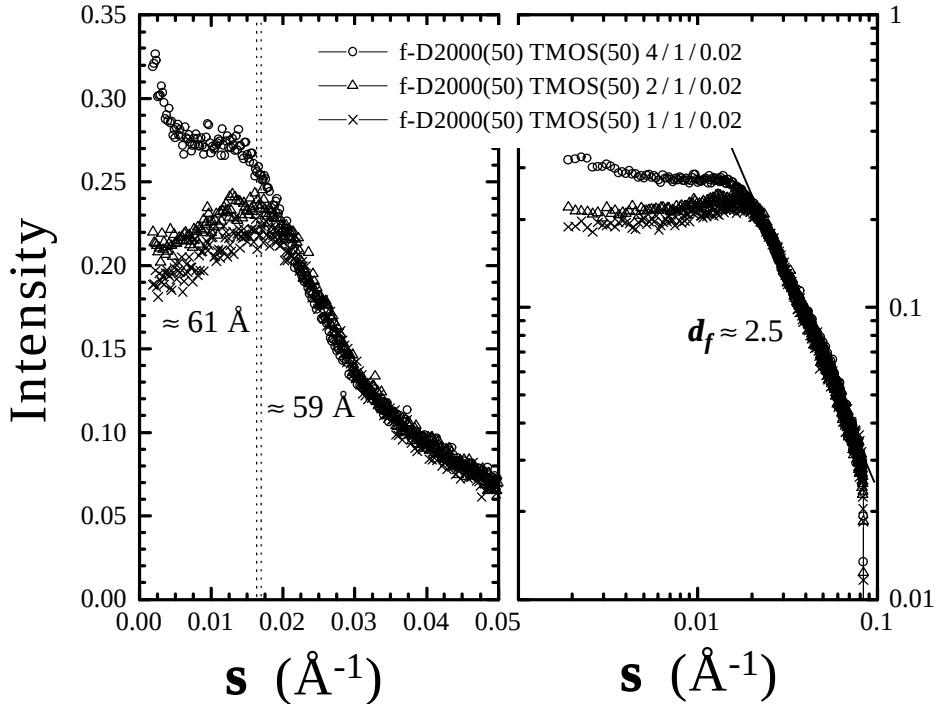

Figure 8. The influence of water content on the SAXS behavior of f-D2000(50) TMOS(50) ceramers. Plot on right is a double–log presentation of the same data in the plot on the left, which brings out the mass fractal character of these ceramers.

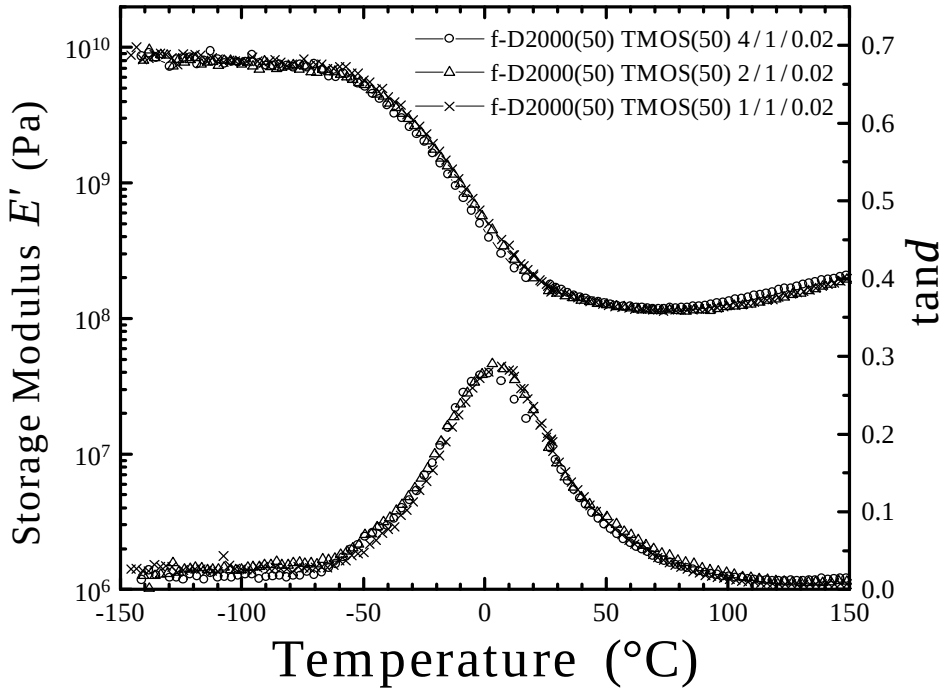

Figure 9. The influence of water content on the thermomechanical spectra of f-D2000(50) TMOS(50) ceramers.

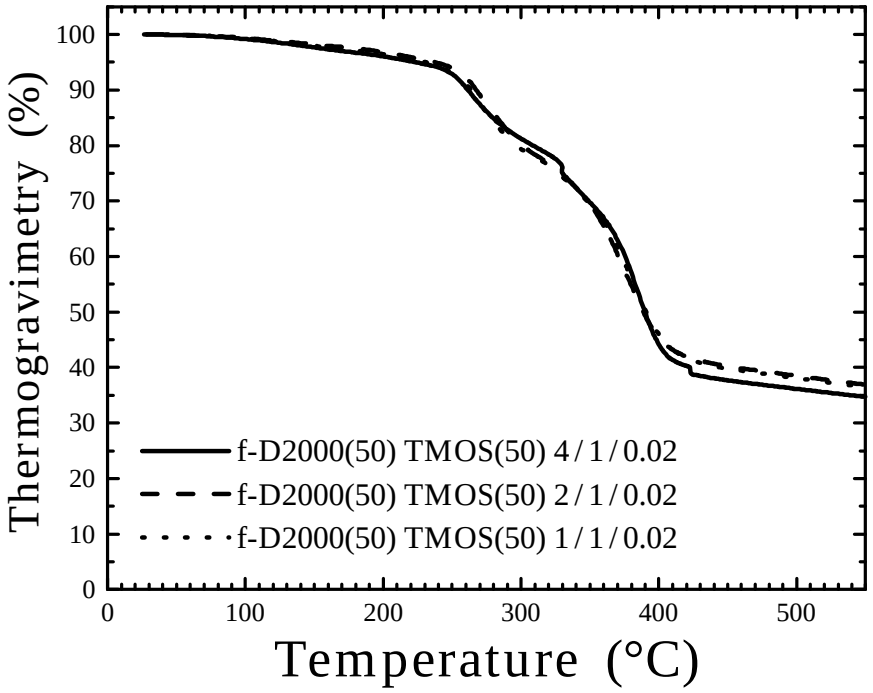

Figure 10. The influence of water content on the thermogravimetry of f-D2000(50) TMOS(50) ceramers.

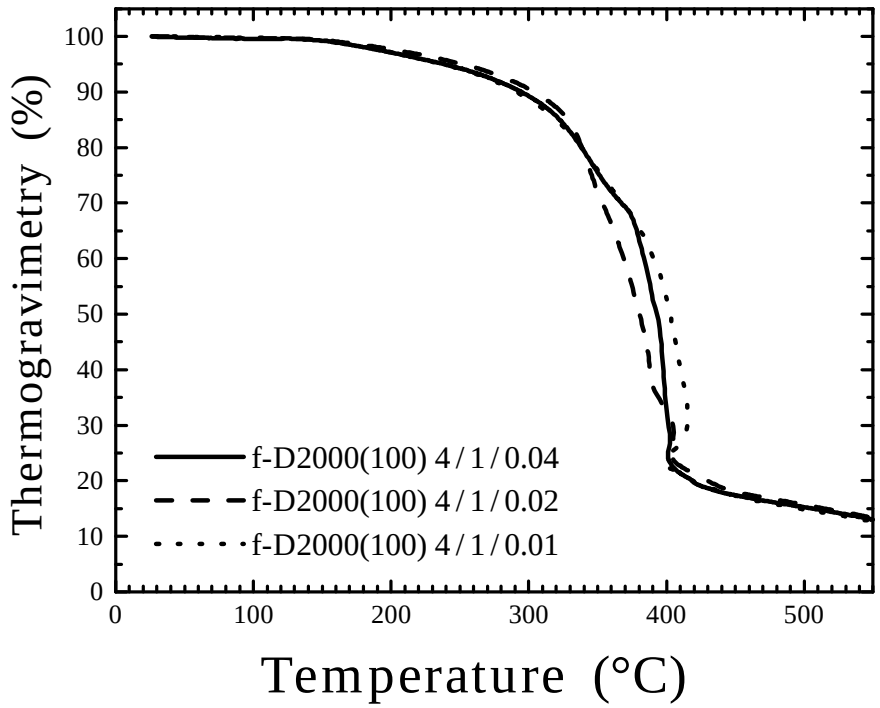

Figure 11. The influence of acid content on the thermogravimetry of f-D2000(100) ceramers.

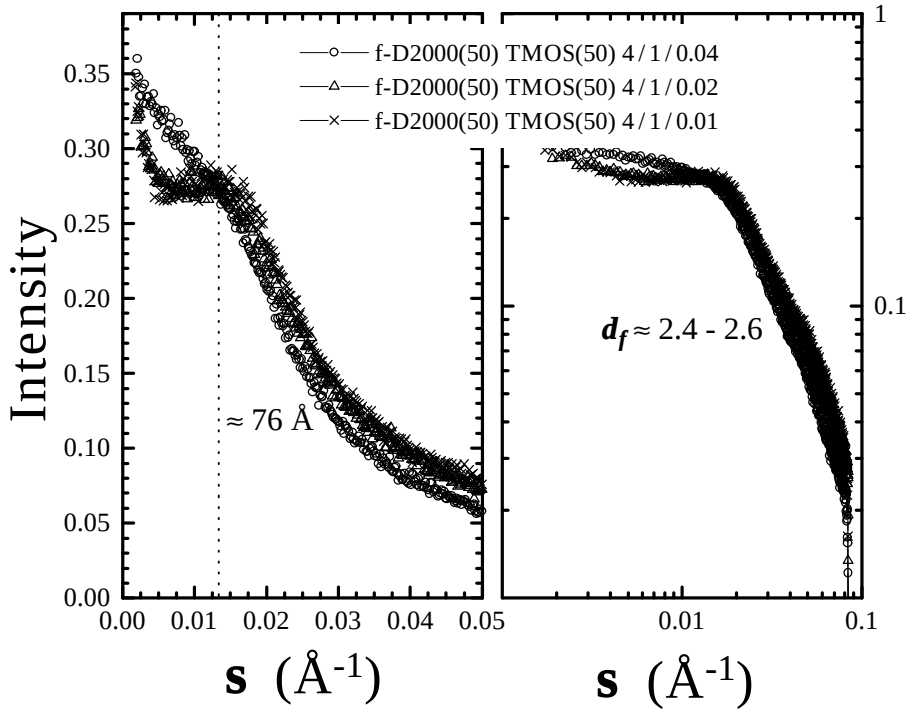

Figure 12. The influence of acid content on the SAXS behavior of f-D2000(50) TMOS(50) ceramers. Plot on right is a double–log presentation of the same data in the plot on the left.

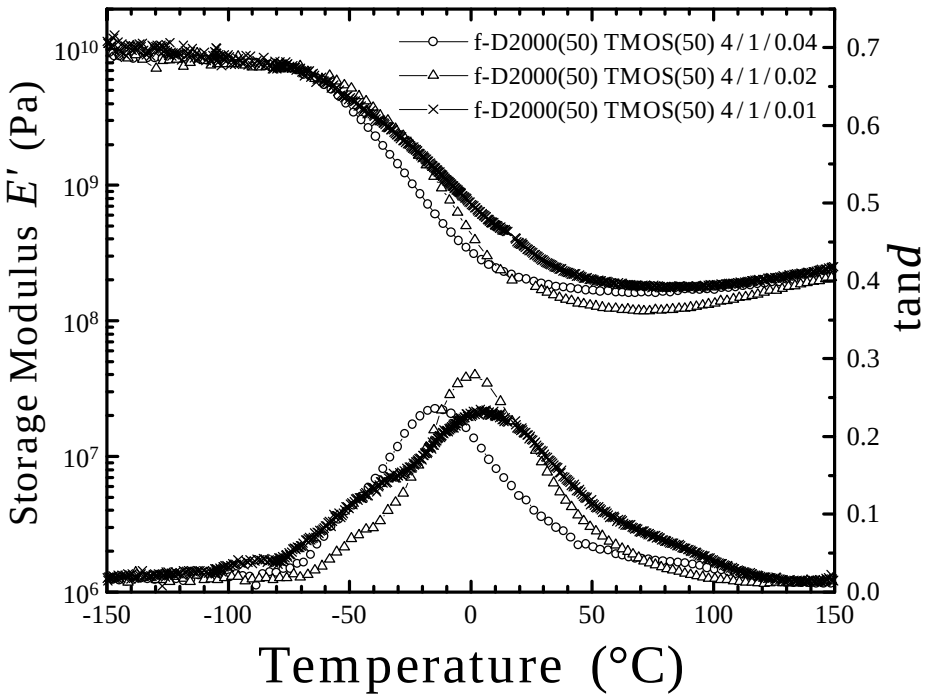

Figure 13. The influence of acid content on the thermomechanical spectra of f-D2000(50) TMOS(50) ceramers.

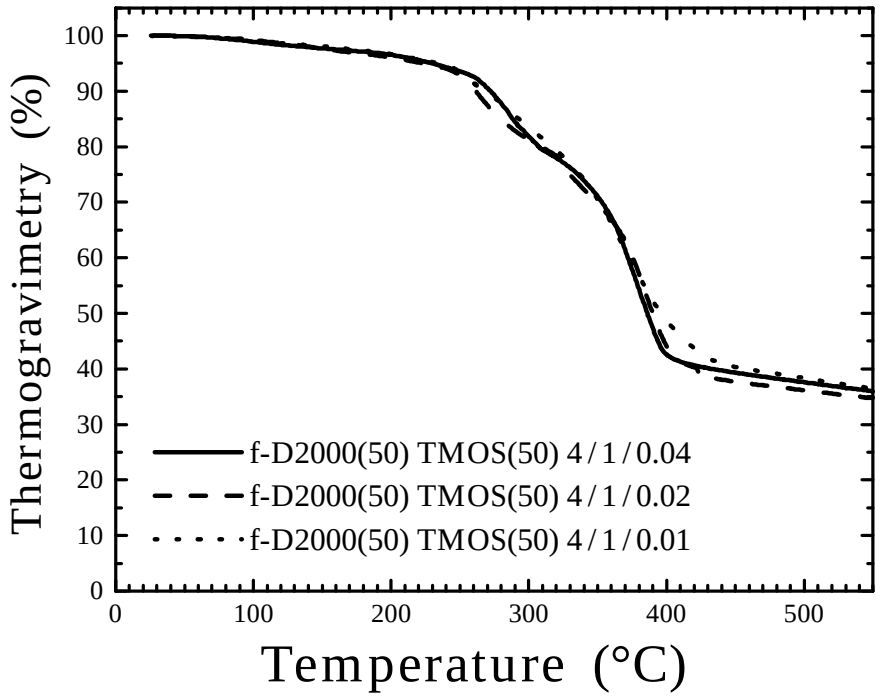

Figure 14. The influence of acid content on the thermogravimetry of f-D2000(50) TMOS(50) ceramers.

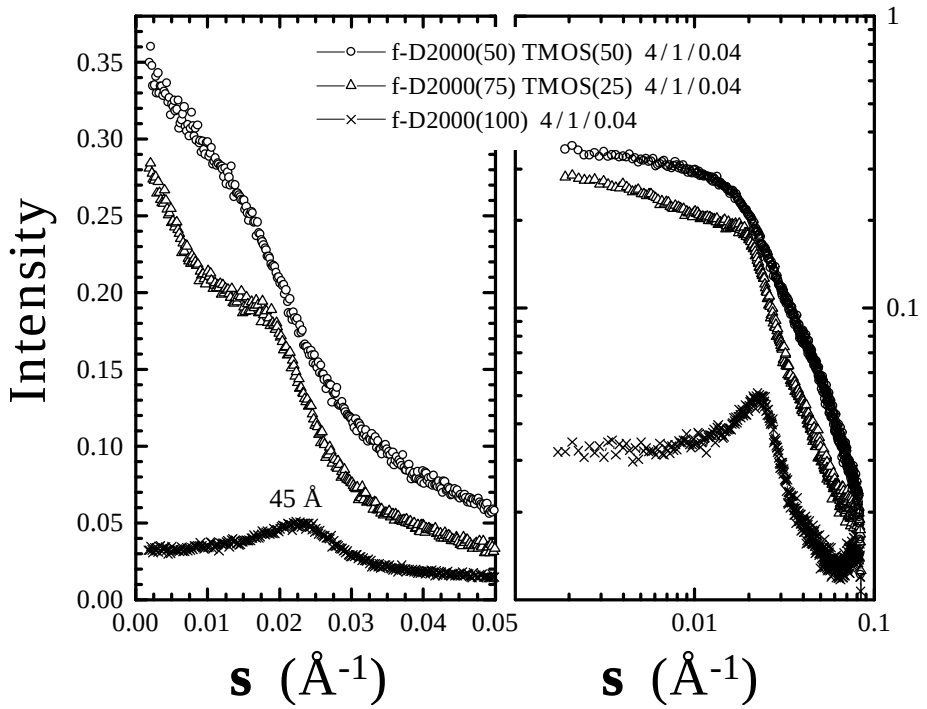

Figure 15. The influence of TMOS content on the SAXS behavior of f-D2000 based ceramers. Plot on right is a double–log presentation of the same data in the plot on the left.

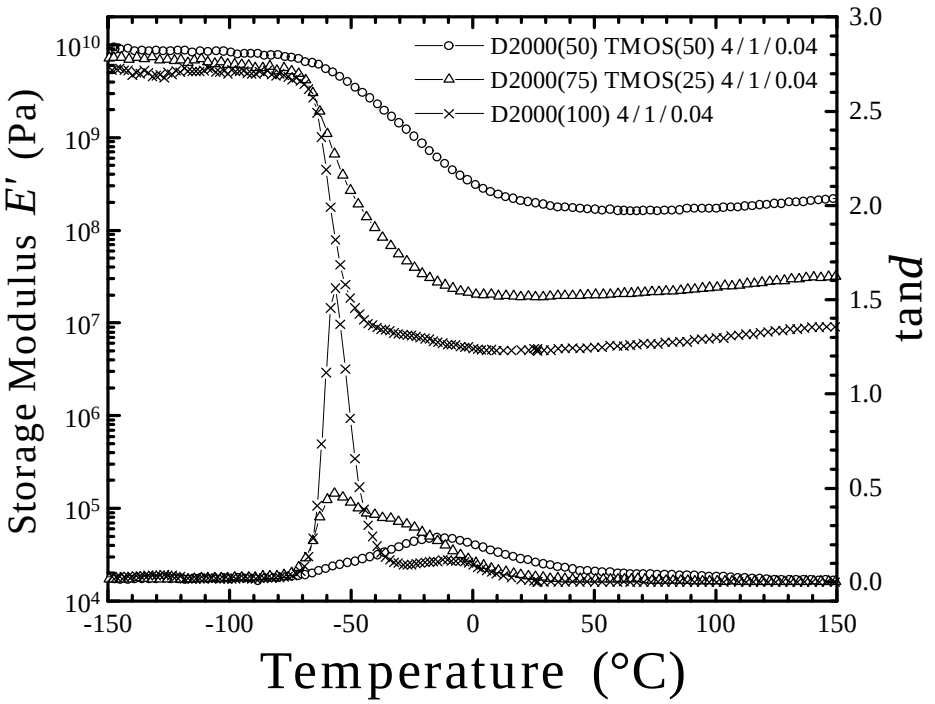

Figure 16. The influence of TMOS content on the thermomechanical spectra of f-D2000 based ceramers.

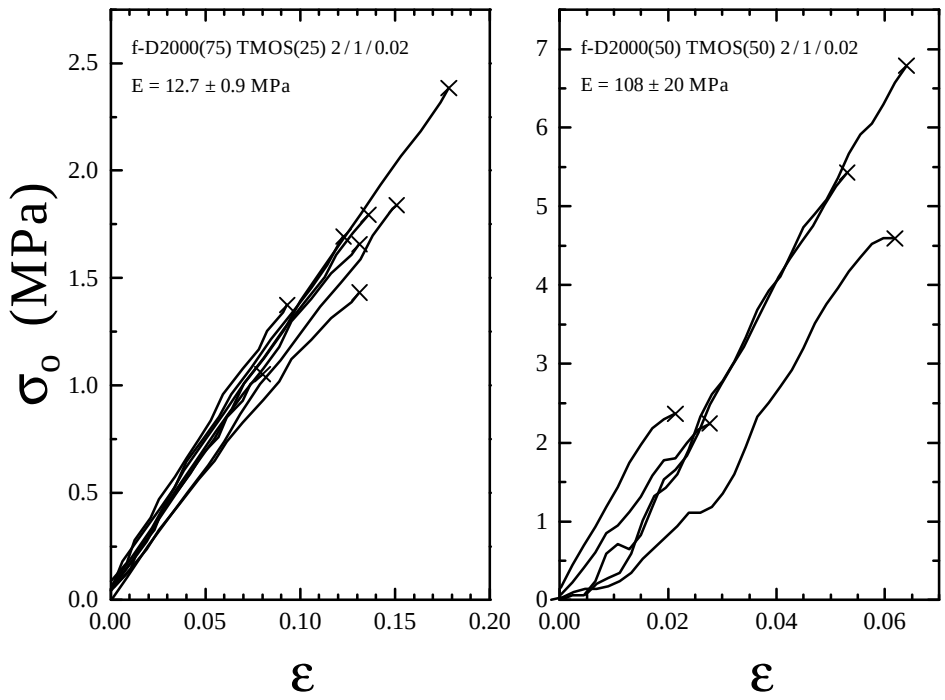

Figure 17. Tensile stress–strain behavior of JEFFAMINE® based ceramers.

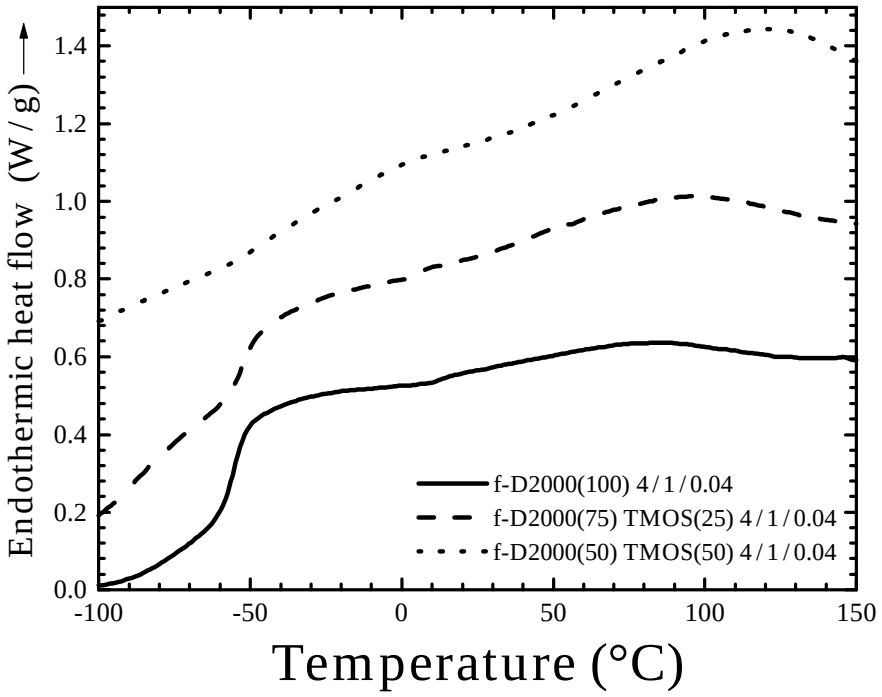

Figure 18. The influence of TMOS content on the DSC scans of f-D2000 based ceramers. Scans displaced vertically for clarity.

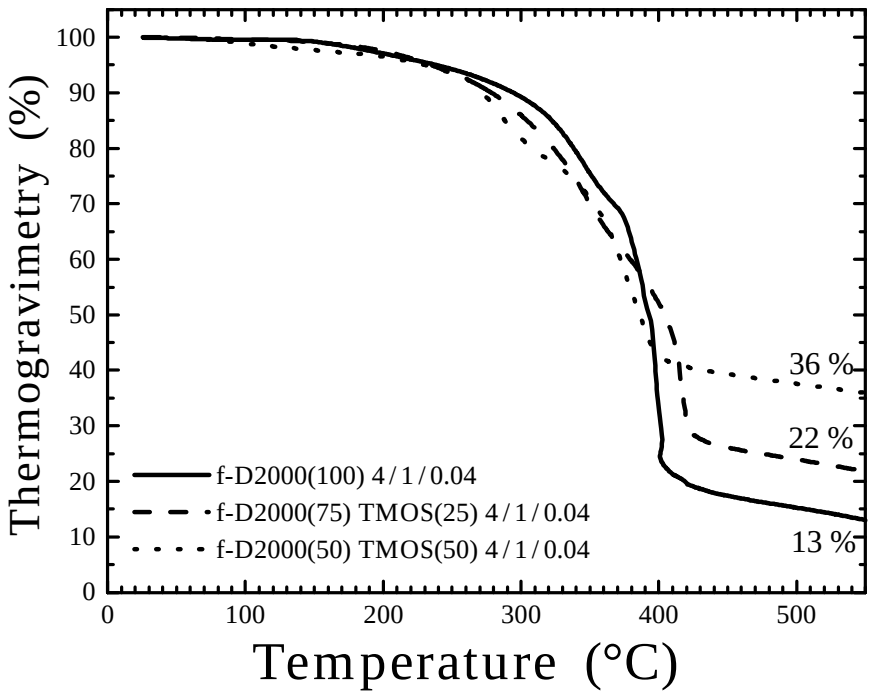

Figure 19. The influence of TMOS content on the thermogravimetry of f-D2000 based ceramers.

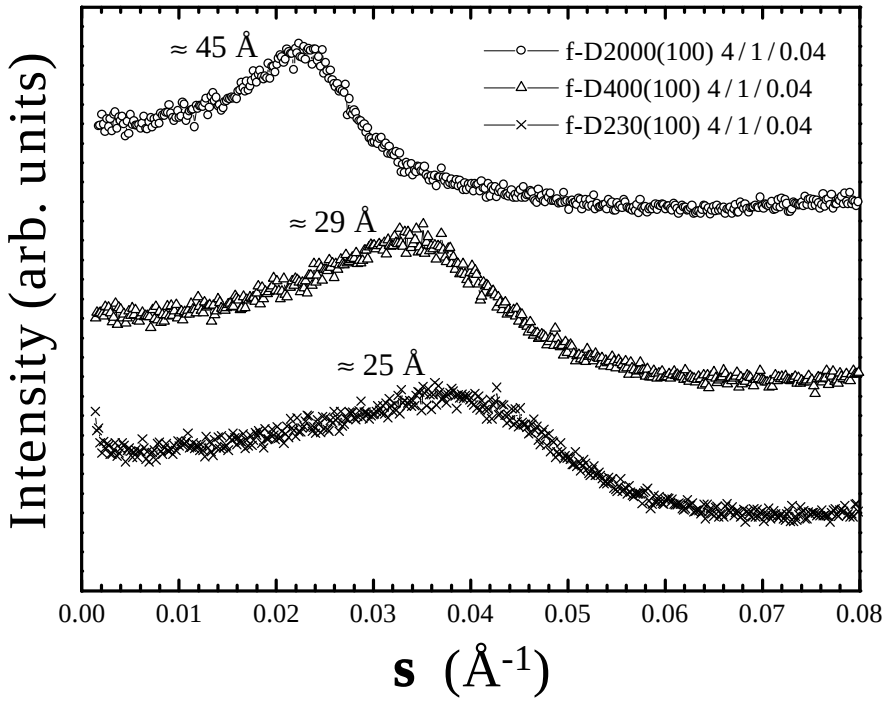

Figure 20. The influence of PPO molecular weight on the SAXS behavior of non-TMOS containing ceramers. Intensities are not absolute and the curves are displaced vertically for clarity.

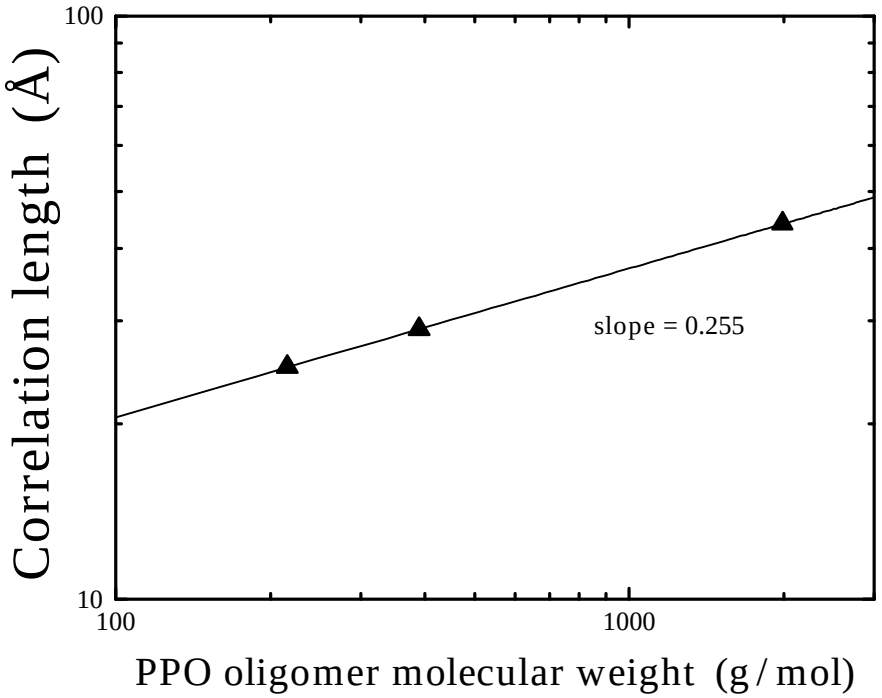

Figure 21. Double–log plot of the SAXS correlation length versus PPO oligomer molecular weight.

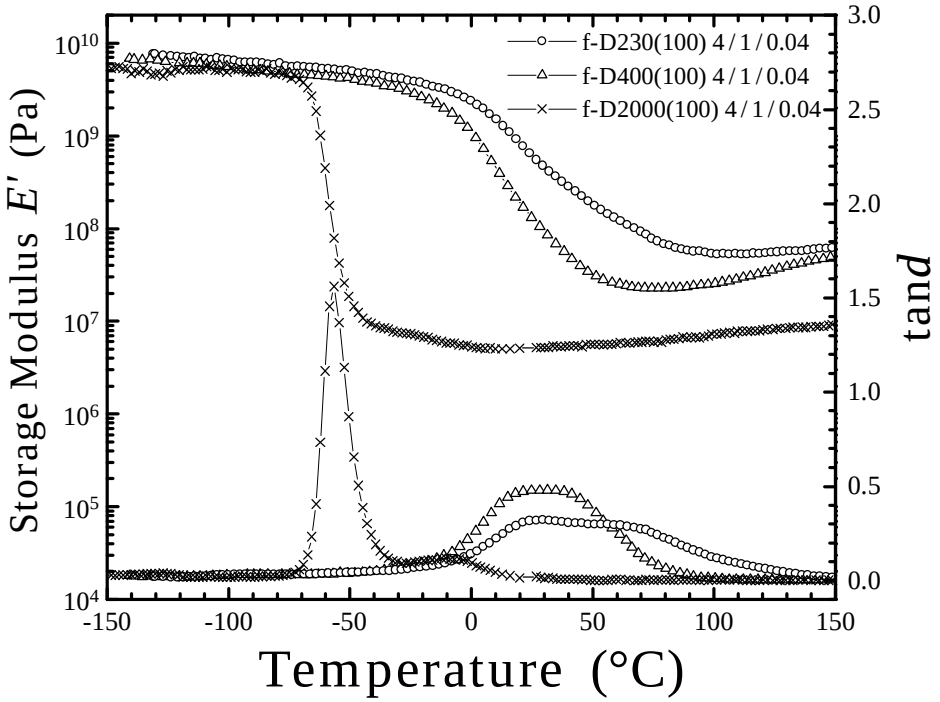

Figure 22. The influence of PPO molecular weight on the thermomechanical spectra of non-TMOS containing ceramers.

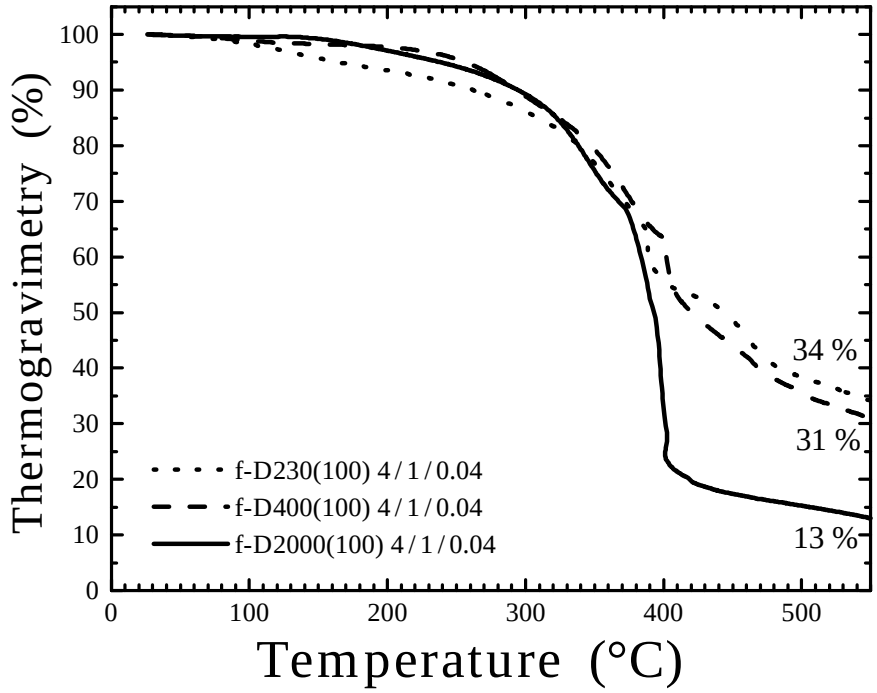

Figure 23. The influence of PPO molecular weight on the thermogravimetry of non-TMOS containing ceramers.

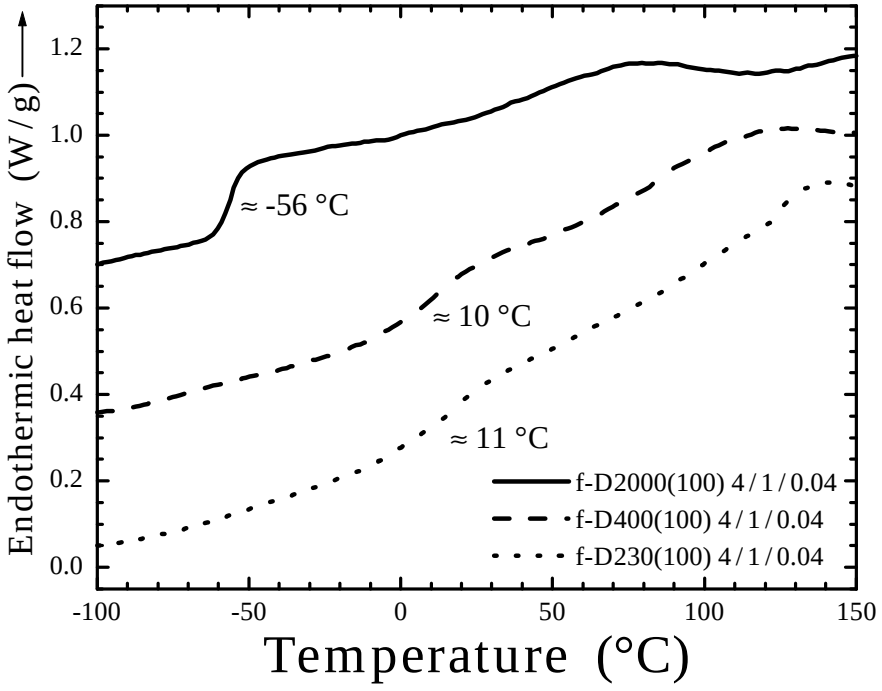

Figure 24. The influence of PPO molecular weight on the DSC scans of non-TMOS containing ceramers. Scans displaced vertically for clarity.

3.6 References

1 G. L. Wilkes, B. Orler, and H. Huang. *Polymer Preprints,* **26(2)**, 300, (1985).

2 H. Huang, B. Orler, and G. L. Wilkes. *Polym. Bull.*, **14**, 557, (1987).

3 H. Huang, B. Orler, and G. L. Wilkes. *Macromolecules*, **20**, 1322, (1987).

4 H. Huang and G. L. Wilkes. *Polym. Bull.*, **18**, 455, (1987).

5 R. H. Glaser and G. L. Wilkes. *Polym. Bull.*, **19**, 51, (1988).

6 H. Huang, R. H. Glaser, and G. L. Wilkes. Chapter 29 in Inorganic and Organometallic Polymers, *ACS Symp. Ser.*, **360**, 354, (1988).

7 H. Huang, G. L. Wilkes, and J. G. Carlson. *Polymer*, **30**, 2001, (1989).

8 D. E. Rodrigues, A. B. Brennan, C. Betrabet, B. Wang, and G. L. Wilkes. *Chem. Mater.*, **4(6)**, 1438, (1992).

9 D. E. Rodrigues and G. L. Wilkes. *J. Inorg. Organomet. Polym.*, **3(3)**, 197, (1993).

10 N. G. McCrum, B. E. Read, and G. Williams. Anelastic and Dielectric Effects in Polymeric Solids, *reprint of 1967 text*, Dover Publications, Inc., NY, 1991.

11 L. E. St. Pierre and C. C. Price. *J. Am. Chem. Soc.*, **78**, 3432, (1956).

12 R. N. Work, R. D. McCammon, and R. G. Saba. *Bull. Am. Phys. Soc.*, **8**, 266, (1963).

13 G. Allen. *Soc. Chem. Ind. Monograph*, **17**, 167, (1963).

14 G. Williams. *Trans. Faraday Soc.*, **61**, 1564, (1965).

15 Leroy E. Alexander. X-ray Diffraction Methods in Polymer Science, Kreiger Publishing Company, Malabar, FL, 1985.

16 L. R. G. Treloar. The Physics of Rubber Elasticity, Third Edition, Clarendon Press, Oxford, 1975.

17 T. M. Miller, L. Zhao, and A. B. Brennan. *J. Appl. Polym. Sci.*, **68**, 947, (1998).

18 C. J. Brinker, K. D. Keefer, D. W. Schaefer, R. A. Assink, C. D. Kay, and C. S. Ashley. *J. Non-Cryst. Solids*, **63**, 45, (1984).

19 D. W. Schaefer and K. D. Keefer in Better Ceramics Through Chemistry II, (*Mater. Res. Soc. Symp. Proc.)*, **73**, 277, (1986).

20 K. D. Keefer in Better Ceramics Through Chemistry, C. J. Brinker, D. E. Clark, and D. R. Ulrich, eds., North Holland, New York, (1984).

21 Lawrence E. Nielsen. Mechanical Properties of Polymers and Composites Volume 2, Marcel Decker, Inc., NY, 1974.

22 F. R. Schwarzl, H. W. Bree, C. J. Nederveen, G. A. Schwippert, L. C. E. Struik, and C. W. Van der Wal. *Rheol. Acta*, **5**, 270, (1966).

23 R. F. Landel and T. L. Smith. *ARS J. (American Rocket Society Journal)*, **31**, 599, (1961).

24 F. Surivet, T. M. Lam, J. Pascault, and C. Mai. *Macromolecules*, **25(21)**, 5742, (1992).

25 D. Tyagi, J. E. McGrath, and G. L. Wilkes. *Polym. Eng. Sci.*, **26(20)**, 1371, (1986).

26 T. Miyamoto, K. Kodama, and K. Shibayama. *J. Polym. Sci., Part A-2*, **8**, 2095. (1970).

27 Paul J. Flory. Statistical Mechanics of Chain Molecules. Hanser Publishers, New York, 1988.

Chapter 4

Novel Ceramer Materials Based on Poly(propylene oxide) and Tetramethoxysilane: Comparison of ACCLAIM™ polyether polyol and JEFFAMINE® polyoxyalkyleneamine as the poly(propylene oxide) source

Abstract

Novel hybrid inorganic–organic network materials were generated through a modified sol–gel process based on poly(propylene oxide) (PPO) and tetramethoxysilane. The PPO sources chosen for study were (a) JEFFAMINE® D2000, an amine terminated PPO oligomer available commercially from the Huntsman Corporation, and (b) ACCLAIM™ 2220N, a polyether polyol available from Lyondell which is a copolymer of ethylene oxide (≈ 25%) and propylene oxide (≈ 75%). Overall, the structure–property relationships of ceramers made from these two oligomers are similar. Among the few differences is the tensile stress–strain behavior. The ACCLAIM™ based ceramers can be drawn to higher extents before failure. Also among the discrepancies is the dynamic mechanical behavior in the rubbery region. The ACCLAIM™ based ceramers appear to more closely obey ideal rubber elasticity, whereas the JEFFAMINE® based materials show less than direct proportionality of the storage modulus to temperature. These differences in behavior are due to the less than

ideal functionality of the JEFFAMINE® oligomers, which is ≈ 1.94 (ideally 2.0), compared to the ACCLAIM™ oligomer which is greater than 1.99. This lower functionality leads to a notable sol–fraction, as well as many dangling ends in the JEFFAMINE® based materials. Other minor differences and many similarities were found from small angle x-ray scattering, differential scanning calorimetry, and thermogravimetry experiments.

4.1 Introduction

Ceramers are hybrid network materials, typically composed of polymeric or oligomeric species which are reacted into a network oxide through the sol-gel reaction. The first ceramer material made in 1985 was based on an oligomeric form of hydroxyl terminated poly(dimethyl siloxane) (PDMS) and tetraethoxysilane (TEOS).[1] Recently, a new, similar ceramer based on poly(propylene oxide) (PPO) and tetramethoxysilane (TMOS) has been prepared and was the subject of the previous chapter and a related manuscript.[2] That research explored the structure–property relationships in ceramer materials based on PPO oligomers derived from the family of JEFFAMINE® polyoxyalkyleneamines of the Huntsman Corporation. These JEFFAMINE® materials are generally imperfect in their chemistry, however; the functionality of these "diamines" is actually less than two[2] (Table 1). This non–ideal functionality led to an imperfect ceramer network which may contain dangling ends and a sizable sol-fraction.[2] However, due to a new catalyst and synthetic pathway, PPO oligomers can be made with high functionality (very near 2) and hence low monol content. Lyondell makes such a family of materials that are newly available, known as the ACCLAIM™ polyether polyols. This allows an interesting comparison of ceramers based on these two PPO oligomers. The focus of this chapter and a corresponding manuscript to be submitted is to compare the properties of ceramers of similar formulation based on JEFFAMINE® and ACCLAIM™ PPO sources.

4.2 Experimental Approach

4.2–A Materials and Synthesis

The ACCLAIM™ poly(propylene oxide) (PPO) oligomer utilized in this study was provided by Lyondell, and is known as ARCOL® R-2744 polyol (ACCLAIM™ polyol 2220N). It is an ethylene oxide (EO) end–capped PPO diol with a number average molecular weight of ≈ 2200 g / mol (approximate structure shown in Figure 1). The total EO content in the copolymer is approximately 25%, and 85% of the terminal groups are primary hydroxyls. The balance of the termini are secondary hydroxyls resulting from a propylene oxide group. This large portion of primary hydroxyl end–groups causes the EO end–capped oligomer to be more reactive with an isocyanate than a purely PPO oligomer, and the EO component makes the oligomer more hydrophilic in character than pure PPO. As can be seen in Table 1, the functionality of this oligomer is greater than 1.99, which is very close to the ideal case of 2.

The JEFFAMINE® PPO oligomer employed in this study was provided by the Huntsman Corporation, and is known as D2000. It is a primary amine terminated PPO oligomer where the "D" stands for difunctional (ideally) and the subsequent number roughly corresponds to the number average molecular weight. The actual functionality of this material is less than 2, as shown in Table 1, where the measured molecular weights and breadth indexes ($\overline{M}_w/\overline{M}_n$), provided by the manufacturers, are also listed.

Other chemicals used in this study include tetramethoxysilane (TMOS, 99+%, obtained from Gelest), isocyanatopropyltriethoxysilane (ICPTES, 95%, Gelest), isopropanol (IPA, reagent grade, obtained from EM Sciences), dibutyltin dilaurate (95%, Aldrich Chemical) and 1 M aqueous HCl solution (Aldrich Chemical).

The synthesis of ceramers based on various JEFFAMINE® oligomers has been addressed in the previous chapter. Briefly, the amine terminated JEFFAMINEs® are end–capped with an isocyanate silane (ICPTES) to form urea linkages. The silane functionality (specifically, the alkoxysilane end–groups) can subsequently participate in the sol–gel reaction.

The synthetic pathway to generating ceramers based on the ACCLAIM™ materials is more difficult than with JEFFAMINEs®. The urea formation involved in the functionalization of the JEFFAMINEs® occurs readily at room temperature. However, due to the hydroxyl termination on the ACCLAIM™ oligomers, reaction with an aliphatic isocyanate leads to a urethane linkage, which is not readily formed at room temperature. Hence the reaction involved here, outlined in Figure 1, was carried out at elevated temperature with added catalyst in an inert atmosphere. This was accomplished as follows. The ACCLAIM™ polyol was first added to a sealed, argon purged flask by syringe, and was heated to 90 °C. This was followed by addition of the liquid catalyst (dibutyltin dilaurate), in an amount of 250 ppm based on the polyol. After the temperature stabilized, the isocyanate (ICPTES) was slowly added by syringe. The flask was then left sealed and kept between 80 and 100 °C for eight hours. This generates a new molecular species (Figure 1) that can participate in the sol–gel reaction through the alkoxysilane end–groups.

The main distinctions between the functionalized JEFFAMINEs® and functionalized ACCLAIM™ materials are the linkages between the alkoxysilane and the PPO are urea and urethane, respectively. Also, the JEFFAMINEs® are strictly PPO chains whereas the ACCLAIM™ material is an ethylene oxide end–capped PPO oligomer. Also important to the results of this work, the molecular weight and functionality of the original oligomers are different. The ACCLAIM™ material has higher functionality due to the recent improvements in the synthetic pathway (Table 1).

Formation of hybrid networks is then accomplished by employing the functionalized oligomers in the sol–gel reaction. Both the functionalized ACCLAIM™ and JEFFAMINE® materials, with their alkoxysilane end–groups, are able to undergo the sol–gel reaction in the presence of water. Or, as shown in Figure 2 for the case of f-2220N (functionalized ACCLAIM™ oligomer), the functionalized oligomers can co-react with tetramethoxysilane. TMOS contributes only inorganic character to the resulting material, as it condenses to form a structure similar to amorphous silicon dioxide. When the sol-gel reaction is carried out at room temperature, however, some

uncondensed groups tend to linger. Hence many alkoxy and silanol groups remain, and a more polysiloxane–like structure is formed.

Once the sol–gel reaction is initiated and allowed to stir for approximately three minutes, the reacting solution is poured into a polystyrene petri dish, covered, rapidly degassed in a vacuum chamber, and allowed to cure for one week at lab conditions. After this, the samples are stored under vacuum for at least one day before testing.

4.2–B Characterization

All small angle x-ray scattering (SAXS) experiments were performed with nickel filtered, slit collimated Cu*Ka* radiation (1.542 Å)[3] produced by a Philips generator, model PW1729. A Kratky camera and a one–dimensional M. Braun position–sensitive detector were used to collect the scattered radiation. Absolute intensities were calibrated through the use of a polyethylene (Lupolen) working standard.[3]

The differential scanning calorimetry (DSC) experiments were performed on a Seiko DSC 220C with nitrogen purge gas. A heating rate of 20 K/min was employed for all scans, and samples weighed between 5 and 10 mg.

Thermogravimetry (TG) was accomplished with a Seiko TG/DTA under an air purge. A heating rate of 10 K/min was used and samples weighed between 5 and 10 mg.

A Seiko DMS 210 was utilized for dynamic mechanical spectroscopy (DMS) experiments. Rectangular samples had a gauge length of 10 mm, and were cut such that their cross–sectional area was between 2 and 7 mm^2. Scans were started at room temperature, and cooled slowly (1.5–2 K/min) with liquid nitrogen to ≈ –150 °C while collecting data. After this cooling scan, the sample was allowed to equilibrate back to room temperature, and a heating scan was then started under nitrogen purge gas with a heating rate of 1.5–2 K/min. The data from the heating and cooling scans were then combined to give the thermomechanical spectrum for each sample.

Tensile stress–strain experiments were carried out at lab conditions with an Instron model 4204 equipped with a 1 kN load cell using a crosshead speed of 2.54 mm/min. Dogbone shaped samples were cut with a die from exceptional films, and had a gauge

length of ≈ 10 mm and a width at the gauge of ≈ 2.7 mm Cross–sectional areas of each sample differed due to variations in the thickness of films which ranged between 0.25 and 0.7 mm. At least eight specimens were tested for each formulation which lead to the statistical averages to be presented.

4.2–C Nomenclature

Due to the numerous variables explored in this work, a simplified system of nomenclature has been employed so that samples can be easily differentiated. This will be illustrated by the following example:

f-2220N(50) TMOS(50) 2 / 1 / 0.02

The f-2220N(50) represents alkoxysilane end–functionalized ARCOL® R-2744 polyol (ACCLAIM™ polyol 2220N) which is 50 weight percent of the original reaction medium. The functionalized JEFFAMINE® oligomer is referred to as f-D2000 in place of the f-2220N. The TMOS(50) represents 50 wt.% tetramethoxysilane, and the 2 / 1 / 0.02 represents the molar ratio of water / alkoxysilane / HCl employed during the sol–gel reaction. Note that the moles of alkoxysilane groups used in this ratio are derived from *both* the TMOS and the functionalized oligomers.

4.3 Results and Discussion

The general behavior of the ACCLAIM™ based ceramers will be addressed first since the general behavior of the JEFFAMINE® based ceramers has been reported in the previous chapter and in a related manuscript.[2] This will be followed by a direct comparison of ceramers of similar formulation based on functionalized ACCLAIM™ and JEFFAMINE® oligomers.

4.3–A ACCLAIM™ based ceramers: General behavior

Influence of TMOS content on ACCLAIM™ based ceramers

The SAXS profiles for ceramers based on f-2220N with varied TMOS contents are displayed in Figure 3. Several trends can be noted in this plot. Firstly, as the TMOS content increases from 0 wt.% to 25 and 50 wt.%, the correlation length (manifested as a

peak in the SAXS profile) increases from 53 Å to 64 Å and 70 Å, respectively. This peak corresponds to a phase separated structure, one phase being rich in PPO (which is the continuous phase) and the other being rich in the inorganic component. If the PPO chains are assumed to be the same size in each ceramer (occupy roughly the same pervaded volume), then increasing the TMOS content would be expected to increase the size of the inorganic domains, thereby increasing the correlation length accordingly. This same trend was previously observed for ceramers based on poly(tetramethylene oxide) with titanium isopropoxide as the metal alkoxide source.[4] However, increasing the TMOS content to 75 wt.% leads to a SAXS profile with no clear peak. Hence this material has no obvious correlation distance evidenced from the raw data. The morphology of this material is quite different from the lower TMOS containing ceramers. The connectivity between the silicate phase is much greater, which is likely the continuous phase for this sample. This material also does not display fractal character.

Another notable trend is that the integrated intensity varies with TMOS content, or in other words, the invariant is a distinct function of TMOS content. This is also an expected result,[2] however the explanation requires a brief discussion of the scattering power and the invariant. The invariant, Q_s, can be expressed as:[3]

$$Q_s = \int_0^\infty s \cdot I(s)\, ds \tag{1}$$

for slit–smeared absolute intensity $I(s)$. The invariant is proportional to the mean square fluctuation in the electron density $\langle \Delta r^2 \rangle$ (or scattering power) which, for a two phase system displaying sharp phase separation with each phase of uniform electron density, the following simplified mathematical relationship holds:

$$\langle \Delta r^2 \rangle = f_{PPO} \cdot f_{sil} \cdot (r_{PPO} - r_{sil})^2 \propto Q_s \ . \tag{2}$$

By employing this equation we are assuming that the ceramers are two phase systems, composed of a PPO–rich phase of volume fraction f_{PPO} and electron density r_{PPO}, and a separate silicate–rich phase of volume fraction f_{sil} =1–f_{PPO}, and electron density r_{sil}.[2]

With the value of $(r_{PPO} - r_{sil})^2$ remaining constant, $\langle \Delta r^2 \rangle$ reaches a maximum at f_{PPO} = f_{sil} = 0.5. Hence we would expect the integrated intensity of the SAXS profiles to be a maximum for a sample which has a silicate volume fraction of 0.5. This appears to be in agreement with the data of Figure 3, where the maximum integrated intensity occurs for the f-2220N(50) TMOS(50) ceramer (50 wt.% TMOS). However, the 50 wt.% TMOS content reflects the weight fraction of liquid TMOS in the formulation *prior* to the sol-gel reaction, and the condensation reaction leads to a loss of mass as by–product water and alcohol. Hence the silicate content in the final ceramer is not the same as the initial TMOS content in the formulation. The weight fraction of silicate for several ceramers can be estimated from thermogravimetry (Figure 4), and these results are listed in Table 2.* Estimating the silicate content in this fashion leads to a value of 51 wt.% silicate for the f-2220N(25) TMOS(75) ceramer. Since this value is the closest* to f_{PPO} = f_{sil} = 0.5, one might expect that the integrated SAXS intensity should be the greatest for this material. This is not the case as noted above, where the f-2220N(50) TMOS(50) ceramer appears to have the greatest integrated intensity. However, the thermogravimetrically estimated value of 51 wt.% also does not reflect the true amount of polysiloxane (or "silicate") in the ceramer *before* the thermogravimetry scan, as the sol–gel reaction can occur as the material is heated during this measurement. The alkoxy and silanol groups of the polysiloxane phase can continue to condense as the temperature is increased, thereby leading to weight loss of this phase. This proposal is supported by the TG scan for this ceramer as seen in Figure 4, where there is a substantial weight loss (≈ 10 wt.%) which occurs in the region of 50 to 150 °C. Since no degradation is expected in this low temperature range, the observed weight loss is evidence of further reaction due to the release of volatile water and alcohol. Accounting for this, the estimated silicate content for this ceramer now becomes ≈ 58 wt.%. Such a result, however, still dictates that this sample is closest to f_{ail} = 0.5.*

---

* *Note that the value of silicate content estimated from thermogravimetry is a weight fraction, and f_{sil} in equation (2) reflects a volume fraction.*

The TMOS content also drastically influences the dynamic mechanical behavior of the f-2220N based ceramers, as seen in Figure 5. First consider the storage modulus data for the ceramer with no added TMOS, the f-2220N(100) material. This sample has the sharpest glass transition, which occurs at ≈ –55 °C, within a temperature window of –70 to 0 °C. The storage modulus shifts from ≈ 4 GPa in the glassy state (a typical value for an organic glass) to ≈ 3 MPa in the rubbery state (a typical value for a rubber or elastomer). This three order–of–magnitude reduction in the storage modulus across the glass transition is characteristic of amorphous, high molecular weight organic polymers and lightly crosslinked amorphous organic networks. However, for the f-2220N(75) TMOS(25) ceramer, the glass transition is increased slightly to ≈ –43 °C and broadened (occurs over the temperature range of –70 to 30 °C). The storage modulus in the glassy state is similar to that of the TMOS–free ceramer, however, the change in the storage modulus across the glass transition for this sample is about 2.5 orders–of–magnitude. Hence the storage modulus in the rubbery state is somewhat higher than the non–TMOS containing ceramer. Finally, the f-2220N(50) TMOS(50) ceramer possesses the broadest (temperature window of –70 to 80 °C) and highest glass transition, near –10 °C. The storage modulus in the glassy state for this material is similar to the other two samples, in this case almost 10 GPa, but the drop across the glass transition is only two orders–of–magnitude. Hence the major effect of increasing the TMOS content is to increase and broaden the glass transition, and increase the storage modulus in the rubbery state. In this manner, the influence of TMOS is similar to the influence of a reinforcing filler on an elastomer.[5] This is not surprising since the TMOS reacts to form a rigid, inorganic, silicate–like phase. These trends have also been observed for the JEFFAMINE® based ceramers,[2] as well as other similar ceramer materials based on poly(tetramethylene oxide) and TEOS,[6–8] and poly(vinyl acetate) and TEOS.[9,10]

An interesting point to note is that the modulus in the rubbery state (which is located between ≈ 0 and 200 °C) for the f-2220N(100) ceramer actually increases slightly with temperature. This is due to a combination of the rubber elastic effect and an increase in

the crosslink density as the sample reacts further above room temperature. For an ideal elastomer, the equilibrium Young's modulus E is given by:[11]

$$E = 3N_v kT = \frac{3rRT}{M_c} \tag{3}$$

N_v is the number of crosslinks per volume, k is Boltzmann's constant, r is the density of the material at the absolute temperature T, R is the universal gas constant, and M_c is the molecular weight between crosslinks. Although equation (3) is derived for ideal networks with functionality of four, and also the dynamic mechanical experiment provides storage modulus data (E') and not equilibrium modulus data, the proportionality to the absolute temperature is expected to endure (i.e., the rubber elastic effect). In fact dynamic mechanical experiments have provided data which are compliant with equilibrium swelling experiments for similar ceramers based on poly(tetramethylene oxide) and TEOS (although the authors employed a slower heating rate of 0.75 K/min in their DMS experiments).[12] It can be seen from this equation that the modulus would also increase as the crosslink density increases (N_v). This is the second possible explanation for the behavior observed in Figure 5, since these materials were cured at room temperature and the reaction may continue when higher temperatures are reached during the dynamic mechanical experiment. The true source of this observed modulus increase is easily deciphered by the cyclic DMS experiment in Figure 6. During the first heating scan, the storage modulus increases due to both the rubber elastic effect (T increasing) and further reaction (N_v increasing). After annealing at 150 °C for an hour, the storage modulus data for the subsequent cooling and second heating scans coincide. The data for these two subsequent steps have the same shape as that predicted by ideal rubber elasticity (proportionality to temperature), also included in this plot as a dark line. Hence the first heating step displays the combined effects of rubbery elasticity and increased crosslink density, while the rubber elastic effect alone is active for the two subsequent steps. Similar, but not exactly the same behavior has been noted for the JEFFAMINE® based ceramers.[2]

The influence of increasing TMOS content on the glass transition behavior of these ceramers is analogous to the discussion addressed in the previous chapter. Briefly, the physical and chemical environment in which the PPO chains inhabit dictate their glass transition behavior. This molecular environment is best interpreted through the dynamic tan*d* data. The f-2220N(100) ceramer possesses one major, sharp relaxation peak in the tan*d* data at ≈ –55 °C. This corresponds to the glass transition of a phase rich in PPO (pure homopolymeric PPO has a reported dilatometric glass transition between –78 and –73 °C)[13–16], which has little constraint imposed upon it by the silicate phase. Note that this silicate phase in this sample is located solely at the PPO chain ends, as no TMOS was added to this formulation. The small shoulder in the tan*d* data, just above the main relaxation, has been tentatively assigned to the relaxation of segments at the interface between the silicate and the PPO–rich phases.[2] These segments would be more constrained than those in the bulk PPO phase (where their behavior is similar to homopolymeric PPO) due to their direct connection to the rigid silicate, and hence would relax at a higher temperature. An analogous shoulder has been observed for similar ceramers based on polybutadiene,[17] and as will be shown later (and was discussed in the previous chapter), a small related peak is present for the JEFFAMINE® f-D2000(100) ceramers.

With the addition of TMOS to the ACCLAIM™ based ceramers, the silicate component can impose additional constraints upon the PPO segments, particularly at locations other than solely the chain ends. Therefore, adding TMOS tends to decrease the relative intensity of the tan*d* peak at ≈ –55 °C associated with the homopolymeric-like PPO phase, while introducing relaxation phenomena at higher temperatures associated with the more highly constrained segments.[18] This can be seen in Figure 5 for the f-2220N(75) TMOS(25) ceramer, where the low–temperature peak (≈ –55 °C) in the tan*d* data is reduced considerably in magnitude compared to the f-2220N(100) ceramer. This is accompanied by an increase in the magnitude of the higher temperature relaxation, the relaxation which is merely a shoulder to the main glass transition for the f-2220N(100) material. Hence the tan*d* data for the f-2220N(75)

TMOS(25) ceramer appears somewhat bimodal in shape, where both relaxation phenomena are similar in magnitude. The relaxation phenomenon occurring at higher temperature may be associated with the constrained PPO segments at the interface between the silicate and bulk PPO phase. The addition of 25 wt.% TMOS leads to a larger silicate content and hence a higher concentration of constrained interfacial material, and therefore a larger magnitude of the higher temperature relaxation process. For the material with 50 wt.% TMOS, one broad relaxation phenomenon is observed in the tan*d* data. The whole relaxation spans from ≈ –60 to ≈ 80 °C, and the peak of this relaxation occurs at ≈ –5 °C. The broadness reflects the wide distribution of molecular environments inhabited by the PPO segments, some regions being highly constrained, and some being less constrained. Similar environments have been described for PTMO segments in a related ceramer material.[18]

The TMOS content also influences the tensile stress–strain (σ_0–ε) behavior for these ceramers. The f-2220N(100) ceramer was too soft and weak for tensile testing with the Instron. The mechanical properties of this material are like that of gelatin, and as such the samples were crushed during the gripping process. However, the σ_0–ε data for the 50 wt.% and 25 wt.% TMOS samples are shown in Figure 7 and Figure 8, respectively. Note the order–of–magnitude difference in the scale of the stress ordinate when comparing Figure 7 to Figure 8. The data for the f-2220N(50) TMOS(50) 2/1/0.02 ceramer (and also the 0.5/1/0.02 and 1/1/0.02 formulations to be shown later in the section concerning water content) have a similar shape to that of an elastomer, although the present materials do not reach nearly as high a value of strain at break as a true elastomer. Such a shape has been observed for similar ceramers based on poly(tetramethylene oxide) and TEOS.[6] The variation in mechanical properties with TMOS content can be easily seen; the f-2220N(50) TMOS(50) material has a much higher modulus (*E*), stress at break (σ_b, location denoted by the symbol ×), and toughness than the f-2220N(75) TMOS(25) sample Table 3). This is expected since the reacted TMOS forms a silicate (polysiloxane) structure which acts as a reinforcing filler for the soft PPO. It should be noted that the data for the f-2220N(75) TMOS(25) ceramer

are within the noise region of the load cell employed, evidenced by the slight vibrations in the stress data. For this reason the reported parameter values for this sample are provided with caution.

Influence of water content on f-2220N(50) TMOS(50) ceramers

The three SAXS curves of Figure 9 illustrate the variation in the morphological structure of f-2220N(50) TMOS(50) ceramers with water content, in the range of 0.5/1/0.02 to 2/1/0.02. All curves are similar, possessing a clear correlation length. However, the exact location of the peak does depend mildly on the water content; the correlation length increases slightly with increasing water content from 63 Å to 65 Å and 70 Å for the range probed. This trend may be a result of the improvement in the overall "solvent quality" of the reaction medium with increasing water concentration.

The water content shows no significant effect on the thermomechanical spectra for these materials as seen in Figure 10. All three samples in this plot display a broad glass transition (onset ≈ –70 °C, end–point ≈ 70 °C by the tan*d* data) with a peak at ≈ 0 °C. The storage modulus in the glassy state is ≈ 10 GPa for all three materials, and drops two orders of magnitude across the glass transition into the rubbery state.

The σ_0–ε data show a slight variation with water content; however, no direct relationships exist for the range probed in this study. The 2/1/0.02 formulation of Figure 7 displays the lowest statistical value of *E*, however all the other tensile parameters for this material are intermediate to the 0.5/1/0.02 (Figure 11) and 1/1/0.02 (Figure 12) formulations. The values of *E* may not be statistically different for these varied water formulations, however, as all three are within 10% of each other. Noting this, the 1/1/0.02 material appears to be the stiffest (highest *E*) and least tough. The water deficient material (0.5/1/0.02) has the largest values of σ_b, ε_b (strain at break), and toughness. The distinction between the mechanical properties of these materials are more easily seen in the plot of Figure 13. Also included in this plot are data for the f-2220N(75) TMOS(25) ceramer, whose mechanical properties are seen to be very much different than the three 50 wt.% TMOS containing ceramers as discussed in the previous section regarding TMOS content.

4.3–B Comparison of JEFFAMINE® and ACCLAIM™ based ceramers

Tensile stress–strain behavior

The greatest distinction between the two ceramer families lies in the mechanical properties, specifically the tensile σ_0–ε behavior. While the σ_0–ε data for the ACCLAIM™ based ceramers were thoroughly discussed in the previous section, the JEFFAMINE® based ceramers were quite inferior in this respect. The sample–to–sample variation (within a given JEFFAMINE® based formulation) was rather great, and the materials generally had values ε_b less than 0.15. The σ_0–ε curves had a linear shape, like that of a Hookean spring. Low ε_b and Hookean shape were observed for similar ceramers based on poly(dimethyl siloxane) and TEOS.[19,20] The distinction in the σ_0–ε behavior between the JEFFAMINE® and ACCLAIM™ based ceramers is a direct result of the difference in the functionality between the two original oligomers. The ACCLAIM™ oligomer is superior with a very high functionality of greater than 1.99, whereas the JEFFAMINE® oligomer has an estimated functionality of 1.94 (Table 1). Lower functionality generally leads to more dangling ends in the final network material, which explains the variance in the σ_0–ε behavior.

Small angle x-ray scattering behavior

The SAXS profiles for various ceramers made from both JEFFAMINE® and ACCLAIM™ sources are shown in Figure 14. As can be seen in this plot, the ceramers made without TMOS (the f-2220N(100) and f-D2000(100) samples) have very similar SAXS patterns. Both posses a clear correlation length; however, the ACCLAIM™ based ceramer has a larger spacing of 53 Å compared to the 45 Å spacing of the JEFFAMINE® based material. This discrepancy is believed to be due to two factors; firstly, the ACCLAIM™ oligomers are slightly higher in molecular weight (compare 2200 to 1577 g/mol). Secondly, as mentioned before, the ACCLAIM™ oligomer is a copolymer containing EO. The molecular weight of EO per repeat unit is less than that of propylene oxide. Hence the contour length of the EO containing oligomer would be longer than that of a purely propylene oxide oligomer of identical molecular weight.

These factors can easily account for the slightly larger correlation length in the ACCLAIM™ based ceramer.

The ceramers containing 25 wt.% TMOS cannot be compared as fairly as the other materials since the f-D2000(75) TMOS(25) 4/1/0.04 material was synthesized with twice the water and acid concentration as the f-2220N(75) TMOS(25) 2/1/0.02 sample. Acknowledging this fact, it can be seen from Figure 14 that the ACCLAIM™ based ceramer possesses a clear correlation length at 64 Å, while the JEFFAMINE® based sample has no clear peak, but rather has a shoulder. As mentioned in the previous chapter the f-D2000(75) TMOS(25) 4/1/0.04 sample has mass fractal character, or dilation symmetry (fractal dimension of ≈ 2.7). This implies that the material has the property that it is not space filling or of uniform density in three dimensions (which would correspond to a fractal dimension of 3.0). Hence the silicate (polysiloxane) structure is slightly "open" compared to a uniform, three–dimensional solid.

Comparing the two 50 wt.% TMOS containing ceramers leads to the observation that the ACCLAIM™ based material has a larger long spacing of 70 Å compared to the 61 Å spacing of the JEFFAMINE® material. The explanation of this is the same as that for the two non–TMOS ceramers; the slightly higher contour length of the oligomeric ACCLAIM™ materials compared to the JEFFAMINE® oligomers can account for the discrepancy. Therefore the sizes of the silicate domains in each 50 wt.% TMOS sample are not necessarily different, as the oligomer alone can account for the difference in long spacing. This is supported by the fact that the difference in the long spacing for the 50 wt.% TMOS containing materials is ≈ 9 Å, which is roughly the same as the non–TMOS samples which differ by ≈ 8 Å.

The f-2220N(50) TMOS(50) 2/1/0.02 sample shows a sharper or more narrow correlation peak than the f-D2000(50) TMOS(50) 2/1/0.02 material. This is likely due to sharper phase separation in the f-2220N(50) TMOS(50) material. The sharper phase separation is partly a result of the higher molecular weight 2220N oligomer.

Dynamic Mechanical Behavior

The comparison of the thermomechanical spectra for the ACCLAIM™ and JEFFAMINE® based ceramers is shown in Figure 15. The similarities between the ceramers made from both oligomers are apparent in this plot. First considering the non–TMOS containing ceramers, both the f-2220N(100) and f-D2000(100) materials have essentially the same main glass transition at –55 °C. Just above the main glass transition, the f-2220N(100) sample shows a shoulder in the tan*d* data, whereas the f-D2000(100) material displays an additional small peak in this region. These post–T_g relaxations were discussed above, and were assigned to the segments at the interface between the bulk PPO phase and the silicate phase. The fact that the f-2220N(100) sample has just a shoulder and the f-D2000(100) sample has a small peak is likely due to the slightly different chemistry at the silicate–bulk PPO interface. In the f-D2000(100) material, these interfacial segments are likely composed of urea groups and propylene oxide units, however, in the f-2220N(100) material the interfacial segments would be composed of urethane and ethylene oxide units. Hence these slightly different moieties are likely responsible for the slightly different relaxation behavior. Note that in the previously mentioned study on butadiene–based ceramers, the dynamic mechanical tan*d* data displayed a shoulder just above the main glass transition, and this material also possessed urethane groups between the silicate and bulk rubbery phase.[17]

Another notable difference in the dynamic mechanical data is that the ACCLAIM™ based ceramers have a lower value of the storage modulus in the rubbery state than the JEFFAMINE® ceramers. This is mainly due to the higher molecular weight of the ACCLAIM™ oligomer, which can be rationalized by recalling equation (3). The value of M_c for the ceramers is expected to approximately correspond to the molecular weight of the original oligomers (or perhaps more precisely the *functionalized* oligomers). Hence the D2000 oligomer, which has a number average molecular weight of ≈ 1577 g / mol (Table 1), would be expected to produce a ceramer with a higher rubbery modulus than the 2220N oligomer of ≈ 2200 g / mol as observed in Figure 15. This is true for the TMOS containing ceramers as well; the D2000 based materials always have

a higher storage modulus above the glass transition than the corresponding (equal TMOS containing) 2220N based samples.

As previously discussed and shown in Figure 6, the f-2220N(100) 2/1/0.02 ceramer complies with ideal rubber elasticity once it has been annealed at an elevated temperature. This was evidenced by the coinciding of the storage modulus data upon cooling and second heating with the line representing ideal rubber elasticity. However, the f-D2000(100) ceramer did not correspond perfectly with ideal rubber elasticity during the cooling and subsequent heating steps. Particularly, the observed storage modulus was lower than the predicted values at elevated temperatures. This was attributed to the imperfect chemistry of the D2000 oligomers, specifically to the network imperfections which it would generate. However, due to the improved chemistry of the ACCLAIM™ oligomers (specifically the functionality of 1.99+), the f-2220N(100) ceramer behaves more like an ideal elastomer. This is another one of the major distinctions between the JEFFAMINE® and ACCLAIM™ based ceramers. The improved functionality in the ACCLAIM™ oligomer generates a ceramer material which closely obeys the relationship to temperature predicted by ideal rubber elasticity theory.

The 25 wt.% TMOS ceramers have very similar thermomechanical spectra, despite the differences in their SAXS patterns and the fact that the f-D2000(75) TMOS(25) 4/1/0.04 was generated with twice the water and acid content as the f-2220N(75) TMOS(25) 2/1/0.02 material. Both show a peak in the tanδ data corresponding to the bulk PPO phase at ≈ –50 °C, and a second peak or relaxation just above it, of nearly equal strength. Again, this second, higher temperature relaxation would correspond to the interfacial segments, between the bulk PPO and silicate phases.

The materials containing 50 wt.% TMOS are also very similar in their thermomechanical spectra. Both possess one broad relaxation in the tanδ data, centered at ≈ 0 °C. Although the JEFFAMINE® based material appears to have shoulders in the tanδ data at ≈ –50 °C and 100 °C,[2] no such shoulders are apparent in the ACCLAIM™ ceramer.

Differential scanning calorimetry

Figure 16 contains the DSC traces for the various ceramers made from both JEFFAMINE® and ACCLAIM™ oligomers. Confirming the observations from the DMS data, the DSC data for the JEFFAMINE® and ACCLAIM™ based ceramers of similar formulation are nearly identical. For the two samples that contain no TMOS, a clear glass transition is noted at ≈ –55 °C, the same value which is observed mechanically. Also note that the change in the heat capacity across the glass transition, ΔC_P (or perhaps better labeled the change in heat flow, since absolute heat capacities were not measured), is roughly the same for both samples. Although the value of ΔC_P is generally a function of chemistry, the JEFFAMINE® and ACCLAIM™ oligomers are similar enough to lead to roughly the same ΔC_P in these ceramers (which also have roughly the same mass fraction of each oligomer in them). The two ceramers containing 25 wt.% TMOS show a slightly increased and broadened glass transition at ≈ –50 °C. This is a few degrees lower than that observed mechanically at 1 Hz (as the midpoint of the drop in the storage modulus). The value of ΔC_P for these two materials is again approximately the same, but is less than the ΔC_P for the non–TMOS containing ceramers. This is expected since ΔC_P is proportional to the mass of material undergoing the glass transition, and the relative mass of the PPO component is decreasing with increasing TMOS content (relative to the total sample mass). Finally, the glass transition is most broad and highest for the 50 wt.% TMOS materials, centered at ≈ –30 °C. The true location of the glass transition is difficult to locate for these high TMOS content samples.

4.4 Conclusions

For the novel ceramer materials synthesized in this study based on ACCLAIM™ EO endcapped PPO oligomers and tetramethoxysilane, the following conclusions can be drawn:

- Increasing the TMOS content led to an increase in the correlation length due to an increase in the size of the silicate domains. However, the highest TMOS content ceramer [f-2220N(25) TMOS(75)] did not possess a correlation length by SAXS.
- Increasing the TMOS content also led to an increased and broadened glass transition temperature, similar to the JEFFAMINE® based ceramers.
- *E'* in the rubbery region for f-2220N(100) displays a direct proportionality to absolute temperature, obeying the dictates of ideal rubber elasticity. The analogous JEFFAMINE® based ceramer did not behave as closely to rubber elastic theory. This is most likely due to the lower functionality of the initial JEFFAMINE® oligomer which would lead to network imperfections.
- The influence of water concentration on the final properties of ACCLAIM™ based ceramers is minor. This trend was also noted for JEFFAMINE® based ceramers.
- The largest distinction between the ACCLAIM™ and JEFFAMINE® based ceramers is the stress–strain behavior. The JEFFAMINE® materials displayed "Hookean spring" (linear) behavior, and broke at small strains (ε_b less than 0.15). The ACCLAIM™ materials displayed an S-shaped stress–strain curve similar to elastomers, and broke at considerably higher values of strain (≈ 0.4, however still not as high as an elastomer).
- Aside from the stress–strain behavior, the ACCLAIM™ and JEFFAMINE® based materials behaved in a similar manner in the SAXS, DSC, TG, and DMS experiments.

4.5 Acknowledgments

The author wishes to acknowledge Lyondell for providing the ACCLAIM™ polyether polyol used in this study. The author also wishes to express gratitude specifically to Dr. Bruce Lawrey of Lyondell for his helpful guidance concerning urethane synthesis. Also, thanks to the Huntsman Corporation for graciously supplying the JEFFAMINE® polyoxyalkyleneamine used in this research. Finally,

thanks to Debra Direnfeld of the Huntsman Corporation for providing the molecular weight data for the JEFFAMINE® oligomer employed in this study.

Table 1. Comparison of JEFFAMINE® and ACCLAIM™ poly(propylene oxide) oligomers.

Material	$\overline{M}_n$	$\overline{M}_w$	$\overline{M}_w/\overline{M}_n$	**f***
ACCLAIM™ 2220N	≈ 2200	≈ 2420	≈ 1.1	1.99+
JEFFAMINE® D2000	1577	1656	1.05	1.94

* *Average functionality; i.e., the average number of either hydroxyl (ACCLAIM™) or primary amine (JEFFAMINE®) end–groups per molecule.*

Table 2. Glass transition, estimated silicate content, and correlation length data for various ACCLAIM™ and JEFFAMINE® ceramers of the 2/1/0.02 formulation.

Sample	**T_g* (°C)**	**silicate content† (wt.%)**	**correlation length‡ (Å)**
f-2220N(100)	–55	10	53
f-2220N(75) TMOS(25)	–43	19	64
f-2220N(50) TMOS(50)	–10	34	70
f-2220N(25) TMOS(75)	–§	51	*none observed*
f-D2000(100)	–57	13	45
f-D2000(75) TMOS(25)**	–46	22	*none observed*
f-D2000(50) TMOS(50)	–23	36	61

* *Determined from DMS experiments as the midpoint (on the* log–scale*) of the drop in storage modulus across the glass transition.*

† *Estimated from char yield measured by thermogravimetry.*

‡ *Slit–smeared SAXS result.*

§ *Not measured.*

** *4/1/0.04 formulation.*

Table 3. Tensile stress–strain parameters for the some of the ACCLAIM™ based ceramers.

Formulation	**E (MPa)**	**σ_b (MPa)**	**ε_b**	**toughness (MJ/m^3)**
f-2220N(50) TMOS(50) 2 / 1 / 0.02	46.8 ± 2.8	15.1 ± 1.9	0.38 ± 0.03	2.9 ± 0.6
f-2220N(50) TMOS(50) 1 / 1 / 0.02	51.3 ± 2.3	13.1 ± 1.3	0.30 ± 0.03	1.98 ± 0.36
f-2220N(50) TMOS(50) 0.5 / 1 / 0.02	48.5 ± 2.7	21.8 ± 4.9	0.46 ± 0.07	4.7 ± 1.6
f-2220N(75) TMOS(25) 2 / 1 / 0.02*	6.9 ± 0.3*	1.61 ± 0.29*	0.29 ± 0.06*	0.26 ± 0.1*

* *Data is into the noise region of the load cell for this sample and hence is suspect.*

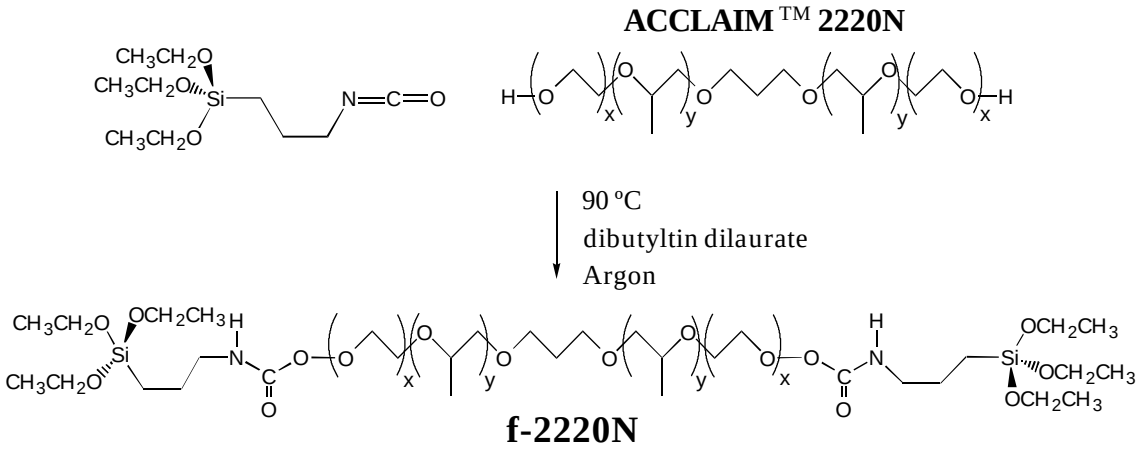

Figure 1. Schematic of the alkoxysilane functionalization of hydroxyl terminated ACCLAIM™ 2220N polyether polyol.

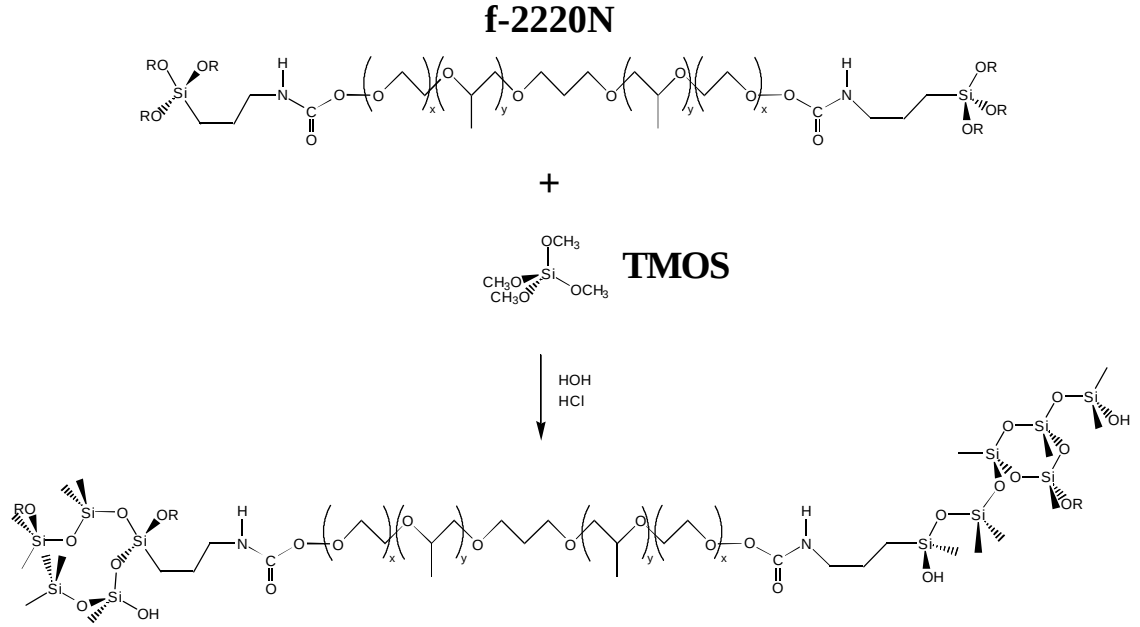

Figure 2. Schematic of the sol–gel reaction of f-2220N with TMOS.

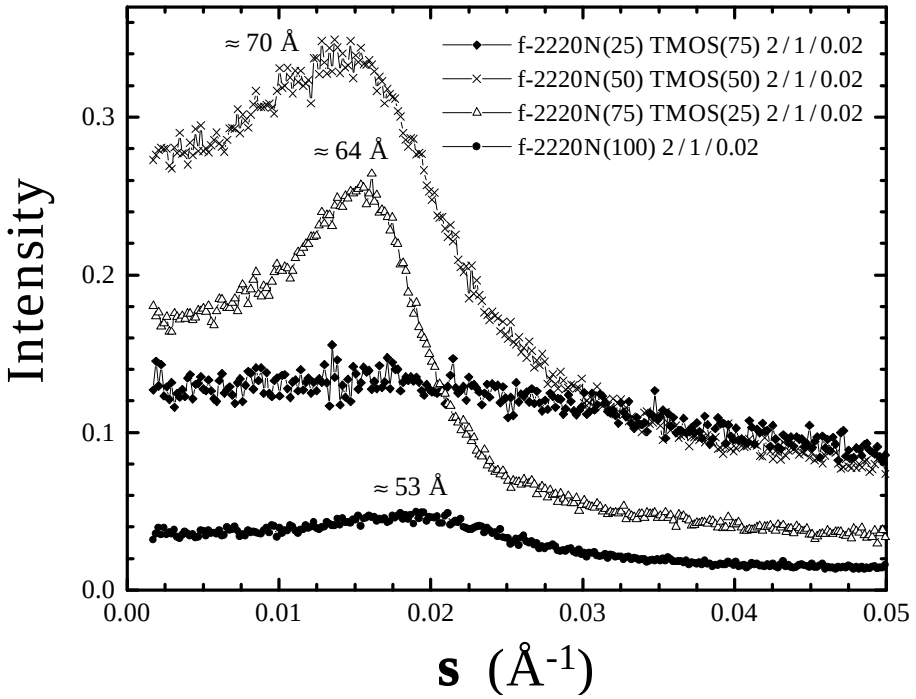

Figure 3. SAXS profiles for ceramers of varied TMOS content based on f-2220N.

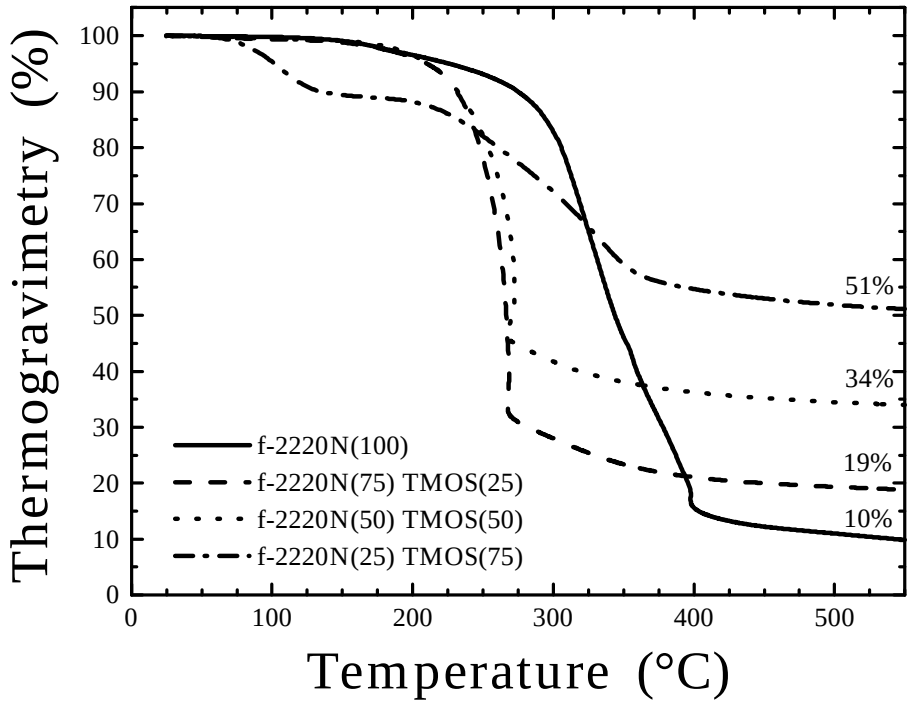

Figure 4. Thermogravimetry scans of f-2220N based ceramers of varied TMOS content.

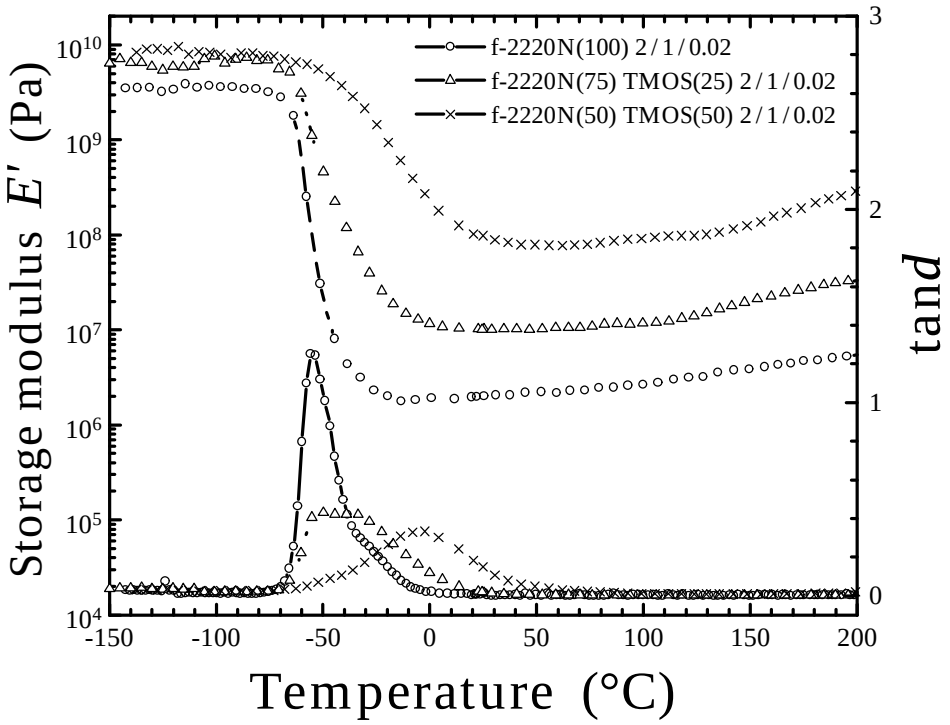

Figure 5. Thermomechanical spectra of f-2220N based ceramers of varied TMOS content.

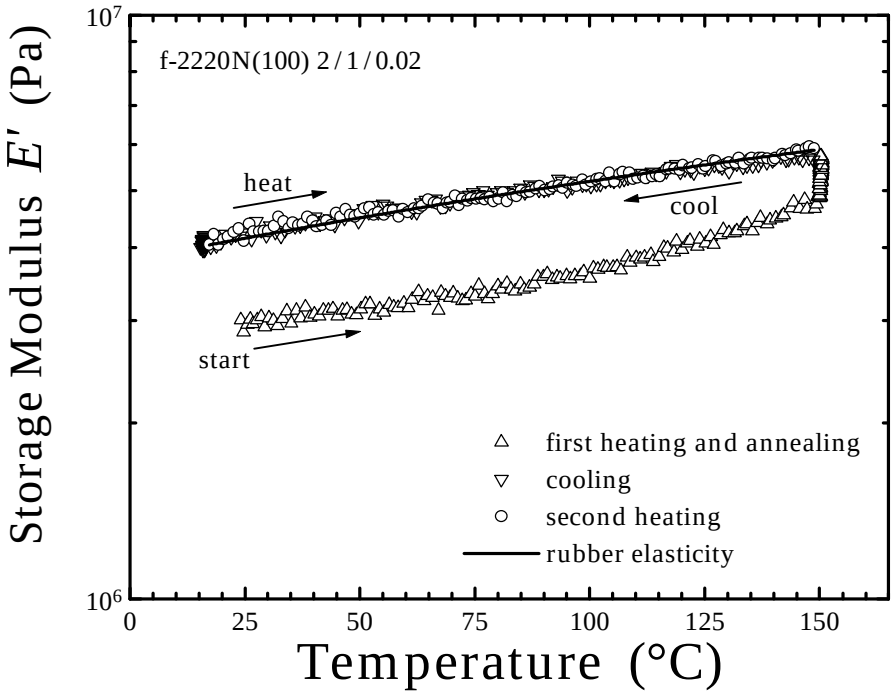

Figure 6. A cyclic dynamic mechanical experiment for f-2220N(100).

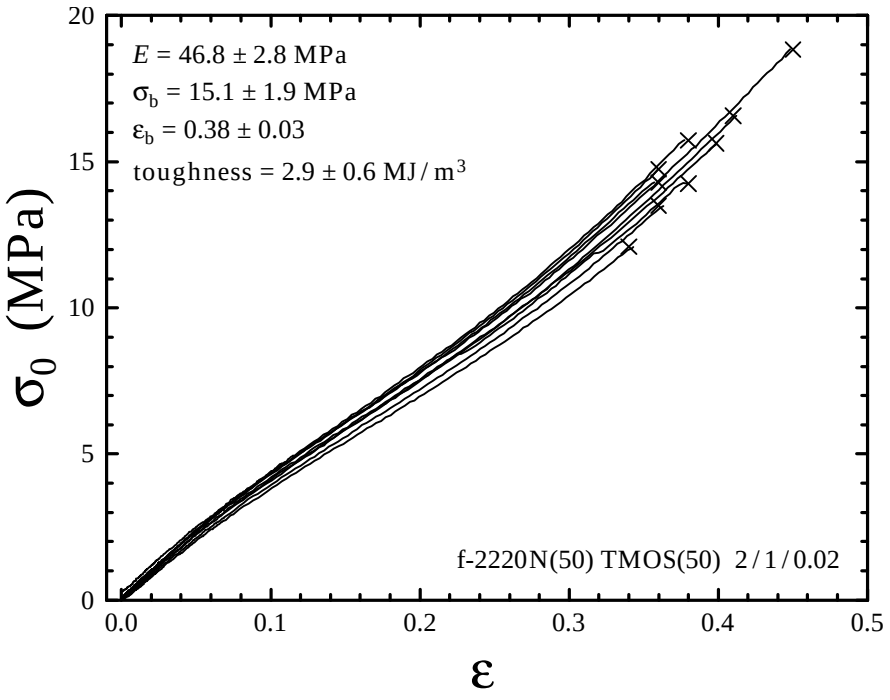

Figure 7. Tensile stress–strain data for f-2220N(50) TMOS(50) 2 / 1 / 0.02. Statistical values if E, σ_b, ε_b, and toughness shown.

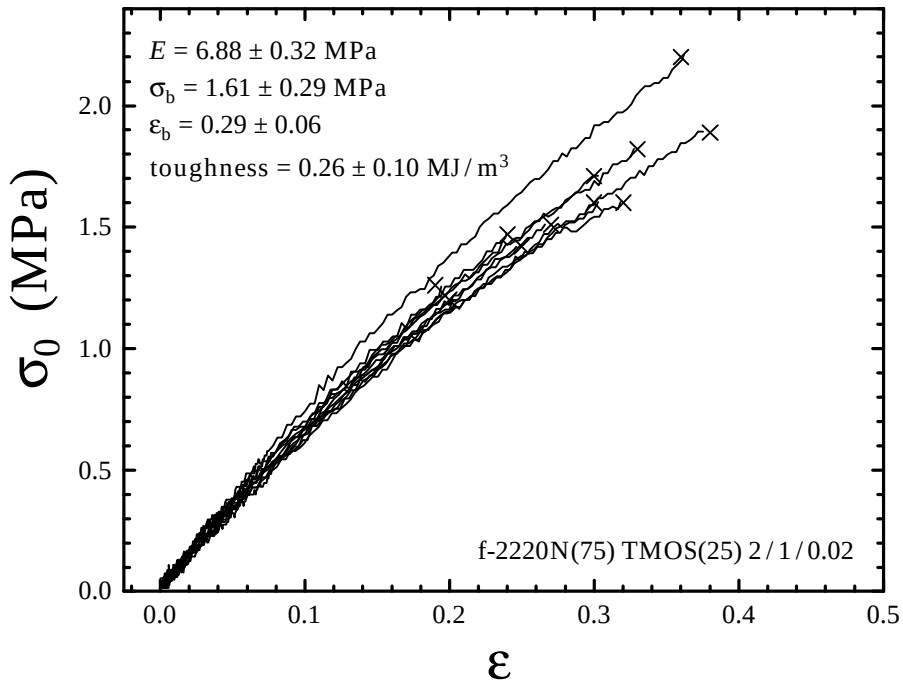

Figure 8. Tensile stress–strain data for f-2220N(75) TMOS(25) 2 / 1 / 0.02. Statistical values if E, σ_b, ε_b, and toughness shown.

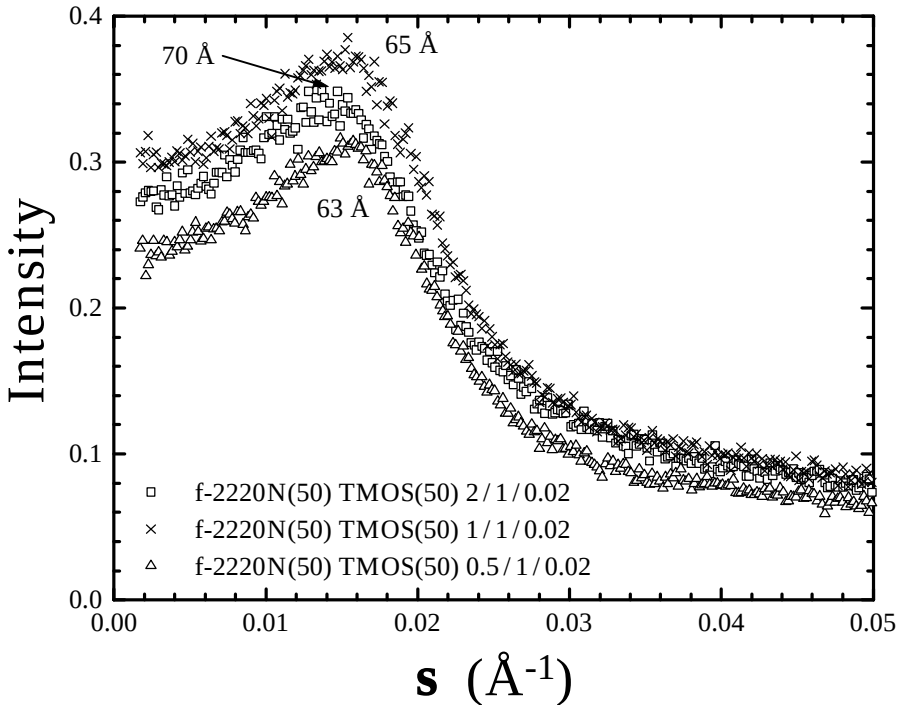

Figure 9. SAXS curves for f-2220N(50) TMOS(50) ceramers of varied water content.

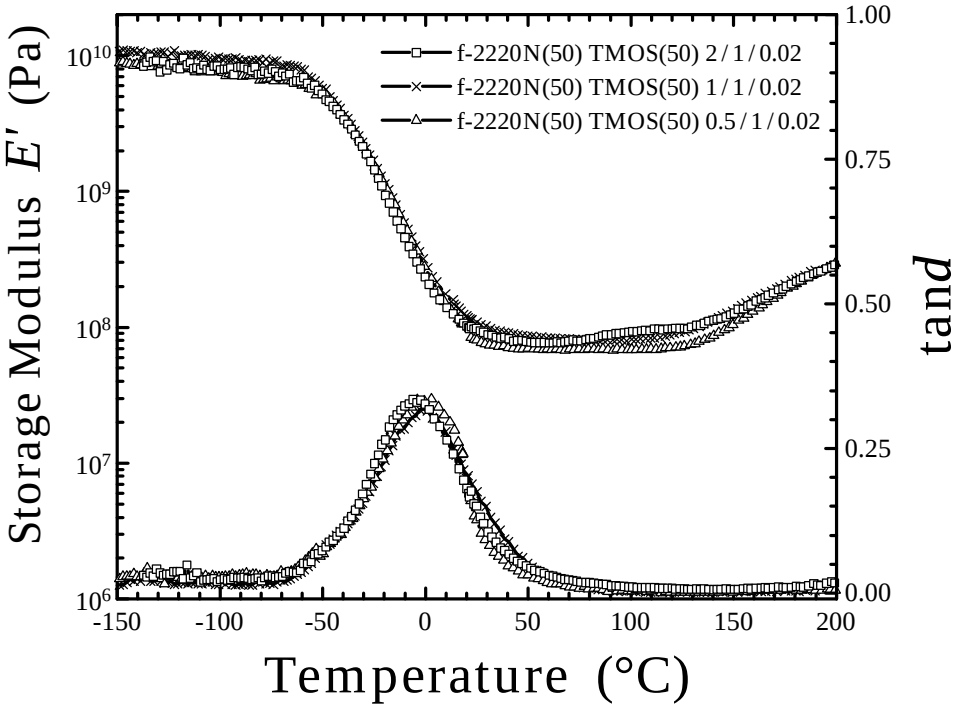

Figure 10. Thermomechanical spectra for f-2220N(50) TMOS(50) ceramers of varied water content.

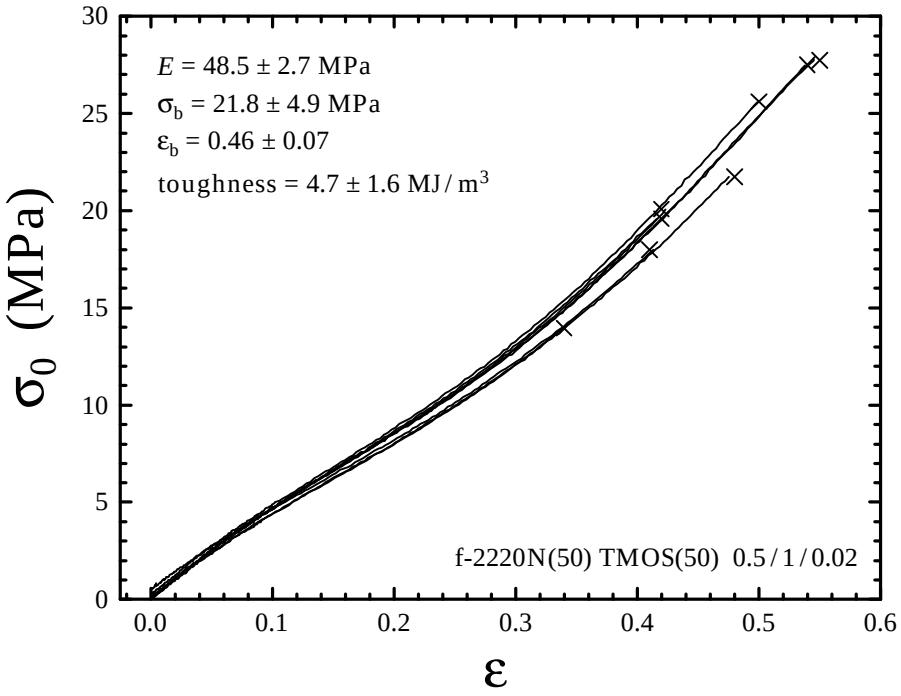

Figure 11. Tensile stress–strain data for f-2220N(50) TMOS(50) 0.5 / 1 / 0.02. Statistical values if E, σ_b, ε_b, and toughness shown.

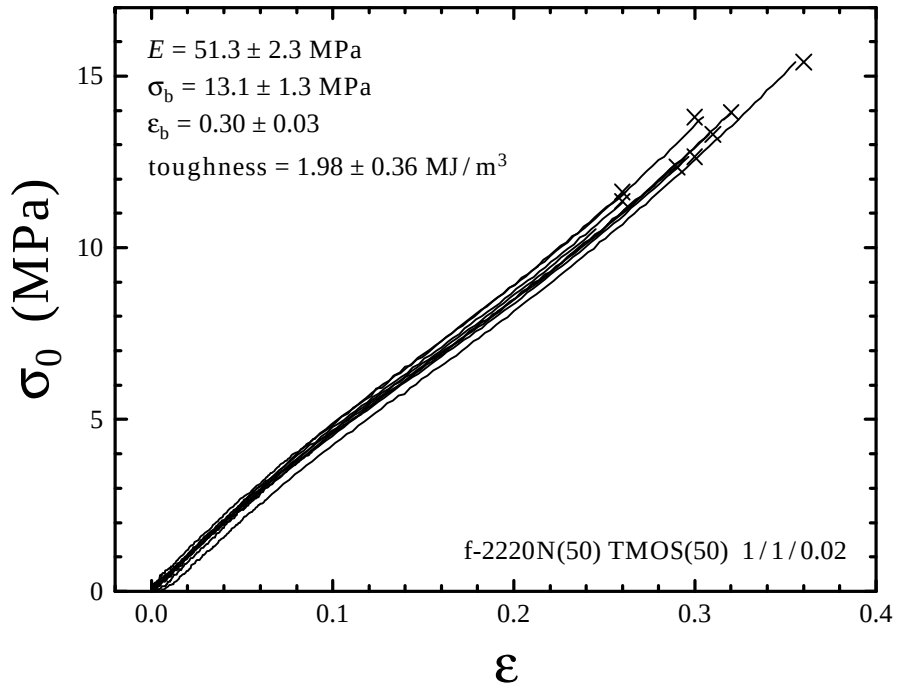

Figure 12. Tensile stress–strain data for f-2220N(50) TMOS(50) 1 / 1 / 0.02. Statistical values if E, σ_b, ε_b, and toughness shown.

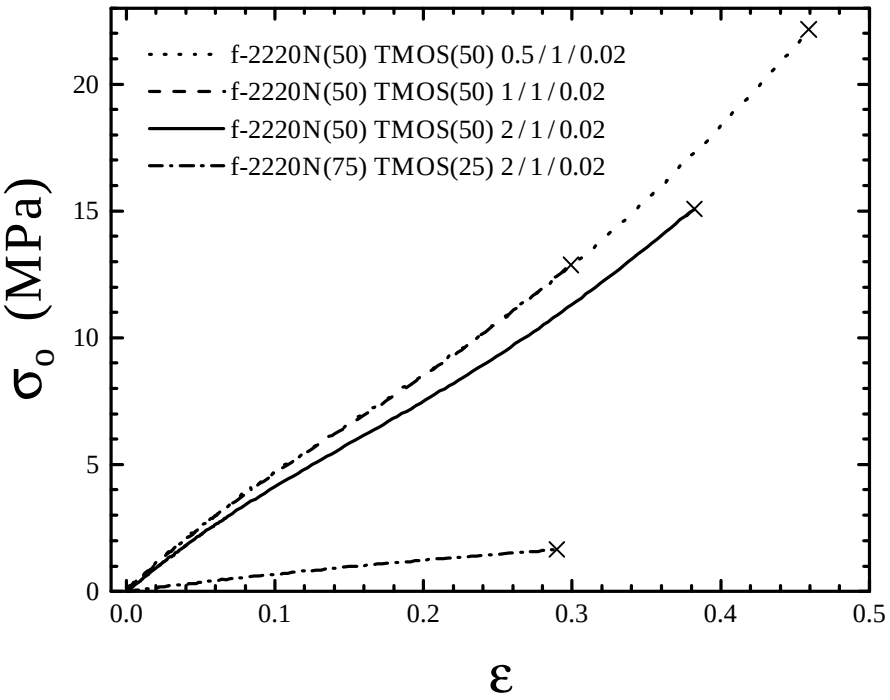

Figure 13. Tensile stress–strain data for ACCLAIM™ ceramers of varied TMOS and water content. One curve for each formulation is plotted which was the best representative of the statistical results.

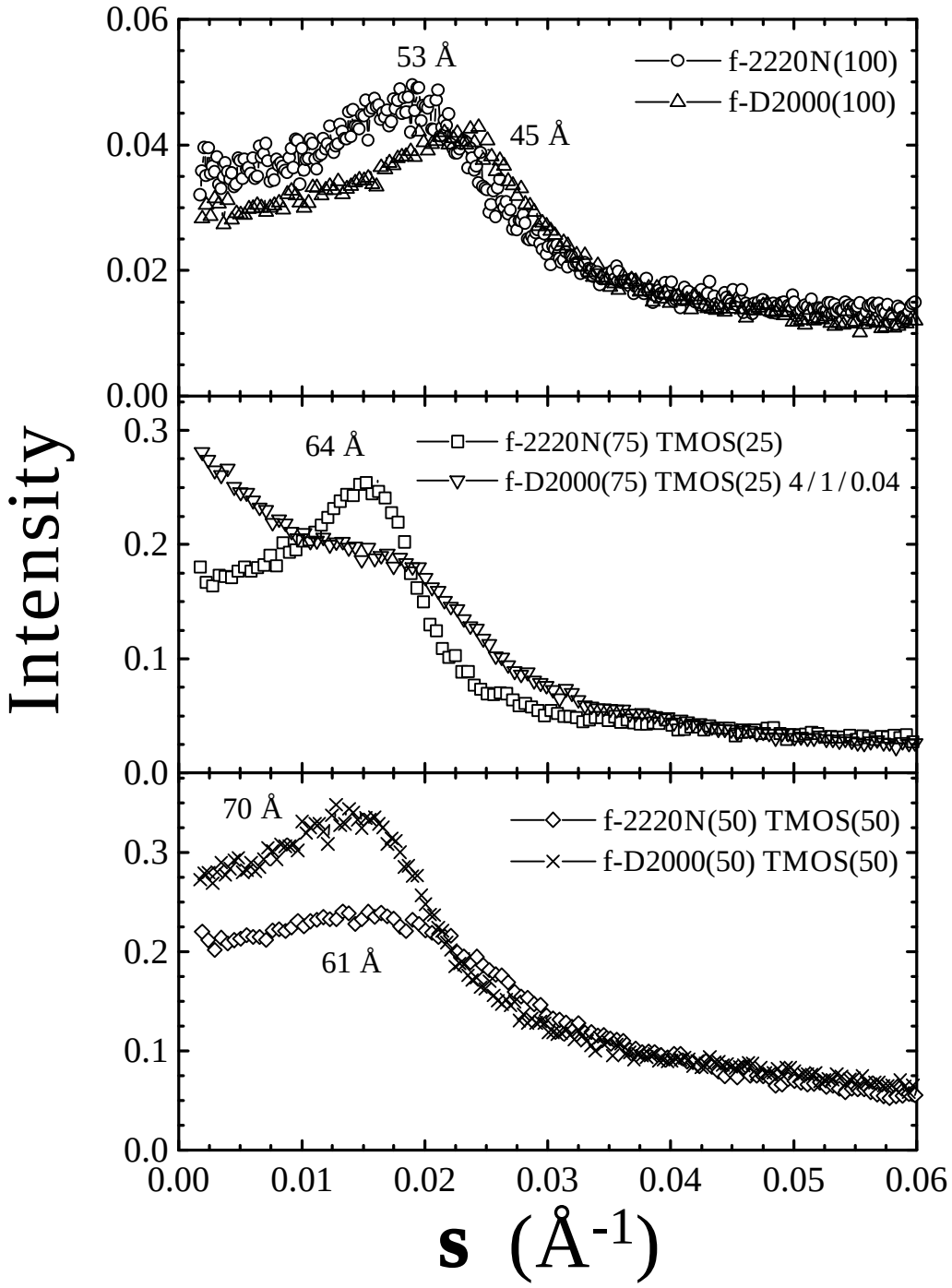

Figure 14. SAXS profiles for JEFFAMINE® and ACCLAIM™ based ceramers with varied TMOS content. No TMOS (top); 25 wt.% TMOS (center); 50 wt.% TMOS (bottom).

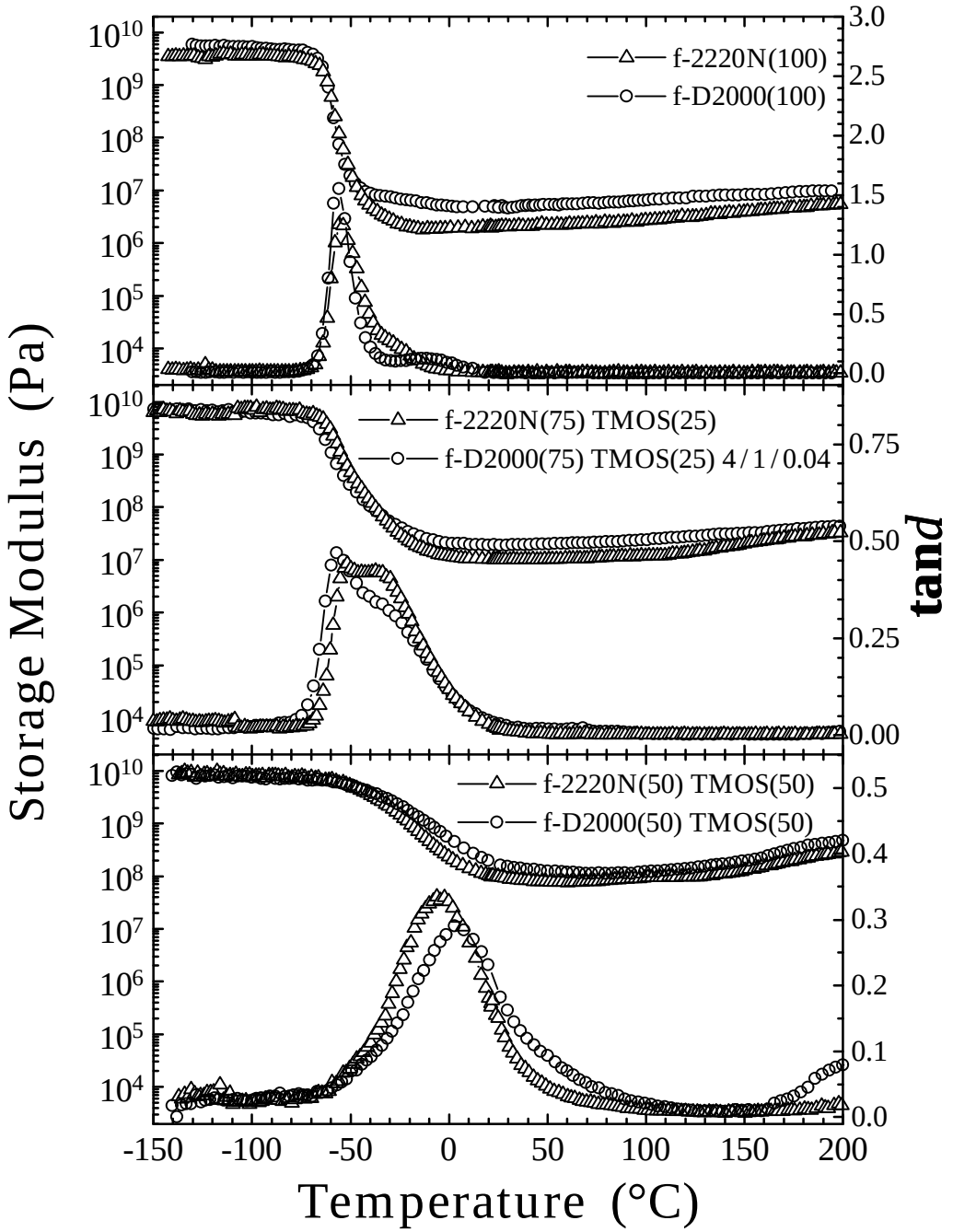

Figure 15. Thermomechanical spectra for JEFFAMINE® and ACCLAIM™ based ceramers of varied TMOS content. No TMOS (top); 25 wt.% TMOS (center); 50 wt.% TMOS (bottom).

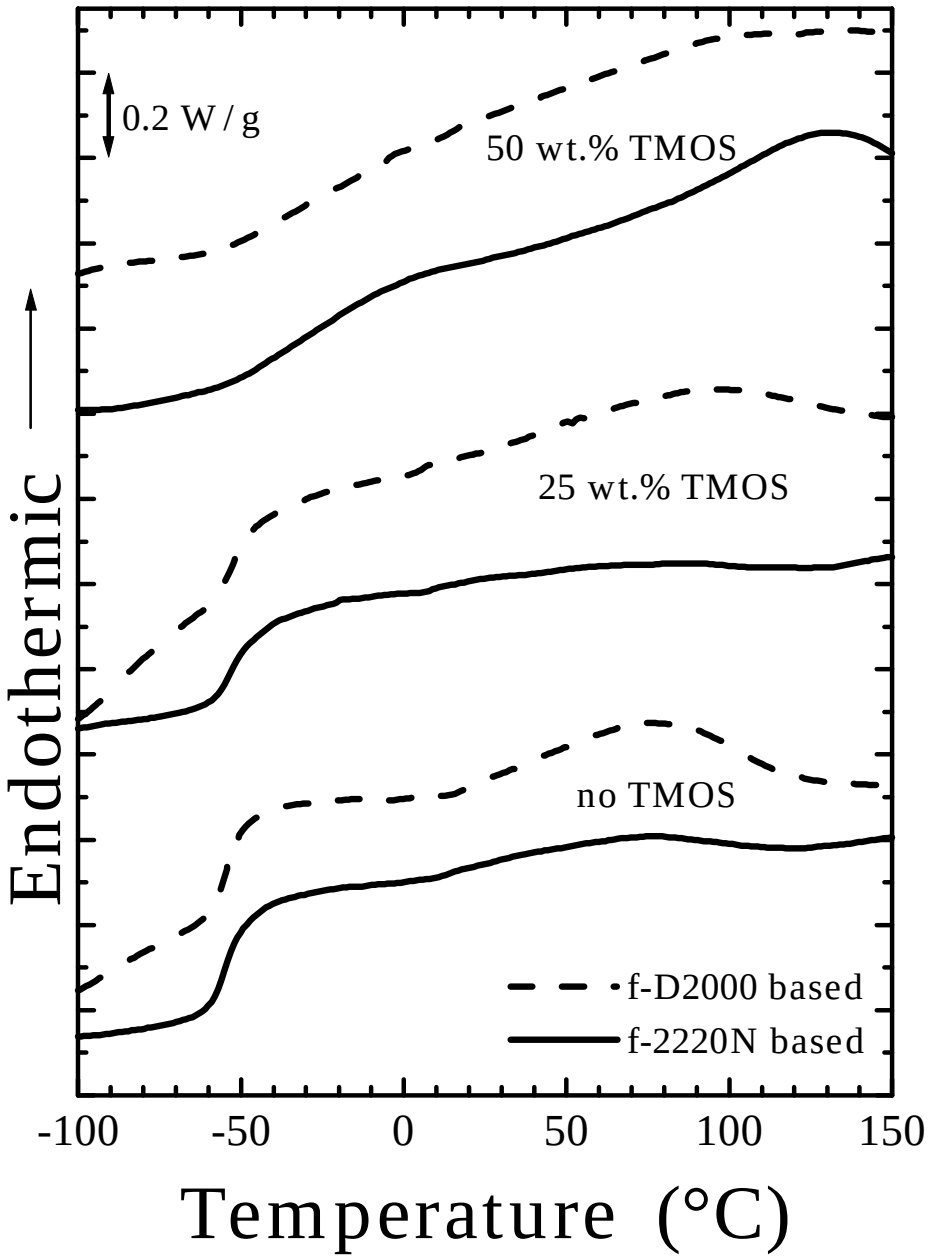

Figure 16. Differential scanning calorimetry scans for JEFFAMINE® and ACCLAIM™ based ceramers of varied TMOS content.

4.6 References

1 G. L. Wilkes, B. Orler, and H. Huang. *Polymer Preprints,* **26(2)**, 300, (1985).

2 K. Jordens and G. Wilkes. *J.M.S. Pure & Appl. Chem.*, accepted.

3 Leroy E. Alexander. X-ray Diffraction Methods in Polymer Science. p. 29, 286 Kreiger Publishing Company, Malabar, FL, 1985.

4 D. E. Rodrigues, A. B. Brennan, C. Betrabet, B. Wang, and G. L. Wilkes. *Chem. Mater.*, **4(6)**, 1437, (1992).

5 Lawrence E. Nielsen. Mechanical Properties of Polymers and Composites Volume 2, Marcel Decker, Inc., NY (1974).

6 H. Huang, R. H. Glaser, and G. L. Wilkes. Chapter 29 in Inorganic and Organometallic Polymers, *ACS Symp. Ser.*, **360**, 354, (1988).

7 H. Huang and G. L. Wilkes. *Polymer*, **30**, 2001, (1989).

8 A. B. Brennan and G. L. Wilkes. *Polymer*, **32(4)**, 733, (1991).

9 S. Yano, K. Nakamura, M. Kodomari, and N. Yamauchi. *J. Appl. Polym. Sci.*, **54**, 163, (1994).

10 C. J. T. Landry, B. K. Coltrain, J. A. Wesson, N. Zumbulyadis, and J. L. Lippert. *Polymer*, **33**, 1496, (1992).

11 L. R. G. Treloar. The Physics of Rubber Elasticity, Third Edition, Clarendon Press, Oxford, (1975).

12 T. M. Miller, L. Zhao, and A. B. Brennan. *J. Appl. Polym. Sci.*, **68**, 947, (1998).

13 L. E. St. Pierre and C. C. Price. *J. Am. Chem. Soc.*, **78**, 3432, (1956).

14 R. N. Work, R. D. McCammon, and R. G. Saba. *Bull. Am. Phys. Soc.*, **8**, 266, (1963).

15 G. Allen. *Soc. Chem. Ind. Monograph*, **17**, 167, (1963).

16 G. Williams. *Trans. Faraday Soc.*, **61**, 1564, (1965).

17 F. Surivet, T. M. Lam, J. Pascault, and C. Mai. *Macromolecules*, **25(21)**, 5742, (1992).

18 H. Huang and G. L. Wilkes. *Polym. Bull.*, **18**, 455, (1987).

19 H. Huang, B. Orler, and G. L. Wilkes. *Polym. Bull.*, **14**, 557, (1987).

20 H. Huang, B. Orler, and G. L. Wilkes. *Macromolecules*, **20**, 1322, (1987).

Chapter 5

Abrasion Resistant Coatings for Metal Substrates

Abstract

Novel hybrid inorganic-organic network materials have been synthesized and applied as transparent abrasion resistant coatings for metal substrates. A specially functionalized low molecular weight organic material serves as a precursor to coating formulations. The research presented in this chapter focuses on diethylenetriamine as the organic component. Combination of this functionalized organic material with metal alkoxides in the sol–gel reaction leads to hybrid inorganic–organic networks. While still a liquid, the initiated coating formulations are applied to the desired metal substrates by a spin coating process followed by thermal curing. Substrates include aluminum, plain steel, conversion coated steel, stainless steel, copper, and brass. The effects of coating formulation, cure temperature, and cure time on abrasion resistance has been determined.

5.1 Introduction

The ceramer project within Professor Wilkes' laboratory has evolved over the years from novel inorganic–organic materials to abrasion resistant coatings. These coatings were first applied to bisphenol–A polycarbonate substrates (PC), which put an upper constraint on the cure temperature of the coatings, set by the glass transition

temperature of PC (≈ 145 °C). Some of the varied organic components in these coatings were bis and tris maleimides,[1] melamine and tris(m–aminophenyl) phosphine oxide,[2] 4,4'–diaminodiphenylsulfone,[3] diethylene triamine,[3–5] several aliphatic diols, resorcinol, iminobispropylamine, and poly(ethylene imine).[4,5] Some coating formulations have been altered to include a u.v. absorbing species to protect the PC substrate and enhance the lifetime of the coatings.[6] The current chapter focuses on similar coatings based on diethylenetriamine with various metal alkoxides, but applied to metal substrates. This allowed the exploration of higher cure temperatures. Also, new formulations include a fluorinated species which systematically lowered the surface free energy of the final coatings. The coatings addressed in this chapter can be used in many applications where an abrasion resistant coating is desired for a metal surface. Some possibilities include cars, airplanes, submarines and other military applications, metal sink basins, etc.

5.2 Experimental Procedure

5.2–A. Materials

Diethylenetriamine (DETA) 99% pure, ethylacetoacetate (EAcAc) 99+%, aluminum tri-*sec*-butoxide (Al) 97%, zirconium (IV) propoxide 70 wt.% solution in 1-propanol (Zr), titanium isopropoxide (Ti), 3–(aminopropyl) triethoxysilane 99%, 3–(trimethoxysilyl) propyl methacrylate 97% (MASi), and 1N HCl, were purchased from Aldrich and used as received. Tetramethoxysilane (TMOS) 99+% pure, isocyanatopropyltriethoxysilane (ICPTES) 95%, and 3,3,3–(trifluoropropyl) trimethoxysilane were obtained from United Chemical Technologies, Inc., PETRARCH® silanes and silicones, and Gelest, Inc., and used as purchased. 2–Propanol (IPA) and acetone, ACS specifications, were used as–received from Mallinckrodt Analytical Reagents. Norbloc 7966, a u.v. absorbing molecule, was obtained from Noramco Inc. of New Brunswick, NJ.

The substrates chosen for study include: aluminum (0.020" thick, complies with ASTM D1730), plain steel (0.020", complies with ASTM D609 type 3 A366), and both

zinc phosphate and iron phosphate conversion coated steels (0.020”), purchased from Q Panel; also stainless steel (0.036”, type 304, 2B finish), copper (0.032”, complies to federal specification QQ-C-576, ASTM B152, type ETP), and brass (0.032”, QQ-B-613, alloy 260, ASTM B19, B36) purchased from McMaster Carr; and finally a chemically cleaned, highly polished aluminum alloy (5657-H18). This material has a mirror-like finish, and itself is easily abraded. (Mere rubbing with a Kimwipe™ creates obvious scratches). All panels were cut to a size between ≈ 3”× 3“ and 4”× 4“ which were then employed as the substrates.

The aluminum, steel, and copper substrates were first sanded with emery paper using an electric hand–held sander and washed with either acetone or IPA before application of the coating formulations. The surface characteristics of sanded aluminum and sanded steel are shown in the scanning electron microscopy images of Figure 1 and Figure 2, respectively. The aluminum surface is well roughened by the sanding process. The steel displays a smoother surface with curved scratches which are generated by the circular motion of the sander. The varied response for the two substrates is likely dominated by the difference in hardness of the two metals. The harder steel is less affected by the action of the aluminum oxide particles from the emery paper.

Since the conversion coated steels, stainless steel, brass, and polished aluminum substrates contained polished, cosmetic surfaces, they were only washed with either IPA or acetone prior to coating application.

5.2–B. Instrumentation

A Cambridge Stereoscan 200 scanning electron microscope (SEM) was employed for high magnification surface images at 15-20 kV. All SEM samples were first sputter–coated with gold.

Fourier Transform Infrared spectroscopy (FT-IR) was performed on a Nicolet instrument.

A Taber Abraser standardized abrasion test apparatus was employed with 500 grams of load on Calibrase CS-10 wheels. The wheels are composed of aluminum oxide

particles embedded in a rubber matrix, and were refreshed every 350-500 cycles with the abrasive disks described by the manufacturer. An SEM image of a CS–10 wheel is shown in Figure 3. The "smooth" areas in this image are rubber, and the particulate matter is the aluminum oxide particles. Note that the primary particle size is ~ 10 μm, and agglomerations of particles are ~ 100 μm.

Water contact angles were measured at room temperature with a contact angle goniometer using deionized water. At least eight measurements were made per sample, and a statistical average was derived from these eight measurements.

All coated samples that are shown as images in this chapter are not photographs (unless noted), but rather *scans of actual samples*. This was accomplished with a flat–bed, Hewlett Packard ScanJet 4P. A piece of transparent overhead film was laid between the coated samples and the scanner to prevent the samples from scratching the surface of the scanner glass. Images were modified electronically to maximize the visibility of wear tracks and other important features.

5.2–C. Coating Preparation

Triethoxysilane functionalization of diethylenetriamine

The first step in coating preparation involves synthesis of triethoxysilane functionalized DETA, a monomer in the coating formulation. This was achieved by mixing 5.00 g of DETA with 18.37 g IPA in a roundbottom flask which was immediately submerged in an ice bath (to prevent unwanted side reactions). In a separatory funnel was placed 39.76 g of ICPTES (≈ 3 moles ICPTES per mole DETA) and this liquid was added dropwise to the DETA-IPA mixture over the course of ≈ 30 minutes. A DETA molecule ideally combines with three ICPTES molecules forming three urea linkages, as illustrated in Figure 4. When the addition of ICPTES was complete (30 minutes), the roundbottom flask was sealed with septa and the mixture was stirred in the ice bath for 8 hours. After this period the reaction was complete as determined by the disappearance of the isocyanate peak from FT-IR spectroscopy (≈ 2273 cm^{-1}). The product of this reaction will be referred to as f-DETA (functionalized

DETA solution) throughout the remainder of this document. Note that the f–DETA molecules are present in a 70 wt.% solution of IPA.

f-DETA(100) coating formulation

The second step in the coating preparation involves sol-gel chemistry. f-DETA solution, either in the neat form or with added metal alkoxide(s) and other components, undergoes hydrolysis and polycondensation in the presence of water and either acid or base catalyst. Note that the water employed in all coating formulations was derived from the aqueous acid catalyst, and perhaps slight amounts from the moisture in the ambient air. A typical recipe for a neat f-DETA coating [labeled f-DETA(100)] is made as follows:

- 3.00 g f-DETA solution
- 1.50 g IPA
- dropwise addition of 0.15 g of aqueous 0.5 M HCl while under brisk stirring.

The reaction is shown schematically in Figure 5. IPA is usually added to the coating formulations in the amount of one-half of the mass of the f-DETA solution employed (the exception being the mixed–metal alkoxide formulations). This liquid is immediately applied by a spin coating process to the desired substrate, since the viscosity is rapidly increasing due to development of molecular weight during the sol-gel reaction. Spin coating is accomplished with a simple turntable device with a variable transformer which controls the rotation rate (generally ≈ 3000 rpm). The substrate is attached to the turntable with double–stick tape, and the liquid coating is applied by pipette to the center of the substrates (which may be already rotating or not). After the spin coating process, the samples are set under cover (away from dust) until the coating reaches a non-tack state (≈ 5 to 10 minutes). Following this, the coated samples are transferred to a forced–convection oven, where they are exposed to the desired temperature program. A typical cure schedule involved holding at 60 °C for 30 minutes, heating to 175 °C at a rate of 5°/min, and holding at this temperature for an hour. Other temperatures and cure times were also explored to determine the effects of these variables on the resulting coating performance.

f-DETA(50) TMOS(50) coating formulation

A coating comprised of 50% f–DETA and 50% TMOS by weight [f-DETA(50) TMOS(50)] is generated as follows:

- 2.00 g f-DETA solution
- 1.00 g IPA
- 1.40 g TMOS
- dropwise addition of 0.25 g of 0.5 M HCl under brisk stirring

This reaction is shown schematically in Figure 6. The coating is then applied and cured as before.

Mixed metal alkoxide coating formulations

In coating formulations involving non-silicate metal alkoxides (zirconium (IV) propoxide, or aluminum tri-*sec*-butoxide), a coordinating ligand (EAcAc) was added to the non-silicate alkoxide to retard the sol–gel reaction rate.[7] This is generally necessary for all non–silicate alkoxides due to the rapid precipitation of metal oxide particles in the absence of coordinating ligands. This result is undesirable since obtaining *transparent* coatings was the author's goal. However, titanium isopropoxide was not employed with a coordinating ligand. This was done under the advice of an experienced colleague, who had success preparing coatings in this fashion.[4,8] A typical recipe for a coating composed of 40 wt.% f-DETA, 40 wt.% TMOS, and 20 wt.% aluminum tri-*sec* butoxide [DETA(40) TMOS(40) Al(20)] is made as follows:

BEAKER 1

- 1.60 g IPA
- 1.59 g aluminum tri-*sec* butoxide
- 0.31 g EAcAc

Beaker 1 was allowed to stir for ca. one minute. Meanwhile, the following were combined in another beaker:

BEAKER 2

- 0.55 g 0.5 M HCl
- 1.00 g IPA

Beaker 2 was allowed to mix for ca. one minute, while adding the following to beaker 1:

add to BEAKER 1

- 3.40 g f-DETA solution
- 2.38 g TMOS

After allowing another minute for beaker 1 to mix, the contents of beaker 2 were added to beaker 1 in a dropwise fashion. The reaction is shown schematically in Figure 7. A spin coating process is then employed as before.

Fluorinated coating formulations

The surface free energies of the ceramer coatings have also been tailored. In an attempt to lower the surface free energy of some of the coatings (i.e. create a hydrophobic surface), a fluorinated monomer was added to the coating formulation.[9] Namely, (3,3,3–trifluoropropyl)trimethoxysilane (structure shown in Figure 8) was introduced into the formulations. The trimethoxysilane groups of this molecule can participate in the sol–gel reaction and hence the fluorinated species would be covalently bonded to the network. This is more desirable than simply adding a non–bonded fluorinated species to the coatings which could easily diffuse out of the coating with time, leading to an increase in the surface free energy. Hence the covalently bonded, fluorinated molecules have a more persistent value of surface free energy. A typical recipe for a fluorinated coating contains the following components [denoted as f-DETA(47.5)-TMOS(47.5)-F(5)]:

- 2.00 g IPA
- 4.00 g f-DETA
- 2.80 g TMOS
- 0.295 g (3,3,3–trifluoropropyl)trimethoxysilane (F)
- 0.52 g 0.5 M HCl added dropwise

The coating is then applied to the desired substrate and thermally cured as before. Other similar recipes were formulated with varying fluorinated monomer content so that its influence on the resulting water contact angles (and hence the surface free energies) of the coatings could be obtained.

Coating formulations with u.v. absorber

A final modification to the coating properties involved incorporating an ultra–violet absorbing species into the coating formulations to improve the u.v. resistance of the coating, and also, in some cases (for instance PC and PMMA), to protect the substrate from destructive u.v. radiation. Again it was preferred to covalently bond the u.v. absorbing species directly to the hybrid network in order to prevent diffusion and loss of the species with time. The u.v. absorber chosen for this purpose was Norbloc 7966, the structure of which is shown in Figure 9. Although an alkoxysilane functional u.v. absorbing species could not be readily found, this Norbloc material has a vinyl group which was exploited. Vinyl containing alkoxysilanes can be readily found, and such a molecule can be used as a link between the sol–gel network and the u.v. absorber. Specifically, trimethoxysilylpropyl methacrylate was employed, the structure of which is shown in Figure 10. This material has trimethoxysilane groups which can participate in the sol–gel reaction, and also a vinyl group which can be polymerized along with the vinyl groups of the Norbloc 7966 material (with added free-radical initiator, benzoyl peroxide). A formulation procedure is as follows [f-DETA(45) TMOS(50) MASi(4) UV(1)]:

- 2.00 g IPA
- 0.06 g Norbloc 7966
- 0.24 g trimethoxysilylpropyl methacrylate (MASi)
- 3.00 g TMOS
- 3.86 g f-DETA solution

Let the above mix at ambient conditions until a homogeneous solution results (the Norbloc takes ≈ 5 to 10 minutes to dissolve completely). Once a homogeneous solution is formed, add:

- 1.00 g 0.3 wt.% benzoyl peroxide in acetone (initiates methacrylate copolymerization)

Let this react for ≈ 1 minute. Finally, add:

- 0.34 g 0.5 M HCl, dropwise

The reaction is shown schematically in Figure 11. The coating formulation is applied to the desired substrate and thermally cured as before.

5.3 Results and Discussion

5.3–A. Aluminum Substrates

One of the first goals of this research was to determine the optimum cure temperature and cure time combination for the f-DETA(100) and f-DETA(50) TMOS(50) coating formulations on aluminum substrates. Previously it had been determined that increasing the cure temperature of such f-DETA based coatings led to an increase in the abrasion resistance when applied to PC.[4] This was thought to be due to the higher extent of reaction attainable at higher temperatures. However, the upper limit for curing was ≈ 145 °C since above this temperature (which is the glass transition temperature of PC) the substrates would soften and rapidly warp from frozen–in stresses.[3] Since this is not a concern for metal substrates, higher temperatures were easily explored. First, a ten hour cure time was held constant and the cure temperatures were varied as 75, 125, 175, and 225 °C. Under these conditions both chemistries displayed the best abrasion resistance when cured at 175 °C. At 225 °C, degradation is evident by discoloration (golden to brown) of the otherwise transparent coatings. This is likely due to the degradation of the urea linkages, which in general are not very stable above 200 °C for extended periods. At temperatures below 175 °C the abrasion resistance is inferior to samples cured at 175 °C, due to the lower crosslink density (extent of reaction) of the hybrid network generated at the lower temperatures. Figure 12 shows the influence of cure temperature on the abrasion resistance of f-DETA(50) TMOS(50) coatings on aluminum. Note that the annular wear tracks are most evident on the samples cured at 75 and 225 °C, and least visible on the 175 °C sample. Cure temperature had a similar effect on f-DETA(100) formulations on aluminum.

Also shown in previous studies, longer curing times led to better abrasion resistance.[4] However as previously mentioned, the cure temperature for this study was

held below 145 °C. In the present work, while the cure temperature was held constant at 175 °C, the cure times were varied as 1, 5, 10, 15, 20, 40, 60, 120, 180, and 600 minutes. For the f-DETA(100) coating, a minimum of 40 minutes of cure time are required for optimal abrasion performance. The f-DETA(50) TMOS(50) system required a shorter cure time of only 20 minutes for peak performance. This was determined by the results of the Taber Abraser test as the shortest cure time which displayed the best abrasion resistance (i.e., least obvious wear track by careful inspection). Due to the very slight optical appearance of wear tracks in this aspect of the study, scanned images do not display notable distinctions, and hence are not presented.

The chemical structure of the network also influences abrasion resistance. For aluminum substrates, both f-DETA(50) TMOS(50) and f-DETA(100) coatings greatly exceeded the performance of the uncoated control sample, as shown in Figure 13. However, f-DETA(50) TMOS(50) was a better protective coating than f-DETA(100) from an abrasion standpoint. This is not difficult to perceive from the molecular structure of the network; the addition of TMOS to the reaction results in mostly —Si—O—Si— linkages in the final network (which is much like amorphous silicon dioxide), thereby producing a harder, more abrasion resistant material. In fact, increasing the relative amount of TMOS in f-DETA based coatings improves the abrasion resistance accordingly, as expected. This is shown in Figure 14 where TMOS contents range from 0 to 60 wt.% of the coating formulation. Upon closer inspection (by SEM) of an abraded f-DETA(50) TMOS(50) coating on aluminum, a tearing mechanism of abrasive wear[1,2,4] is apparent (Figure 15). The criss–cross abrading action is a result of the opposing spin of the two Taber Abraser wheels. Notice that most of the coating surface remains undamaged, and the scratches are for the most part, far between.

Simple salt water immersion tests served as an index of corrosion resistance for these coated systems. A solution of 3.5 wt.% NaCl (this is the approximate concentration of dissolved salts in ocean water*) in deionized water served as the corroding medium. Samples were either half or completely submersed in the salt water for anywhere from

* *Note that ocean water contains many different dissolved salts however the most abundant is NaCl.*

one to seven days. Evaluation of performance was accomplished by the physical appearance after the exposure. Both coating chemistries on aluminum display improved corrosion resistance in the salt water immersion when compared to uncoated control samples. After twenty four hour exposure, the control exhibits pitting corrosion visible to the naked eye. Analogous examination of the coated samples confirms that no damage is apparent at this level. No distinction can be made between the corrosion resistance of either coating formulation by these experiments.

Another type of environmental exposure test is the hot-wet test. This involves complete immersion of the coated sample in boiling deionized water for one hour. After drying the sample, it is exposed to the Taber Abraser compared to samples that were not boiled to determine if the hot–wet exposure had an effect on the abrasion resistance of the coating. Hot-wet exposure for a duration of one hour decreased the abrasion resistance of f-DETA(100) on aluminum. However, it has been noted that little to no change in abrasion behavior occurs in the f-DETA(50) TMOS(50) coating on aluminum after this test.

Mixed metal alkoxide formulations provide improved hot–wet resistance over f-DETA(100) and f-DETA(50) TMOS(50) formulations on polycarbonate substrates.[4] Mixed metal alkoxide formulations on sanded aluminum have not exceeded the performance of the f-DETA(50) TMOS(50) coating in the hot-wet tests. The reason for this is believed to be due to reaction conditions. Since the non–silicate metal alkoxides generally require a coordinating ligand to retard the reaction rate, and the silicate metal alkoxides require a catalyst to increase the reaction rate, it is difficult to generate a desired mixed metal alkoxide formulation. A certain amount of fine tuning of ligand content, acid content, and cure schedule is required to produce a uniform, high crosslink density network coating. Since all components are finally mixed together, it is anticipated that the reaction rates between the silicate and non–silicate alkoxides would be mismatched and non–uniform network chemistries would result. Under the conditions attempted, none have generated a superior coating to the f-DETA(50) TMOS(50) material. It can be seen from Figure 16 that f-DETA(40) TMOS(40) Al(20)

and f-DETA(40) TMOS(40) Ti(20) perform poorly in the abrasion test both before and after the hot–wet exposure.

The effect of adding a fluorinated monomer to the coating formulations was monitored through the measurement of the water contact angle. There is a nearly linear increase in the water contact angle with increasing fluorinated monomer content, as shown in Figure 17. Since fluorinated species are typically expensive, an alternative route was devised to maximize its influence on surface properties. A normal, fluorine free f-DETA(50) TMOS(50) coating was applied by a spin coating process to a substrate, and while still spinning, a small amount of the fluorinated monomer (≈ 5 wt.% of the coating formulation) was applied by pipette to the top. This confined the fluorinated material primarily to the surface, hence maximizing its influence there. Note that by coating the fluorinated monomer on top of a normal f-DETA(50) TMOS(50) coating, a high contact angle is observed (90 ± 4° in Figure 17). This required only ≈ 5 wt.% of the fluorinated monomer. The other formulation with 5 wt.% of the fluorinated monomer distributed throughout the entire coating, has a contact angle of only 68 ± 2°. Hence, applying the fluorinated material only on the surface can greatly enhance the water contact angle. This secondary fluorinated layer could be applied to the f-DETA(50) TMOS(50) formulation before (90 ± 4°) *or* after (88 ± 2°) the thermal curing step (of the base f-DETA(50) TMOS(50) layer) with essentially the same resulting water contact angle. However, the fluorinated layer itself must be thermally cured to generate a durable surface free energy, so if a previously cured f-DETA(50) TMOS(50) coating is to have a fluorinated layer added to it, the entire sample must be thermally cured a second time after application of the fluorinated species. The surface fluorinated coatings can be rigorously washed with soap and water, followed by isopropanol, and the contact angle remains essentially the same, ≈ 87 ± 2°. Table 2 presents the contact angle data for all coating systems containing 5 wt.% fluorinated monomer of these different preparation procedures. All values for the samples which had the fluorinated layer applied on top of the f-DETA(50) TMOS(50) coating are nearly the same.

An attempt at quantification of the strength of the adhesive bond between the coating and the substrate has been undertaken with a direct pull off test.[10] In this experiment, an Instron is utilized in tension in an effort to remove the coating from the substrate using a specially designed apparatus, illustrated in Figure 18. If failure from this test occurs between the coating and substrate, then dividing this failure load by the cross–sectional area of the failure surface will yield a practical strength of adhesion.

Direct pull off tests have failed to provide quantitative coating–substrate adhesion strengths. For every such experiment conducted, failure never occurred at the coating–substrate interface but rather at some other location in the apparatus (usually between the coating and the epoxy adhesive). For this reason it can be concluded that coating–substrate adhesion is quite significant, although not rigorously quantified. Therefore, the adhesive strengths thus measured, shown in Table 1, are all listed as "greater than" the values shown due to the lack of failure at the coating–substrate interface. Other adhesives were chosen in addition to epoxy, e.g. cyanoacrylate, acrylic, etc., all with the same results. The good adhesion for these coating–substrate systems can in part be the result of the potential for direct covalent bonding between the coating and aluminum surface.[11] Surface hydroxyls on the aluminum (which are generally present on many metals[12]) can react with alkoxysilane groups of the coating formulation, thereby generating covalent links (the chemistry is shown schematically in Figure 19). This is particularly important in explaining the good adhesion between the coatings and the highly polished aluminum (to be addressed in a separate section), where mechanical interlocking as a mode of adhesion is not likely. This is not a surprising result since silanes are used as coupling agents for bonding various adhesives to metal substrates such as steel, titanium, and aluminum.[13,14]

5.3–B. Plain Steel Substrates

For the plain steel substrates the abrasion behavior of the f-DETA(50) TMOS(50) coating is unexpectedly poor.[15] During the abrasion test, rather large pieces (~1 mm^2) of this coating detach. This result is unexpected since this same chemistry is an excellent performer on aluminum. f-DETA(100) displays much better performance on

steel in the abrasion tests, but this coating is not as hard as a coating incorporating TMOS. The performance results can be seen in Figure 20. The sample with the f-DETA(100) coating shows a relatively uniform wear track (although it is quite pronounced), whereas the sample with the f-DETA(50) TMOS(50) coating is non–uniform in its wear process. The coating on this sample displays large areas where complete breakthrough to the steel surface is achieved. Three SEM images of the same area of an abraded sample, of various magnifications, are shown in Figure 21. The very bright patches are bare steel surface, where the coating has fractured and detached. Some areas display a similar criss–cross pattern generated by the tearing mechanism of abrasive wear (as was observed for this coating on aluminum), but the majority of wear in this sample appears to be brittle fracture wear, surface fatigue wear, or perhaps corrosive wear.[16,17]

Since a silane can form similar covalent bonds to the steel surface[18] as it may with the aluminum substrates, as discussed in the above section, some other controlling factor must be present which leads to the poor performance of the f-DETA(50) TMOS(50) coatings in the abrasion tests. In the case of both the aluminum and steel, rough sanded surfaces are created on these substrates so that mechanical interlocking can take place on both. Also the coating is applied while the viscosity of the mixture is low and therefore wetting and spreading should be satisfactory. However, since aqueous HCl is present in the coating formulations as a catalyst for the sol–gel reaction, it is possible that this acid may attack the steel surface leading to rapid corrosion of the surface. Subsequent curing of the coating would leave a weak boundary layer (corroded passive oxide layer) which could be a possible explanation for the poor abrasion performance. The abrasion test could easily lead to break–up of the brittle, corroded layer which would cause rather large pieces of the coating to detach, as observed. This is consistent with the mechanism of corrosive wear,[16] as addressed in the literature review of chapter 2. The possibility of corrosion as the important factor is supported by the fact that almost twice as much acid is present in the f-DETA(50) TMOS(50) formulation (which displays poor adhesion) than in the f-DETA(100) formulation (good adhesion).

Obviously corrosion is not evident on a large scale, as no rust was visible, however the formation of a thin weak boundary layer is sufficient to generate the observed performance. However, the direct pull off test does not show low values of the coating–steel substrate adhesive strength (Table 1). Again the coatings can not be pulled directly off with this test.

Salt water exposure of uncoated steel samples leads to pronounced corrosion after twenty four hours. Massive discoloration covers the surface. The f-DETA(100) coated samples show no obvious damage after this experiment. An uncoated and f-DETA(100) coated sample are shown in Figure 22 after a half immersion in salt water for one day. The uncoated sample shows massive corrosion (the lower half was exposed to salt water. The corrosion on the upper half occurred later, over time, due to exposure to ambient lab conditions). The f-DETA(100) coated sample shows no signs of corrosion from the salt water exposure. The rusty line seen on this coated sample resulted from corrosion of the opposite, uncoated side of the sample; these rust particles floated on the surface of the salt water and deposited themselves on the coating at the location of the waterline.

For steel, the abrasion resistance of the f-DETA(100) coating is degraded after a one hour hot–wet exposure as shown in Figure 23. f-DETA(50) TMOS(50) on steel was not tested due to the poor abrasion performance of this coating on this substrate.

5.3–C. Conversion Coated Steel Substrates

Coatings on the two conversion coated steels behave similarly. Both f-DETA(100) and f-DETA(50) TMOS(50) coatings were poorly adhered to these substrates after curing. The reason for this is suggested to be due to unpreferred chemical groups at the substrate surface, and a lack of sufficient surface roughness. As previously mentioned, these steels were not sanded due to the thin conversion coatings, and the very smooth surface does not lend to much mechanical interlocking as a mode of adhesion between the substrate and abrasion resistant coating. Hence, the conversion coated steels provide no advantage over plain steel for any application. A similar cure temperature study for f-DETA(100) coatings on zinc phosphated steel was performed,

and the resulting samples are shown in Figure 24 after abrasion testing. As this figure shows, the coatings wear unevenly as large particles detach from some areas, exposing the bare metal surface. f-DETA(50) TMOS(50) coatings perform similarly on both the zinc and iron phosphated steels.

5.3–D. Stainless Steel Substrates

Stainless steel is very well protected from abrasion by f-DETA(50) TMOS(50) coatings, in contrast to the plain and conversion coated steels. *Wear track visibility is essentially negligible up to at least 200 cycles for these coatings, while a clear wear track is apparent after only 10 cycles for the uncoated substrate* (Figure 25).

5.3–E. Copper Substrates

Copper is a relatively soft metal, although its density is higher than steel (compare 8.9 g/cm^3 to 7.8 g/cm^3).[19] Despite the high density of this metal, ceramer coatings provide abrasion resistance far superior to the bare metal. Figure 26 shows the performance of f-DETA(50) TMOS(50) coatings on copper substrates, compared to an uncoated control. *In the uncoated sample a clear wear track can be seen after only 10 cycles on the Taber Abraser. The two coated samples display little evidence of a wear track after 350 and* ***500*** *cycles.* It is also noteworthy that the coatings on the copper substrates have a pleasing, cosmetic appearance.

5.3–F. Brass Substrates

The next substrate chosen for study was brass. Figure 27 shows the performance of the f-DETA(50) TMOS(50) abrasion resistant coating on this alloy. *Again, the uncoated control shows distinct wear after only 10 cycles, whereas the two coated samples exhibit little visible wear after 100 and 200 cycles, respectively*.

5.3–G. Polished Aluminum Substrates

The polished aluminum substrates addressed in this chapter have applications in decorative molding for lighting fixtures, among other areas. This highly polished

material is easily abraded, in fact it can be scratched by lightly wiping with a Kimwipe™.

With these substrates the possibility of stacking coated samples on top of one another before thermally curing the applied coatings has been explored. This was based on the fact that often a long length of aluminum sheet is rolled–up after coating for storage. To simulate such a situation, two small pieces of sheet were employed. The pieces of sheet were curved by bending them over the side of a large coffee can. After applying the coating to the bent sheets and allowing the coatings to reach a non–tacky state, the two samples were pressed together with a weight while thermally cured. The samples did not stick together during the curing process, as long as the coatings were non-tack before stacking the layers. This provides an alternative method for employing this ceramer coating system in an industrial environment.

A more academic approach was also taken in probing the performance of the coating formulations on the polished aluminum substrates. These substrates benefit greatly from a hybrid coating. Figure 28 shows two such coated substrates and an uncoated control after abrasion testing. *The control shows massive wear after only* ***two*** *cycles, but the coated substrates show little wear after 50 cycles.*

One of the coatings in this figure has the u.v. absorber incorporated. This may prolong the durability of the coating itself, or perhaps can protect a u.v. sensitive substrate (important for coatings on polycarbonate which changes chemistry after exposure to u.v.). The abrasion resistance of the u.v. containing coating appears to be similar to the f-DETA(50) TMOS(50) coating on this polished aluminum substrate.

5.4 Conclusions

The performance of alkoxysilane functionalized diethylenetriamine–based ceramer coatings applied to various metal substrates was probed. In general, increasing the TMOS content led to a harder, more abrasion resistant coating. An optimum cure temperature of 175 °C was determined. This temperature was higher than conventional cure temperatures employed for such coatings in the past, due to the limitations of the

glass transition temperature of the previously employed polycarbonate substrates. At this higher cure temperature, an optimum cure time of ≈ 40 minutes was found for f-DETA(100) and 20 minutes for f-DETA(50) TMOS(50) coatings. Adhesion between the coatings and aluminum substrates was excellent, although not quantified. Direct pull–off tests failed to remove the coating from the substrates. Coating formulations may form direct covalent bonds to surface hydroxyls on the metal substrates, thereby contributing to excellent adhesion. f-DETA(50) TMOS(50) coatings on plain steel and the two conversion coated steels performed poorly in the abrasion tests. This is proposed to be due to corrosion of the steel (i.e. the presence of a passive oxide layer) by the acid catalyst in the case of plain steel, and undesirable surface chemistry in the case of the phosphated panels. f-DETA(50) TMOS(50) coatings proved to protect stainless steel, copper, and brass very well from abrasion. A fluorinated monomer was incorporated into the coating formulations, which led to a systematic decrease in the surface free energy of the resulting coatings. A u.v. absorber was also incorporated into the ceramer coatings, through a covalent bonding process, in an attempt to lengthen the lifetime of the coatings in a u.v. environment.

5.5 Acknowledgments

The author wishes to express his gratitude to the United States Air Force Office of Scientific Research for their support and the Center for Adhesive and Sealant Science at VPI&SU as well as the Adhesive and Sealant Council Education Foundation for their financial assistance. He also would like to thank Dr. Hideko Oyama and Prof. James Wightman for use of their contact angle goniometer.

Table 1. Results of direct pull off tests for a few coating systems.

Substrate	**Coating Formulation**	**Bond Strength (MPa)**
Aluminum	f-DETA(50) TMOS(50)	> 20.3
Aluminum	f-DETA(40) TMOS(40) Zr(20)	> 12.7
Steel	f-DETA(50) TMOS(50)	> 20.9
Polished aluminum	f-DETA(50) TMOS(50)	> 5.7

Table 2. Water contact angles for coatings prepared by various procedures containing **5 wt.%** of the fluorinated monomer.

Fluorination procedure	**Contact angle (°)**
fluorinated monomer distributed throughout coating layer	68 ± 2
fluorinated monomer coated *on top* of f-DETA(50) TMOS(50)	90 ± 4
as above, washed vigorously	87 ± 2
fluorinated monomer coated on top of *previously cured* f-DETA(50) TMOS(50), then *cured again*	88 ± 2

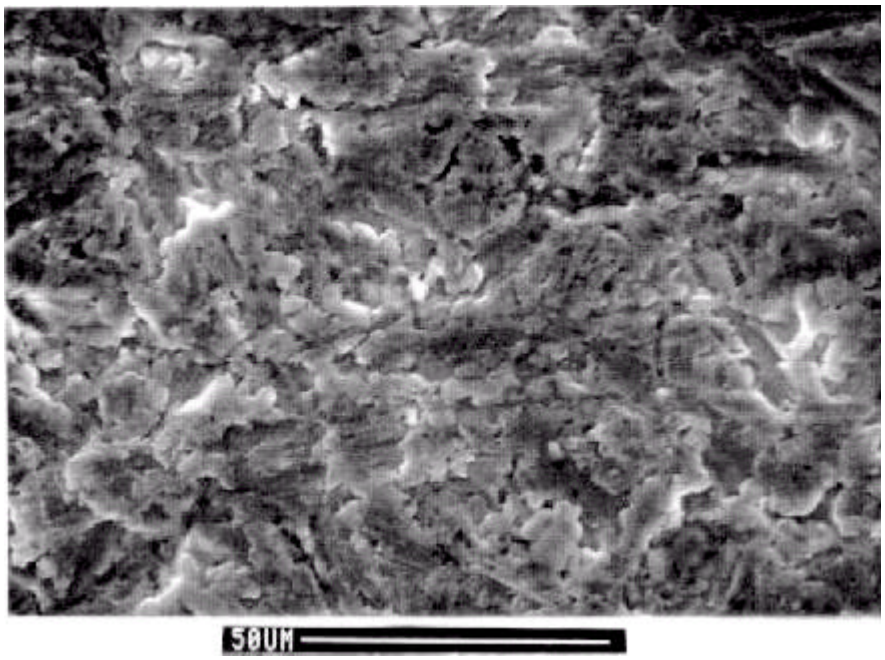

Figure 1. SEM image of emery sanded aluminum substrate. 50 μm marker.

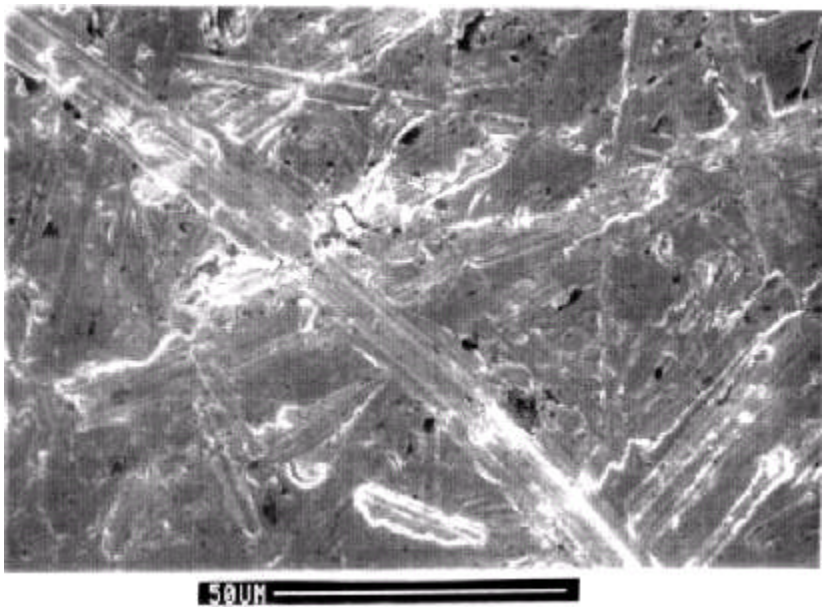

Figure 2. SEM image of emery sanded, plain steel substrate. 50 μm marker.

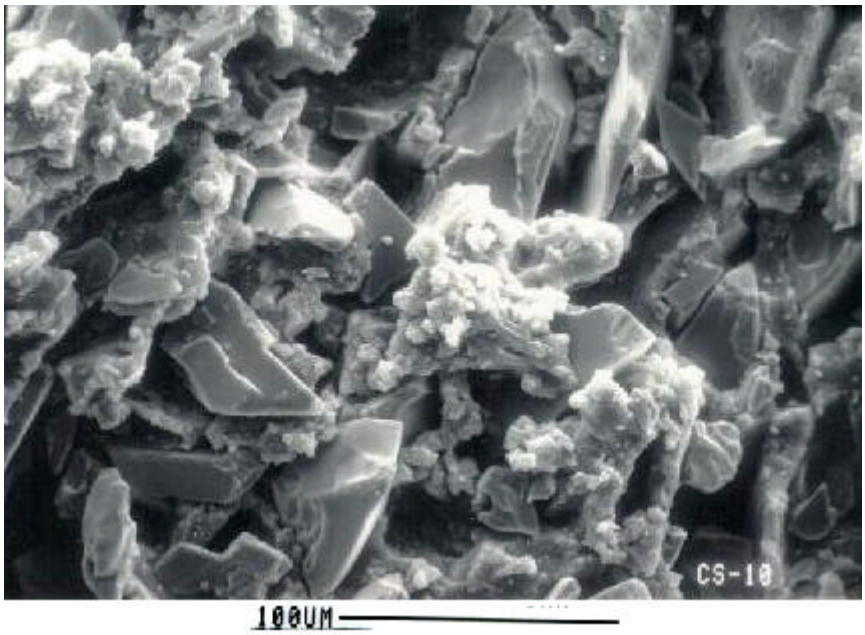

Figure 3. SEM image of a Taber Abraser CS–10 abrading wheel, composed of aluminum oxide particles embedded in a rubber matrix.

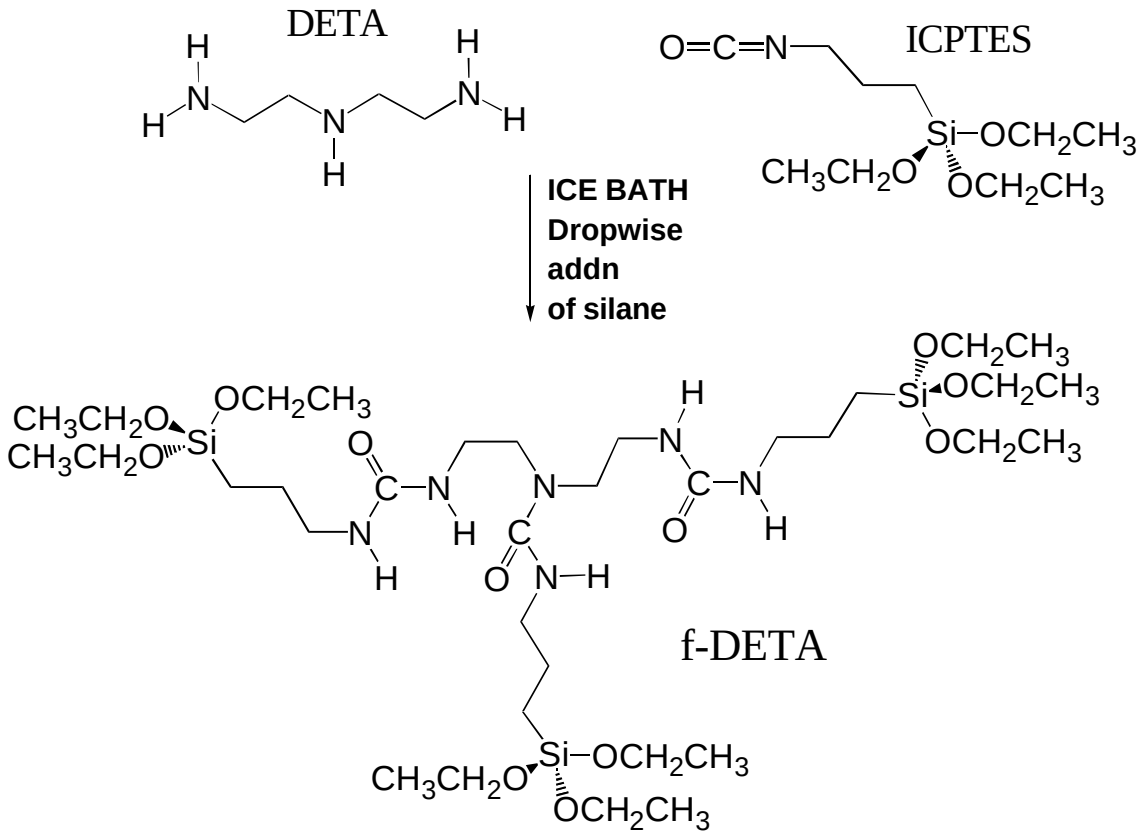

Figure 4. Functionalization of diethylenetriamine (DETA) with isocyanato-propyltriethoxysilane (ICPTES) to form the coating precursor, functionalized DETA (f-DETA).

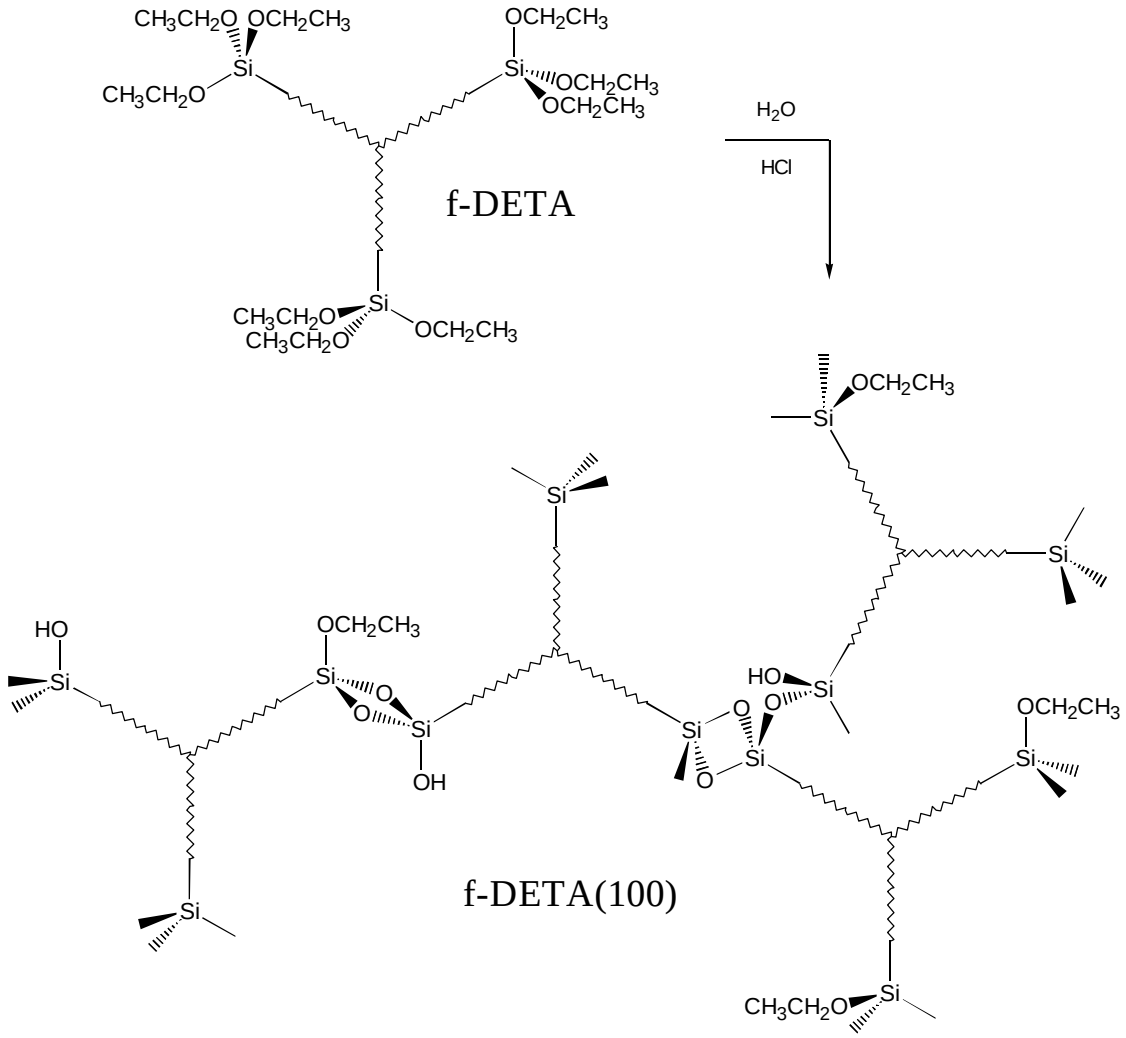

Figure 5. The sol–gel reaction of f-DETA (simplified representation), forming a coating designated as f-DETA(100). The structure is meant to reflect an infinite network.

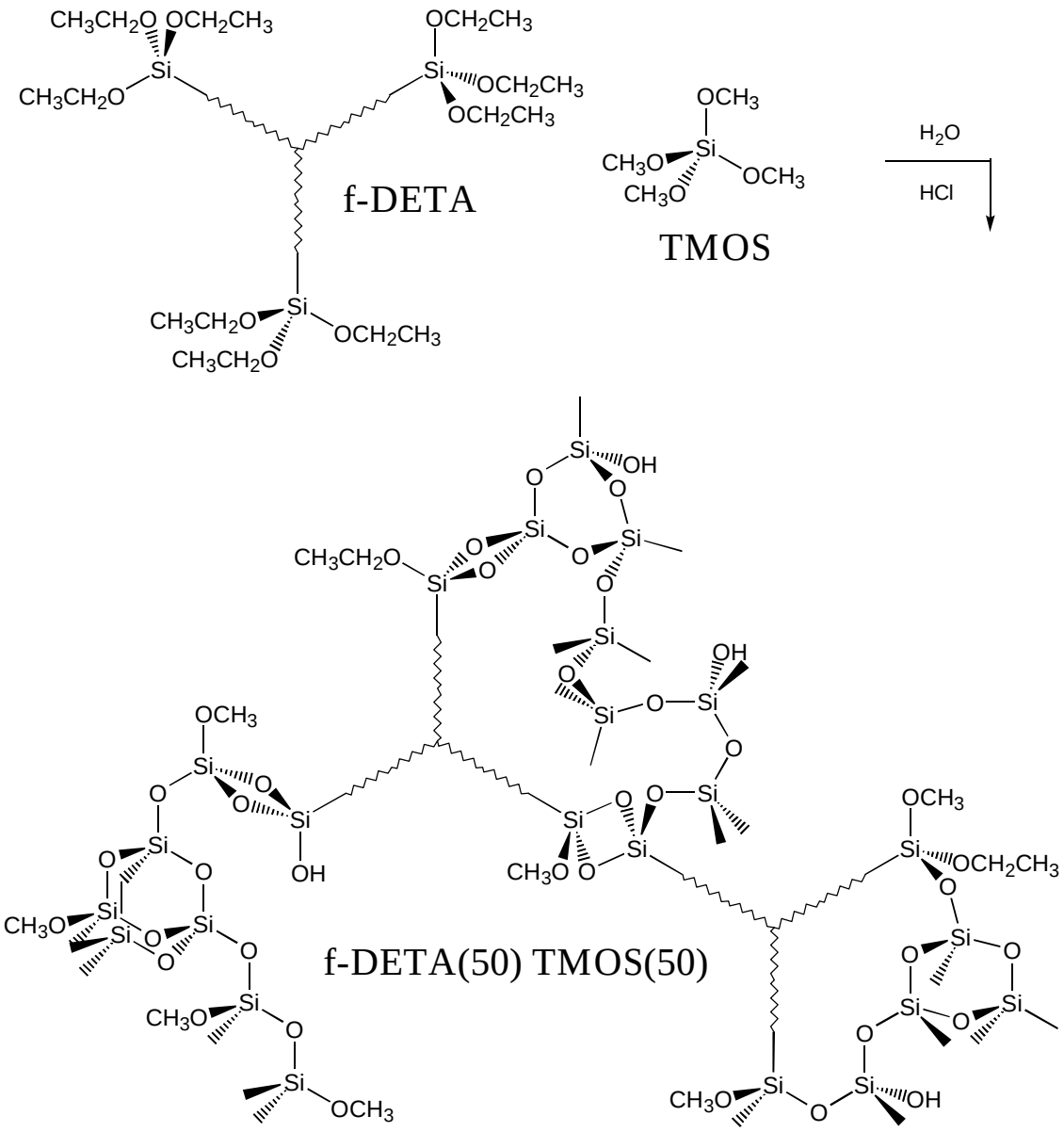

Figure 6. The sol–gel reaction of f-DETA with TMOS, forming a coating designated as f-DETA(50) TMOS(50). The resulting structure is meant to reflect an infinite network.

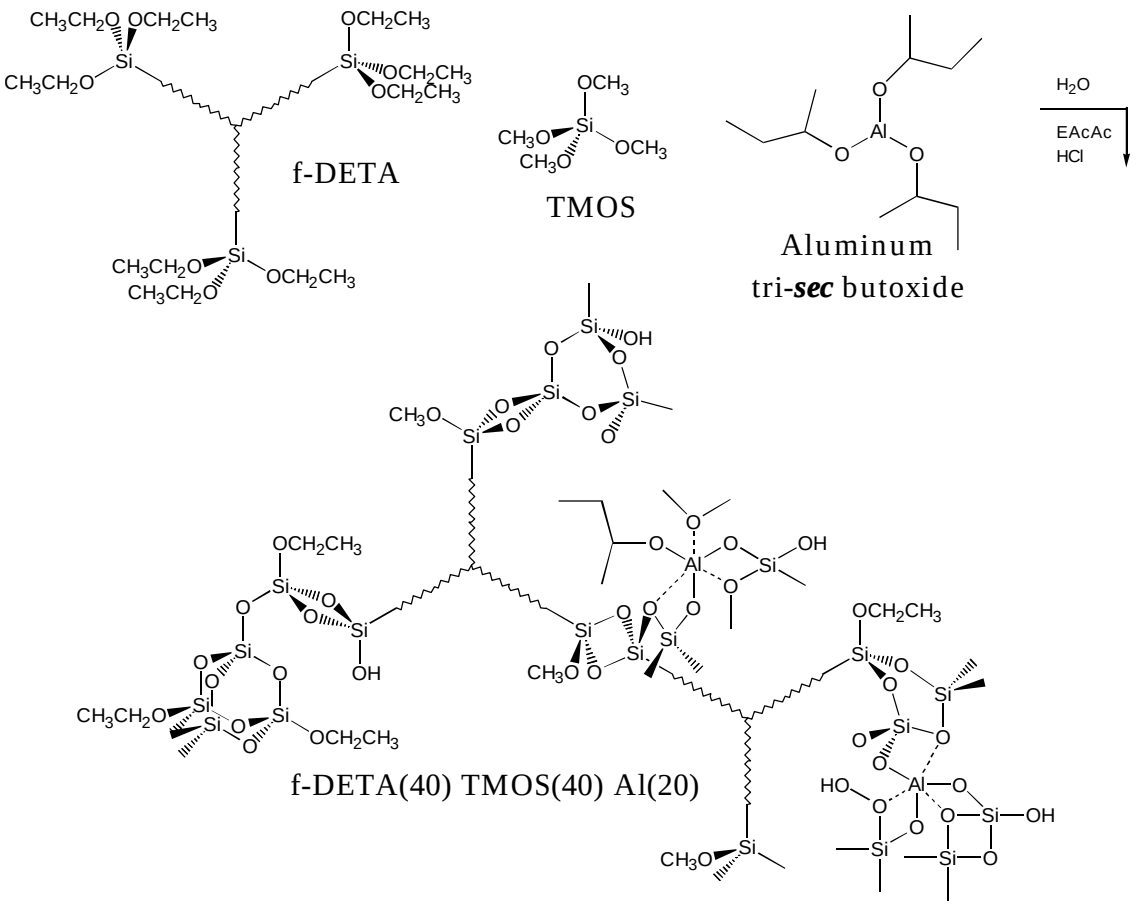

Figure 7. The sol–gel reaction of f-DETA, TMOS, and aluminum tri-*sec* butoxide, forming a coating designated as f-DETA(40) TMOS(40) Al(20). The resulting structure is meant to reflect an infinite network.

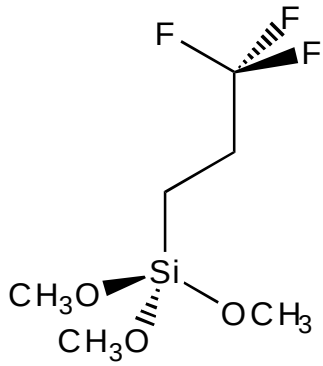

Figure 8. Structure of the fluorinated monomer introduced into the hybrid inorganic-organic abrasion resistant coatings.

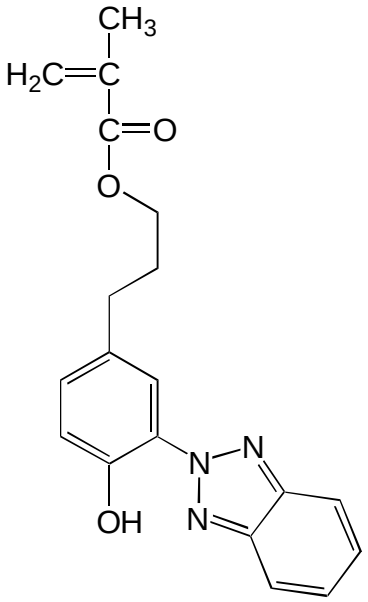

Figure 9. Structure of the u.v. absorbing species, Norbloc 7966.

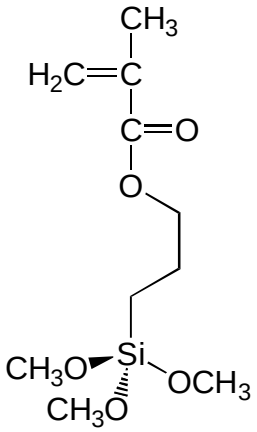

Figure 10. Structure of trimethoxysilylpropyl methacrylate, the linking molecule between the sol–gel network and the Norbloc 7996 u.v. absorber.

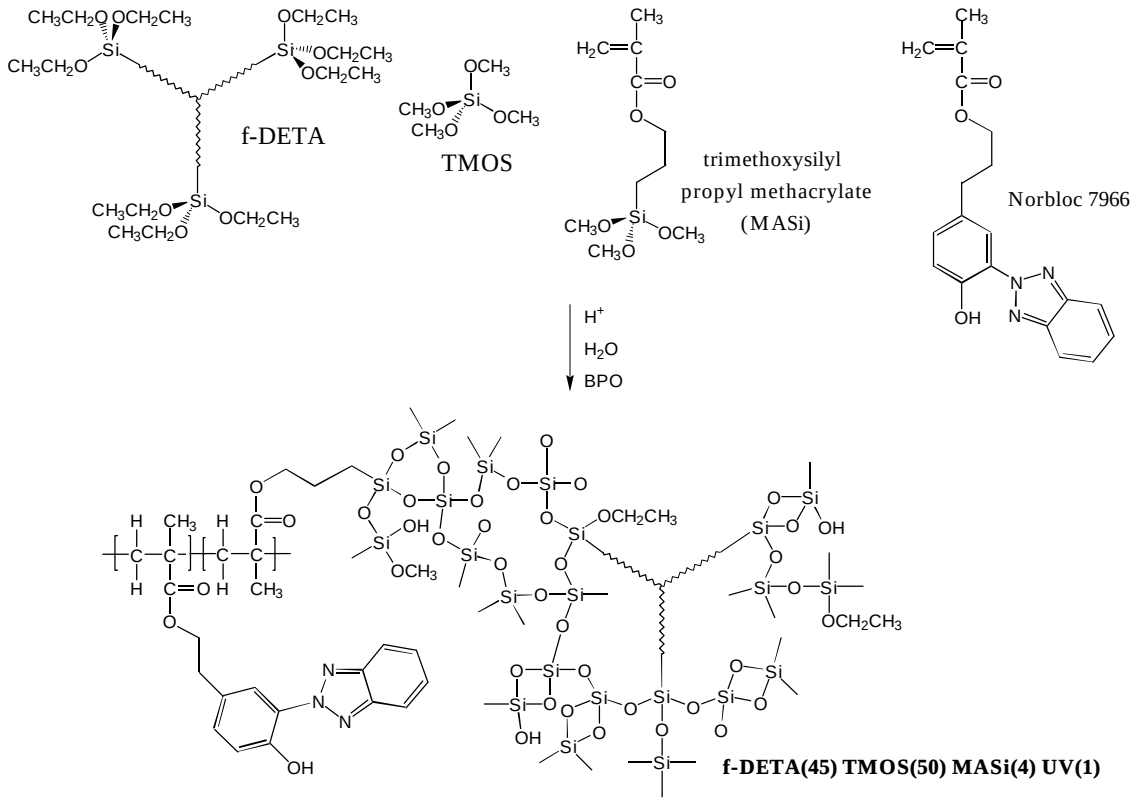

Figure 11. The sol–gel and free radical reactions of f-DETA, TMOS, MASi, and Norbloc 7966, forming a coating designated as f-DETA(45) TMOS(50) MASi(4) UV(1). The resulting structure is meant to reflect an infinite network.

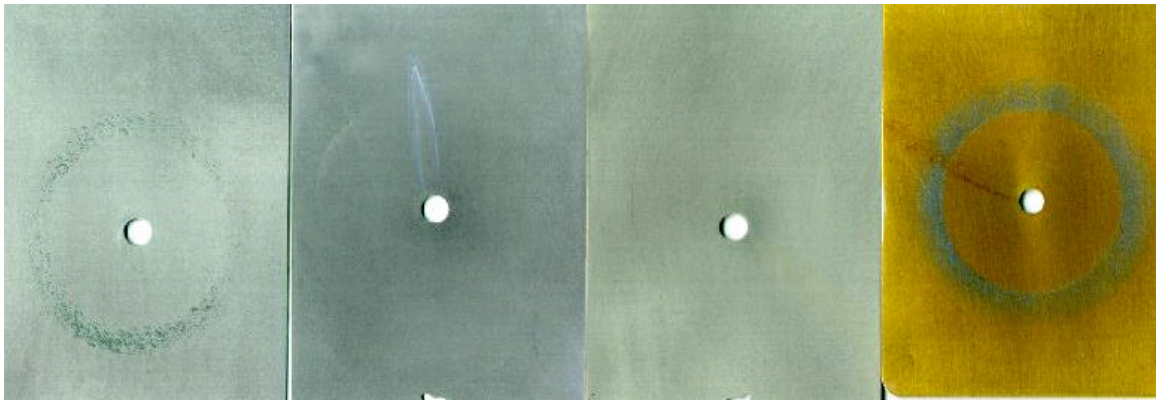

Figure 12. Effect of cure temperature on the abrasion resistance of f-DETA(50) TMOS(50) coatings on aluminum. All samples abraded to 350 cycles. Cure temperatures, from left to right: 75, 125, 175, and 225 °C.

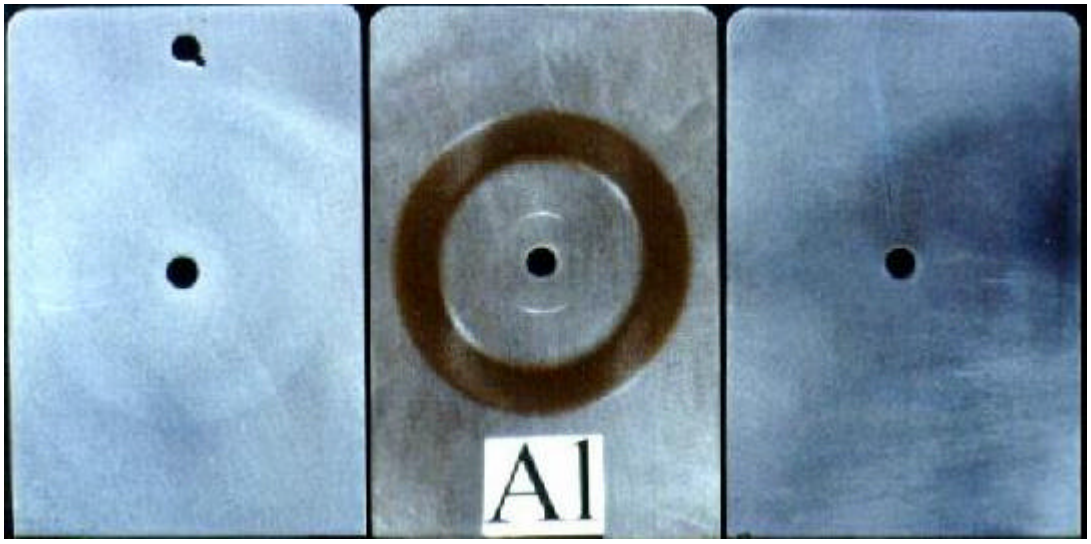

Figure 13. A photograph illustrating coating performance after 350 cycles on aluminum. f-DETA(100) left; Uncoated control, center; f-DETA(50) TMOS(50), right.

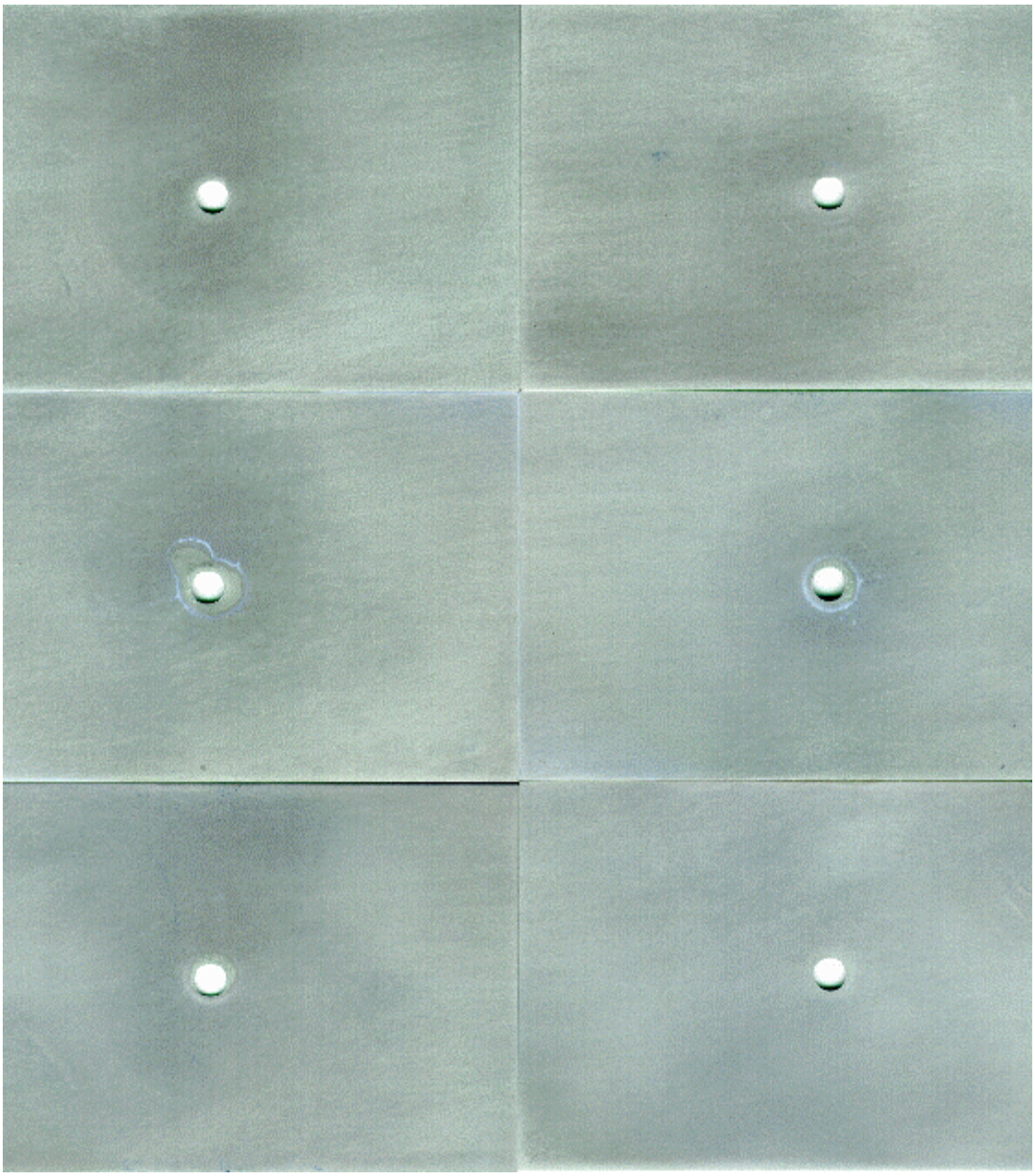

Figure 14. Influence of TMOS content on the abrasion resistance of f-DETA based coatings after 250 cycles. f-DETA(100), top left; f-DETA(80) TMOS(20), top right; f-DETA(70) TMOS(30), left center; f-DETA(60) TMOS(40), right center; f-DETA(50) TMOS(50), bottom left; f-DETA(40) TMOS(60), bottom right.

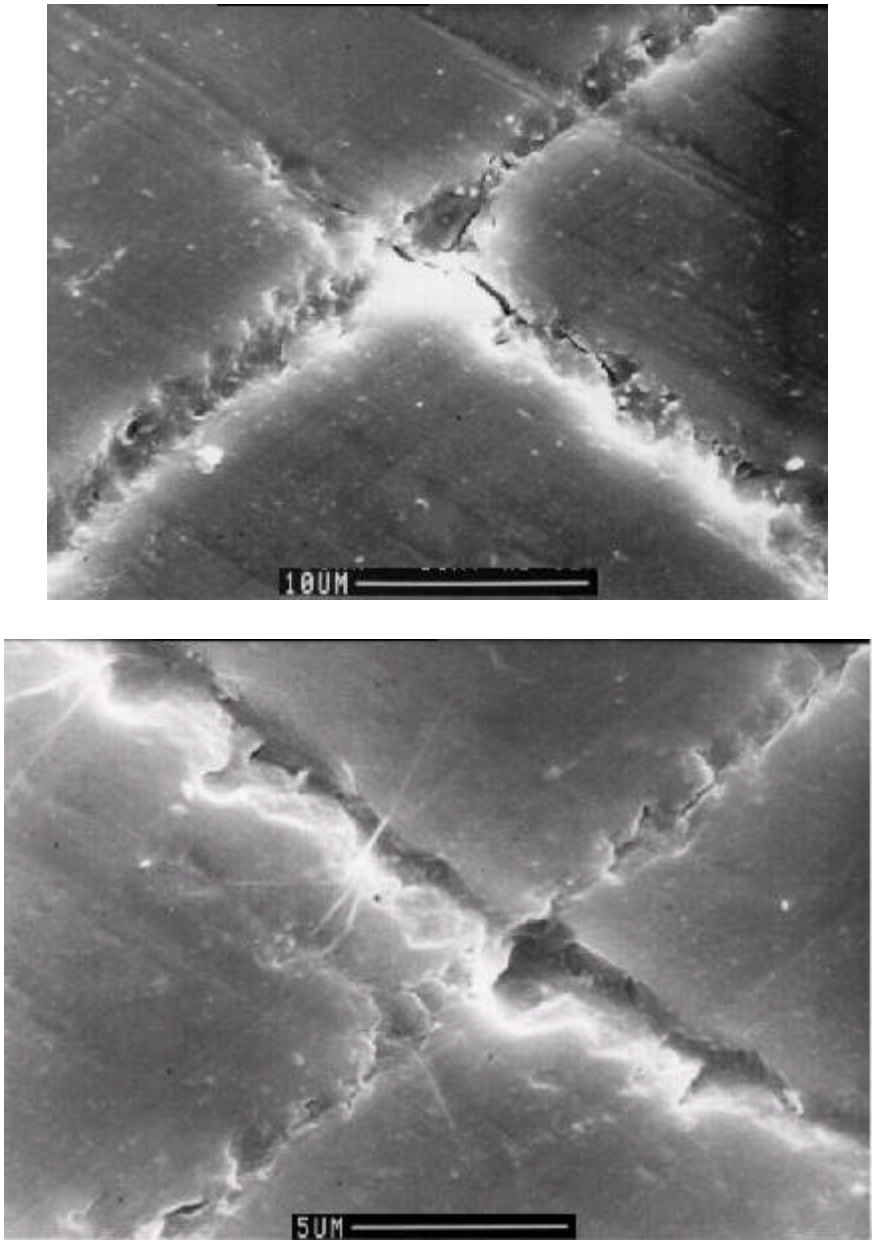

Figure 15. SEM images of part of a wear track in a f-DETA(50) TMOS(50) coating on aluminum after 350 cycles. The images are not of the same area of the coating. 10 and 5 μm markers.

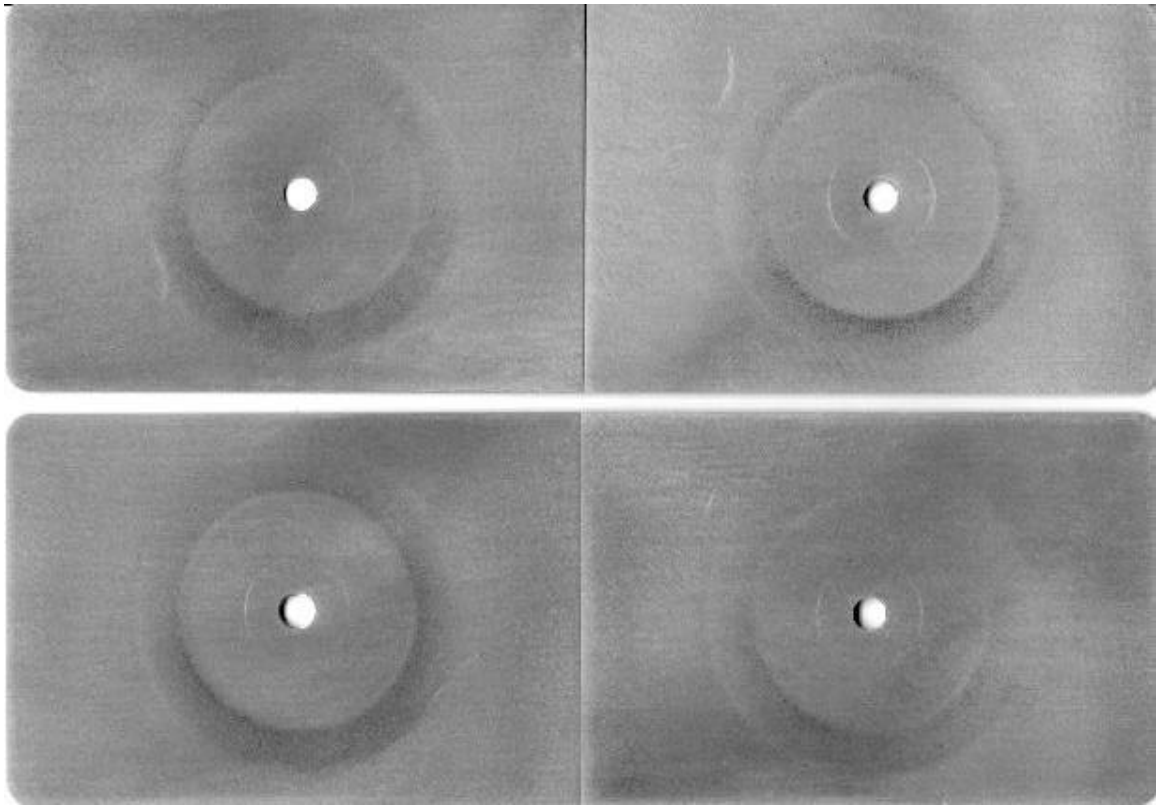

Figure 16. Influence of boiling water treatment on the abrasion resistance of mixed metal alkoxide formulations on aluminum after 100 cycles. TOP: f-DETA(40) TMOS(40) **Al(20)**, dry, left; Boiled, right.
BOTTOM: f-DETA(40) TMOS(40) **Ti(20)**, dry, left; Boiled, right.

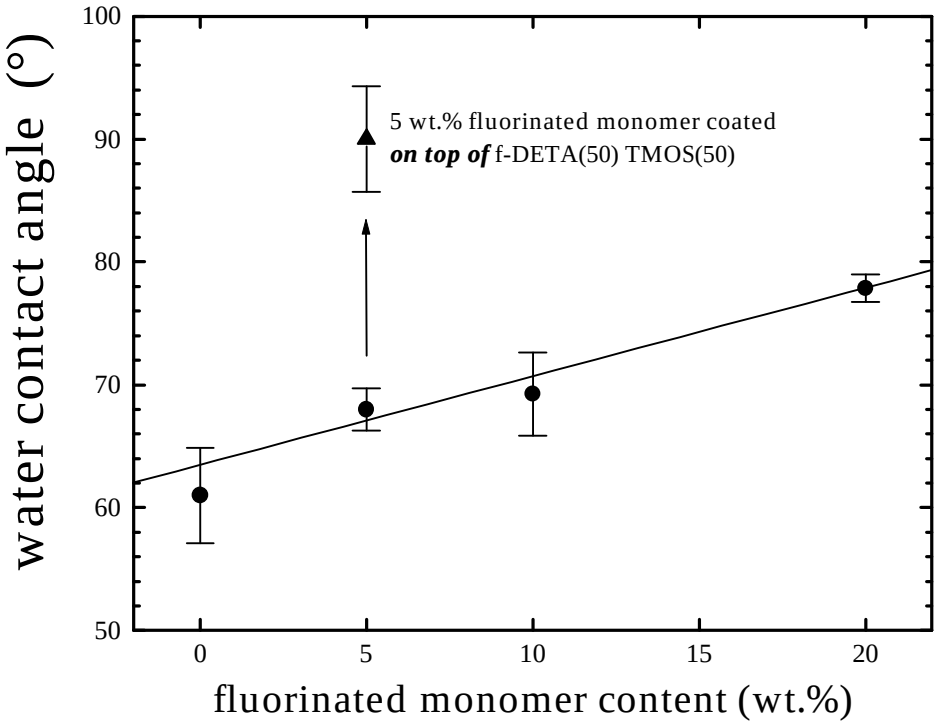

Figure 17. The influence of fluorinated monomer content on the water contact angle of resultant coatings.

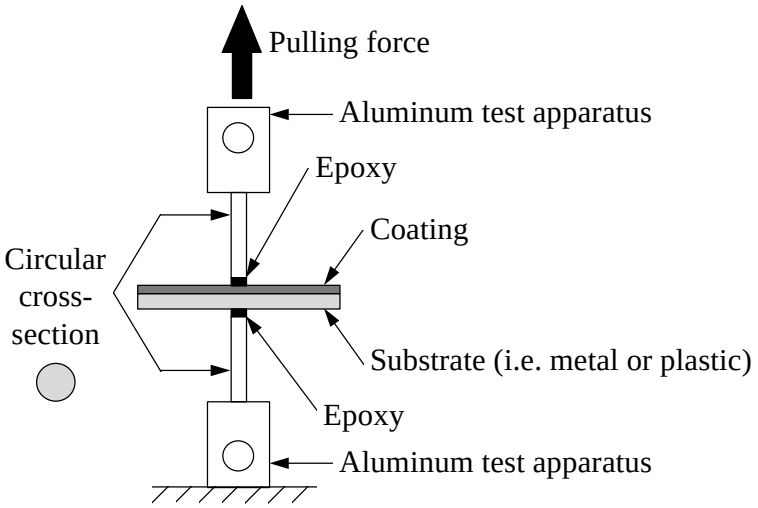

Figure 18. A schematic of the direct pull off testing apparatus used to ascertain a practical value of adhesion between coatings and substrates.

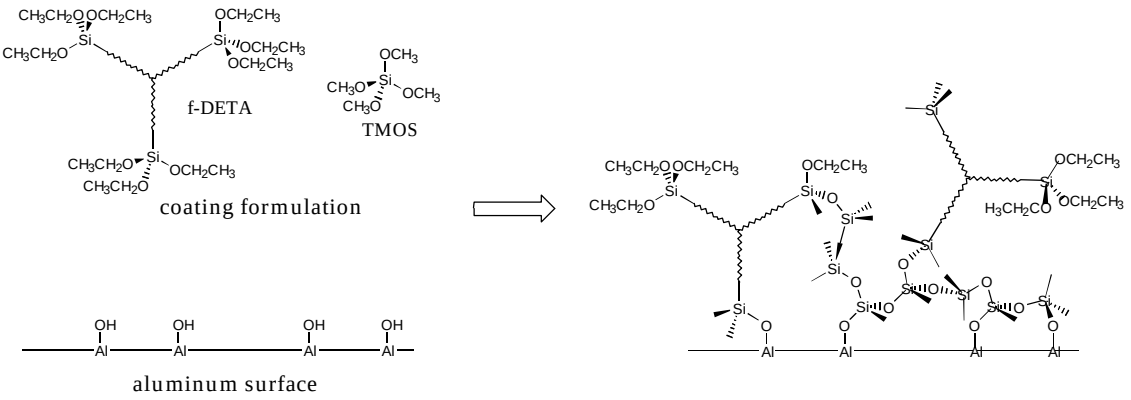

Figure 19. Possible structure at the f-DETA(50) TMOS(50) coating–aluminum substrate interface. Similar structures would exist for other coating formulations and metal substrates as well.

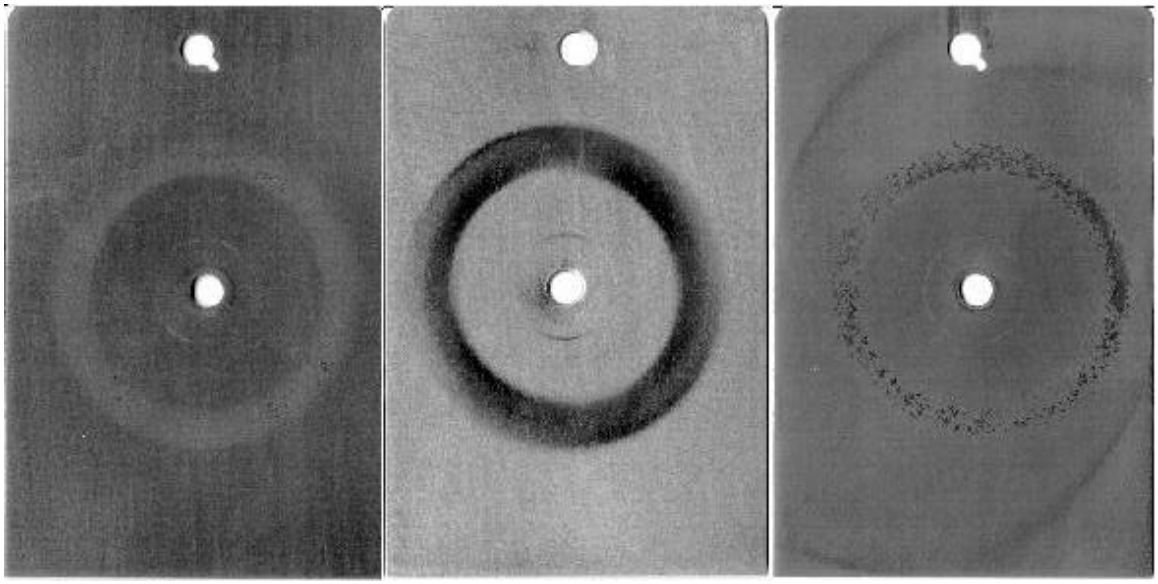

Figure 20. Coating performance after 350 cycles on steel. f-DETA(100) left; Uncoated control, center; f-DETA(50) TMOS(50), right.

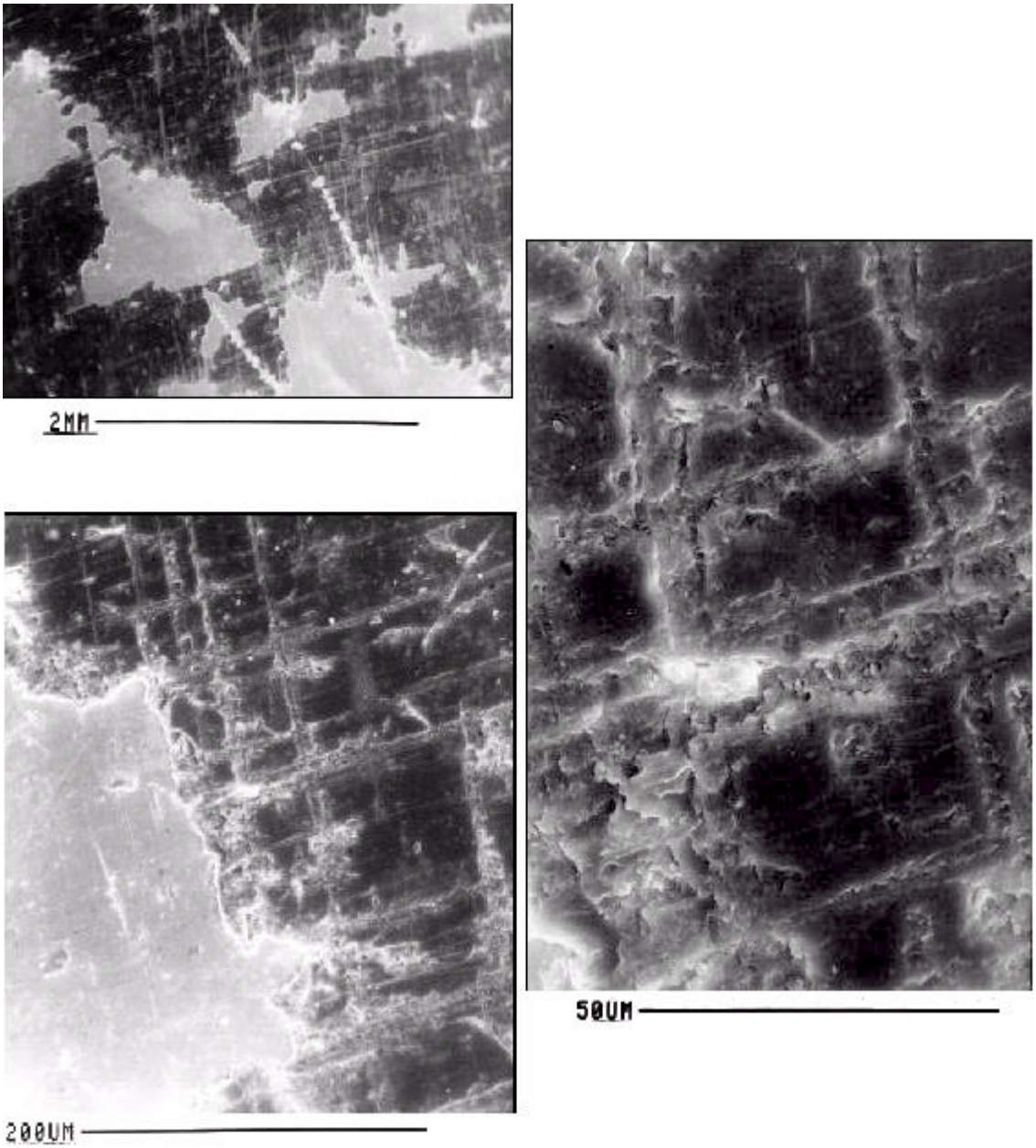

Figure 21. SEM images of an abraded f-DETA(50) TMOS(50) coating on steel after 350 cycles. 2 mm, 200 μm and 50 μm markers.

Figure 22. Comparison of the corrosion resistance of uncoated (left) and f-DETA(100) coated (right) steel. Samples were half immersed in salt water.

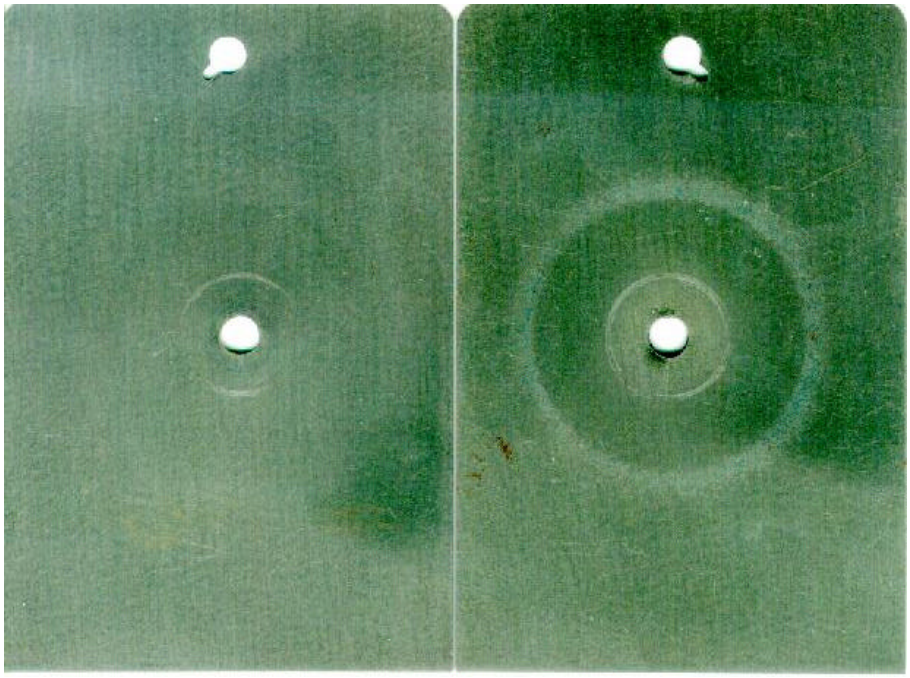

Figure 23. Influence of boiling water treatment on the abrasion resistance of f-DETA(100) on steel after 100 cycles. Dry, left; Boiled, right.

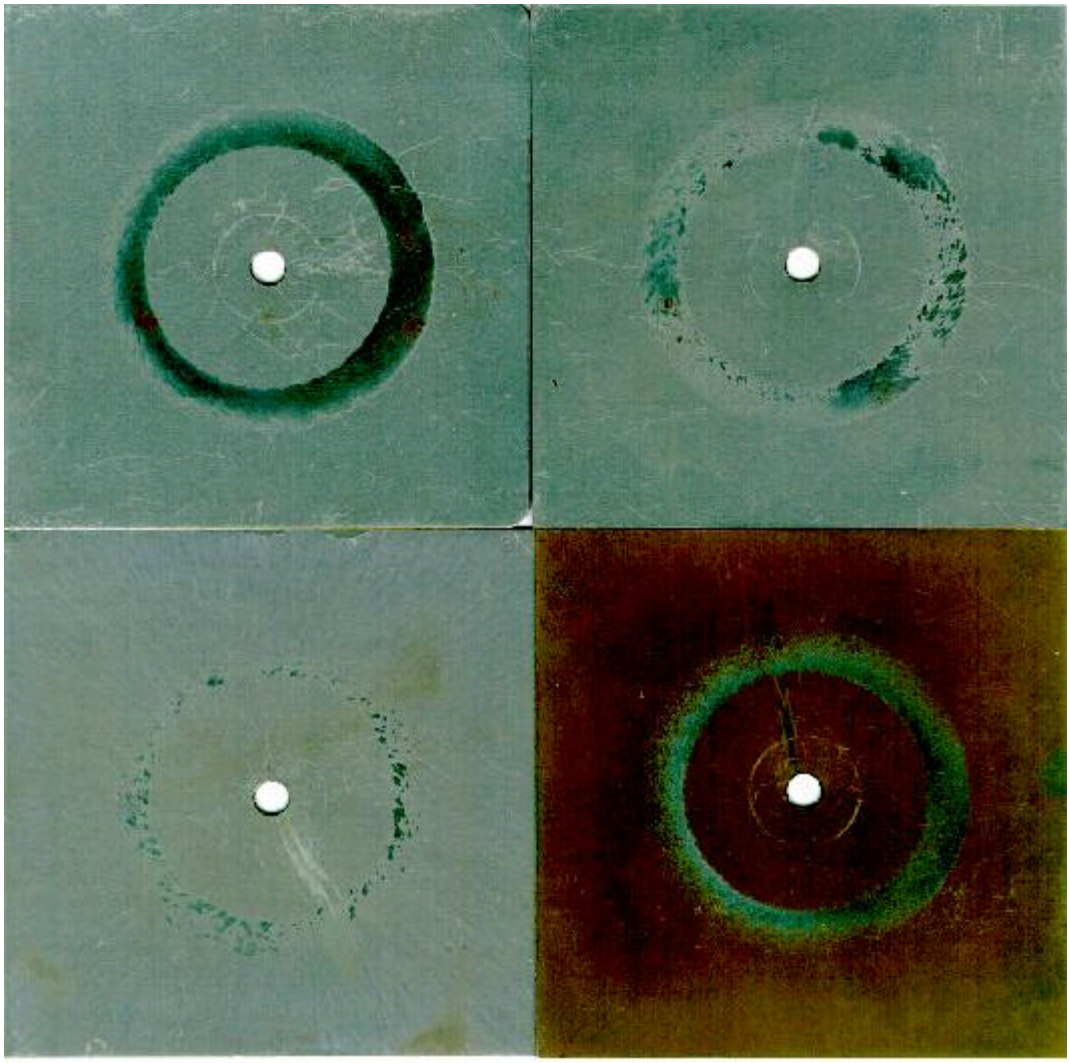

Figure 24. Influence of cure temperature on the abrasion resistance of f-DETA(100) coatings on zinc phosphated steel after 350 cycles. Cure temperature of 75 °C, top left; 125 °C, top right; 175 °C, bottom left; 225 °C, bottom right.

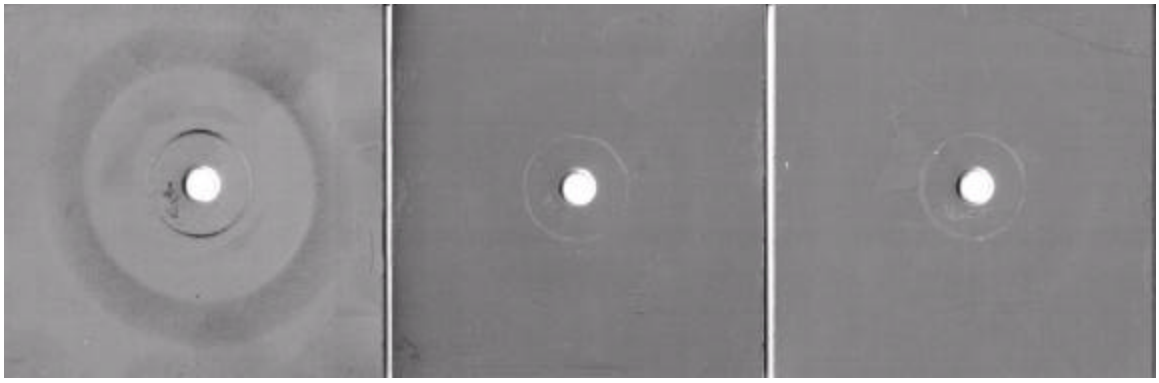

Figure 25. Coating performance on stainless steel substrates after the Taber Abraser test. Uncoated control after 10 cycles, left; f-DETA(50) TMOS(50) coated after 100 cycles, center; f-DETA(50) TMOS(50) coated after 200 cycles, right.

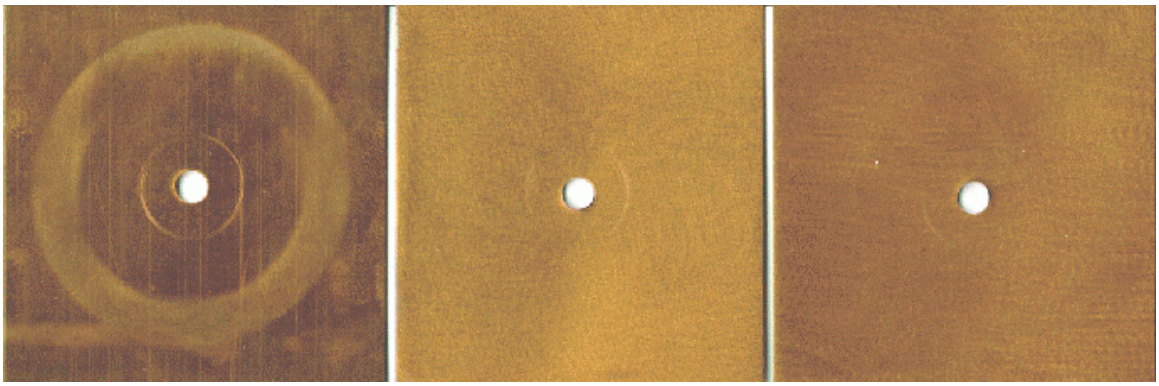

Figure 26. Coating performance on copper substrates after the Taber Abraser test. Uncoated control after 10 cycles, left; f-DETA(50) TMOS(50) coated after 250 cycles, center; f-DETA(50) TMOS(50) coated after ***500 cycles***, right.

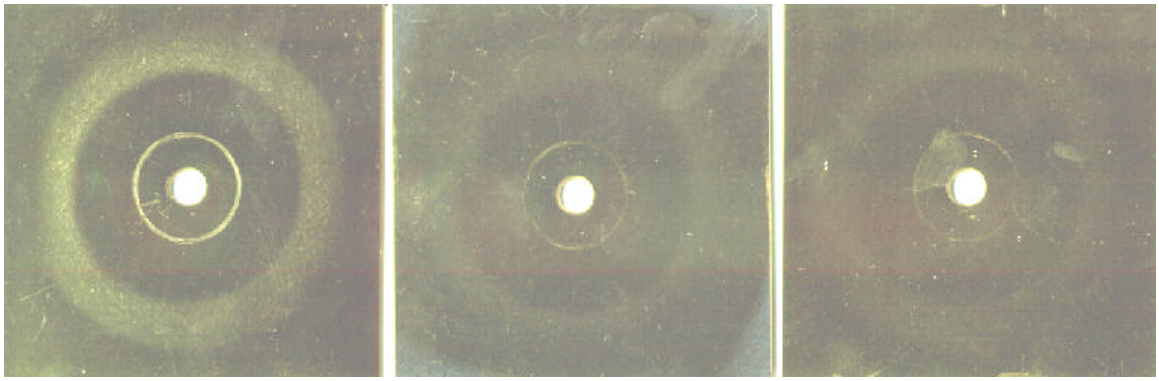

Figure 27. Coating performance on brass substrates after the Taber Abraser test. Uncoated control after 10 cycles, left; f-DETA50-TMOS50 coated after 100 cycles center; f- DETA50-TMOS50 coated after 200 cycles, right.

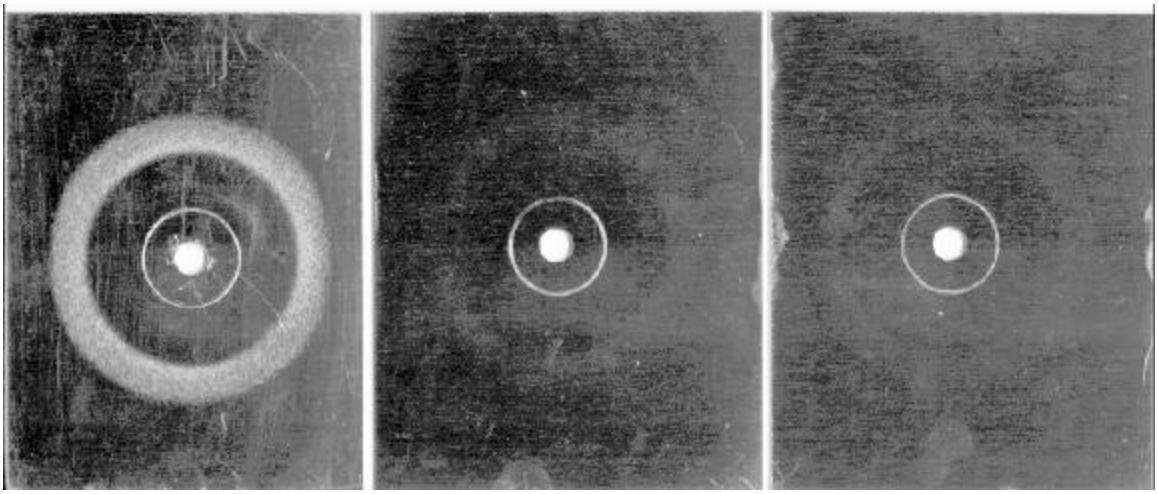

Figure 28. Abrasion test results for polished aluminum substrates. Uncoated control after ***two cycles***, left; f-DETA(50) TMOS(50) coated after 50 cycles, center; and a f-DETA(45) TMOS(50) MASi(4) UV(1) coating after 50 cycles, right.

5.6 References

1 B. Tamami, C. Betrabet, and G. L. Wilkes. *Polym. Bull.*, **30**, 39, (1993).

2 B. Tamami, C. Betrabet, and G. L. Wilkes. *Polym. Bull.*, **30**, 393, (1993).

3 B. Wang and G. L. Wilkes. *J.M.S.–Pure Appl. Chem.*, **A31(2)**, 248, (1994).

4 J. Wen and G. L. Wilkes. *J. Inorg. Organomet. Polym.*, **5(4)**, 343, (1995).

5 J. Wen, V. J. Vasudevan, and G. L. Wilkes. *J. Sol–Gel Sci. Tech.*, **5**, 115, (1995).

6 J. Wen, K. Jordens, and G. L. Wilkes in Better Ceramics Through Chemistry VII: Organic/Inorganic Hybrid Materials, Bradley K. Coltrain, Clément Sanchez, Dale W. Schaefer, and Garth L. Wilkes, ed., *Mater. Res. Soc. Symp. Proc.*, **435**, 207, (1996).

7 C. Sanchez and F. Ribot. *New J. Chem.*, **18**, 1007, (1994).

8 J. Wen (presently with Cabot Corporation). *Personal communication*, 1995.

9 Duncan J. Shaw. Introduction to Colloid and Surface Chemistry, third edition, Butterworths, London, 1980.

10 S. G. Croll. "Adhesion and Internal Strain in Polymeric Coatings" in Adhesion Aspects in Polymeric Coatings, K. L. Mittal, ed., Plenum Press, NY, 1983.

11 A. J. Kinloch, W. A. Dukes, and R. A. Gledhill. "Durability of Adhesive Joints", p. 597 in *Polymer Science and Technology, vol **9B**, Adhesion Science and Technology*, Lieng–Huang Lee, ed., Plenum Press, NY, 1975.

12 J. D. Minford. "Adhesives", p. 135 in Durablility of Structural Adhesives, A. J. Kinloch, ed., Applied Science Publishers, NY, 1983. See particularly figure 3 of p. 150.

13 S. C. Aker. "The Function of Adhesive Primers in Adhesive Bonding of Aircraft Structures", p. 23 in *Appl. Polym. Symp.*, **19**, Processing for Adhesives Bonded Structures, M. J. Bodnar, ed., Interscience Publishers (John Wiley & Sons), NY, 1972

14 A. J. Kinloch. Adhesion and Adhesives: Science and Technology, Chapman and Hall, 1987.

15 K. Jordens and G. L. Wilkes. *PMSE Preprints.* **73**, 290, (1995).

16 Ernest Rabinowicz. Friction and Wear of Materials., John Wiley and Sons, New York, 1965.

17 J. Holling, ed. Principles of Tribology., The Macmillan Press Ltd., London, (1975, 1978).

18 M. Gettings and A. J. Kinloch. *J. Mater. Sci.*, **12**, 2511, (1977).

19 CRC Handbook of Chemistry and Physics, Robert C. Weast, ed., 68th ed., p. B-88, CRC Press, Inc., Fl, 1987.

Chapter 6

Epoxy–Clay Nanocomposites

Abstract

In this study the influence of the incorporation of an organically modified montmorillonite clay into various epoxy adhesives was monitored through the single lap shear experiment. Lap shear specimens bonded with epoxies made with and without clay incorporation were exposed to a boiling water environment for five hours and their lap shear strengths were subsequently determined. Increasing the clay content in the epoxy decreases the lap shear strength, and yields no discernible improvement in the resistance to boiling water. The reduction in the lap shear strength with increasing clay content is due to a decrease in the toughness of the adhesive. Also, the clay particles may act as points of stress concentration. The lack of improvement in the barrier properties is believed to be due to the way in which the clay becomes incorporated into the epoxy adhesive. Instead of the desirable, delaminated (or exfoliated) structure, where the clay sheets are separated and randomized within the epoxy (generating a tortuous path to penetrant molecules), only an intercalated state is achieved.

6.1 Introduction

The main goal of this study was to determine if a specially modified clay could be incorporated into an epoxy adhesive and improve the durability of the epoxy in a bonding situation. Specifically, incorporating such clays into organic polymers has been shown to improve barrier properties.[1-4] This is believed to be a result of the structure formed, namely a delaminated structure (see Part II of chapter 2 concerning polymer–clay nanocomposites literature review for details), which means that the individual clay layers separate and become well dispersed within the polymer matrix generating a tortuous path for penetrant molecules. Since water is known to often rapidly degrade adhesive bonds,[5–7] it was perceived that incorporating the clay into the epoxy matrix might improve the durability of the bond by hindering the diffusion of water through the adhesive layer. However, aside from the delaminated structure, another possible structure exists that is more often formed between organoclays and organic polymers. This is the intercalated structure. In this structure, the polymer molecules insert in between the clay sheets (in the "gallery"[8] regions) in a highly confined conformation, and thus slightly increase the spacing between clay layers. The individual clay sheets tend to remain agglomerated as stacks (typically five or more individual layers), and the long spacings can be monitored by x-ray scattering. Obviously the improvement to barrier properties is expected to be less pronounced for the intercalated structure, due to the non-uniform dispersion of clay and hence the lack of a tortuous path which is present in the ideal delaminated structure.

6.2 Experimental Procedures

6.2–A. Materials

Epon828 was chosen as the liquid epoxy resin for this study due to its wide spread popularity. Its structure is shown in Figure 1. This material has also been referred to in the past as DGEBA, or the DiGlycidylEther of Bisphenol–A, although as can be seen in the figure, the Epon828 variety has between zero and three repeat units (DGEBA

corresponds to zero repeat units). Shell has claimed an equivalent weight of 185-192 g/functionality for this material, and for calculations involved in this work, a value of 188 g/functionality was assumed.

A series of curing agents was employed, mainly the JEFFAMINE® family of liquid primary amine terminated poly(propylene oxide) (PPO) oligomers (Figure 2). The two JEFFAMINE® materials chosen for study here are D400 (equivalent weight 104 g/functionality) and D2000 (equivalent weight 514 g/functionality); the "D" represents "Diamine" (ideally two terminal primary amines) and the number roughly represents the average molecular weight. The true functionality is somewhat less than two for both of these JEFFAMINE®s.* Since both JEFFAMINE®s are diamines (which would lead to a functionality of four in the reaction with epoxy), but their molecular weights are very different, vastly different amounts of each are needed to satisfy stoichiometry with the Epon828 resin. This can easily be seen from the large difference in the equivalent weights of each material. For this reason, a considerably larger amount of the D2000 curing agent is required to react with a specific amount of Epon828 compared to the D400 curing agent. For example, based on 5 g of Epon828 resin, balanced stoichiometry requires 2.75 g of D400, whereas 13.65 g of D2000 would be necessary. This has an important influence on the properties of the final cured network, namely the glass transition temperature.

In many network reactions, the glass transition temperature of the final material is often the temperature at which the material was cured. This is due to the time–temperature–transformation phenomenon described by Gillham,[9] which can briefly be described as follows: At the start of the epoxy reaction, the components are low molecular weight liquids, and hence are well above their glass transition temperatures. As the reaction proceeds and molecular weight increases, the glass transition of the system is also increasing.[10] Often the glass transition temperature of the system can reach the cure temperature, at which point vitrification occurs – the system becomes

* *More detailed information such as functionality and molecular weight of the JEFFAMINE® materials can be found in Table 1 of Chapter 3.*

glassy, loses mobility and as a result (in most cases) the reaction can no longer proceed. However, this does not occur for the epoxy system cured with D2000 studied here. This is due to the chemical nature of D2000, namely that it is a PPO oligomer. The glass transition temperature for high molecular weight, homopolymeric PPO is ≈ –78 to –73 °C.[11—14] Although the D2000 is a low molecular weight form of PPO (≈ 33 repeat units), it is still expected to have a glass transition in reasonable proximity to that of high molecular weight PPO. In addition, a rather large proportion of D2000 is required to satisfy stoichiometry with the Epon828 resin as mentioned above, and hence the D2000 is likely to dominate the final properties of the cured epoxy system. Specifically, an epoxy system based on Epon828 and D2000 would be expected to have a sub–ambient glass transition temperature. This is indeed the case (–37 °C). This behavior is in contrast to D400, which has a very short length of PPO (≈ 5–6 repeat units), and is in lesser proportion to the Epon828. Hence the glass transition temperature of an Epon828–D400 system is higher (45 °C) than that of PPO homopolymer.

One final curing agent was employed in this study, known as Epicure 3140, from Shell. It will be referred to as 3140 throughout this document. The structure of this curing agent is not revealed by Shell, however it is a polyamide amine (approximate structure in Figure 3), along with a mixture of other small molecules such as triethylenetetramine. Its equivalent weight is ≈ 375 g/functionality. Reacting Epon828 with this curing agent leads to the highest (and broadest due to the multiple components) glass transition temperature of the three systems, at roughly 105 °C. Hence a wide span of glass transitions was probed with the three curing agents used in this study (D2000 < D400 < 3140).

The montmorillonite organoclays employed in this study were obtained from two different sources. The first, from Southern Clay Products, is labeled organoclay PS3 (or just PS3 for the remainder of this document). It is a (tallow) *quaternary* amine exchanged montmorillonite, where the exchange molecules have primarily 18 carbon member chains. This organoclay by itself has a long spacing of ≈ 21 Å. A second clay was obtained from Nanocor, labeled C18–AMS and is a different form of

montmorillonite. This clay was exchanged with a protonated *primary* amine, namely $CH_3(CH_2)_{17}NH_3^+$ (18 carbon members in the alkyl chain and hence the C18 designation). It has a reported long spacing of 18 Å.[15,16]

Lap shear specimens were constructed of ½ hard steel panels (ASTM D609, type 2) which measured 1×4 inches, and were approximately 1.5 mm thick. They were ground on one side (by the manufacturer) and after washing with acetone, this side was used in the adhesive bond. The substrates were purchased from the Q Panel Company.

6.2–B. Epoxy formulation

All epoxy systems were made from the liquid reactants with balanced stoichiometry. The Epon828 resin was first mixed with the desired curing agent (at 75°C in some cases to reduce viscosity and improve the mixing process) and allowed to react for a few minutes. The mixture was then degassed in a vacuum oven. Then the reacting liquid was either poured into a mold to make specimens for x-ray analysis and calorimetry or used immediately to make single lap shear specimens. Lap shear specimens were made on a specially designed jig to minimize variations in adhesive layer thickness (generally near 0.6 mm) and uniformity. Thermal curing was carried out according to the following schedule, unless otherwise noted:

- 75 °C for 3 hours
- heating at 5° / min to 125 °C
- 125 °C for 3 hours

If an epoxy–clay nanocomposite was to be made, the preparation was slightly modified. First the clay was added to the Epon828 resin and heated to 75 °C, where it was thoroughly mixed. The mixture was then sonicated at this temperature in an attempt to break up the agglomerated clay particles. Sonication was accomplished with a Tekmar Sonic Disruptor model TM300 equipped with a microtip. The sonication process involved periods of rest to prevent excessive heating of the medium (one second on, one second off). Then curing agent was added, mixed thoroughly, and the mixture was degassed and utilized to generate samples as before.

6.2–C. Characterization techniques

An Instron model 4400 with a 100 kN load cell was employed for breaking the lap shear specimens. In most cases, 5 to 6 specimens were tested for each condition. The testing procedure was similar to that described by ASTM D1002. The adhesive bond thickness was on the order of 0.6 mm for all samples. Since the epoxy was applied as a liquid, samples inevitably contained some amount of spew. Since spew can carry load and hence influence the outcome of a lap shear experiment,[17,18] the excess was gently removed from the samples with a file before testing. Lap shear specimens were stored in a desiccator until analysis. Some lap shear specimens were exposed to a boiling water treatment to probe the influence of clay on the durability of the adhesive bond in a hot–wet environment. These samples were fully immersed in boiling, deionized water for five hours. Following this they were allowed to dry at laboratory conditions overnight before being tested in the Instron on the following day.

Tensile stress–strain experiments were performed on a model 4400R Instron with a 1 kN load cell. The load cell was calibrated with a 2–kg standard, and ultimate loads never exceeded 8–kg. Tests were conducted at lab conditions with a crosshead speed of 2 mm/min. Specimens were stamped out of free standing films with a dogbone die. Statistical averages of the stress–strain parameters were generated based on the six to ten specimens tested for each condition.

The nanocomposite structure of the epoxy materials was probed using small angle x-ray scattering (SAXS). Nickel filtered, Cu$K\alpha$ radiation (1.542 Å)[19] was generated by a Philips model PW1729 and was employed along with a Kratky camera and an M. Braun one dimensional position sensitive detector. Data will be presented in some cases in raw form, without calculation of absolute intensities, and in other cases absolute intensities will be measured through the use of a Lupolen working standard.[19] Data will therefore be presented either as “counts” (not absolute, but related to intensity) or “intensity” (absolute) versus $s = \frac{2}{\lambda}\sin\theta$, the magnitude of the scattering vector, where λ is the x-ray wavelength, and θ is one half of the radial scattering angle.

The slit–smeared data were not corrected in any manner. If any correlation length is present, it will appear as a peak at a certain value of s^*. If we label this value as s^*, then the correlation distance is roughly given by $1/s^*$.† This distance will correspond to the long period, or long spacing of the nanocomposite as defined in Chapter 6 (briefly, one clay layer and one gallery region).

A Philips model 420T transmission electron microscope (TEM) was employed at 100 kV for probing nanocomposite structure at high magnification. The results will be compared to those obtained with SAXS.

Differential scanning calorimetry (DSC) was achieved with a Seiko DSC 220C at a heating rate of 20 K/min under a nitrogen atmosphere. Samples typically weighed between 5 and 10 mg.

Water uptake experiments were performed on five samples for each formulation for statistical purposes. Rectangular bar samples (5 × 1.3 × ≈ 0.2 cm) were submerged in de–ionized water (in a polystyrene petri dish) and taken out at various intervals to measure the mass, followed by immediate submerging of the samples again. From this a percent mass uptake was calculated along with a standard deviation. Measurements were made over a period of more than 100 days.

6.3 Results and Discussion

6.3–A Intercalated Hybrids of the Organoclay with Individual Epoxy Components

The first step was to explore the properties of the clay when mixed individually with the epoxy components. The resulting structure was probed using SAXS, where a long spacing can be measured. The PS3 organoclay itself shows a very subtle shoulder in the SAXS curve near 21 Å, and the C18–AMS clay has the spacing reported by the manufacturer of 18 Å. These values are similar to other reported organoclay long

† *It is realized that smearing causes a shifting of the scattered radiation to smaller* s, *and hence* $1/s^*$ *would be larger than the true size of the correlation. These effects are ignored in the present chapter since the important factor is whether or not a correlation distance exists, rather than the absolute spacing.*

spacings.[15,16,20,21] Blending the Epon828 resin with the PS3 organoclay (the clay being the minor component, ≈ 5 to 20 wt.% of the total) leads to a spacing of 37 Å. This increase from 21 Å to 37 Å represents the intercalation of the Epon828 molecules into the clay galleries. The structure is identified as intercalated due to this slight increase in spacing, and is not considered delaminated since such a structure should have no correlation length in the SAXS region if the clay sheets are well dispersed and randomized.

Mixing the D400 curing agent with the PS3 organoclay leads to a 41 Å spacing, again evidence of an intercalated structure. The spacing is different from that of the Epon828–PS3 mixture, due to the different size and conformation of the D400 molecules within the gallery regions (compared to the Epon828 molecules). The D2000 material, although a much longer chain than the D400, intercalates the PS3 organoclay and leads to a 42 Å spacing. Since this spacing is essentially the same as that for the D400 intercalated composite, a different molecular orientation and/or conformation of the D2000 chains is therefore conjectured to take place.

The 3140 curing agent also forms an intercalated structure with the PS3 organoclay, however this leads to a much larger spacing, namely 55 Å. Hence all three curing agents and also the epoxy resin itself will individually intercalate into the gallery regions of the PS3 organoclay. The SAXS curves for the PS3 organoclay, the Epon828–PS3, and the curing agent–PS3 mixtures are shown in Figure 4. The slit smeared long spacings for all formulations, including the cured epoxies to be discussed next, are listed in Table 1.

6.3–B Intercalated Hybrids of Cured Epoxy Systems

When the epoxy resin, PS3 organoclay, and the curing agent are all mixed together, an unexpected spacing results. Instead of an exfoliation or delamination event, where the reacting epoxy would open up the clay sheets during the molecular weight build-up, an apparent preferential intercalation of only the Epon828 resin occurs. The reason why intercalation of only the Epon828 resin is the suspected event is due to the final spacing of cured epoxy systems, which takes on a value of ≈ 36–38 Å for *all epoxy*

formulations (essentially equivalent to the 37 Å spacing of Epon828 and PS3 organoclay intercalated composite, see Figure 5 and Table 1).

Figure 6 shows a transmission electron micrograph of an Epon828–D400–PS3 hybrid material. Note that the clay sheets still maintain a fair amount of order (regular stacking) but they are separated slightly by the intercalated molecules. This is a typical morphology observed for an intercalated nanocomposite.[212223,24] The SAXS curve in Figure 5 with the 36 Å spacing corresponds to the same material in the micrograph of Figure 6. However, the clay is not found in high concentrations throughout the entire sample; since only ≈ 5 wt.% was incorporated into this sample, most of the bulk is exclusively epoxy (i.e. Figure 6 is not representative of the entire sample, but rather a local area where clay is present).

6.3–C Influence of Clay on the Glass Transition Temperature of Cured Epoxy Systems

The three different curing agents generate cured epoxy systems with widely varied glass transition temperatures. This has been observed by DSC, as shown in Figure 7. The D2000 curing agent leads to a cured epoxy with the lowest glass transition temperature, at ≈ –37 °C, followed by the D400 curing agent, at ≈ 45 °C, and finally the highest from the 3140 cured system, at ≈ 105 °C. Hence at room temperature one epoxy is above its glass transition temperature, while the other two are below.

An important concern was the possible influence of the incorporated clay on the glass transition temperature of the cured epoxies. The DSC curves for a series of Epon828–D400 cured epoxies with varied PS3 organoclay content (and one formulation with 5 wt.% C18–AMS) are shown in Figure 8. Note that no significant difference in the location of the glass transition (represented by the vertical line at 45 °C) is evident for the range of 0–20 wt.% clay. Any small deviations are likely due to slight mismatch in the stoichiometry due to weighing errors made by the author. This also holds true for the other two epoxy systems (Figure 9 and Figure 10). Hence the bulk of the epoxy material is not influenced by the clay, at least from the standpoint of calorimetry. In contrast, Gianellis et. al report[25] the absence of a calorimetric glass transition for an

intercalated atactic poly(styrene)–montmorillonite composite (undisclosed weight fraction of clay), implying that the confined polymer chains cannot undergo a glass to rubber relaxation. However, this author's interpretation of their data is in contrast to this, as their DSC trace (Figure 3 of their paper) appears to display a glass transition at ≈ 100 °C for the intercalated nanocomposite. Also included in their plot is a DSC trace of a physical mixture of the clay and polymer (a control sample that does not have an intercalated structure) which shows a glass transition at approximately the same temperature (and appears to have the same ΔC_P, although this is difficult to determine from the data). However, the DSC trace for this sample also displays the recovery of some relaxed enthalpy due to physical aging of the polystyrene before the DSC scan. Unfortunately, all of their DSC data are shown over a brief interval of temperature, from 100 to 120 °C, which makes the glass transition difficult for the reader to examine quantitatively.

Also extractable from the calorimetry data is the relative content of the clay in the intercalated composite. Although this is a known quantity for all of the samples, it provides a good "check" of the data. Since the only the epoxy portion of the intercalated composite is undergoing the glass transition, then the magnitude of the transition should be directly related to the weight fraction of epoxy in the composite. The magnitude of the glass transition is quantified through the change in heat capacity across the glass transition, ΔC_P. It follows then, that the weight fraction of epoxy in the composite, w_{Epoxy}, is given by:

$$w_{Epoxy} = \frac{\Delta C_P(Composite)}{\Delta C_P(Pure\ Epoxy)} \tag{1}$$

where $\Delta C_P(Composite)$ corresponds to the nanocomposite data, and $\Delta C_P(Pure\ Epoxy)$ corresponds to the data for the epoxy without clay. For the data evaluated in this chapter, the absolute values of heat capacity were not measured. However, the value of w_{Epoxy} can be determined from the basic heat flow data generated by the DSC. The results are fairly close to the actual weight fractions, as seen in Table 2.

6.3–D Influence of Clay on the Lap Shear Strength of Epoxies

The most important property of the epoxy systems would be the performance in the lap shear experiments. Since the Epon828–D400 system has a glass transition temperature that is just above room temperature, physical aging during sample storage at room temperature is a valid concern. It is well known that physical aging leads to embrittlement (increase in modulus, etc.),[26] so to avoid having this phenomenon influence the lap shear measurements, these samples where reheated to 75 °C and held there for 30 minutes, followed by rapid quenching to lab conditions just prior to lap shear testing.

The Epon828–D2000 epoxy had extremely low lap shear strengths (< 200 psi) due to the fact that this material was rubbery at the testing conditions. This is not surprising since 73 wt.% of this epoxy formulation is the D2000 component (and recall that the D2000 is a low T_g poly(propylene oxide) oligomer). The Epon828–3140 epoxy system displayed a relatively high lap shear strength (≈ 2800 psi), but the Epon828-D400 epoxy proved to have the highest strength (≈ 3450 psi). It was found that adding clay to this formulation actually decreased the lap shear strength, which was also true for the Epon828–3140 system. The Epon828–D2000 system showed no significant difference in the lap shear strength for 0 and 5 wt.% clay incorporation. It might be expected that an increase in the lap shear strength would be observed for this system since the epoxy is above its glass transition at the testing conditions. The clay would likely act as a reinforcing filler in this material, thereby increasing the stiffness.[27] Often, the Guth–Smallwood equation[28,29] has been employed for rubbery materials to estimate the ratio of filled to unfilled moduli E_f/E_0 as a function of the *volume* fraction of reinforcing filler f_f:

$$\frac{E_f}{E_0} = 1 + 2.5f_f + 14.1f_f^2 + \cdots \qquad (2)$$

This equation is s modification of the Einstein equation[30] for the enhancement in the viscosity of fluids containing a low concentration of small spherical particles. For the

very small amount of clay employed in the Epon828–D2000 material (5 wt.%, which would translate to a smaller value on a volume basis), very little increase in the modulus would be anticipated from equation (2).

Boiling water tests have only been performed on the Epon828–D400 and Epon828–3140 cured epoxies of varied clay content. Unfortunately, the clay does not seem to provide a sufficient barrier to the boiling water to increase the durability of the bonds. Figure 11 shows the lap shear strengths of the Epon828–D400 and Epon828–3140 cured epoxy systems (both dry and after the boiling water test) as well as the Epon828–D2000 formulations (dry conditions only). It can be seen from this plot that the dry lap shear strengths of the Epon828–D400 and Epon828–3140 decrease with increasing clay content. This is certainly not a desirable result. However, all hope was not lost until the boiling water tests were performed. Alas, the incorporated clay also does not impede the boiling water from degrading the bond. It can be seen that the boiled Epon828–D400 formulation without clay has the highest lap shear strength of all the boiled Epon828–D400 samples which contain clay. Hence the major goal for this project, to improve the hot-wet durability of epoxies by incorporating clay, was not obtained. In such a situation it is necessary and important to understand why.

Adding clay to any of the epoxy formulations can have a number of effects. It is possible that adding clay to the liquid epoxy changes the flow properties and surface free energy of the adhesive and hence affects the wetting and spreading of the mixture onto the lap shear substrates. This can influence the strength of the bond, as poor wetting and spreading generally lead to adhesive failure. However it should be noted that in general (but not for every case), the formulations without clay failed adhesively, while the clay formulations tended to fail cohesively. The cohesive failures were obvious since adhesive remained on both substrates of the lap shear specimen. The adhesive failures displayed a one clean substrate and one possessing the adhesive layer. Cohesive failure of the clay containing specimens implies that the clay leads to a reduction in the fracture energy, or energy required to cause failure in the adhesive within the lap shear specimen. This is indeed the case. This has been confirmed by

tensile stress–strain (σ_0–ε) experiments performed on free films of epoxy. It is duly noted that tensile σ_0–ε experiments do not provide direct quantitative data which can be applied to lap shear experiments (due to the difference in the nature of the deformation), however qualitative support is expected.* This aside, Figure 12 shows the tensile σ_0–ε data for Epon828-D400 and Figure 13 shows the same system with 5 wt.% PS3.† Note the drastically different behavior. The material with no clay shows a distinct yield point, whereas the sample with 5 wt.% clay is brittle and does not. Most important to the current discussion is the toughness values (shown in Figure 12 and Figure 13 which also contain the other σ_0–ε parameters of Young's modulus *E,* and yield stress and strain, σ_y and ε_y). The clay containing sample, although having a slightly higher modulus, has a value of toughness (0.45 MJ/m^3) that is roughly one fourth of the value for the material without clay (1.82 MJ/m^3). Hence the observed decrease in the lap shear strength with increasing clay content is due to a reduction in the cohesive strength or toughness of the adhesive. This is believed to be due to the clay acting as areas of stress concentration.

Another possible effect is a disruption of stoichiometry between the Epon828 resin and the curing agent, caused by the presence of the clay. If the Epon828 is the preferred intercalation molecule for the clay, then it can actually displace any curing agent molecules from the clay galleries. This is a plausible conclusion from the SAXS data, which shows the same value of correlation length (≈ 36 to 38 Å) for all cured epoxy systems as the Epon828–PS3 mixture. It follows then that these intercalated Epon828 molecules may not be readily accessible for reaction with the curing agent due to concealment by the clay sheets, thereby leading to improper stoichiometry (excess curing agent) in the bulk. As is well known, unbalanced stoichiometry leads to lower molecular weight, or perhaps network imperfections such as dangling ends. This

---

* *In other words, the quantitative value of the lap shear strength for a sample which fails cohesively is not expected to be the same as the quantitative value of toughness determined from a separate tensile test.*

† *Stress–strain data for systems containing 10 wt.% and more clay could not be easily obtained. This is due to the paste–like consistency of these formulations, which generally lead to films of non–uniform thickness making samples unsuitable for mechanical testing.*

would lead to lower lap shear strengths and perhaps lower glass transition temperatures. Although the lap shear strengths certainly decrease with increasing clay content, the glass transition temperatures of the cured networks are essentially unaffected by the amount of clay present (recall Figure 7 through Figure 9).

Another important consideration is the structure of the clay composite. The desired structure to maximize the barrier properties would be the delaminated structure. As the SAXS results proved, all of the PS3 formulations possess intercalated structures. This structure is not expected to produce as tortuous a path for diffusing water as would the delaminated structure. Hence adding clay to the epoxy formulations is also not expected to greatly enhance the barrier properties of the adhesive layer, particularly at the low clay loadings employed in this study. This has been confirmed by simple water uptake experiments, where Epon828–D400 epoxy systems of varied PS3 content were soaked in de–ionized water over a long period while measuring the mass uptake of water. As can be seen in Figure 14, there is no drastic difference in the barrier properties between neat Epon828–D400 and various clay containing systems (5, 10, and 20 wt.% PS3). In fact, if any trend is to be noted from this plot, it is that the water uptake *increases* with increasing clay content. Due to the rather large magnitude of the error bars in this plot, this trend is not strongly supported. However, such a trend does support the lap shear results.

6.3–E Influence of Varied Formulation Procedures on the Resulting Structure of the Nanocomposites

In an attempt to generate the desirable delaminated nanocomposite structure, many different formulation procedures were employed. Various cure schedules were attempted, the organoclay was added to the epoxy at different stages, sonication was employed to aid in breaking up clay agglomerates, and a second form of clay (C18–AMS) was utilized.

As previously mentioned, the Epon828 appears to be the preferred intercalation molecule for the PS3 organoclay. The majority of the epoxy–PS3 nanocomposites discussed up to this point were prepared by first mixing the clay with the Epon828

resin, before adding curing agent. It may then be argued that perhaps first mixing the clay with curing agent, then adding the epoxy resin would be a possible method for preventing the intercalation of only the Epon828. Perhaps this would allow ample time for the curing agent to form an intercalated composite, and once the fresh Epon828 is added the immediate reaction could prevent any displacement of the curing agent molecules from the clay galleries. However, this is not the observed result, which has been proven by the experimental data shown in Figure 15. First, two mixtures were prepared, one containing D400 and PS3, the other containing 3140 and PS3. These two materials generated the SAXS curves shown on the left hand side of Figure 15. Both show intercalation of the curing agent components, just as the seen previously in Figure 4 (correlation lengths of 41 and 55 Å). Taking these two mixtures, and adding separately to each a stoichiometric amount of Epon828 and curing at 150 °C lead to the SAXS curves on the right hand side of the figure. This led to nanocomposite structures with roughly the same spacing for each material, ≈ 36 to 38 Å. This is good evidence for the displacement of curing agent by the Epon828 resin. This could be better proven by a real–time SAXS experiment where the entire dynamic process could be monitored, i.e. the 55 Å peak should diminish as a ≈ 38 Å appears and grows. This would require a high intensity x-ray beam such as that generated by a synchrotron source.

Other methods and cure temperatures were attempted, including a previously described hot–mold casting method,[31,32] all with no success in generating a delaminated structure.

Another formulation procedure attempted was pre-reacting the epoxy for a short period, allowing the molecular weight to increase, and subsequently adding clay and curing. The SAXS profile for this sample is shown in Figure 16. As this plot shows, an intercalated nanocomposite results with a spacing of 36 Å, again the same as the Epon828–PS3 nanocomposite.

Sonication can aid in breaking down agglomerates of clay particles into individual components (ideally into individual layers). This seemed like a natural step to take in making the nanocomposites. In Figure 17 various SAXS curves are shown for

Epon828–3140–5 wt.% PS3 formulations with and without sonication, and with sonication at elevated temperature (90 °C). All curves show a distinct peak at ≈ 37 Å, illustrating no influence of the sonication step on the final structure.

An alternate form of montmorillonite clay was employed in an attempt to achieve the delamination phenomenon. This C18-AMS clay was exchanged with a protonated primary amine rather than a quaternary amine. It was anticipated that this clay may have a "catalytic" effect on the epoxy reaction, as the protonated primary amine exchange molecules in the clay galleries may actually react with the Epon828 resin. This is contrary to what was observed however, as shown in the SAXS curves of Figure 18. As can be seen in this plot, the correlation lengths observed for Epon828–D400–5 wt.% C18–AMS as well as 10 wt.% C18–AMS are both near 21 Å. This is roughly the same as the spacing for the C18–AMS organoclay in the absence of epoxy. This would imply that for this clay, there is no intercalation of either Epon828 or the D400 curing agent. This is supported by the TEM image of Figure 19, which clearly shows in the low magnification image, that the clay particles remain agglomerated. The high magnification image in the region of a clay particle shows a very small long spacing congruent with the SAXS results.

Similarly to the PS3 containing materials, some attempts were made at varying the formulation procedure to possibly promote the delaminated structure in the C18–AMS samples. Figure 20 shows the SAXS results for two samples; one sample was thoroughly sonicated at 90 °C, and the other was rapidly blended in a specially designed apparatus at ≈ 100 °C. Both show a correlation length near 21 Å, evidence of no delamination, and in fact, no intercalation of the epoxy components either.

6.4 Summary of Epoxy–Clay Nanocomposites

The epoxy resin (Epon828) and the three different curing agents (D400, D2000, and 3140) all form individual intercalated composites with the PS3 organoclay of varied long spacings. Also, the cured epoxy–PS3 systems all possess an intercalated structure as well, however all such cured materials have the same long spacing of ≈ 36 to 38 Å.

This spacing is shared by the Epon828–PS3 intercalated system. For this reason it is concluded that the Epon828 resin is the preferred intercalation molecule and will actually displace any of the employed curing agents that are previously intercalated in the clay. The incorporation of the clay shows no influence on the location of the glass transition temperatures of the cured epoxies for the clay loadings employed in this study. Increasing the clay content leads to a decrease in the lap shear strength of bonded samples. This is due to the reduction in the toughness of the adhesive with increasing clay content, which is supported by tensile σ_0–ε data on free films of the epoxy. Likely the clay regions act as stress concentrators, thereby reducing both the lap shear strength and the toughness. Also, no improvement in the hot-wet durability is afforded by the clay, mainly due to the presence of an intercalated structure, rather than the preferred delaminated structure. However, no such delaminated composites could be made from the epoxy–PS3 formulations attempted in this study, even after rigorous sonication, various curing schedules, and after utilizing a second form of clay (C18–AMS).

6.5 Thermoplastic Polymer-Clay Nanocomposites

6.5–A Intercalated Hybrids of Polystyrene and Poly(vinyl acetate)

One of the projects proposed by the author had the goal of employing an organoclay as a compatibilizing agent for an incompatible polymer pair. The pair chosen for study was atactic polystyrene (PS, Styron 666, obtained from Dow Plastics) and atactic poly(vinyl acetate) (PVAc, obtained from Monomer, Polymer, and Dajac Labs), the molecular weight data for each is shown in Table 3. These two polymers are certainly immiscible, as shown in the DSC traces of Figure 21. The pure PVAc homopolymer has a glass transition temperature of ≈ 38 °C, and the PS homopolymer has a glass transition of ≈ 100 °C in this figure. The 50 wt.% PS, 50 wt.% PVAc blend [PVAc(50)–PS(50)] clearly shows two glass transitions at the same locations as the homopolymer traces. As can be seen in the figure, the measured values of ΔC_P across the two glass transitions of the blend lead to a calculation of ≈ 50.6 wt.% PVAc (w_{PVAc}=0.506) and 51.2

wt.% PS (w_{PS}=0.512) in the blend (Table 4), which is very close to the actual values of 50 wt.% for each. Obviously the two components must add up to 100 wt.% of the blend, however the measurements which lead to the values of 50.6 and 51.2 wt.% (which add to 101.8 wt.%) are *independent* measurements. One should use either one or the other (and subtract the value from 100 wt.% to get the other component weight fraction), or employ an average of the two measurements.

Both homopolymers, when blended separately with the organoclay, form intercalated structures as shown in Figure 22. The PVAc–PS3 nanocomposite displays a correlation length of ≈ 37 Å, and the PS–PS3 nanocomposite shows a correlation length of ≈ 41 Å. The DSC data for the two homopolymers and their individual blends with the clay are shown in Figure 23. The resulting DSC–measured weight fractions of the polymers in the clay blends are compared to the actual weight fractions in Table 4.

Blending together all three components (PS, PVAc, and the PS3) also leads to an intercalated structure (Figure 24). There is a slight difference in the correlation length for 1 wt.% PS3 in the blend (≈ 43 Å) and the 10 wt.% PS3 in the blend (≈ 45 Å), however it is clear that an intercalated structure exists for both cases. DSC reveals that this three component blend displays two distinct glass transition temperatures, corresponding to separated phases of the two homopolymers (Figure 25, measured weight fractions of each phase in Table 4). Hence the goal of this project was not satisfied. This is not unexpected in light of the nature of *intercalated* nanocomposites. In the intercalated structure, the clay does not contact the majority of the bulk polymer phase(s), and hence cannot act as a good compatibilizing agent.

Some researchers have reported a significant enhancement in Young's modulus for unsaturated polyester–clay nanocomposites compared to the pure homopolymer.[4] The tensile σ_0–ε data for PVAc and an intercalated PVAc-5 wt.% PS3 nanocomposite are shown in Figure 26. It can be seen from this figure that the PVAc is a rather brittle material, with E=2100 MPa and ε_b=0.033. However, after melt blending with the PS3, the modulus *drops* to 380 MPa and ε_b increases to 1.43. This is an unexpected result, but can be explained easily. The melt blending process led to degradation of the PVAc,

actually reducing the molecular weight. Although the molecular weight of the PVAc in the nanocomposite cannot be easily measured (due to the presence of the clay which is not easily removed), DSC provides sufficient evidence by displaying a reduced glass transition temperature for the PVAc–PS3 nanocomposite compared to the PVAc homopolymer (refer back to Figure 23).

6.5–B Intercalated Hybrids of an Estane Thermoplastic Elastomer

Although no particular project goals were assumed for this part of the clay work, a novel intercalated material was formed and hence will be reported here. A thermoplastic elastomer (one of the Estane® polyether–based polyurethane materials made by BF Goodrich), was both melt blended with the PS3 clay, and also solution blended with the clay in dimethyl formamide (DMF). The SAXS profiles for solution cast Estane® and solution cast Estane®–PS3 blends are shown in Figure 27. Note that the neat Estane material shows a peak in the low angle region (≈ 220 Å), corresponding to the microphase separation of the hard domains in the urethane. The nanocomposite displays a shoulder in this same low angle region, corresponding to the same phase separated structure. However, the nanocomposite also shows a sharp peak at 36 Å, corresponding to an intercalated structure. Both the solution blending and melt blending procedures produced an intercalated structure (Figure 28), although the solution method tended to produce "stronger" peaks in the SAXS data, suggesting more complete intercalation. The kinetics of the melt intercalation process are likely much slower than the solution intercalation process, and hence these results are expected. Melt blending at higher temperatures or for longer times is expected to provide similar results to solution blending, assuming that thermal degradation (or other changes in chemistry) of the polymer does not occur at these conditions.

6.6 Acknowlegments

The author wishes to express his gratitude to Southern Clay Products, Nanocor, Huntsman, and Shell for supplying the clays and epoxy components utilized in this study. Steve McCartney is appreciated for his excellent electron microscopy skills.

Table 1. Correlation lengths of various mixtures of the epoxy components and the organoclays.

Sample formulation	Correlation length (Å)
PS3 organoclay	21
C18–AMS organoclay	18
Epon828 and PS3	**37**
D400 and PS3	41
D2000 and PS3	42
3140 and PS3	55
Epon828, D400, and PS3	**36**
Epon828, D2000, and PS3	**38**
Epon828, 3140, and PS3	**38**
Epon828, D400, and C18–AMS	21

Table 2. Relative weight fraction of epoxy in the nanocomposites determined from DSC compared to the actual weight fractions.

Nanocomposite formulation	w_{Epoxy} (actual)	w_{Epoxy} (from DSC)
Epon828–D400-5%PS3	0.95	0.96
Epon828–D400-5%C18–AMS	0.95	0.96
Epon828–D400-10% PS3	0.90	0.94
Epon828–D400-20% PS3	0.80	0.82
Epon828–D2000-5% PS3	0.95	0.97
Epon828–D2000-20% PS3	0.80	0.92

Table 3. Molecular weight data for the polystyrene and poly(vinyl acetate) materials.

Polymer	$\overline{M}_n$ **(kg/mol)**	$\overline{M}_w$ **(kg/mol)**	$\overline{M}_w/\overline{M}_n$
Styron 666 (PS)	74	238	3.2
Poly(vinyl acetate) (PVAc)	81	195	2.4

Table 4. Relative weight fraction of each thermoplastic polymer in the blends determined from DSC compared to the actual weight fractions.

Sample	w_{PVAc}		w_{PS}	
	actual	from DSC	actual	from DSC
PVAc–PS3	0.92	0.75	0	0
PS–PS3	0	0	0.91	0.84
PVAc(50)–PS(50)	0.50	0.506	0.50	0.512
PVAc(45)–PS(45)–PS3(10)	0.45	0.408	0.45	0.432

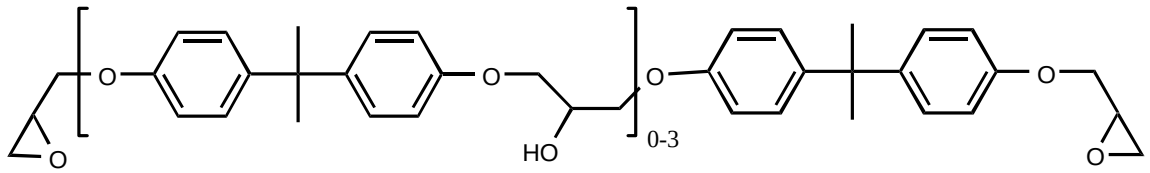

Figure 1. The chemical structure of Epon828 (Shell). Equivalent weight: 188.

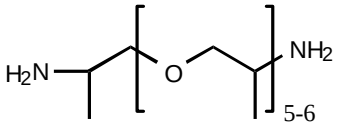

Jeffamine D400

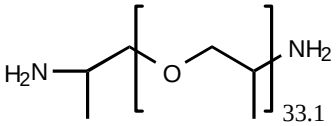

Jeffamine D2000

Figure 2. The structure of the JEFFAMINE® D400 and D2000 epoxy curing agents. Equivalent weights: 104 and 514, respectively.

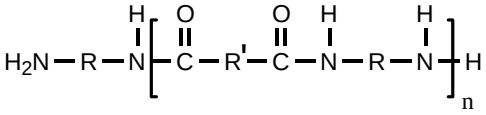

Epicure 3140 (old V-40)

R = aliphatic

R' = fatty acid residue

Figure 3. The general structure of the major component of the Epicure 3140 curing agent. Equivalent weight: ≈ 375.

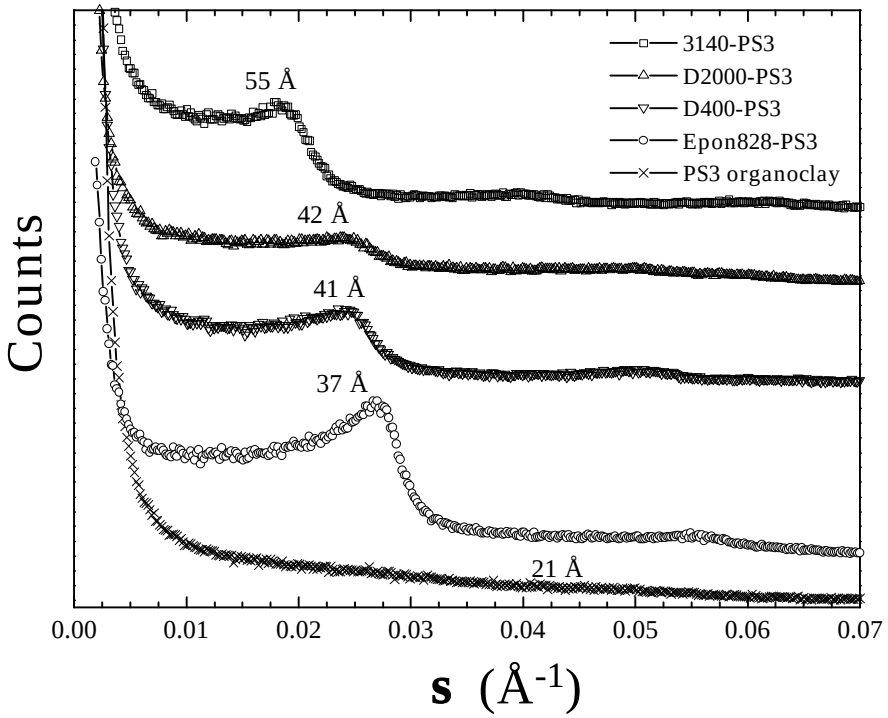

Figure 4. SAXS profiles of the PS3 organoclay, and mixtures of the clay with the individual epoxy components. Curves displaced vertically for clarity.

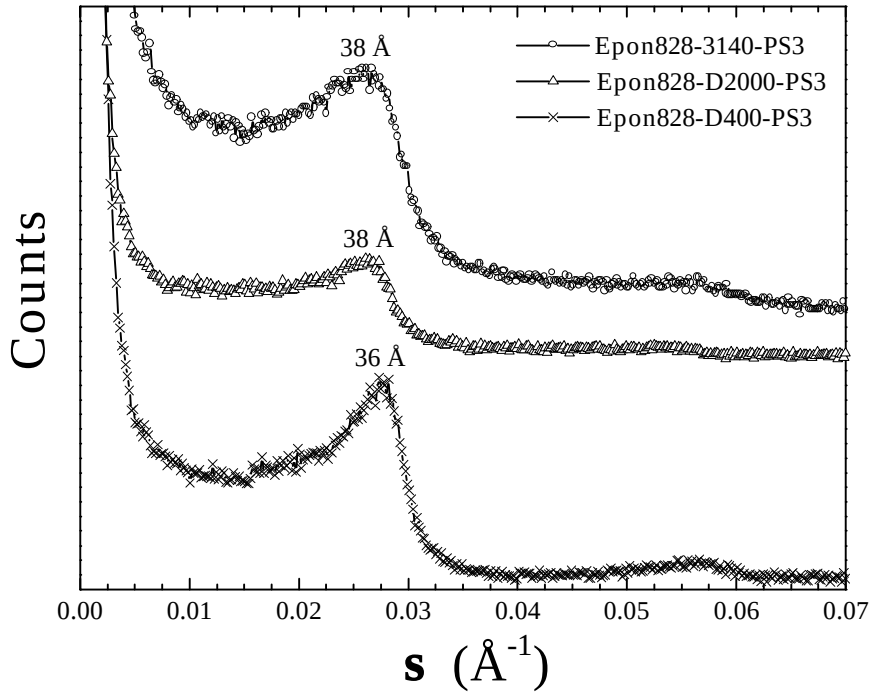

Figure 5. SAXS profiles for cured epoxy systems containing PS3 organoclay. Curves displaced vertically.

Figure 6. TEM image of an intercalated, cured epoxy system based on Epon828–D400 with PS3 organoclay.

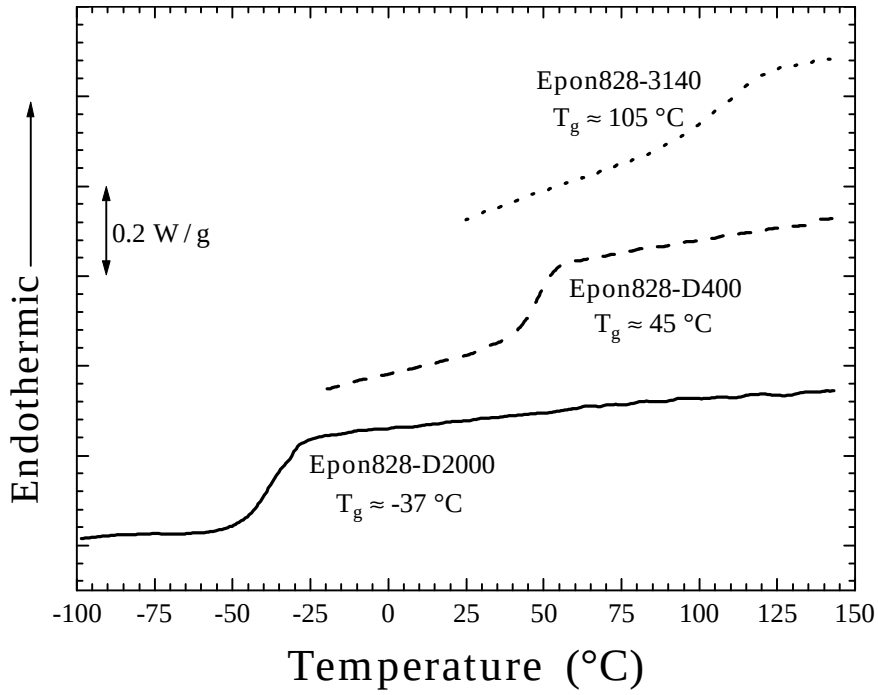

Figure 7. DSC traces for various cured epoxy systems without added organoclay. Curves displaced vertically.

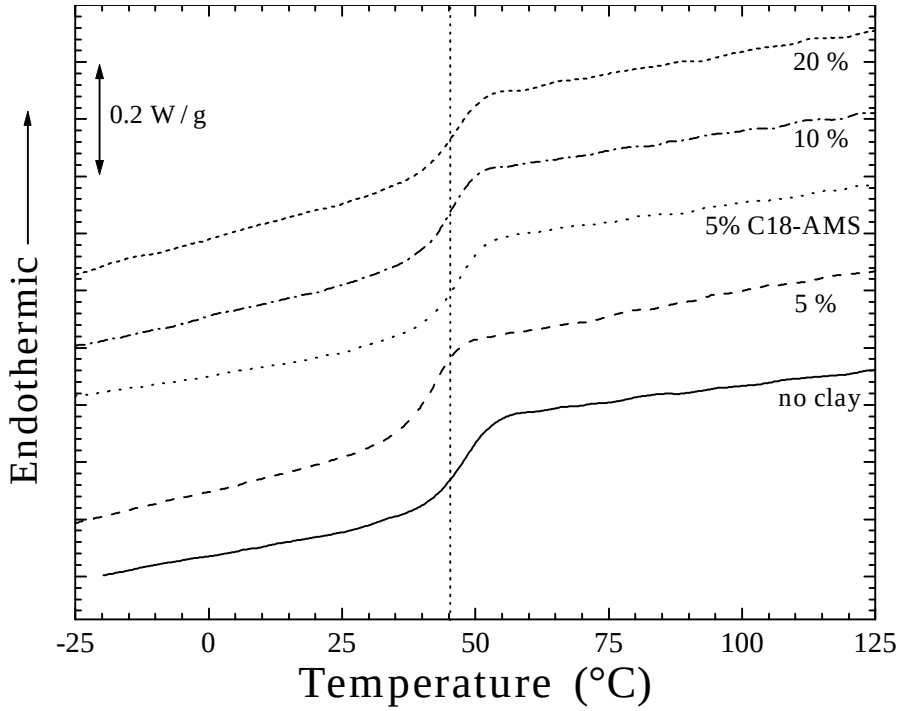

Figure 8. DSC traces of intercalated, cured epoxy systems based on Epon828–D400 with varied organoclay contents. All clays are PS3 except the one noted C18–AMS. Curves displaced vertically.

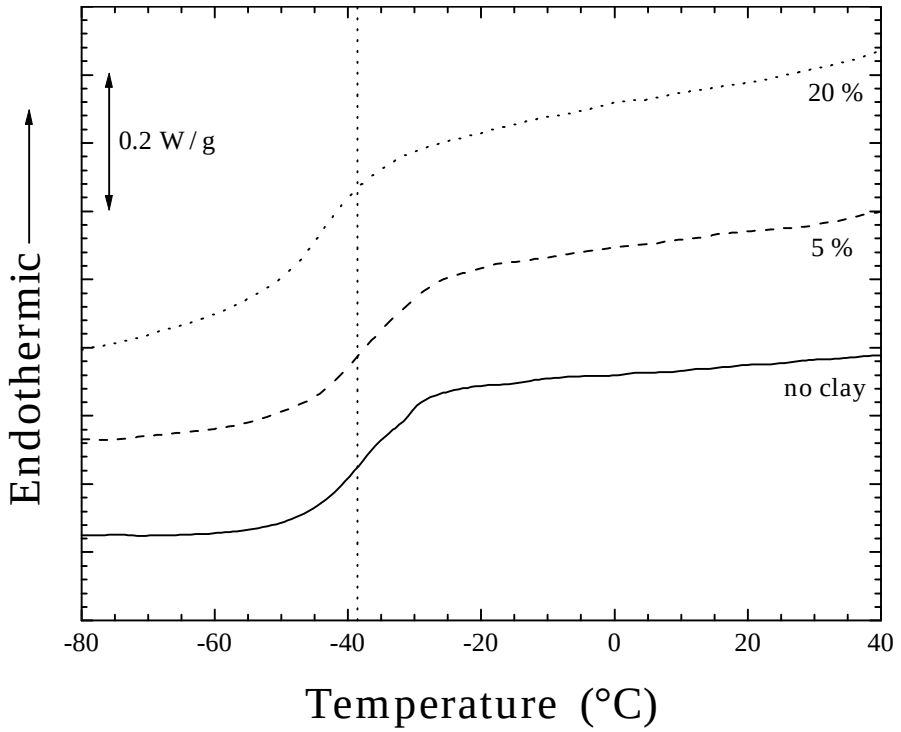

Figure 9. DSC traces of intercalated, cured epoxy systems based on Epon828–D2000 with varied PS3 organoclay contents. Curves displaced vertically.

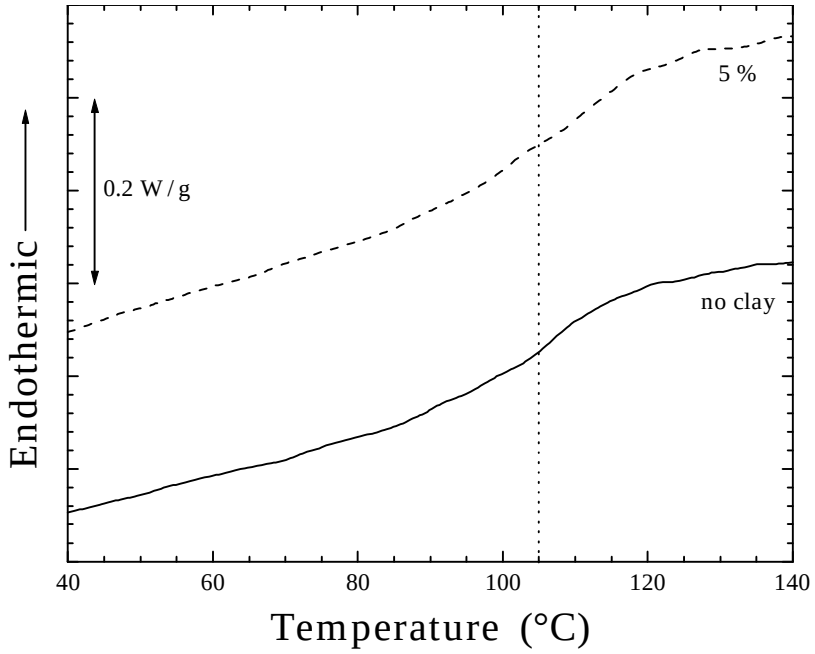

Figure 10. DSC traces of intercalated, cured epoxy systems based on Epon828–3140 with 5 wt.% and without PS3 organoclay. Curves displaced vertically.

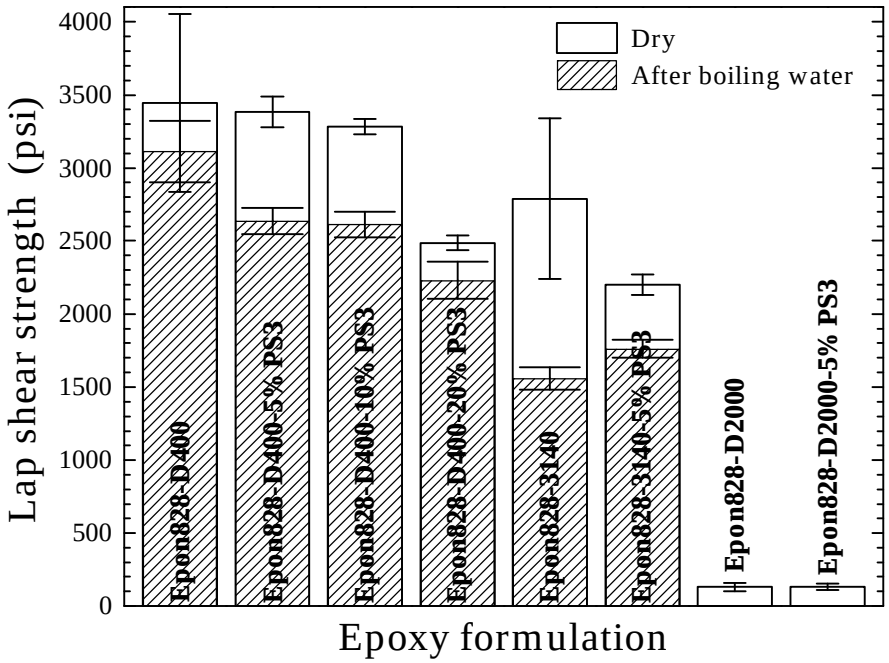

Figure 11. Single lap shear strength of various epoxy formulations, with and without clay. The D400 and 3140 cured epoxies have data for both dry conditions and after boiling water exposure superimposed to illustrate the effect of this environment on the shear strengths.

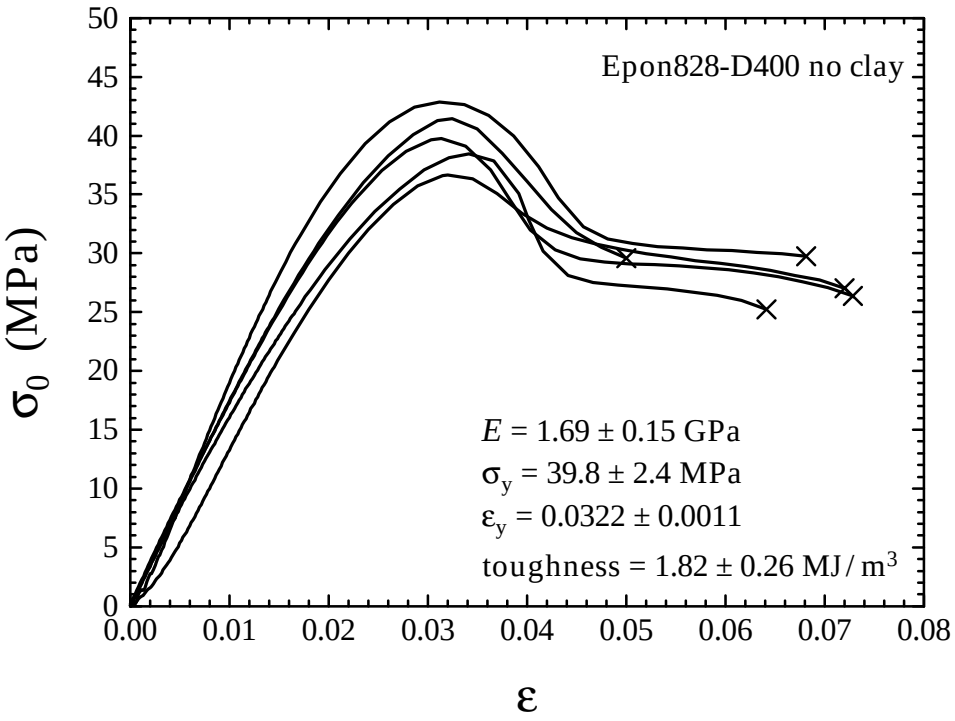

Figure 12. Tensile σ_0–ε data for Epon828–D400. Sample is somewhat ductile.

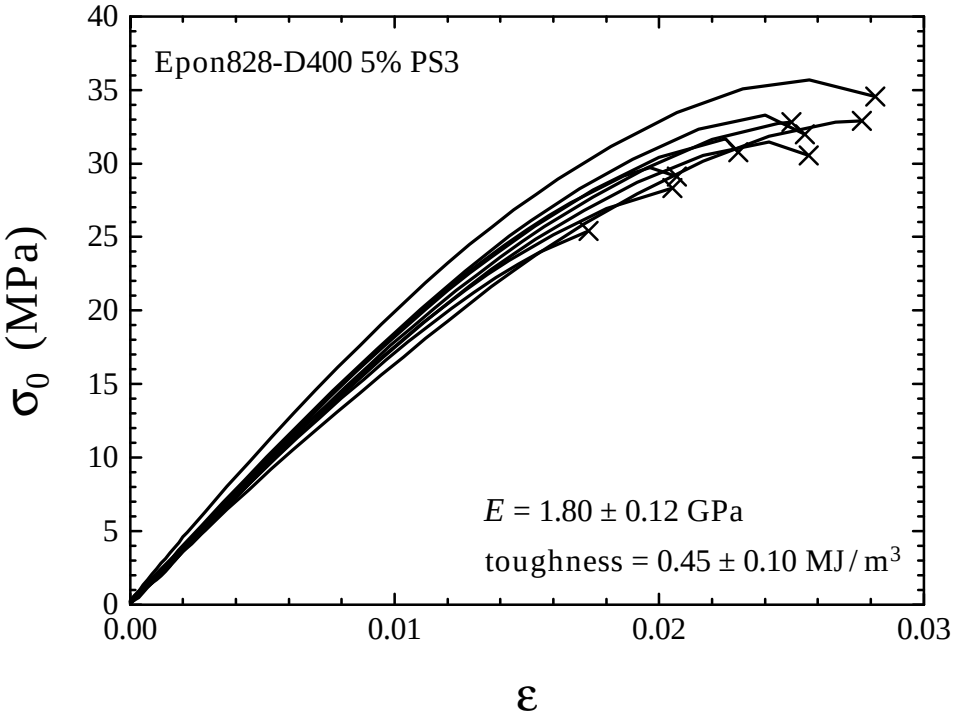

Figure 13. Tensile σ_0–ε data for Epon828–D400 with 5 wt.% PS3 showing brittleness.

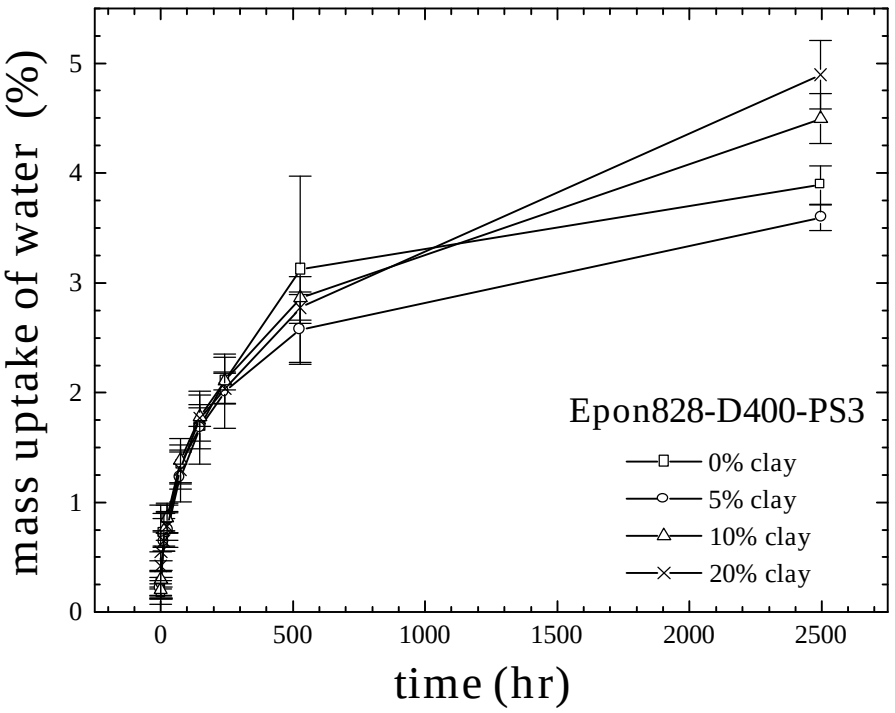

Figure 14. Water uptake experiments for Epon828–D400 formulations of varied clay content.

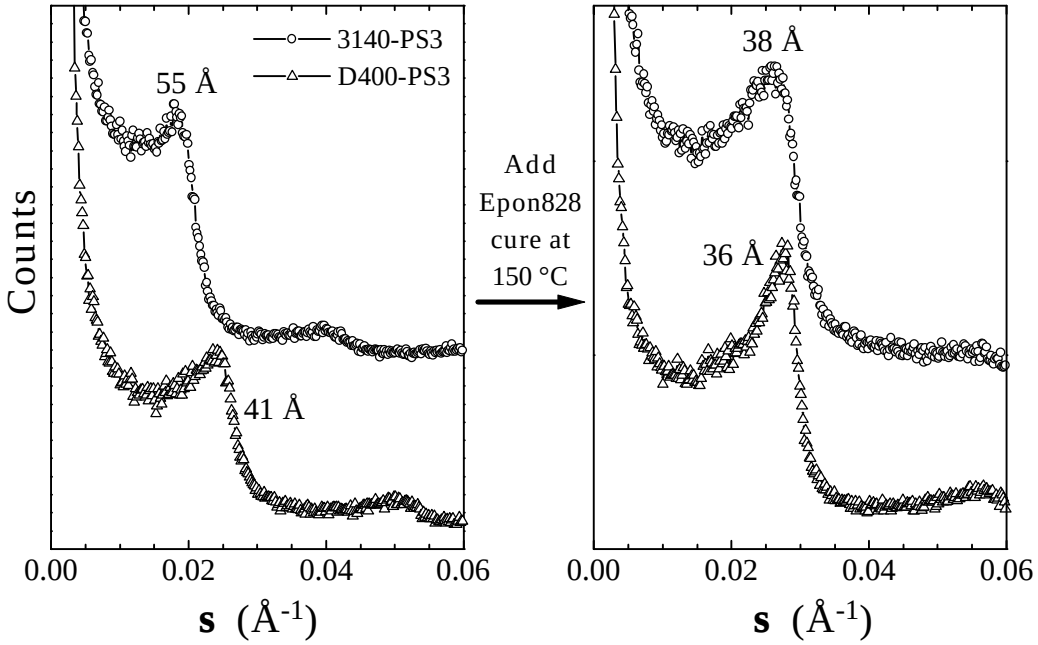

Figure 15. SAXS curves for intercalated curing agent–PS3 mixtures before (left) and after Epon828 addition and curing (right). Curves displaced vertically.

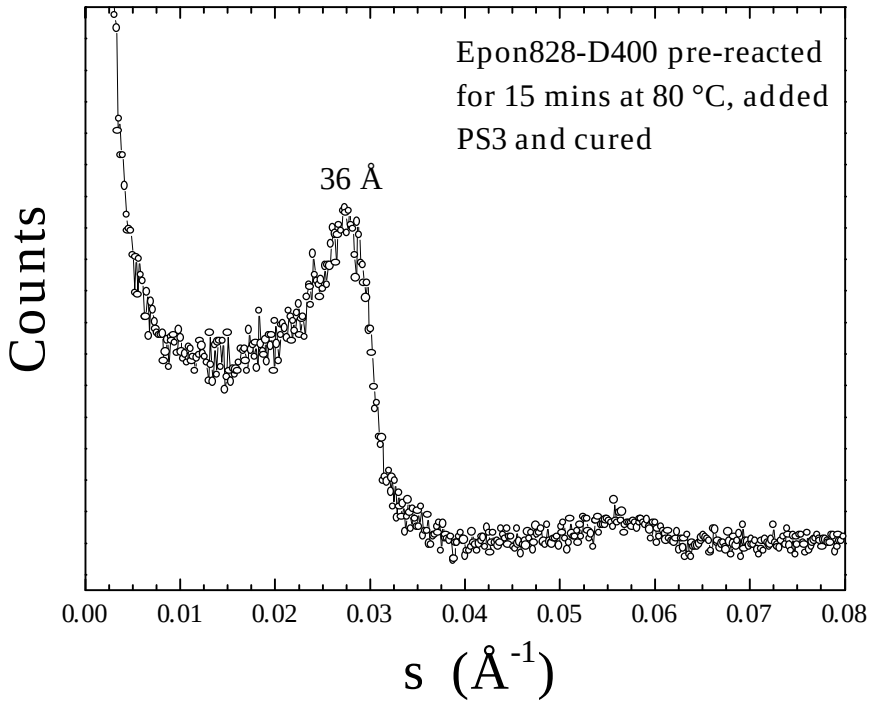

Figure 16. SAXS profile for pre-reacted Epon828–D400 (15 minutes) followed by clay addition and curing. 5 wt.% PS3.

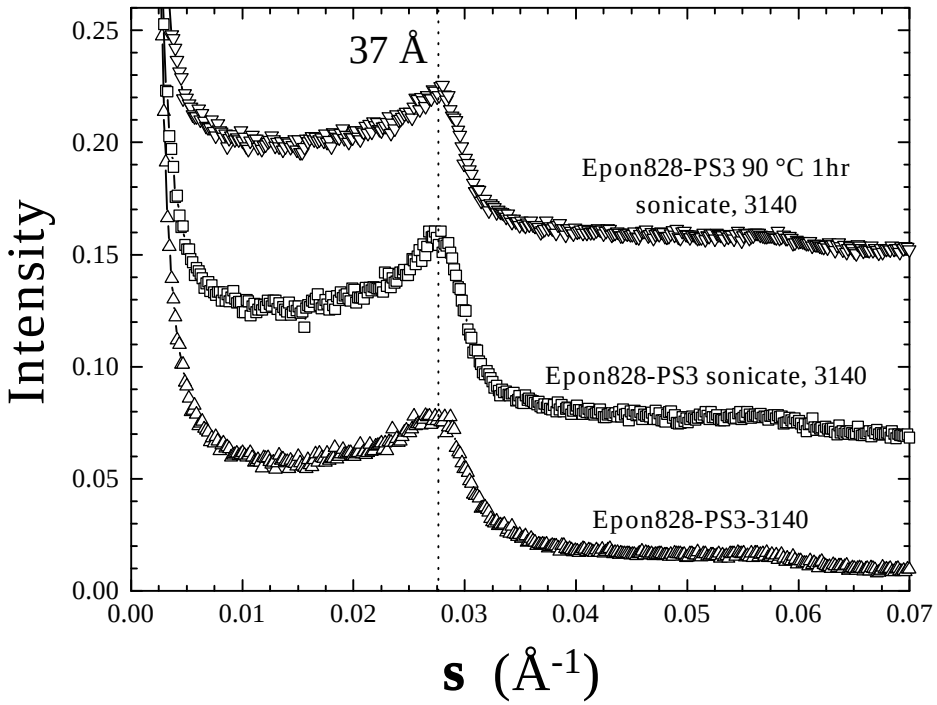

Figure 17. Influence of sonication on the final structure of Epon828–3140–5 wt.% PS3 formulations. Curves displaced vertically.

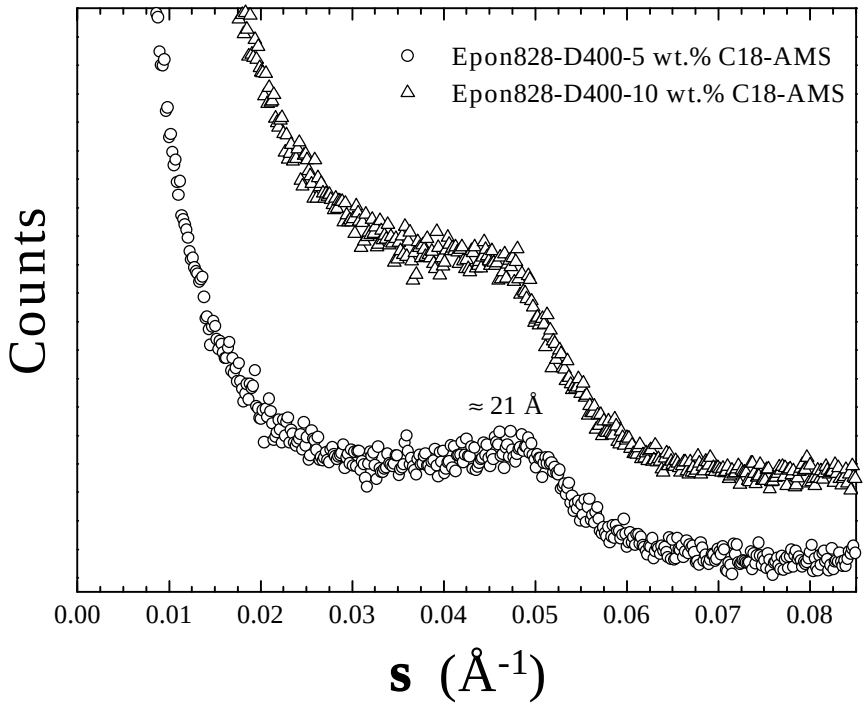

Figure 18. Epoxy–clay mixtures based on Epon828–D400 and C18–AMS clay.

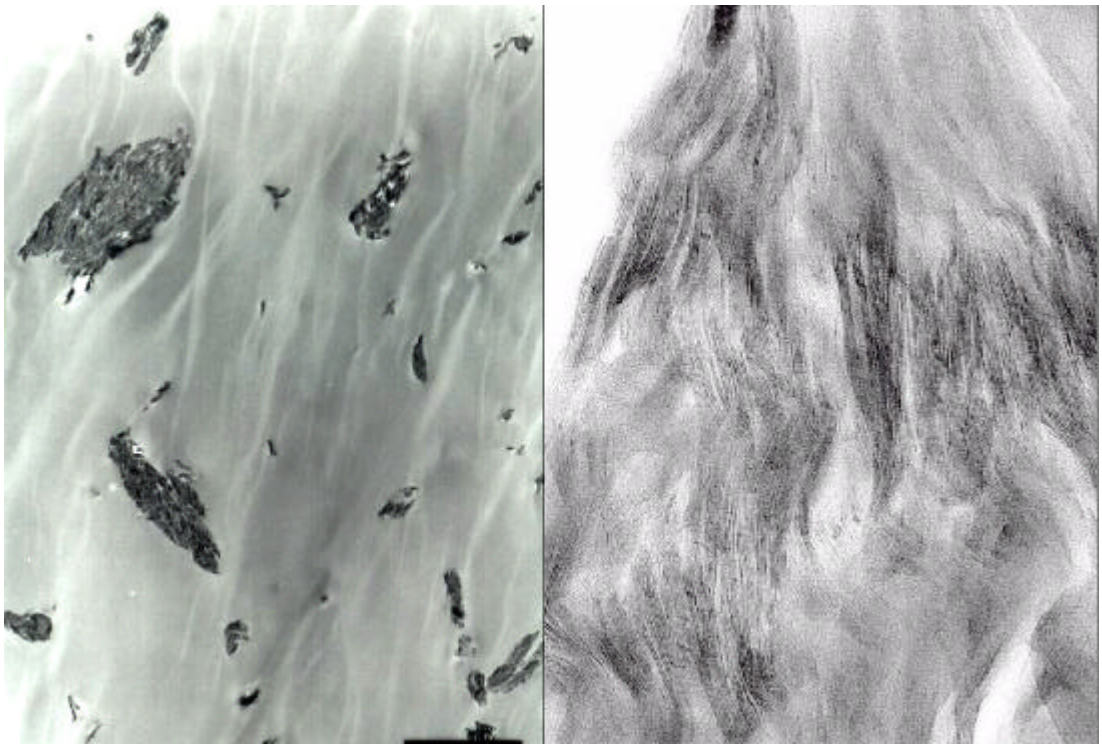

Figure 19. TEM image of Epon828–D400–5 wt.% C18–AMS prepared by rapid blending (same sample which produced the 21 Å peak in the previous SAXS plot). Magnification: 2,300× (left); 280,000× (right).

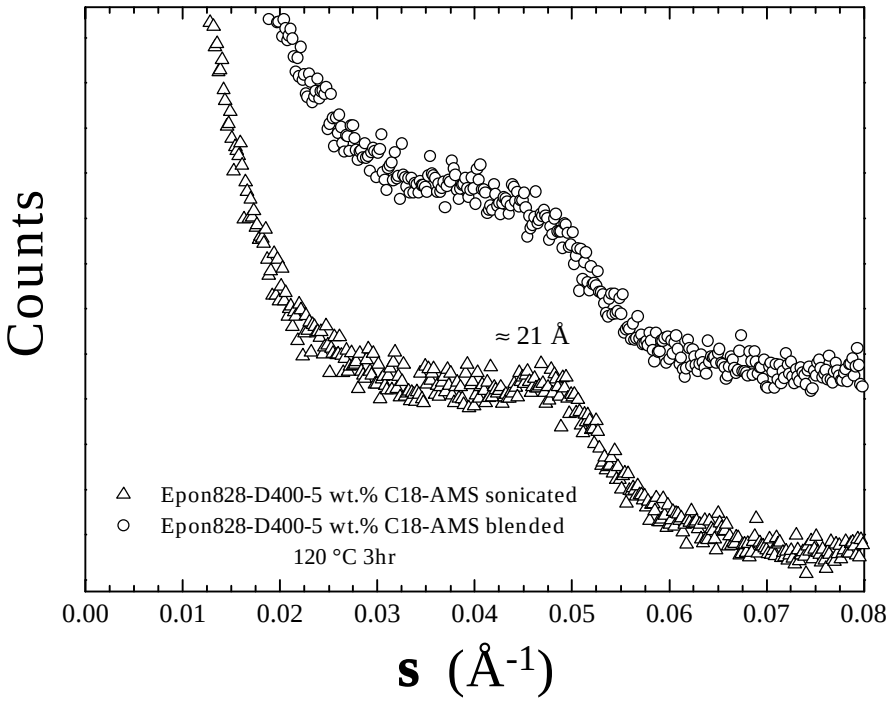

Figure 20. Influence of sonication and rapid blending on the structure of Epon828–D400–5 wt.% C18–AMS mixtures.

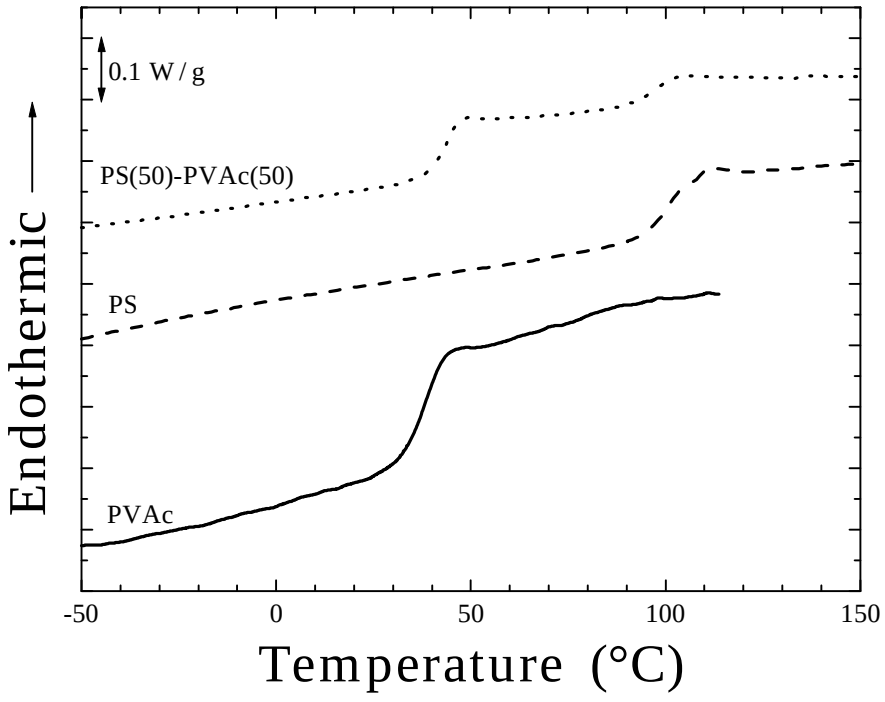

Figure 21. DSC scans of PS, PVAc, and a blend of 50 wt.% PS and 50 wt.% PVAc. Curves displaced vertically.

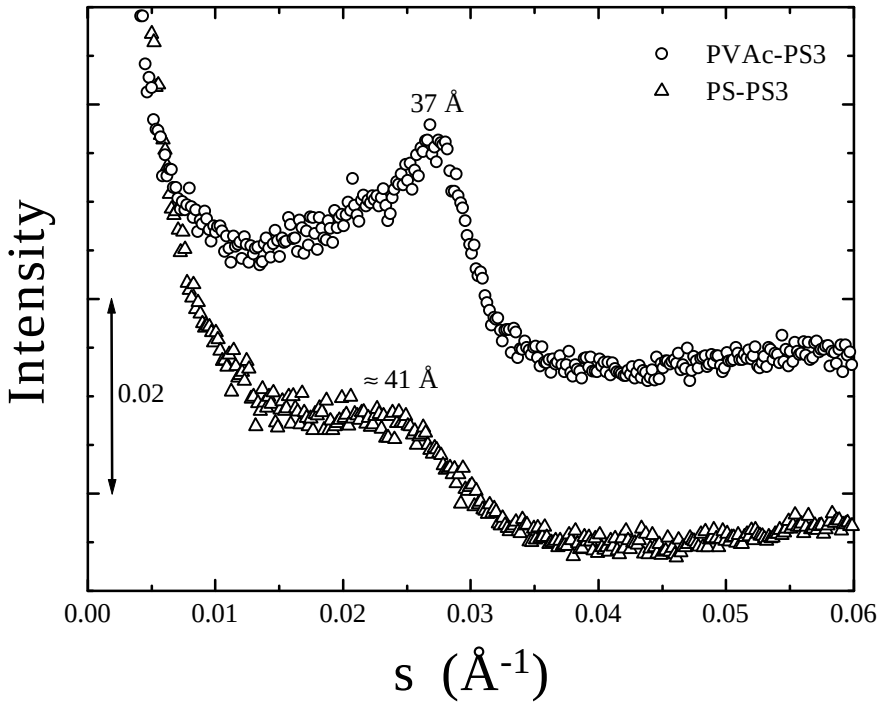

Figure 22. SAXS curves for thermoplastic polymer–PS3 intercalated nanocomposites (both polystyrene and PVAc). Curves displaced vertically.

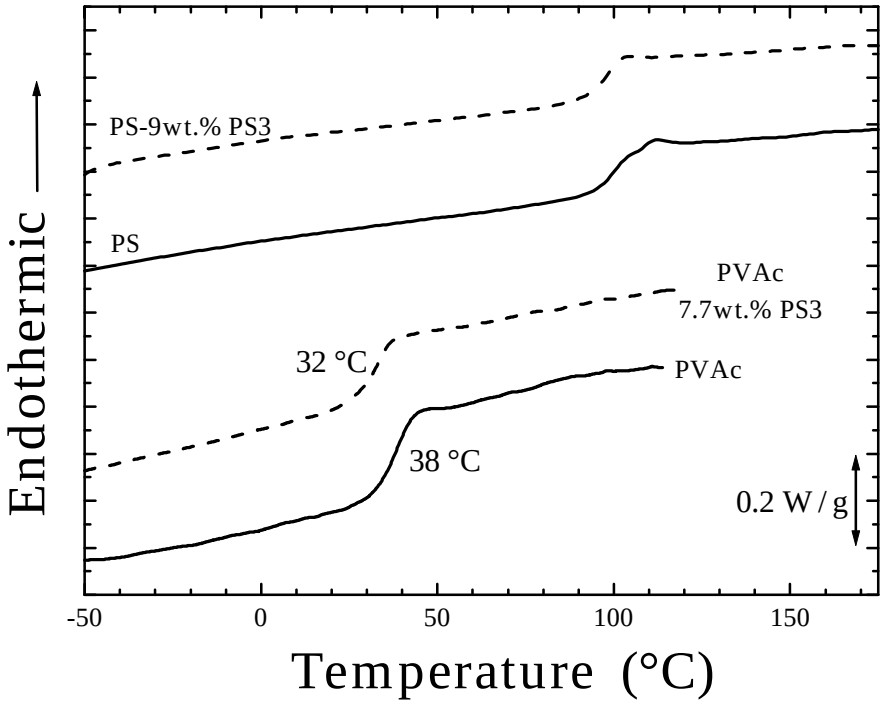

Figure 23. DSC scans of PVAc, PS, and their blends with PS3 organoclay.

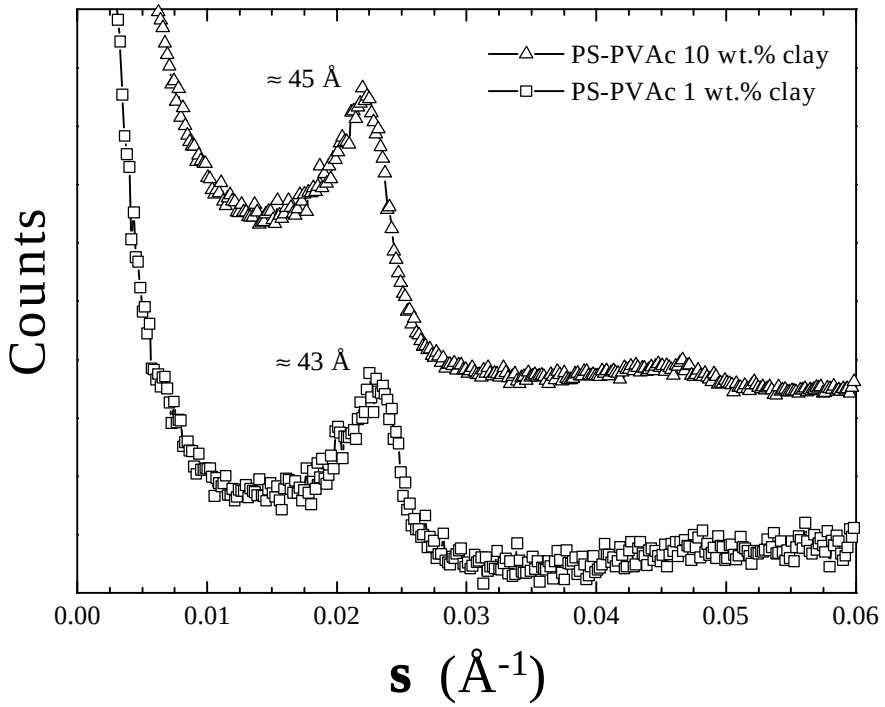

Figure 24. SAXS profiles for intercalated PS–PVAc–PS3 nanocomposites. Curves displaced vertically.

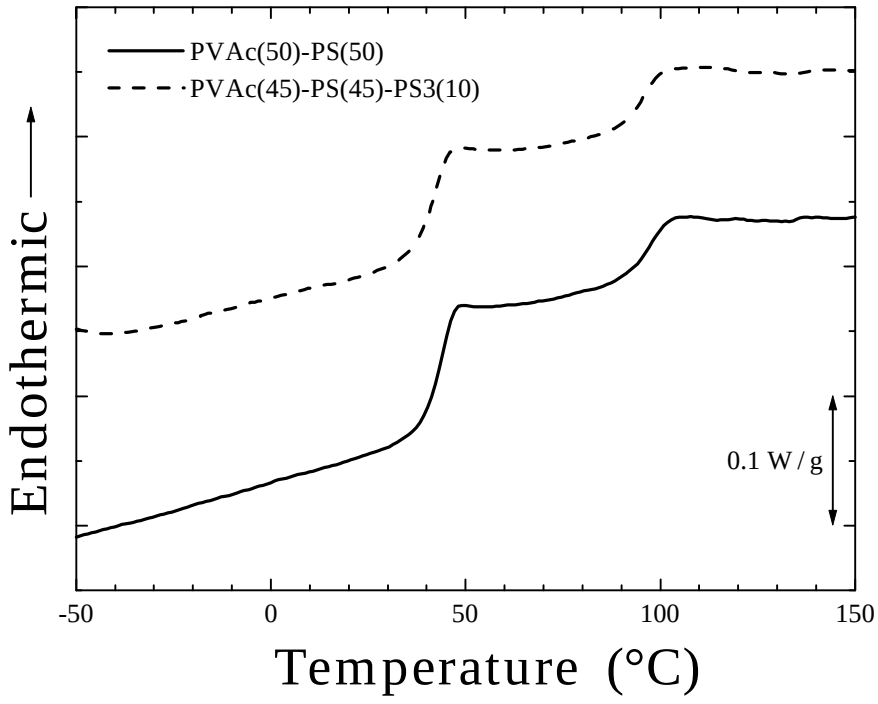

Figure 25. DSC scans of the immiscible polymer blend with and without PS3 organoclay. Curves displaced vertically.

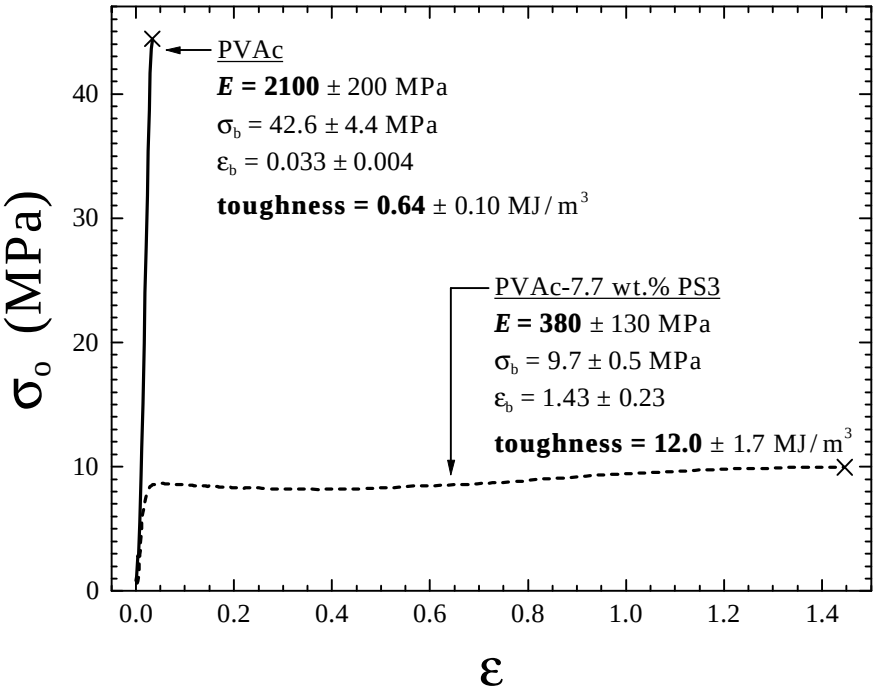

Figure 26. Tensile σ_0–ε data for PVAc and melt blended PVAc–PS3.

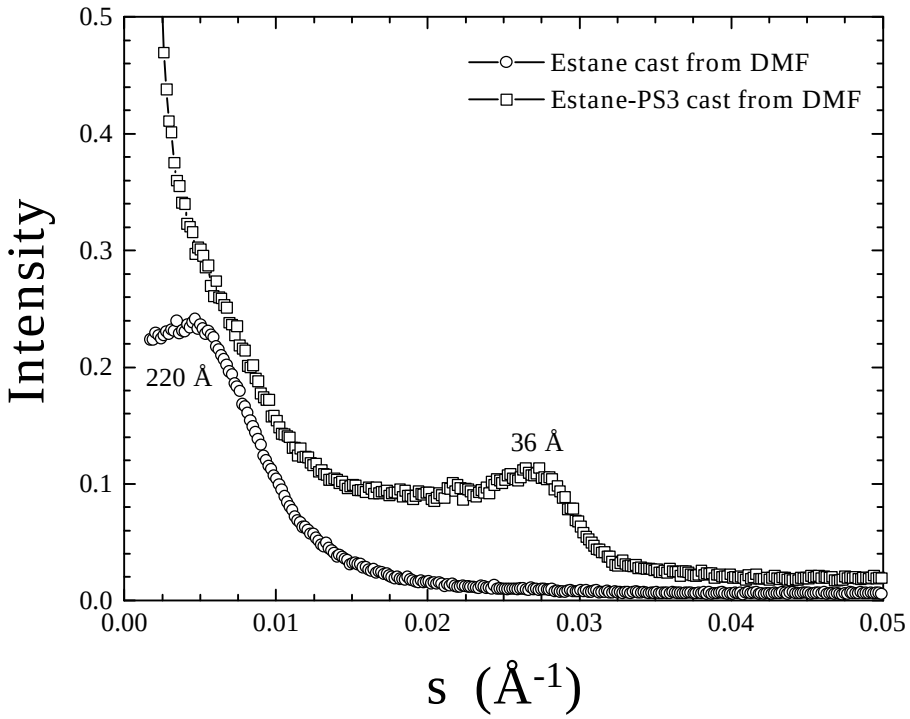

Figure 27. SAXS curves for Estane polyurethane and an Estane–PS3 nanocomposite.

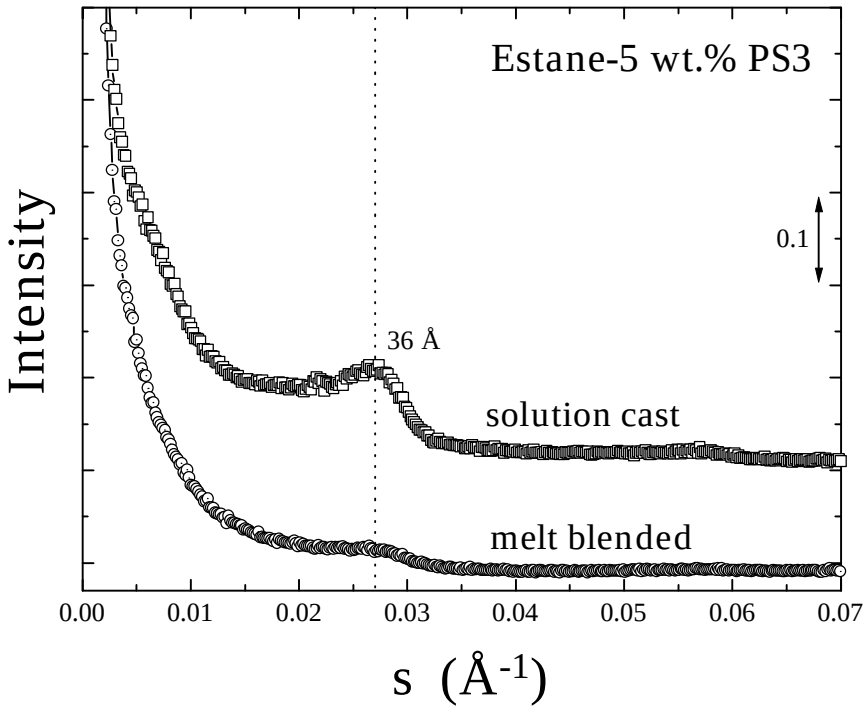

Figure 28. SAXS curves for solution cast and melt blended Estane®–PS3 intercalated nanocomposites. Curves displaced vertically.

6.7 References

1 Y. Kojima, A. Usuki, M. Kawasumi, A. Okada, T. Kurauchi, and O. Kamigaito. *J. Appl. Polym. Sci.* **49**, 1259, (1993).

2 K. Yano, A. Usuki, A. Okada, T. Kurauchi, and O. Kamigaito. *J. Polym. Sci.: Part A: Polym. Chem.*, **31**, 2493, (1993).

3 A. Okada and A. Usuki. *Mater. Sci. Engr.* **C3**, 109, (1995).

4 X. Kornmann, L. A. Berglund, J. Sterte, and E. P. Giannelis. *Polym. Eng. Sci.*, **38(8)**, 1351, (1998).

5 A. J. Kinloch, W. A. Dukes, and R. A. Gledhill. "Durability of Adhesive Joints", p. 597 in *Polymer Science and Technology, vol **9B**, Adhesion Science and Technology*, Lieng–Huang Lee, ed., Plenum Press, NY, 1975.

6 A. J. Kinloch. "Introduction", p. 1 in Durablility of Structural Adhesives, A. J. Kinloch, ed., Applied Science Publishers, NY, 1983.

7 J. Comyn. "Kinetics and Mechanism of Environmental Attack", p. 85 in Durablility of Structural Adhesives, A. J. Kinloch, ed., Applied Science Publishers, NY, 1983.

8 E. P. Giannelis. *JOM*, **44(3)**, 28, (1992).

9 J. K. Gillham. *Polym. Eng. Sci.*, **26(20)**, 1429, (1986).

10 R. B. Prime, Chapter 5 in Thermal Characterization of Polymeric Materials, E. A. Turi, ed., Academic Press, NY, (1981).

11 L. E. St. Pierre and C. C. Price. *J. Am. Chem. Soc.*, **78**, 3432, (1956).

12 R. N. Work, R. D. McCammon, and R. G. Saba. *Bull. Am. Phys. Soc.*, **8**, 266, (1963).

13 G. Allen. *Soc. Chem. Ind. Monograph*, **17**, 167, (1963).

14 G. Williams. *Trans. Faraday Soc.*, **61**, 1564, (1965).

15 T. Lan, P. D. Kaviratna, and T. J. Pinnavaia. *Chem. Mater.*, **7**, 2144, (1995).

16 T. J. Pinnavaia, T. Lan, Z. Wang, H. Shi, and P. D. Kaviratna. Chapter 17 of *ACS Symp. Ser., Nanotechnology*, **662**, 250, (1996).

17 R. D. Adams and W. C. Wake. Structural Adhesive Joints in Engineering, Elsevier Applied Science Publishers, NY, (1984).

18 David Dillard. *Personal Communication (Class notes, Adhesion Science CHEM 5654 at VPI & SU)*, Spring 1996.

19 Leroy E. Alexander. X-Ray Diffraction Methods in Polymer Science, Robert E. Kreiger Publishing Company, Malabar, Fl., (1969).

20 P. B. Messersmith and Emmanuel P. Giannelis. *Chem. Mater.*, **6**, 1719, (1994).

21 R. A. Vaia, K. D. Jandt, E. J. Kramer, and E. P. Giannelis. *Macromolecules,* **28(24)**, 8080, (1995).

22 R. A. Vaia, K. D. Jandt, E. J. Kramer, and E. P. Giannelis. *Chem. Mater.*, **8(11)**, 2628, (1996).

23 T. Lan and T. J. Pinnavaia. *Chem. Mater.*, **6**, 2216, (1994).

24 A. Usuki, Y. Kojima, M. Kawasumi, A. Okada, Y. Fukushima, T. Kurauchi, and O. Kamigaito. *J. Mater. Res.* **8(5)**, 1179, (1993).

25 R. A. Vaia, H. Ishii, and E. P. Gianellis. *Chem. Mater.*, **5**, 1694, (1993).

26 L. C. E. Struik. Physical Aging in Amorphous Polymers and Other Materials, Elsevier, NY, (1979).

27 L. E. Nielsen. Mechanical Properties of Polymers and Composites Volume 2, Marcel Decker, Inc., NY (1974).

28 E. Guth. *J. Appl. Phys.*, **16**, 20, (1945).

29 H. M. Smallwood. *J. Appl. Phys.*, **15**, 758, (1944).

30 A. Einstein. *Annalen der Physik,* **19**, 289, (1906); some corrections found in *Ibid.*, **34**, 591, (1911).

31 H. Shi, T. Lan, and T. Pinnavaia. *Chem. Mater.*, **8(8)**, 1584, (1996).

32 T. Lan, Z. Wang, H–Z. Shi, and T. J. Pinnavaia. *PMSE Preprints,* **73**, 296, (1995).

Chapter 7

The Influence of Molecular Weight and Thermal History on the Thermal, Rheological, and Mechanical Properties of Metallocene–Catalyzed Linear Polyethylenes

Abstract

Several linear polyethylenes of varied molecular weight ($13 \leq \overline{M}_w \leq 839$ kg/mol) were synthesized with a zirconocene catalyst and characterized. This approach resulted in relatively narrow molecular weight distributions ($2.3 < \overline{M}_w/\overline{M}_n < 3.6$) as measured by size exclusion chromatography. The melt rheological data, $|\eta^*(\omega)|$ were modeled by the Carreau–Yasuda equation. The as–polymerized polymer fluff was compression–molded into films of quenched and slowly cooled thermal treatments. This resulted in a range of sample densities between 0.9302 and 0.9800 g/cm^3, due to variations in the crystal content. The thermal, morphological, and mechanical behaviors were probed for their dependence on both molecular weight and thermal treatment. The small–strain tensile deformation properties of Young's modulus, yield stress, and yield strain were directly related to percent crystallinity, independent of molecular weight. However, increasing molecular weight led to a suppression in the peak of the stress–strain curves at the yield point. The large–strain deformation properties of toughness

and strain at break were influenced by the competing effects of percent crystallinity and molecular weight. The long spacings and estimated values of lamellar thickness increased with molecular weight. Estimates of the amorphous layer thickness increased with molecular weight similarly, but were independent of thermal treatment for a given molecular weight. There was a progression from ridged and planar lamellae to curved C and S–shaped lamellae with increasing molecular weight. Thermal treatment had a large influence on the shape of the mechanical α–relaxation, while the crystal content affected the magnitudes of the mechanical γ and β–relaxations.

7.1 Introduction

Metallocene catalysts are typically composed of a group IV transition metal atom which is π–bonded to one or two cyclopentadienyl (Cp) rings (which may or may not be substituted). A metallocene containing a single Cp ring is referred to as a "half–sandwich" metallocene and a Cp_2 containing material is referred to as a "sandwich" metallocene. In the bent sandwich metallocenes, the central metal atom is π–bonded to two Cp rings, and also bonded to two additional groups, usually Cl or CH_3. An example of this type of metallocene, namely Cp_2ZrCl_2, is shown in Figure 1. Metallocenes of this sort often require a co–catalyst, or so–called activator. The most popular and efficient such material is methylaluminoxane (MAO). This material is thought to be in an oligomeric form, with roughly 5 to 30 [–O–Al(CH_3)–] repeat units.[1] The true structure is not yet unequivocally identified, but has been suggested as cyclic or linear or perhaps both.[1] Of minor importance, the MAO co-catalyst acts to scavenge impurities. The major role of the MAO is firstly, to alkylate the metallocene (i.e., replace the Cl group(s) with a CH_3 from the MAO), and secondly (most importantly), to produce and stabilize a cationic metallocene species. This cationic species is thought to be the active center in metallocene polymerizations, and is a d^0 14–electron complex.[2] There are some MAO–free metallocene systems which are also cationic in nature, and the active center for both is thought to be similar.

Metallocene catalysis allows polyolefins of comparatively narrow molecular weight distribution to be produced. This has been attributed to the "single site" nature of metallocene catalysts, which implies that there is only *one* unique active center type. In other words, all active sites have the same reactivity, or rather, have the same ratio of propagation to termination rates. With such a condition, the molecular weight distribution of the resulting polymer should take on the shape of Flory's most probable distribution.[3] This type of distribution would have a corresponding breadth index $\overline{M}_w/\overline{M}_n$ of 2.0. However the term single site is more of a textbook ideality when compared to most real metallocene systems. Particularly in the case of MAO containing catalyst systems, there are undoubtedly different amounts of MAO–metal interaction at different metal atom locations, which would influence the reactivity at these sites (by, for example, electronic and steric factors). This would eliminate the possibility of a single unique site, although the reactivities at these different sites may be so similar as to not significantly broaden the distribution of molecular weights. However, for the case of the cationic MAO–free systems, the term single site is probably accurate.

Under metallocene catalysis, polymer chain length is dependent on the relative rates of propagation versus the numerous possible termination reactions. Among the chain termination reactions are chain transfer to ethylene (or other comonomer if applicable), chain transfer to metal alkyls, chain transfer to hydrogen, and β-hydride (β-H) elimination.[1–5] Polymerization of propylene has the added termination reaction of β–CH_3 elimination. Since temperature has a different effect on each of these termination reactions as well as the propagation reaction, molecular weight is a function of the polymerization temperature. In fact, there is an inverse relationship between molecular weight and reaction temperature due to the relatively high rate of the β-H elimination reaction at high temperatures.[5] This terminating reaction leaves an unsaturated (vinyl) endgroup on the polymer chain. However, for polymerization at very low temperature (below –20 °C), the β-H elimination reaction (as well as most of the other termination reactions) is generally so slow relative to propagation that the molecular weight becomes a function of only the polymerization time, analogous to a living

polymerization.[6] Beyond varying the temperature, molecular weight can also be controlled through the addition of hydrogen as a chain transfer agent, similar to conventional heterogeneous Ziegler–Natta catalyzed olefin polymerizations. However, metallocene catalyzed olefin polymerizations are much more sensitive to hydrogen concentration than are conventional heterogeneous Ziegler–Natta polymerizations.[1]

Depending on the structure and symmetry of the metallocene catalyst, α–olefins can be homopolymerized with extremely high isotactic, syndiotactic, hemiisotactic, or atactic content. For example, syndiotactic polystyrene can be produced with the half sandwich metallocene, $CpTiCl_3$/MAO.[7,8] Also, racemic–ethylene bis(indenyl) zirconium dichloride [$Et(Ind)_2ZrCl_2$] produces isotactic polypropylene,[9] whereas isopropylidene–bridged cyclopentadienyl 9-fluorenyl zirconium dichloride [*i*Pr(CpFlu)$ZrCl_2$] produces syndiotactic polypropylene.[10,11] Temperature has a strong effect on the stereospecificity of the metallocene catalysts, as they tend to "soften" (the bonds become less rigid) at elevated temperatures. This softening causes the stereospecificity to diminish. Hence during a polymerization, the tacticity of the chains can be altered by changing temperature, thereby producing a mixture of chains of different stereochemistry.

Metallocene catalysts can be used to make "stereoblock copolymers", where although the monomer may remain the same, the stereochemistry changes at some point in the backbone due to a change in the catalyst specificity. This produces a "copolymer" which has crystallizable and non–crystallizable blocks of the same monomer. Stereoblock copolymers of propylene have been synthesized with an "oscillating" metallocene catalyst.[12,13] These materials behaved like thermoplastic elastomers. Similar propylene stereoblock copolymers were prepared by an alternative process, namely by employing a mixture of stereospecific and non-stereospecific titanocenes.[14,15]

Initially, metallocenes were applied in a homogeneous catalysis condition during the bench-top research stage. Upon scale–up, this often led to reactor fouling due to polymer particle agglomeration. Such an agglomeration eventually leads to the

formation of an insulating polymer layer on the reactor walls that reduces the ability to control the reactor temperature. The result, referred to as "sheeting",[16] is that the reactor gets very hot and the polymer particles melt, thereby forming "sheets" of polymer on the reactor walls. Hence, this homogeneous condition requires the implementation of new, specially designed reactors and other new hardware.[17] It is most desirable for polyolefin producers to use their existing hardware (i.e. systems originally designed to produce polyolefins by the conventional heterogeneous Ziegler–Natta process, such as the Unipol® or Phillips chromium oxide processes). Such processes generally require that the catalyst be supported. Supports are generally inorganic oxides such as SiO_2,[18,19] Al_2O_3,[19] and $MgCl_2$.[17,19] Supporting the metallocene catalysts initially led to a great decrease in catalyst activity.[1,2,4,5] Technology has progressed to allow the metallocene catalysts to be supported and maintain relatively high activity. This is leading to the transformation of existing, traditional heterogeneous Ziegler–Natta reactors to employ supported metallocene catalysts. These metallocene catalyst systems allow the producer to generate a broad range of polyolefins (with a broad range in density, for example) from one single system, by only changing variables such as polymerization temperature, time, pressure, comonomer, etc. Making such a broad range of products from a single system was not previously possible with the conventional heterogeneous Ziegler–Natta systems.

Exxon put to commercial use the first metallocene solution process for polyolefin production. This is generally known as the Exxpol® process. However, the term Exxpol® is actually associated with the catalyst only and not the nature of the reaction, i.e. not whether it is solution, gas–phase, or slurry etc. Exxon, Union Carbide, their joint venture Univation, and Phillips are currently (at the time of this writing) active in metallocene research. A major potential competitor for the Exxpol catalyst will be the constrained geometry (CG) catalyst systems designed by Dow. These CG materials are similar to "half–sandwich" metallocenes in that they have one Cp ring π–bonded to a similar group IV transition metal, however they are bridged with a heteroatom such as N, or a silyl group. The Cp–metal–heteroatom bond angle is generally less than 115°,

which gave rise to the terminology "constrained geometry". Similar to the metallocenes, a co-catalyst is often used in the form of a Lewis acid. This is believed to generate a cationic active center, again similar to the active center for the metallocenes. Dow has some commercial CG products under the trade name Insite®. Phillips Petroleum is also developing a licensable metallocene system which can be employed in their traditional slurry process. Many other companies are also actively studying metallocene catalyst systems.

Since polyolefins made from metallocene catalyst systems are now commercially available, it is desirable to understand their structure–property relationships. While the molecular weight distributions of this series of polyethylene homopolymers is not as narrow as can be obtained by some other synthetic routes,[3,5] the breadth indexes $\overline{M}_w/\overline{M}_n$ from 2.34 to 3.59 are distinctly less than those of polyethylenes produced from more traditional catalysts, such as heterogeneous Ziegler–Natta which generally have $\overline{M}_w/\overline{M}_n$ = 4–8,[20] or Phillips chromium oxide systems which can have $\overline{M}_w/\overline{M}_n$ >10.

It is the goal of this study to examine the influence of molecular weight and thermal history on the properties of a series of unoriented metallocene–catalyzed linear polyethylenes. A major focus of this study is the tensile deformation properties which are critically important in determining the suitability of a material for a given application. Janzen and Register[21-23] have surveyed a large data set of deformation properties of both commercial and developmental polyethylenes. They examined the influence of density on such properties. Crist and coworkers[24] probed the affect of crystallinity and more specifically lamellar thickness on Young's modulus and yield stress for several fractionated linear polyethylenes with $\overline{M}_w$ between 32.1 kg/mol and 199 kg/mol and a whole polymer of $\overline{M}_w$=52 kg/mol, $\overline{M}_w/\overline{M}_n$ =2.89. Similarly, Kennedy and coworkers[25] examined fractionated linear polyethylenes with $\overline{M}_w$ ranging from 23.3 kg/mol to 911 kg/mol, $\overline{M}_w/\overline{M}_n$ between 1.14 and 1.43, and whole polymers with $\overline{M}_w$ between 40 kg/mol and 351 kg/mol, $\overline{M}_w/\overline{M}_n$ from 1.88 to 2.30. Related studies[26–29] were performed in the same laboratory on random ethylene copolymers.

There the authors probed the effects of molecular weight and its distribution as well as thermal treatment on deformation behavior and ultimate mechanical properties of these polyolefins. An earlier study by Popli and Mandelkern[30] involved examining the influence of the structural and morphological factors on the mechanical properties of polyethylenes which included structural variations such as linear, branched, and copolymer formulations. In general these materials had broad molecular weight distributions. The tensile deformation experiments discussed in this manuscript are similar to the previously mentioned studies. However, some distinct differences exist between laboratories in terms of the experimental procedures. One of the most notable disparities is the variation in sample preparation methods. The materials studied by Janzen and Register[21] were prepared according to ASTM D1928. The compression–molded samples prepared by Crist et. al[24] were quenched in ice water. In the cited studies by Mandelkern and workers, they have adopted a wider range of thermal treatments which allowed them to span a broader window of crystallinities and morphologies for each sample. These involved quenching from the melt to –130 °C, quenching to –78 °C, quenching in boiling water, slowly cooling in air, and slowly cooling inside the hot press, without pressure.[25] The preparations in the current study are less varied. Only two thermal treatments were applied for each material, quenching from the melt to room temperature and slowly cooling in the hot press. Details will be given in the next section. The mechanical behavior of the series is further probed with dynamic mechanical spectroscopy from –150 °C (near the γ-relaxation for the frequencies explored in this study) through the α-relaxation and to nearly the melting point. The α, β, and γ-relaxations are examined with respect to the crystal content and thermal treatment for each sample.

To complement the results from the mechanical tests, various other characterization methods have been employed. Examination of the melting endotherms by differential scanning calorimetry provided information regarding the mass fraction of the crystalline phase for each sample. These results are compared to those obtained from density measurements. Details concerning the crystalline phase, for example lamellar

thickness, were estimated from small angle x-ray scattering data. Values thus obtained were compared to transmission electron micrographs of chlorosulfonic acid–stained samples. Linear viscoelastic behavior was examined through melt–rheological measurements and correlation to solid state behavior is made where appropriate.

7.2 Experimental Approach

The polyethylene series examined in this study was prepared by Dr. M. Bruce Welch of Phillips Petroleum using a catalyst system based on bis (n-butyl cyclopentadienyl) zirconium dichloride with added MAO co–catalyst, $(n\text{–}C_4H_{10}Cp)_2ZrCl_2$ / MAO, as described in U.S. Patent 5,411,925 and in patent application EP 612,753. All polymerizations were conducted in an autoclave reactor, with no added comonomer. The reactor was first charged with the solid catalyst under an isobutane atmosphere and liquid isobutane was added. The system was then brought to near polymerization temperature, and hydrogen was added as a chain transfer agent, if desired. Ethylene monomer was then charged to the reactor, and the reactor pressure was held constant by continuous addition of ethylene during the polymerization process. The reaction was terminated after one hour by rapid venting of the apparatus. The reactor was then opened and the dry polymer fluff was removed. The reaction conditions were varied over a wide range to produce the entire series of molecular weights used in this study. Reaction temperatures spanned the range of 60–100 °C and pressures varied from 1.22 to 4.24 MPa.

Size exclusion chromatography (SEC or GPC), performed at Phillips Petroleum, provided the molecular weight distributions for the series. A Waters 150 CV GPC equipped with two Styragel HT 6E mixed–bed columns was employed using trichlorobenzene as the solvent, flowing at a rate of 1.0 mL / min at 140 °C. A small amount of stabilizer (0.5 g / L β–hydroxytoluene, BHT) was added to the polymer solution which had a concentration of 1.86 g / L. A volume of 220 μL was injected into the column for each test. A broad–standard integral method of universal calibration was used, with Phillips Marlex® BHB 5003 as the standard. The parameters used in the

Mark–Houwink–Sakurada equation,[31] $[h] = K \cdot (\overline{M}_v)^a$, were K = 0.0395 mL/g and a = 0.76.

The rheological behavior of the as–polymerized fluff was probed at Phillips Petroleum using small–strain oscillatory shear measurements performed on a Rheometrics RMS-800 parallel–plate instrument under a nitrogen atmosphere. The initial gap was set to 1.6 mm and the polymer was trimmed at the desired start temperature, where it was allowed to reach thermal equilibrium before beginning the experiment.

In utilizing the remaining characterization methods, it was more convenient to work with samples in film form rather than as powders. Films were made from the fluff by thermal compression molding. An appropriate amount of powder was loaded into a picture-frame mold and brought into thermal contact with the plates of a hot press which were at 155 °C (roughly 14° above the equilibrium melting temperature for polyethylene[32,33]). The sample was held at this condition for approximately ten minutes to allow the powder to melt. Following this, pressure was slowly applied to the mold to force the polymer to flow out into the shape of the frame. After 10–15 minutes, pressure was released while still holding the sample at 155 °C to minimize molecular orientation. Two distinct thermal histories were employed for the series of molecular weights studied; the first, referred to as "quenched," was the result of removing the mold from the hot press and sandwiching it between two room temperature steel plates, roughly 1–cm thick. The second, designated as "slowly cooled," was accomplished by leaving the mold in the hot press (again, only in thermal contact, without excess pressure) and turning off the heaters. Cooling to room temperature took approximately 8 hours by this route.

Differential scanning calorimetry (DSC) was performed on a Perkin Elmer DSC 7, which was calibrated using indium and tin standards. DSC samples weighed between 5 and 11 mg each and a heating rate of 20 K/min was applied during each scan. Each scan represents a first heating of the prepared films.

Densities were measured at Phillips Petroleum at room temperature with a density gradient column using the technique described in ASTM D 1505.

Small angle x-ray scattering (SAXS) experiments were performed with nickel filtered, slit collimated Cu*Ka* radiation (1.542 Å)[34] produced by a Philips generator, model PW1729. A Kratky camera and a one–dimensional M. Braun position–sensitive detector were used to collect the scattered radiation. Absolute, slit–smeared scattered intensities *I(s)* were calibrated through the use of a working standard (Lupolen 1811M).[34] *I(s)* will be plotted as a function of the magnitude of the scattering vector $s \equiv (2/l)\sin(q/2)$, where l is the incident beam wavelength and q is the radial scattering angle.

Transmission electron microscopy (TEM) was accomplished with a Philips model 420T at 100 kV. Samples were prepared by staining with chlorosulfonic acid[35,36] to greatly increase the electron density of the amorphous phase. This provides adequate contrast for viewing with TEM. Samples were completely immersed in chlorosulfonic acid for approximately 2 hours at 60 °C. They were then washed and allowed to dry before being microtomed. Room temperature microtomy was sufficient for producing samples which generated good images by the electron microscope. As a result the micrographs (to be presented) show darkened amorphous regions and lighter crystalline domains.

An Instron model 4400R equipped with a 1 kN tension load cell was employed for tensile testing. The cell was calibrated with an 8–kg standard (78.45 N), and ultimate loads never exceeded 140 N. All tensile tests were conducted at 20 °C with a crosshead speed of 25.4 mm/min. Specimens were stamped out of the prepared films with a "dog-bone" die (gauge length approximately 10 mm, thickness approximately 0.4 mm). At least ten specimens were tested for each condition for statistical purposes.

Strain was not determined rigorously, but rather was taken as the crosshead displacement divided by the original gauge length (10 mm). Therefore, values of Young's moduli are not absolute, but rather relative numbers for comparative purposes.

Dynamic mechanical spectra were collected by a Seiko DMS 210 (also labeled DMA or DMTA by other manufacturers). Rectangular samples measured approximately $10 \times 4 \times 0.5$ mm (≈ 2 mm^2 cross–sectional area being desirable for the instrument according to the manufacturer). The strain amplitude was set at 10 μm, which corresponds to 0.1 % strain (within the linear viscoelastic region). The samples were loaded at room temperature and then quenched to –150 °C with liquid nitrogen. The test was then started and various frequencies from 0.1 to 10 Hz were examined while ramping to approximately the melting temperature. Purified nitrogen was employed as a purge gas to prevent oxidation and degradation upon reaching elevated test temperatures. Slow heating rates were used so that many data points could be collected during the scan (0.8–2.0 K / min).

7.3 Results and Discussion

7.3–A. Molecular Weight

Molecular weight averages determined by SEC are presented Table 1. $\overline{M}_w / \overline{M}_n$ ratios, indexes of relative breadths of the molecular weight distributions, range from 2.34 to 3.59. These are somewhat larger than the values around 2.0 that have been reported for some metallocene–catalyzed polyolefins, as mentioned above, but they still are quite low in comparison with the more common Ziegler–Natta catalyzed polyolefins, where they may be at least 4–8,[20] and distinctly lower than for olefins produced with Phillips chromium oxide–type catalysts, where they often exceed 10.

The polyethylene samples will be referred to below by their weight average molecular weights, $\overline{M}_w$, in units of kg / mol.

7.3–B. Melt Rheology

Simple mathematical models formulated for representing steady–flow viscosity data (e.g., the Carreau, power law, Ellis, Cross, etc.), are often written in terms of shear rate. However, modern oscillatory rheometers monitor viscosity as a function of the oscillatory frequency, not shear rate. A common method of translating between the

two kinds of experimental data is to use the Cox-Merz rule[37] which is stated mathematically as follows:

$$h(\dot{g}) = \left|h^*(w)\right|_{w=\dot{g}} \tag{1}$$

where $h(\dot{g})$ is the steady-state shear rate ($\dot{g}$) dependent viscosity, and $\left|h^*(w)\right|$ is the magnitude of the frequency (w) dependent complex viscosity derived from dynamic oscillatory experiments. Sometimes $h(\dot{g})$ and $\left|h^*(w)\right|$ disagree at large deformation rates (which are generally not obtainable in oscillatory rheometers). However, it is well known[38] that:

$$\lim_{\dot{g}\to 0} h(\dot{g}) = \lim_{w\to 0}\left|h^*(w)\right| = h_0 \tag{2}$$

where h_0 is called the zero-shear viscosity.

The Carreau–Yasuda model has the following form:[38]

$$\frac{h(\dot{g}) - h_\infty}{h_0 - h_\infty} = \left[1 + (t_h\dot{g})^a\right]^{(n-1)/a} \tag{3}$$

where h_∞ is the infinite-shear-rate viscosity. t_h is a characteristic viscous relaxation time (denoted as λ in reference 38) which defines the location of the transition from Newtonian to shear thinning behavior. In general t_h is close to or slightly greater than the arithmetic mean time (first moment) of the terminal mode in the relaxation spectrum.[39] a is a dimensionless parameter (sometimes called "the Yasuda constant" since it was a parameter added to the Carreau equation by Yasuda) which describes the transition zone between the Newtonian plateau and the shear thinning region and is inversely related to the breadth of this zone.[39,40] The exponent $(n-1)$ defines the slope of the $h(\dot{g})$ versus $\dot{g}$ curve within the power–law region.

Graessley[41,42] presented a theory of polymer viscosity based on an entanglement concept in 1967. His development had the high–rate limiting slope of $\log h$ vs. $\log \dot{g}$

equal to –9/11. If this relationship is to be adopted in the Carreau–Yasuda model, then the quantity $(n-1)$ of equation (3) must be set equal to –9/11, or $n=2/11$. This approach is part of a protocol set forth by several scientists[39] at Phillips Petroleum, and they claim that it is useful for fitting polyethylene melt viscoelasticity data. However, such a force-fitting of the experimental data in the power law region to a slope of –9/11 requires absolute faith in the model suggested by Graessley. As might be expected, real data often deviate from theoretical models. Although, for the present work, the power law region is hardly realized for any of the experimental conditions employed here. However, if such an approach was applied to data which showed a clear power law region (in which the experimental power–law slope was not –9/11), this protocol should be avoided. In such a case, where the slope is clearly not –9/11 but the value was forced upon the Carreau–Yasuda model, the fitting procedure would return physically meaningless values of t_h, a, and perhaps even h_0. The proper protocol for such an event is to first perform a linear regression analysis on *only* the power–law region of the rheology data, noting the returned value of the slope. Then, force this value of the slope (instead of –9/11) into the subsequent Carreau–Yasuda fitting procedure. In this manner the Carreau–Yasuda fitting procedure is still simplified by fixing the value of (n–1) (as the Phillips protocol does), however the remaining parameters will maintain their physical significance. Again, due to the lack of a substantial power–law region in the data in this study, the Phillips protocol will be used.

Following the Phillips protocol (setting n equal to 2/11), assuming that h_∞ is negligible (zero), and employing the Cox–Merz rule reduces the Carreau–Yasuda model [equation (3)] to a form which was employed for fitting the experimental rheology data:

$$\left|h^*(w)\right| = h_0\left[1+(t_h w)^a\right]^{-\left(\frac{9}{11}\right)\frac{1}{a}} \tag{4}$$

The rheological behavior of the 13 kg/mol polyethylene was unobtainable since this material had too low a viscosity to measure with the rheometer at the experimental conditions employed. For the remainder of the polyethylene series, the magnitude of the complex viscosity versus frequency data at 230 °C is presented in Figure 2. The continuous curves drawn in this figure are the Carreau–Yasuda equation fits of the experimental data and the parameter values derived from the fitting are included in Table 1. Since the materials of lower molecular weights display nearly Newtonian behavior across the entire frequency range probed (for this temperature), the Carreau–Yasuda parameter h_0 is well determined but t_h and a for these materials have large uncertainties. Indeed, the fitting procedure returned error estimates larger than the parameter values for the three lower molecular weights (14, 26, and 37 kg/mol). Hence it should be borne in mind that t_h and a are not well determined for these three specific samples of the series.

In examining the details of Figure 2, it is clear that increasing molecular weight leads to an increase in the zero-shear viscosity, as expected. In fact it is well established that for many different linear polymer systems the value of h_0 scales with $(\overline{M}_w)^{3.4}$ above a critical molecular weight, generally referred to as the entanglement molecular weight[31,43,44] (M_c). Below this characteristic molecular weight, the zero–shear viscosity scales directly with molecular weight: $h_0 \propto \overline{M}_w$.

For polyethylene, the rheologically determined entanglement molecular weight is approximately 3800 g/mol,[45,46] well below the molecular weights of the materials studied here. Figure 3 shows the influence of molecular weight on h_0 for the series. In this plot, values of h_0 (at 230 °C) were derived from the Carreau–Yasuda equation fits, and the line drawn on this plot obeys the previously mentioned relationship: $h_0 \propto (\overline{M}_w)^{3.4}$. There is not a major departure of the experimental data from this line. The data point for the 839 kg/mol sample exhibits the largest deviation. A further observation regarding the series is that the location of the origin of shear thinning

(related to t_h) shifts to lower shear rate (frequency) as molecular weight increases, as expected in light of the increase in the terminal relaxation time.

The zero–shear viscosity generally has an Arrhenius form at temperatures above the melt, that is, $h_0 \propto \exp(E_a/RT)$. Hence a semilog plot of h_0 versus 1/T yields a line from which the melt flow activation energy E_a can be calculated from the slope. E_a is a measure of the temperature sensitivity of viscosity; a small value implies little effect of temperature on the viscosity while a large value implies strong dependence. For polyethylenes, the value of E_a has been shown to be a function of the chain topology. Values for *linear* polyethylene are reported between 25–30 kJ/mol.[47–52] Linear low–density polyethylene (LLDPE), which contains short–chain branching (SCB),* has a reported[51] activation energy near 30 kJ/mol, and is generally a function of SCB content.[53] Isotactic polypropylene, which can be thought of as polyethylene with one methyl branch placed very regularly on every other backbone carbon, has a melt flow activation energy of 39–43 kJ/mol.[51,54–56] However, tacticity has an influence on the melt flow activation energy for polypropylene. The atactic form has the same value as isotactic, ≈ 39 kJ/mol, but syndiotactic has been reported to have a considerably higher value of ≈ 50 kJ/mol.[55,56] Low density polyethylene (LDPE), which has many long chain branches (LCB),† has a dramatically higher activation energy near 50 kJ/mol.[51,57] Other workers have reported[57] E_a as high as 167 kJ/mol for a long chain branched polyethylene containing 7.2 long chain branches per 10,000 backbone carbon atoms. This highly branched polymer sample was generated by gamma irradiation of high density polyethylene (HDPE), which would likely produce some amount of SCB as well. Hence the presence of LCB has a significantly larger influence on the melt flow activation energy than SCB. From Table 1 the values of E_a for the 51 kg/mol and 320 kg/mol samples are both approximately 30 kJ/mol. Since these two samples represent

---

* *LLDPE typically has 2-6 carbon members in the side chain. This is due to the fact that it is made by copolymerzation of ethylene with monomers such as 1-butene, 1-hexene, 1-octene, etc.*

† *A good definition of a long chain branch is one whose length exceeds the entanglement molecular weight of the polymer.*

nearly the highest and lowest molecular weights of the series, it is anticipated that all the intermediate molecular weight samples also have similar values for the activation energy. From this, the behavior in Figure 3, and supporting evidence from DMS to be addressed later, it can be concluded that LCB is essentially undetectable throughout the series.

It is worth noting, however, that recently other researchers have found[53] a surplus in activation energy (than would be expected of polyethylene without LCB) within metallocene polyolefins. They attribute the higher value to very small concentrations of LCB. Since the measured E_a of ≈ 30.1 – 30.3 kJ / mol for this study slightly exceeds even the highest values reported in the literature for linear polyethylene, very small concentrations of LCB may indeed be present in the series. It is interesting to note that new metallocene catalysts have been made recently which can generate LCB in polyolefins.[58]

7.3–C. Differential Scanning Calorimetry

The first heating scans for the series of quenched polyethylene samples are shown in Figure 4, and the corresponding scans of the slowly cooled samples in Figure 5. Each scan is displaced vertically for clarity. The dashed line of Figure 4 at 133.6 °C marks the peak of the melting endotherm for the 13 kg / mol sample, and is drawn to highlight the variation in the location of the melting points with molecular weight. Analogously, a dashed line is drawn in Figure 5 at 135.0 °C, the peak of the melting endotherm for the slowly cooled 13 kg / mol polyethylene material.

The melting endotherms of the higher molecular weight materials appear to be broader than those of the lower molecular weight materials for both thermal treatments. The higher molecular weight polymers are kinetically limited to produce less perfect crystals (have more defects) of a wider size distribution which leads to this observed endotherm broadening.[33] This can be attributed to the presence of a large number of entanglements for the higher molecular weight materials.

A crude calculation of the average number of entanglements per chain can be made by dividing the molecular weight of the polymer by the entanglement–spacing

molecular weight, M_e. One approach to obtain M_e is to determine it from the plateau modulus, G_N^0, as follows:[59–62]

$$G_N^0 = \frac{4rRT}{5M_e} \tag{5}$$

where r is the sample density at the absolute temperature T, and R is the universal gas constant. Equation (5) is reminiscent of that derived from ideal rubber elasticity,[63] (with M_e replaced by the molecular weight between crosslinks), however with the factor of $4/5$. This factor is a result of the Doi–Edwards theory, which dictates that $1/5$ of the stress is relaxed by processes faster than reptation.[64,65] However, many scientists employ the equation without the $4/5$ factor (as synonymous with rubber elasticity) without criticism.[65] Hence there are two slightly different definitions of M_e in the literature.

Using the data of Graessley and Edwards[45] (G_N^0 =2.06 MPa, T=463 K, r=0.76 g/cm^3), one can calculate from equation (5) M_e = 1140 g/mol for linear polyethylene. More recently, Carrella, Graessley, and Fetters[66] have reported a value of M_e = 830 g/mol for polyethylene. Still another value can be estimated from a rule–of–thumb relation, namely $M_e = M_c/2$ or $M_c/3$. Considering the M_c value of 3800 mentioned earlier, this relation yields M_e = 1300 to 1900 g/mol. This is a broad range of values for M_e. Using the value of 830 g/mol for M_e to calculate the number of entanglements, the 839 kg/mol sample has an average of 1011 entanglements per chain in the isotropic melt, whereas the 13 kg/mol specimen has only 16.

Tie molecules and the characteristics of the crystal–amorphous interface will also affect the melting behavior of macromolecules but the quantitative description of this effect is impossible without the knowledge of the molecular structure at the phase boundary.[33]

Taking from the literature the heat of fusion of purely crystalline polyethylene to be 293 J/g (70 cal/g),[32,67,68] the crystal mass fraction (w_c) in each polyethylene sample is given by $w_c = \Delta H_m/293$ J/g, where ΔH_m is the measured heat of melting observed in

the DSC scans. A useful method of evaluating the area under the melting endotherm is to extrapolate the liquid line in the DSC trace (this data being more equilibrium in nature) back to the semicrystalline state. Where this extrapolated line intersects the semicrystalline data will define the start of the melting endotherm. A more rigorous approach would be to construct a baseline in a manner which weight averages the specific heats of the amorphous and crystalline phases as a function of temperature. Using the former technique, the results of the w_c calculation are listed in Table 2. Crystallinities vary from 52% for the quenched 839 kg/mol sample to 87% for the slowly cooled, 13 kg/mol material. Clearly, for a given thermal treatment, increasing molecular weight leads to a decrease in the level of crystallinity. This has been observed in the past[69] and is a result of the reduction in the rate of crystallization with increasing molecular weight due to entanglement and viscosity effects.

7.3–D. Density Measurements

Room temperature densities for the series, as determined by the density gradient method, are listed in Table 2. Percent crystallinity values were calculated using the measured densities to complement those derived calorimetrically. Assuming a two phase system composed of an amorphous phase of density[22] $r_{am} = 0.852$ g/cm^3 and a crystalline phase of density[70] $r_c = 1.010$ g/cm^3, both the crystal volume fraction (f_c) and crystal mass fraction (w_c) can be calculated through the following relations:[34]

$$f_c = \frac{r - r_{am}}{r_c - r_{am}} \quad and \quad w_c = f_c \frac{r_c}{r} \tag{6}$$

Alternate, perhaps more common values for the room temperature crystalline and amorphous phase densities of linear polyethylene are those given by Chiang and Flory[71] as 1.000 and 0.853 g/cm^3. These values are in close proximity to the numbers given above.

Values of w_c for the series vary from 54% for the quenched 839 kg/mol sample to 83% for the slowly cooled 13 kg/mol material. There is a general decrease in the

density, for a given thermal treatment, with increasing molecular weight, as shown in Figure 6. This plot also shows that for a given molecular weight, the slowly cooled samples are more dense than the quenched counterparts. The materials of higher density are also of higher crystal content, as would be expected from equation (6). Percent crystallinities determined from the density are, in general, in good agreement with those ascertained calorimetrically as seen in Figure 7 and also Table 2. The line drawn in the plot has a slope of one, and is not a fit of the data but rather it represents perfect correspondence between the two techniques. Note that there is not a significant deviation of the data points from this line. In light of this agreement it may be concluded that during the DSC heating scans, negligible reorganization occurs at the experimental heating rate (20 K/min). Otherwise, the melting endotherms would be influenced by this reorganization and the resulting crystallinity calculations would be higher than those obtained from the density measurements. w_c calculated from the density will be used for the presentation of data throughout this report. This is an arbitrary choice since density and DSC yield similar values.

7.3–E. Small Angle X-ray Scattering Behavior

Figure 8 shows *I(s)* vs. *s* for the quenched series and Figure 9 for the slowly cooled series. Most of the curves show a characteristic interference peak, associated with a correlation length present in the samples. This correlation length is associated with the long spacing, which is a combination of one lamellar thickness (ℓ_c) and one amorphous layer thickness (ℓ_{am}) for a stacked lamellar structure. For both the quenched and slowly cooled series, the interference peaks shift to smaller angles (and hence the long spacings increase) with increasing molecular weight. Similar results have been noted by Rault and Robelin–Souffaché[72] who have plotted the long spacing versus the square root of molecular weight for various linear polyethylenes. They observed that cooling from the melt at 2 K/min, 10 K/min, and rapid quenching all led to nearly identical slopes in this plot. The increase in the long spacing observed for the materials in this

study could be due to an increase in ℓ_c or an increase in ℓ_{am}, or both. From the TEM results to be discussed in the next section, it is ℓ_c that increases with molecular weight.

For a given molecular weight, the slowly cooled material has a larger long spacing than the quenched material. This is primarily due to a difference in ℓ_c, being larger for the slowly cooled material. The slowly cooled samples have larger ℓ_c because they were effectively crystallized at a smaller undercooling (also called the supercooling). The average initial lamellar thickness (ℓ_g^*, derived from the Lauritzen–Hoffman[73] model of crystal growth for flexible chains) is expected to be related to the undercooling $\Delta T = T_m - T_c$ as:

$$\ell_g^* \propto 1/\Delta T \tag{7}$$

Hence the closer to the melting temperature (T_m) that a polymer is crystallized (T_c), the thicker will be the average lamella.

7.3–F. Transmission Electron Microscopy

TEM was used to probe the morphological structure in the polyethylene series. Micrographs are shown in Figure 10 (A–H). Two magnifications are shown for each sample; the lower reveals the nature of the superstructure and the higher shows the character of the lamellae. Sharper contrast is generally noted for slowly cooled samples when compared to their quenched counterparts. This is due to the sharper separation of a more perfect crystalline phase and amorphous phase (and smaller interphase) in the slowly cooled samples compared to quenched samples of the same molecular weight. For the quenched set, the lack of this sharp separation leads to a more “fuzzy” or less defined lamellar texture. All samples probed by TEM (quenched and slowly cooled 13, 51, 267, and 839 kg/mol materials) possessed stacked lamellar structures. No supermolecular structure is obvious in the micrographs although in two cases structures resembling spherulites are observed–see Figure 10 (D) and (E).

Polyethylene of 13 kg / mol molecular weight displays very long lamellae that remain fairly straight in the lateral direction as seen in Figure 10 (A), quenched, and (B), slowly cooled. To follow existing terminology,[74–76] the lamellae of the quenched 13 kg / mol material are mostly curved, but some appear *planar*. These lamellae are only slightly curved over their long reaching distances, approximately 1 μm or more. The slowly cooled 13 kg / mol sample has both planar and *ridged* lamellae. In the high magnification image of (B), adjacent planar and ridged lamellae lie parallel (near the bottom, center of micrograph), suggesting a common crystallography as reported by Bassett and Hodge.[74] The average thickness of lamellae in the 13 kg / mol materials is certainly greater for the slowly cooled sample (≈ 180 Å) compared to the quenched (≈ 100 Å), as expected from the undercooling argument of equation (7). The thickness of these lamellae appears less than those estimated from the SAXS data (≈ 235 Å and 150 Å, respectively). This discrepancy may be a consequence of the staining procedure since it has been observed[74,77,78] that lamellar thickness is often depressed by the chlorosulfonation technique.

In the low magnification image in (B), the majority of the local lamellae are oriented such that their fold surfaces are most visible rather than the thickness direction. This gives the appearance of stepping up and down between consecutive ridged lamellae, previously observed[74] for an etched polyethylene sample.

The 51 kg / mol slowly cooled material in (D) shows a structure that resembles part of a spherulite (reminiscent of Figure 4 of Bassett and Hodge[74]). The lamellae in this micrograph run fairly straight through the superstructure, with slight splaying outward. Well defined spherulites are not easily seen in a lower magnification micrograph (not shown). The lamellae are also planar in a few areas, although the majority are curved. These lamellae are clearly thicker (≈ 160 Å) than the mostly curved lamellae seen in the quenched 51 kg / mol material (≈ 100 Å) shown in (C). For this quenched material, some *C* and *S–shaped*[74–76,79] lamellae are observed.

For the 267 kg / mol molecular weight materials, a clear transformation to dominant C and S–shapes is seen. Three magnifications are shown, the intermediate

magnification for the quenched material in (E) shows perhaps part of a spherulite which would display optical banding.[80] Optical banding occurs due to spiraling of the *c*-axis (chain axis) about the *b*-axis while traveling along the radial direction of the spherulite.[76,81–84] Four "bands" can be discerned in the image (indicated by arrows in the micrograph). The spherulitic superstructure is not obvious in the lower magnification micrograph, which has some artifacts (dark spots) from the staining procedure. The slowly cooled 267 kg / mol sample in (F) shows irregular curved lamellae, roughly of C and S shapes. However, thickness as determined by TEM is suspect since the lamellae in the micrographs might be viewed from a tilted orientation.

Both thermal treatments for the 839 kg / mol polyethylene show, in (G) and (H), large curvature of relatively short lamellae. Many C and S–shaped lamellae are visible, especially in the high magnification image of the quenched sample (G). The slowly cooled material of (H) displays some of the thickest lamellae of the series, which are on the order of 240 Å, and appear to be slightly longer than the lamellae of the quenched sample.

Generally speaking, low molecular weight samples possess very long, fairly straight (in the lateral direction), lamellae. They are mostly planar, with some areas appearing ridged in nature. Increasing the molecular weight leads to shorter, more curved lamellae. Curved lamellae progress into C and S shapes. Curving has been suggested[74] to be due to deformation during growth predominantly by shear forces which are present under régime II crystallization conditions. The changes in morphology observed with increasing molecular weight for the series has similarly been observed by Bassett, as referenced above,[74–77] and by others as well.[85,86] Fractionated polyethylenes of molecular weights 5.6, 11, 46, and 195 kg / mol, quenched from the melt, have been observed to transform similarly from long, planar, straight lamellae to short, curved lamellae in references 85 and 86.

7.3–G. Mechanical Properties

In this chapter the author adopts the use engineering stress, σ_0, and nominal strain, ε. Yield stress and yield strain, σ_y and ε_y, are defined as the values of σ_0 and ε at the point

where a distinct yield onset is observed, that is, where a peak in the σ_0–vs.–ε curve occurs. Similarly, the values of stress at break and strain at break, σ_b and ε_b, are defined by the point at which the material breaks, except for the case of the quenched 51 kg / mol material which breaks in a peculiar fashion. For this material, the values of σ_b and ε_b are taken at the point just before formation of a hole in the center of the sample width, near one end of the dogbone gauge length, which is accompanied by a sharp decrease in stress, to be discussed later. The term tensile strength is avoided here since in some cases it may refer to yield conditions and in others break conditions. Toughness is defined as:

$$\int_{e=0}^{e_b} s_0 \, de \tag{8}$$

which is simply stated as the area under the σ_0–vs.–ε curve. Although toughness is often reported in units of stress (which is certainly acceptable), it is preferred here to employ the units of energy per volume. Treating it in this way leads one to the simple interpretation of toughness as the total energy (or work) required per unit volume to cause failure in the sample.[87,88]

The lowest molecular weight polyethylene material (13 kg / mol) could not be tested in the Instron due to extreme brittleness. Merely closing the pneumatic grips caused the sample to fracture. This was the case for both the quenched (79% crystalline) and slowly cooled (83% crystalline) thermal treatments. As a result, the lowest molecular weight sample tested was the 51 kg / mol material. The stress–strain traces for the quenched and slowly cooled materials for the various molecular weights are presented in Figure 11 and Figure 12, respectively. Both figures have the same scaling to make differences in the data readily apparent. For each molecular weight and cooling history, one stress–strain curve that was most representative was plotted in the appropriate figure. (That is, the author chose the one of the ten samples that had mechanical properties closest to the statistical averages derived from all ten specimens. The error bars in Figure 15 through Figure 18 represent the standard deviations from these averages). In Figure 11 and Figure 12, breaking points are marked by the symbol

×, except for the quenched 51 kg/mol specimen. This material showed a rather peculiar failure process as mentioned earlier. First of all, as this ductile material was straining beyond the yield point, the stress level remained fairly constant (no strain hardening). At high strains (≈ 7), a small central hole developed in the dogbone at one end of the gauge length. As the level of strain continued to increase, this hole grew until finally the sample broke. It is the growth of this hole that leads to the sharp decrease in the stress, rather than a distinct break point. This behavior was observed for all ten quenched 51 kg/mol specimens. In fact, in the final failed specimens, a characteristic "forked–tongue" shape was noted where the hole finally led to failure. Again, this peculiar shape was observed for all ten specimens, and four representative ones are shown in Figure 13. The reason for this behavior is not understood, but it appears to be a property of the quenched 51 kg/mol material, and not a result of the deformation process being non-uniaxial at high strains (due to imperfect alignment of the samples prior to the test). If alignment were the cause, the other molecular weights such as 105, 165, and 267 kg/mol should have displayed similar behavior since these materials deformed to a similar (and even greater) strain than the 51 kg/mol samples. Not a single hole developed or forked–tongue failure surface was noted for any of the other samples.

Unlike the quenched 51 kg/mol material, the slowly cooled form was brittle under the test conditions, and broke shortly after yielding. Hence for a molecular weight of 51 kg/mol, a ductile–to–brittle transition exists somewhere between 70% crystallinity (quenched, ductile material) and 78% (slowly cooled, brittle material). Mandelkern and coworkers have observed[89] a ductile–to–brittle transition in a comparable linear polyethylene ($\overline{M}_w$ = 54 kg/mol, $\overline{M}_n$ = 23 kg/mol) at a value of 62% crystallinity (these authors varied the thermal history likewise to generate different crystal contents and employed the same drawing conditions). These authors also report that this transition appears to be independent of the type of crystalline superstructure but dependent on

crystal content and molecular weight.* They conclude that a small interlamellar thickness (amorphous layer thickness) is likely responsible for the brittle behavior since small amorphous domains cannot sustain large deformations.[89] Another important factor would be the presence of tie molecules between lamellae. These chains are responsible for carrying a large amount of the stress during the tensile test and the number of tie chains increases with molecular weight.[90] It has also been observed[91] that the number of ties increases with short–chain branch content. The presence (or lack) of tie chains is one of the critical factors in determining whether a semicrystalline polymer (which is above the glass transition temperature of the amorphous phase) is brittle or ductile. Quenching the 51 kg/mol material may lead to more tie molecules than slowly cooling the same material due to kinetic differences in the crystallization process. From the TEM images of Figure 10, the brittle, slowly cooled 51 kg/mol material in (D) has distinctly thicker lamellae of ≈ 160 Å (and would likely have fewer tie chains) compared to the ≈ 100 Å thick lamellae of the quenched 51 kg/mol material in (C).

Figure 14 shows an expanded view of the stress–strain curves in the vicinity of yielding for both quenched and slowly cooled treatments. It can be seen from this figure that the yield peak becomes less distinct with increasing molecular weight. The quenched 839 kg/mol polyethylene sample actually does not show a yield maximum, but rather displays a knee and immediately begins to strain harden as manifested by the rapid increase in stress level with strain. Kennedy et al.[25] have similarly noted that the yield becomes more diffuse with increasing molecular weight for linear polyethylenes of two types: narrow fractions with $\overline{M}_w/\overline{M}_n$ between 1.14 and 1.43, and zirconocene–catalyzed[92] whole polymers with $\overline{M}_w/\overline{M}_n \approx 2.0$.

The other materials of the series between the 51 kg/mol and quenched 839 kg/mol behaved in a more typical manner. That is, each displayed a distinct yield point, followed by some amount of strain hardening, and a clear break point. The amount of

---

* *In this study by Mandelkern only lower molecular weights were probed ($\overline{M}_w \leq 120$ kg/mol) since unobtainable crosshead speeds would be required to observe this transition for samples of higher molecular weight.*

strain hardening (steepness of the curve in the irrecoverable flow region) increased with molecular weight as previously reported elsewhere,[25] presumably because the number of tie molecules increases with molecular weight.

Clearly the stress–strain behavior is dependent on molecular weight and thermal history. Crystal content plays a major role in the small–strain deformation properties (Young's modulus E, ε_y and σ_y) in semicrystalline systems and molecular weight and thermal history determine the crystal content. For both thermal histories, the variation of E, ε_y and σ_y with crystallinity is illustrated in Figure 15.

As expected, E increases with crystal content, in fact in a nearly linear fashion. Janzen and Register[21] have observed a similar relationship between E and density for various polyethylenes. However, at very low values of density, $r < 0.92\ \mathrm{g/cm^3}$ (highly branched molecules), these authors observe a leveling–off in the modulus. The sample set studied here ($r > 0.93\ \mathrm{g/cm^3}$) does not reach a low enough value of density for this to be observed clearly. Popli and Mandelkern[30] also observe a similar lower plateau when they include branched polyethylenes in their E–density analysis.

Not surprisingly, σ_y also increases with crystallinity (Figure 15) in a nearly linear fashion. Janzen and Register reported[21] a sigmoidal shape to the σ_y–density plot (which covers a broader range of density than the series studied here, particularly in the lower density range). The σ_y data of Crist and coworkers[24] extend to even lower densities still, but their results would appear to closely follow the sigmoidal shape proposed by Janzen and Register.[21] Thus the present yield stress results and those reported in references 3 and 24 are in very good general agreement. Also, Kennedy et al. report[25] a linear dependence with an upper plateau for their ranges of crystallinity. Capaccio and Ward have found[93] that σ_y increases with crystallinity at constant molecular weight for unoriented, melt–crystallized polyethylenes, which is similarly observed in the materials of this study.

There is a decrease in ε_y with crystal content (Figure 15), as expected since it is the amorphous fraction that can undergo the necessary deformation. Janzen and Register

noticed a linear relation between density and ε_y, which is in agreement with the data presented here.[21–23]

In Figure 15 the data for the slowly cooled samples coincide with the data for the quenched samples. The significance of this is that the small–deformation parameters *E*, σ_y, and ε_y are only dependent on the crystal content, and not on the molecular weight, crystalline superstructure, or other morphological features. This is typical for isotropic semicrystalline systems.[21]

Normalizing the yield strain (for a material above its glass transition temperature) is an approach that has been applied by Mohajer and Wilkes[94] for a copolyester made from the ring opening polymerization of the dimers of lactic and glycolic acid. These authors normalized ε_y by the spherulite content* for tensile experiments carried out above T_g. For their material, the (isolated) spherulites behave as a hard filler in a soft, rubbery matrix.† They noted that the normalized ε_y maintained a constant value across a broad range of spherulite content (0-90%, by projected area in thin films). In Figure 16 is shown a similar normalized ε_y, which is calculated by multiplying ε_y by the crystalline mass fraction w_c and scaling so the entire possible range is 0 to 1, plotted versus percent crystallinity. For the slowly cooled samples, this normalized ε_y is roughly 1 for the range of crystallinities seen here, however the quenched samples show a slight decrease in the normalized ε_y with increasing crystalline content. This suggests that some other factor, aside from just the crystal content, plays a role in the observed ε_y for these quenched samples. In this figure σ_y has also been normalized, but by dividing σ_y by w_c, and then scaled so that the entire range of possible values again lies between 0 and 1. The resulting normalized σ_y is relatively constant across the range

---

* *In reference 94 both the yield and break strain data are normalized by* ***spherulite content*** *(a* ***semicrystalline*** *entity), for thin films with disk-like spherulites. In the present work the data are normalized by the crystal content directly.*

† *This is in accord with the interpretation in note 33 of reference 22, where the moduli measured for these materials were mentioned as being reasonably well approximated (because of the geometry) by the Van der Poel–Smith–Christensen–Lo binary composite model.*

of crystalline content for both thermal treatments, implying that the crystal content is the main factor which determines the observed yield stress for these materials.

Toughness and ε_b behave differently with respect to crystal content, as both go through a maximum (Figure 17). These are large–strain deformation properties, and as such, molecular weight plays a major role in their behavior in addition to crystal content. As seen in equation (8), toughness is a function of both σ_o and ε. There are many competing processes that cause the observed relationship between toughness and crystal content (or molecular weight). In general, higher molecular weights produce more entanglements per chain, more tie molecules between lamellae, longer relaxation times for reptation,[95] and lower crystal contents (for constant thermal treatment) than do lower molecular weights. In polymers of high molecular weight, the many tie molecules allow the sample to carry large stresses, but prevent the sample from deforming to high strains. Also, long relaxation times may prevent high strains (consider the time constant t_h from the Carreau–Yasuda analysis of the rheological behavior and compare high with low molecular weight; however it should be noted that t_h reflects the melt flow behavior and the current discussion involves the solid state). Lower crystal contents would allow greater ultimate strains while carrying less stress. For low molecular weights, shorter relaxation times, fewer entanglements, and fewer tie molecules would drive ε_b upward, but higher crystal contents would cause it to decrease and increase the stress. It is the combination of all of these processes that result, for a given deformation rate, in the behavior of toughness and ε_b seen in Figure 17. Figure 18 plots ε_b versus $\log \overline{M}_w$, a presentation complementary to Figure 17. Although this plot also shows a maximum, the main point to emphasize here is that the differences in ε_b between quenched and slowly cooled samples decrease with increasing molecular weight. That is, at the given rate of deformation, the level of crystallinity becomes a less dominant factor in determining ε_b as molecular weight increases. (The data for the quenched and slowly cooled samples are converging to a common value of ε_b at very high molecular weights). For example, at 51 kg/mol, the quenched sample has a crystallinity of 70%, the slowly cooled material 78%, and the

difference in ε_b for these two materials is approximately 7. On the other hand, the 839 kg / mol material has crystallinities of 54% and 62% for the quenched and slowly cooled samples respectively (the same difference in percent crystallinity as the 51 kg / mol samples, ≈ 8 %), but ε_b values vary by only 0.5. Others[25,30,93] have plotted ε_b against log(molecular weight) and have observed a decrease in ε_b with increasing molecular weight. These researchers have not tested polyethylenes with molecular weights as low as 51 kg / mol, however, where this author observes a significant drop in ε_b (Figure 18). This drop is most likely due to the large amount of crystalline phase (78%) or rather a lack of the more compliant amorphous material as well as very few tie molecules between lamellae.

7.3–H. Dynamic Mechanical Spectroscopy

The mechanical behavior of the series was further examined by DMS. In these experiments three mechanical relaxations of polyethylene were examined, the α, β, and γ–relaxations. These relaxation processes are described in detail elsewhere.[96–108] Observing all three of these relaxations required scanning from low temperatures (≈ –150 °C for the frequencies used) to nearly the melting point. Plots of storage modulus (*E'*) and tan*d* = *E"/E'* (both at 1 Hz) versus temperature appear in Figure 19 (A) and (B) for the quenched series and in Figure 20 (A) and (B) for the slowly cooled series.

First consider the lowest–temperature relaxation process, the γ–relaxation. This relaxation is obvious in the tan*d* plots, and its magnitude depends on density, or more appropriately, on amorphous content.[96,101] A closer look at the γ process is given in Figure 21 (A) for the slowly cooled series. There are distinct differences, among the samples, in the magnitudes of the γ–relaxation as seen in the tan*d* peaks. This is shown another way in Figure 21 (B), where the peak heights of the γ and β–relaxations are plotted as functions of the calculated amorphous content. Some additional factor must also play a role in the γ process since the data for the quenched series do not coincide with the data for the slowly cooled series (which would be the case if amorphous content were the only factor). The γ process has been described[101] as a single process

occurring exclusively in the amorphous phase of polyethylene and is assigned[102] to the conversion of a "kink" in an otherwise all–trans conformation sequence* (...t t t g^+ t g^+ t t t...), to a mirror image of itself (...t t t g^- t g^- t t t...).[102]

The β–relaxations for this series of polyethylenes are very small in magnitude (and all appear as more of a shoulder to the α–relaxations than a peak), and in fact are difficult to discern in some cases. It has been established[96,97,101] that the magnitude of this relaxation increases with branching content. For linear polyethylene, the β–relaxation[96,97,101,109] usually spans a broad temperature window and the magnitude of the relaxation is almost negligible. The same is observed for the materials of this study which supports the earlier conclusion from the melt flow activation energies that the entire series lacks extensive long chain branching. Again referring to Figure 21 (B), the magnitude of the peak in the β region has been plotted as a function of the amorphous content for the slowly cooled series. Despite the very small magnitudes, there appears to be a weak trend here. A dominant effect on the β–relaxation has been observed[109] in designed experiments where the methyl branch content was steadily increased resulting in an increase in the magnitude of the β peak. However, Cooper and McCrum[110] have also observed an apparent β peak due to quenching a linear polyethylene sample from room temperature to liquid–nitrogen temperature before collecting the dynamic mechanical data upon subsequent heating. Data collected on the same material during slowly cooling from room temperature and waiting for thermal equilibrium at each measurement temperature fails to produce this peak in the β region. This second experimental method is considered preferable since the sample is closer to this equilibrium condition, whereas the quenched sample probably has frozen–in thermoelastic stresses from the cooling.[110] These stresses are perceived to generate the artifact in the β region.[110] Quenching before the experiment also causes an increase the magnitude of the γ relaxation.[110] The bumps observed in the β region in Figure 19 (B) and Figure 20 (B) may be due to quenching before the tests and may not

* *t = trans conformer, g^+ = gauche$^+$, g^- = gauche$^-$*

be true relaxations. The trend in the peak heights of the β relaxation in Figure 21 (increasing with increasing molecular weight and hence increasing relaxation time) is in the correct direction to be in accord with this explanation.

In Figure 19 (B) and Figure 20 (B), the α relaxations clearly have much higher magnitudes than the other, lower–temperature relaxations. The α–relaxation, when observed dielectrically or by nuclear magnetic resonance spectroscopy, has been assigned[96] to reorientation of molecules within the crystals. A plausible interpretation[102] of this relaxation is the 180° rotational jump followed by translation of the chain through the crystallographic *c*-axis (the chain axis) by one methylene group. This gives rise to a relaxation which can be observed dielectrically or with nuclear magnetic resonance spectroscopy. But the way in which this process would produce a *mechanical* relaxation is not known.[96] In fact the mechanical α–relaxation has been assigned[101] to the amorphous fraction, although it requires the presence of a crystal phase. The mechanical α process is broader and has a longer central relaxation time than the dielectric process.[101] The molecular activity for the mechanical relaxation has been associated with the softening or deformation of the amorphous component and the relaxation time is dependent on lamellar thickness.[101] The characteristics of the mechanical α process are also dependent on molecular orientation.[111,112] The temperature of the α process is also known to increase with lamellar thickness for single crystal mats,[113,114] although this trend is not apparent for the data shown in Figure 19 (B) and Figure 20 (B). The α–relaxations all begin at ≈ 0 °C, and show a broad maximum at nearly the same temperature (≈ 110 °C), irrespective of lamellar thickness (which increases with molecular weight, recall the TEM results). There is a marked difference, however, in the shapes of the α–relaxations when comparing the quenched samples of Figure 19 (B) to the slowly cooled samples of Figure 20 (B). In the quenched materials, there is a distinct α peak. However, in the slowly cooled samples, the α–relaxation appears as more of a shoulder than a peak. The breadths of both are similar. The upturn in the tan*d* data at temperatures in excess of 130 °C is due to melting. The data for the slowly cooled samples in the α region most likely represent the properties

of the sample prior to the experiment. However, the quenched samples could easily reorganize during the slow heating scan as appropriate temperatures are reached, and hence the properties of these samples could be changing during the experiment.[97,111] (The heating rate through the crystallization window of polyethylene during the DMS scans is between 0.8 and 2.0 K / min. This would allow more than adequate time for the polymer chains in the quenched samples to reorganize during the test.) The α–relaxation peak for the quenched samples therefore may include some component attributable to the molecular motions during any reorganization process that may occur, however a precise fundamental interpretation is impossible.[97] Hence this reorganization process could account for the observed differences in the general shapes of the α–relaxations when comparing the quenched to the slowly cooled polyethylenes.

7.4 Conclusions

For the metallocene–catalyzed polyethylenes examined in this study, the conclusions below can be drawn concerning the effects of molecular weight and thermal history.

- Increasing molecular weight increases h_0 (at 230 °C) and shifts the onset of shear thinning to lower frequencies or shear rates.
- The 51 and 320 kg / mol materials both have a melt flow activation energy $E_a \approx 30$ kJ / mol. Values for the other molecular weights are likely to be very nearly the same, and this value implies that the entire series is essentially linear. This conclusion is supported by the dynamic mechanical spectroscopy in which all samples in the series displayed very small magnitude β–relaxations, a characteristic of linear polyethylenes.
- For a given thermal history (quenched or slowly cooled), the resulting crystallinity level (and density) decreases with increasing molecular weight.
- The average long spacing, lamellar thickness, and amorphous layer thickness increase with molecular weight for both thermal treatments. The amorphous layer thickness is independent of thermal treatment, but the lamellar thickness is greater

for the slowly cooled materials which accounts for the larger long spacing for a given molecular weight.

- TEM shows that low molecular weight polyethylenes have long, straight (in the lateral direction) planar, and some ridged lamellae, and as molecular weight increases the lamellae become shorter and curved. For the higher molecular weight samples (267 and 839 kg / mol), C and S–shaped lamellae are prevalent.
- For the 51 kg / mol material, a ductile–to–brittle transition exists between 70% (quenched) and 78% (slowly cooled) crystallinity for the drawing conditions employed in this study.
- Increasing molecular weight results in a suppression of the yielding point; the magnitude of the "peak" at the yield point decreases with increasing molecular weight. In fact the quenched form of the highest molecular weight material (839 kg / mol) shows no distinct yield peak in contrast to all lower molecular weights.
- As the crystal content increases, both Young's modulus E and the yield stress σ_y increase, while the yield strain ε_y decreases, all in a linear fashion for the range of crystallinity probed in this study.
- The above three small–deformation mechanical properties E, σ_y, and ε_y, are only dependent on the crystal content, and seemingly not on the molecular weight, crystalline superstructure, or other morphological features.
- The level of crystallinity becomes a less important factor in determining the value of the strain at break ε_b as molecular weight becomes very large.
- The magnitude of the peak of the mechanical γ–relaxation is dependent on the amorphous content.

7.5 Acknowledgments

Major parts of this chapter were put into manuscript form and submitted to *Polymer*. The present author would like to acknowledge the co–authors from Phillips Petroleum on that manuscript for their contributions to this work: Dr. Jay Janzen, Dr. David Rohlfing, and Dr. M. Bruce Welch. The author wishes to extend his gratitude to Steve

McCartney for the transmission electron microscopy work, and to Dr. David F. Register and Fred J. Burwell for the density measurements. Also Dr. Timothy W. Johnson and Delores J. Henson should be acknowledged for the determinations of molecular weight distributions and also Michael J. Hicks for the rheological measurements.

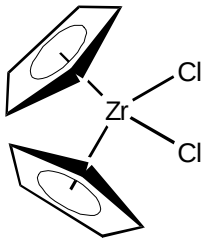

Figure 1. A generic bent zirconocene referred to as Cp_2ZrCl_2.

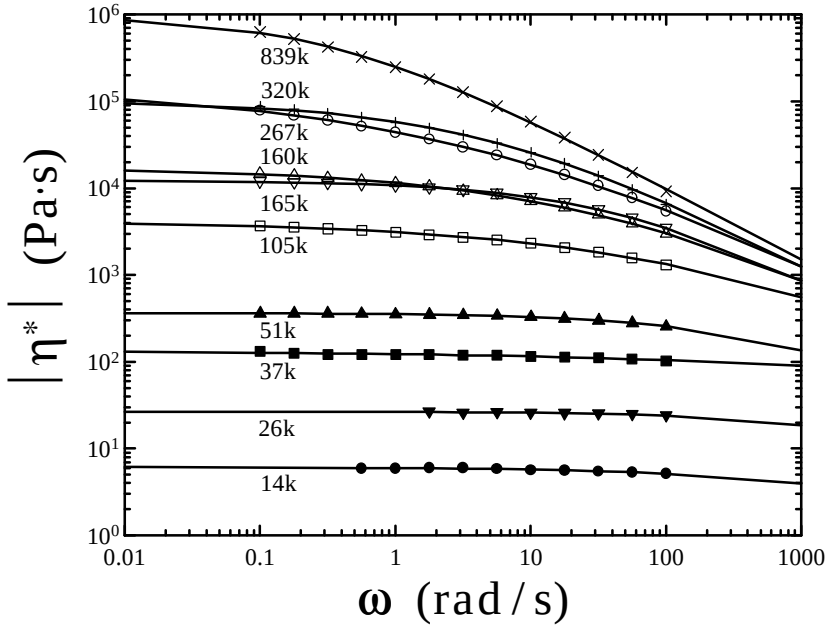

Figure 2. Melt rheological behavior of the polyethylene series: $\left|h^*(w)\right|$ at 230 °C.

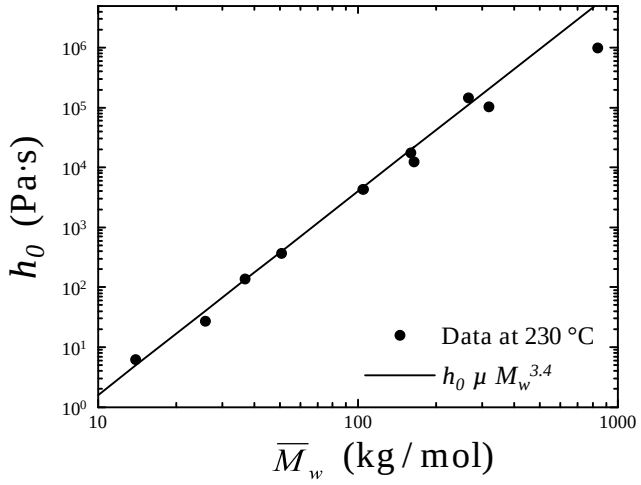

Figure 3. Zero-shear viscosity at 230 °C versus $\overline{M}_w$ for the polyethylene series.

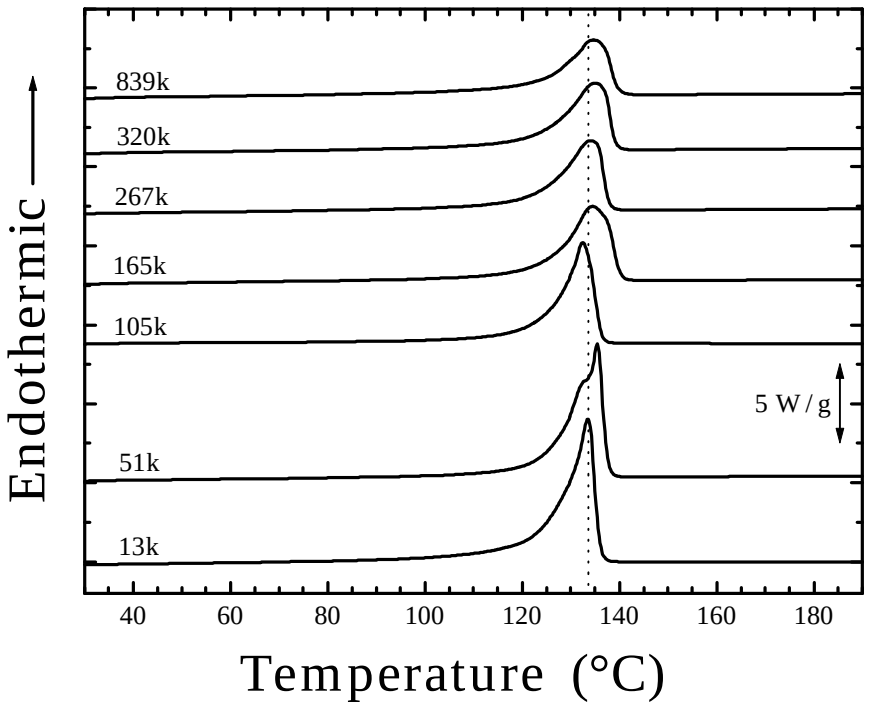

Figure 4. DSC scans of the quenched polyethylene series. Traces are displaced vertically for clarity.

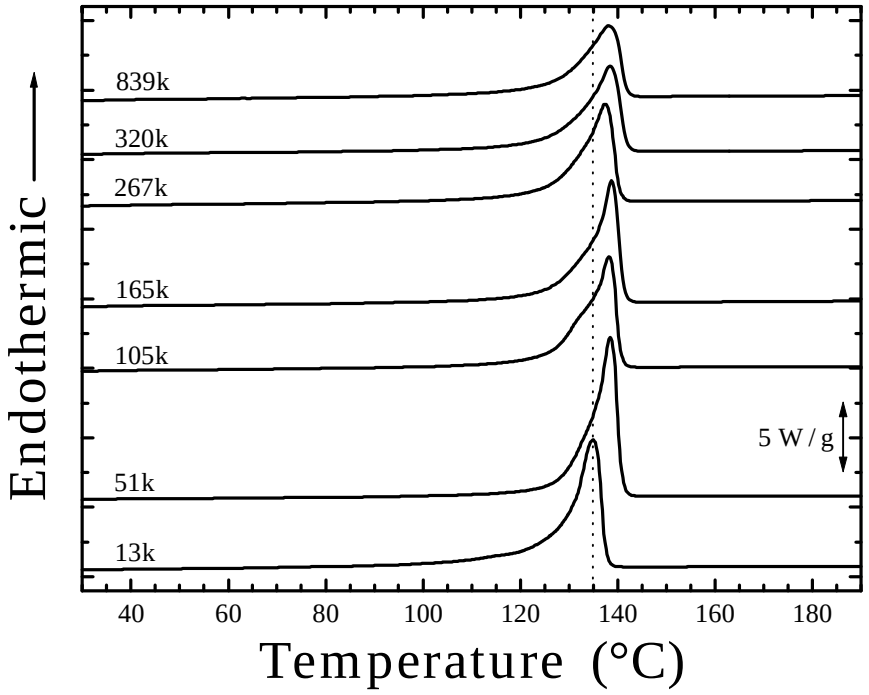

Figure 5. DSC scans of the slowly cooled polyethylene series. Traces are displaced vertically for clarity.

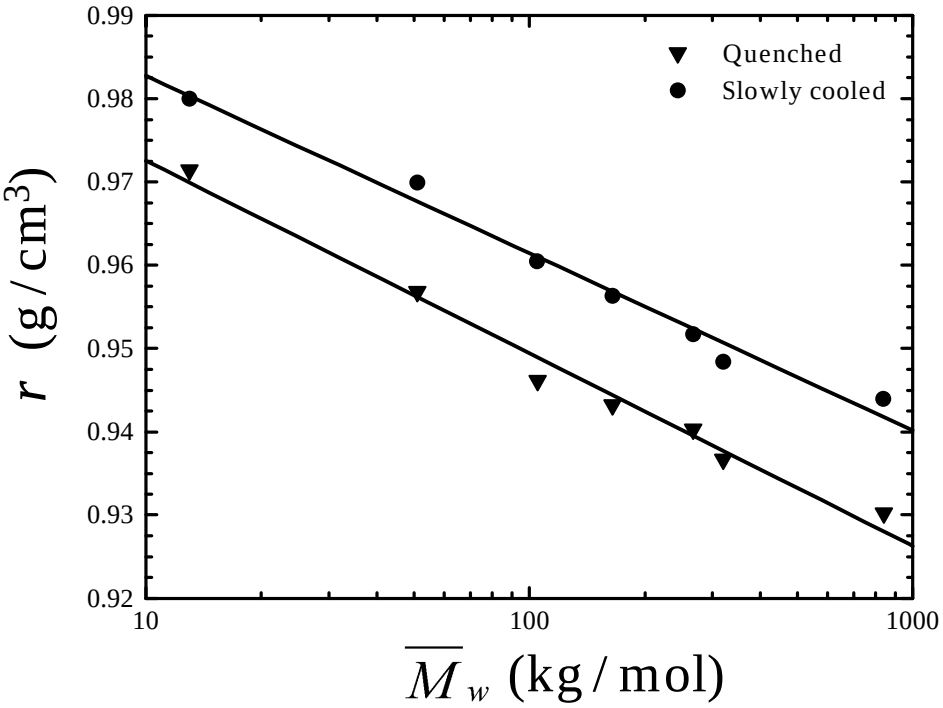

Figure 6. The influence of molecular weight and thermal history on the density of the series.

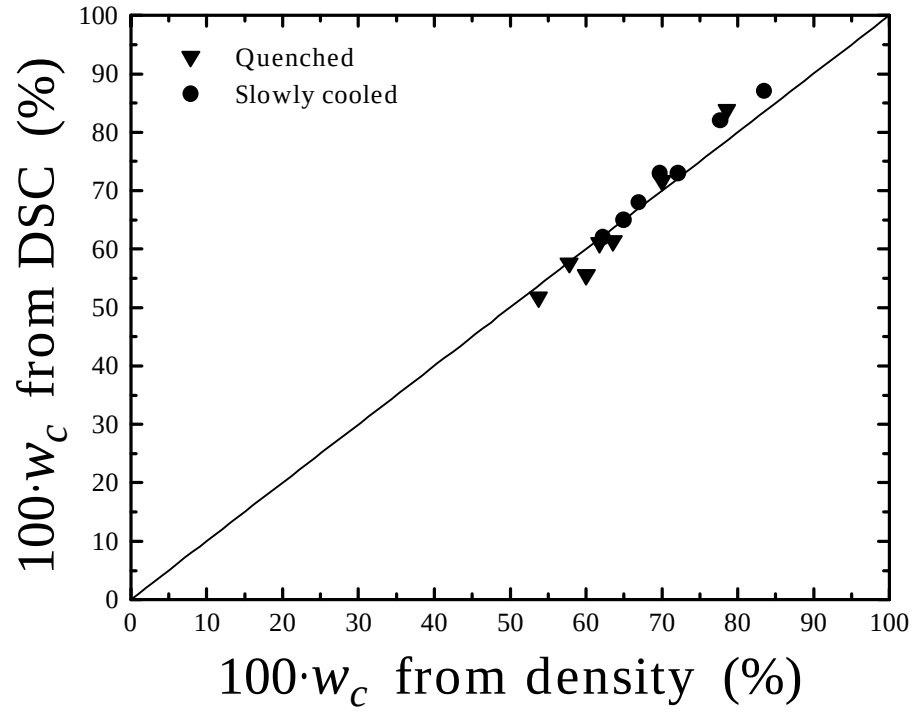

Figure 7. Comparison of w_c values determined by DSC and density.

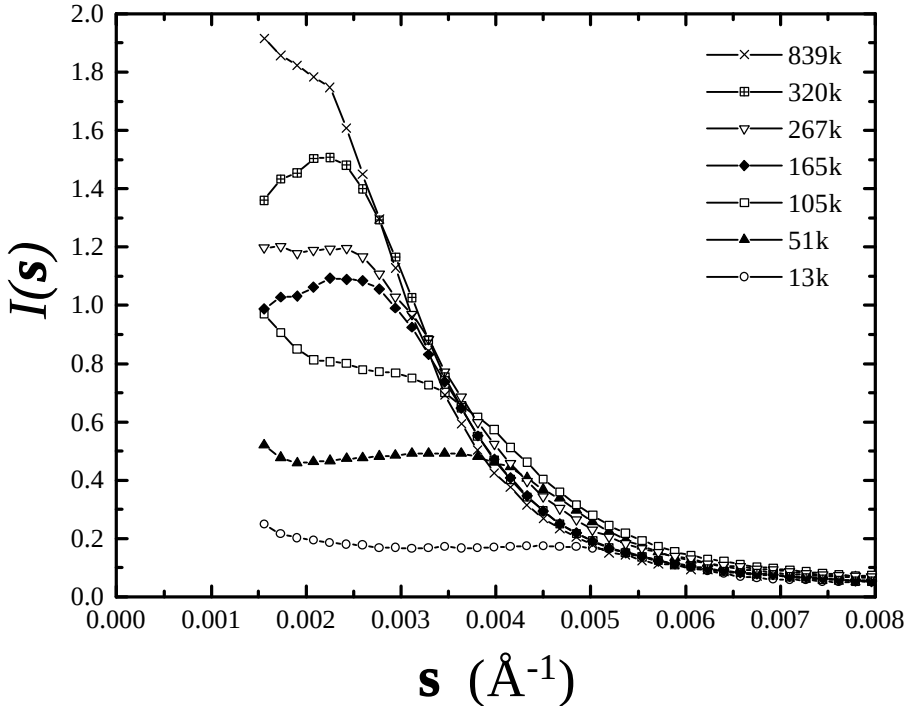

Figure 8. Small angle x-ray scattering profiles for quenched polyethylenes.

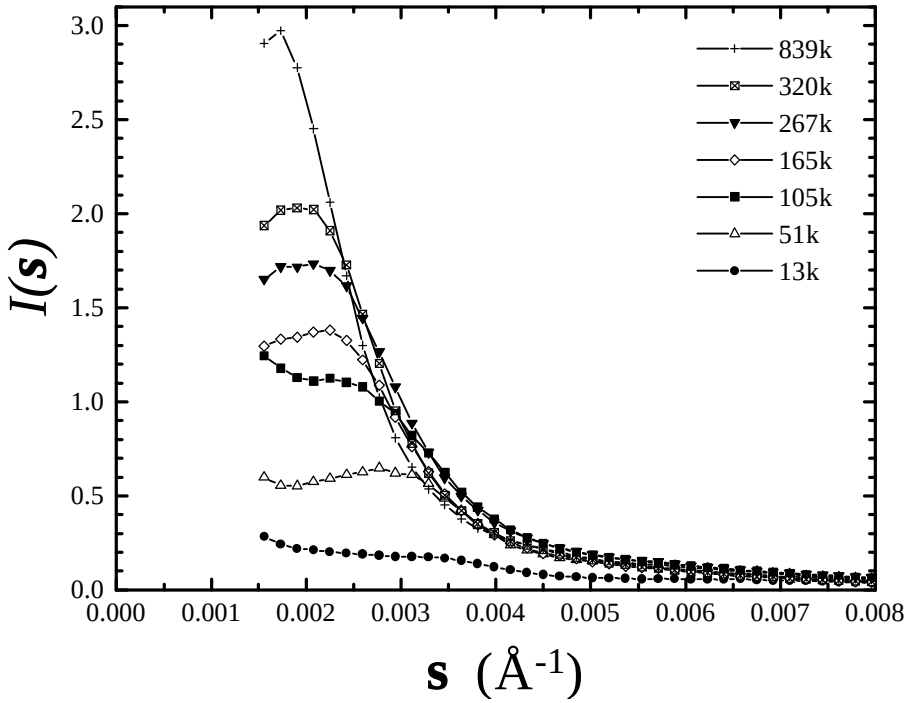

Figure 9. Small angle x-ray scattering profiles for slowly cooled polyethylenes.

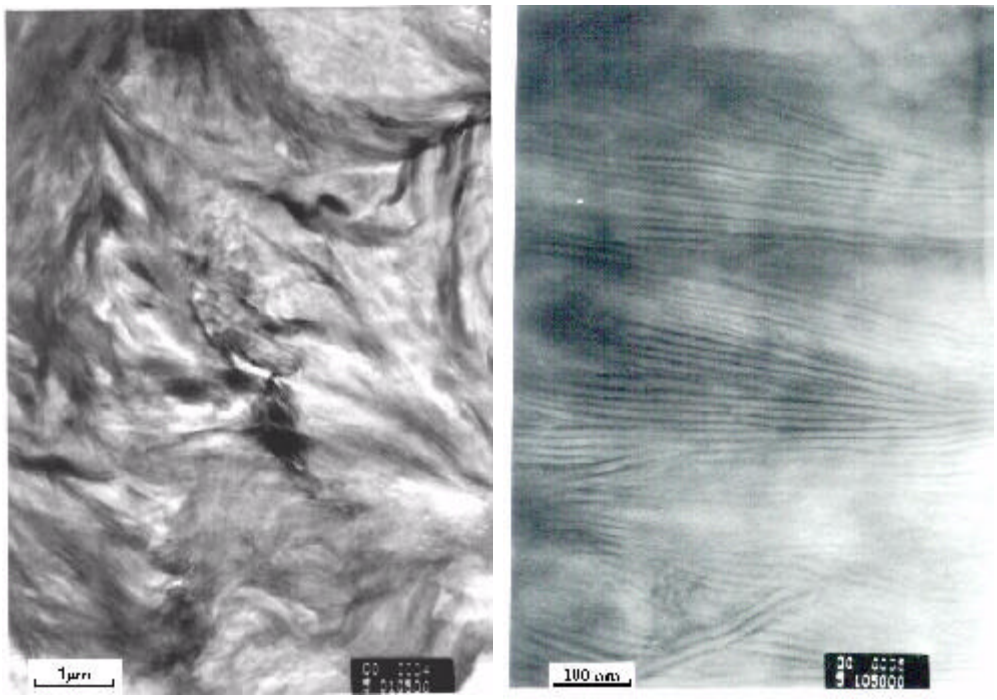

(A) 13 kg / mol quenched

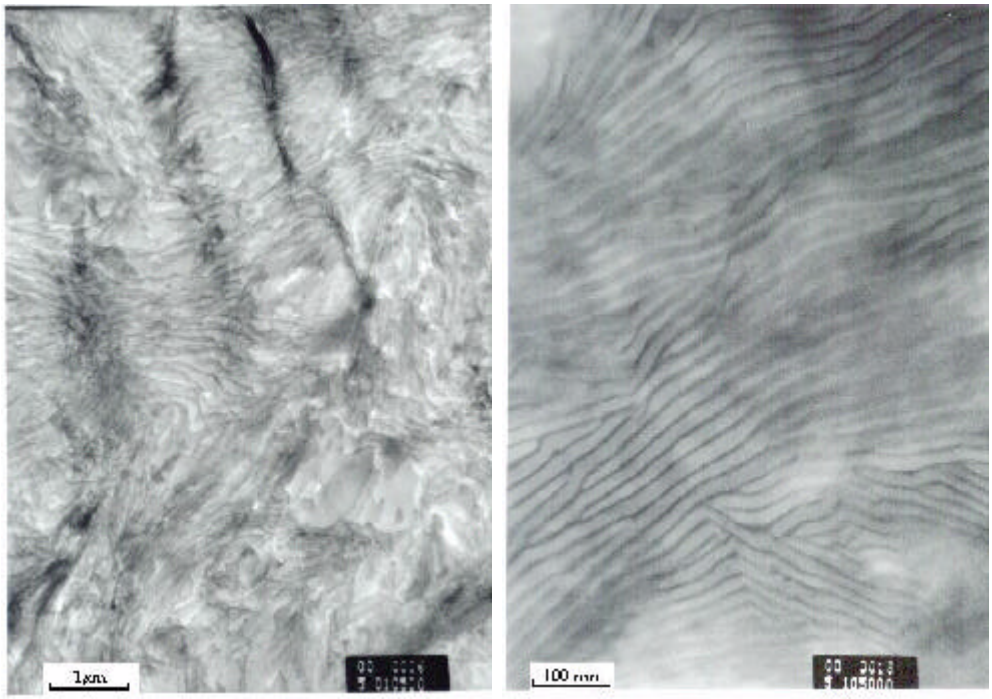

(B) 13 kg / mol slowly cooled

Figure 10. Transmission electron micrographs.

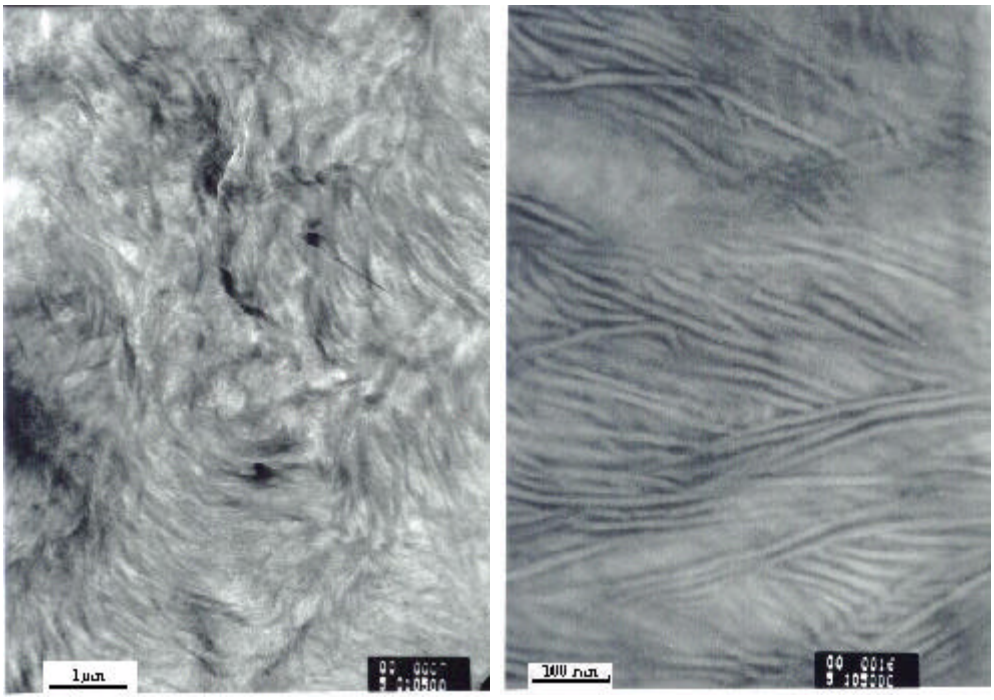

(C) 51 kg / mol quenched

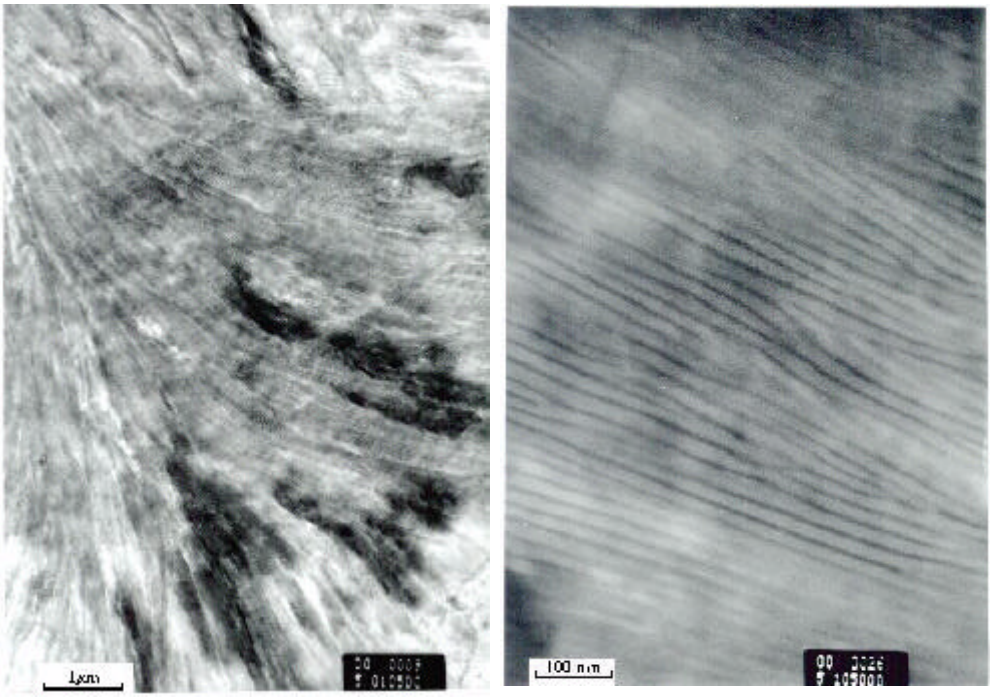

(D) 51 kg / mol slowly cooled

Figure 10. Transmission electron micrographs.

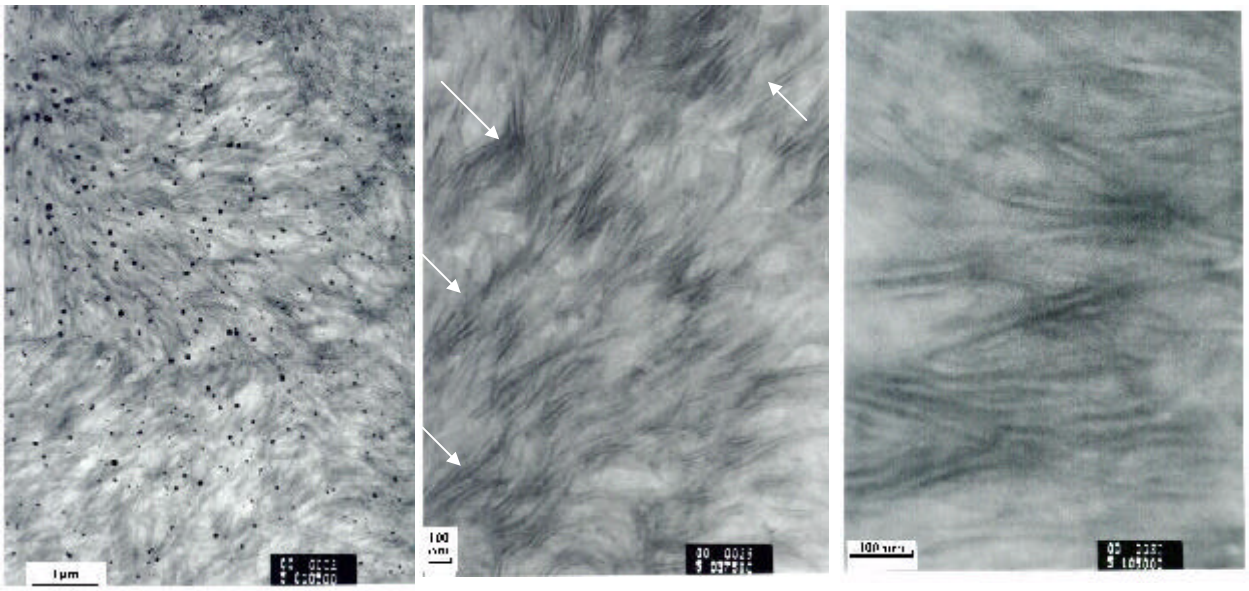

(E) 267 kg / mol quenched

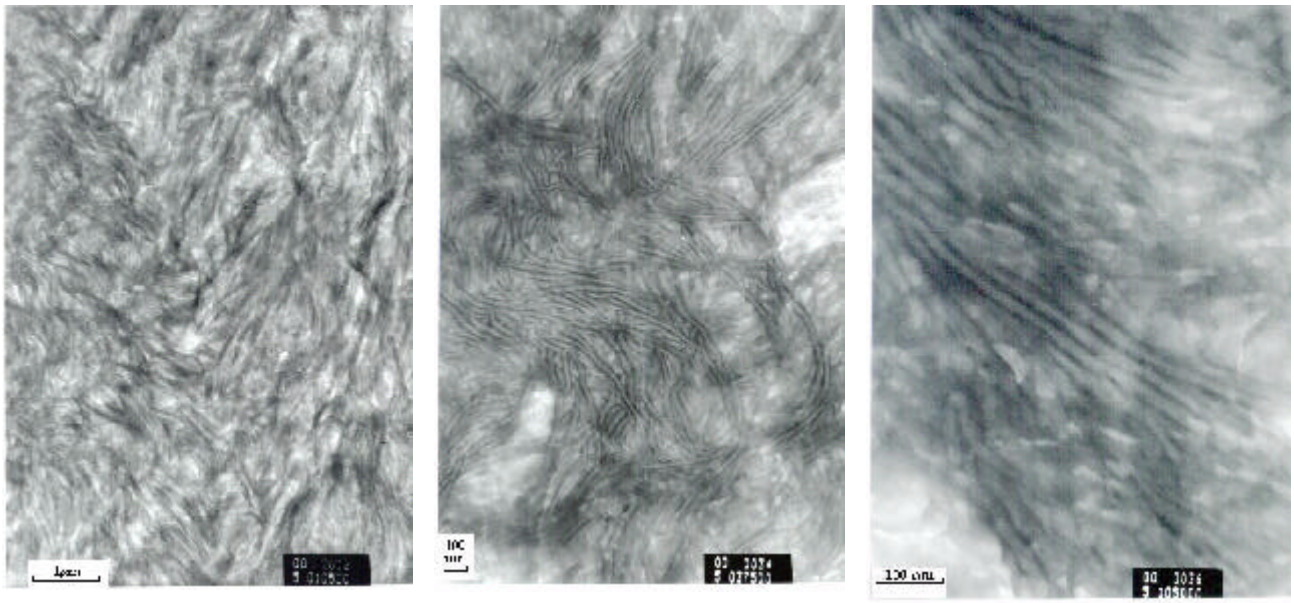

(F) 267 kg / mol slowly cooled

Figure 10. Transmission electron micrographs.

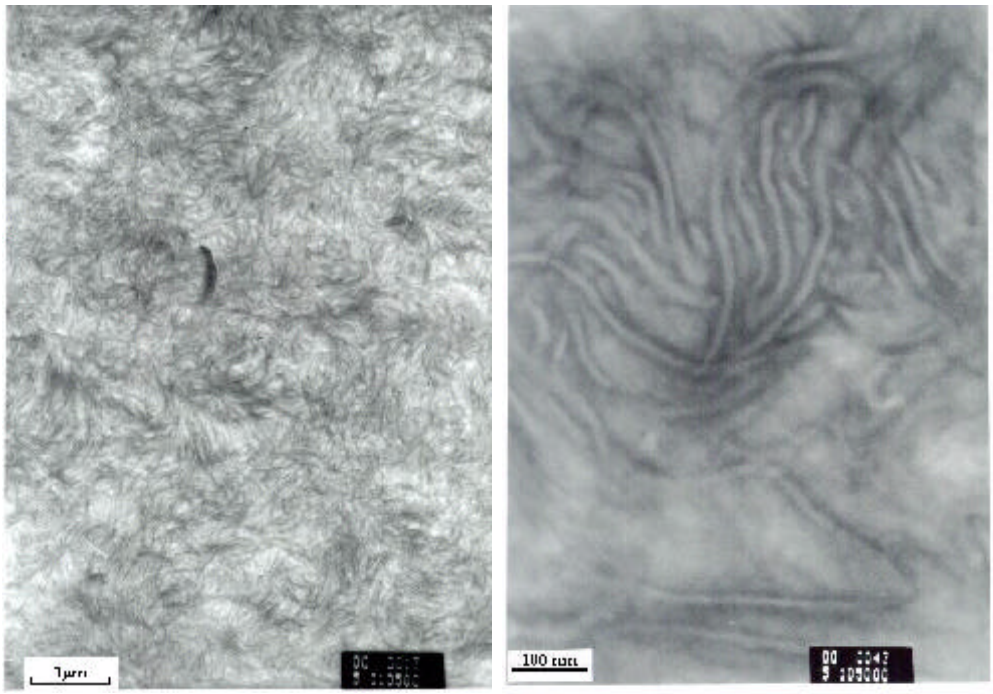

(G) 839 kg / mol quenched

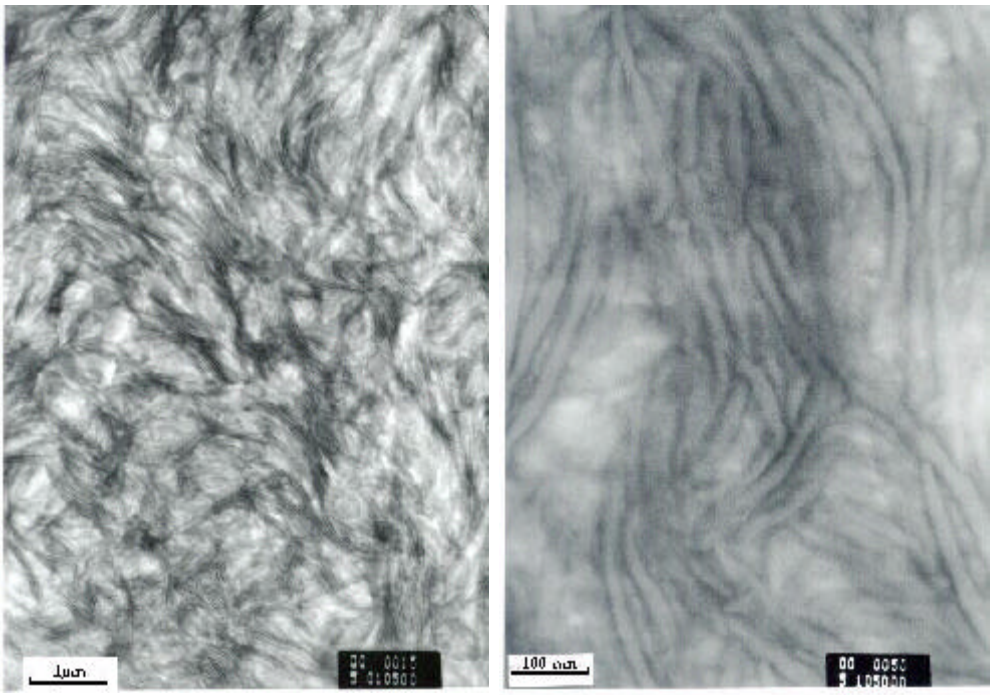

(H) 839 kg / mol slowly cooled

Figure 10. Transmission electron micrographs.

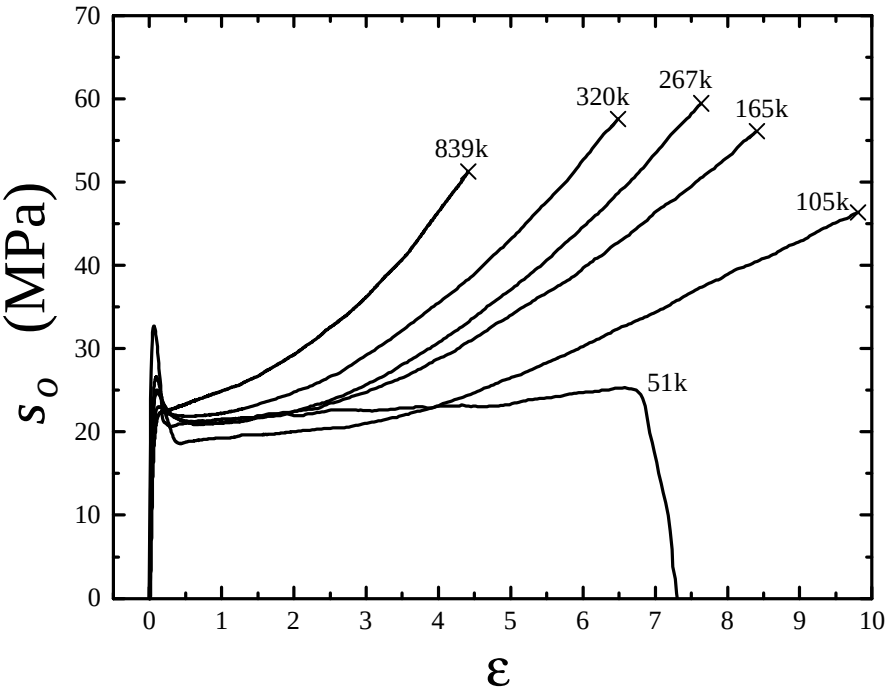

Figure 11. Stress–strain behavior for the quenched polyethylene series.

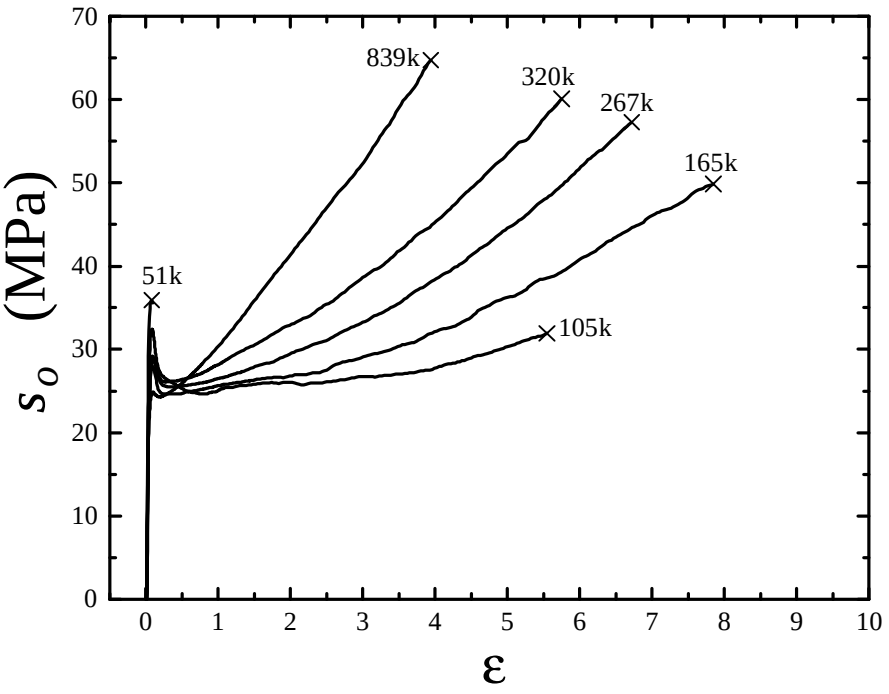

Figure 12. Stress–strain behavior for the slowly cooled polyethylene series.

Figure 13. The "forked–tongue" shape of the quenched 51 kg / mol dog–bone samples after the tensile test.

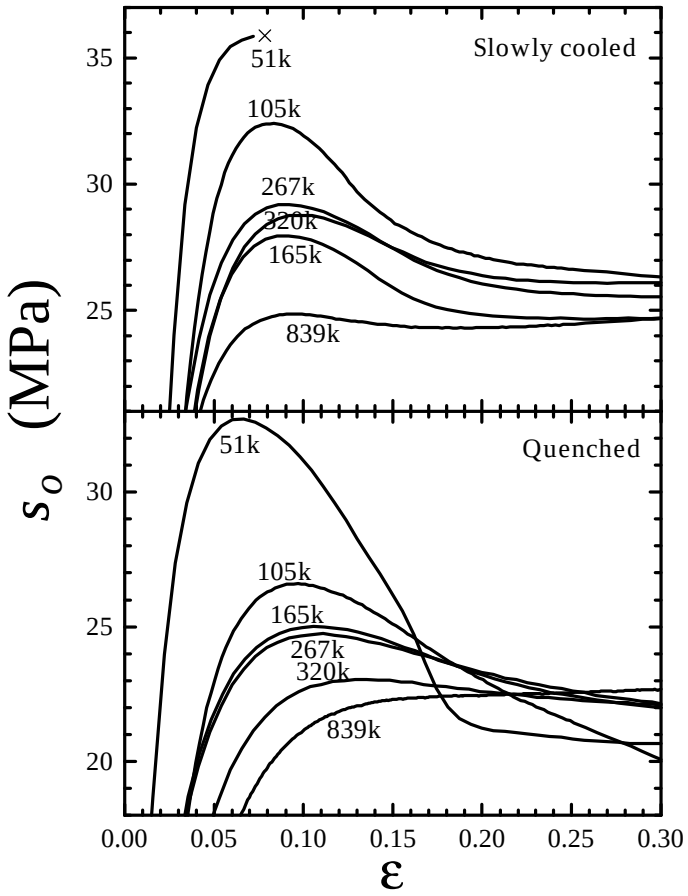

Figure 14. Stress–strain behavior in the vicinity of yield.

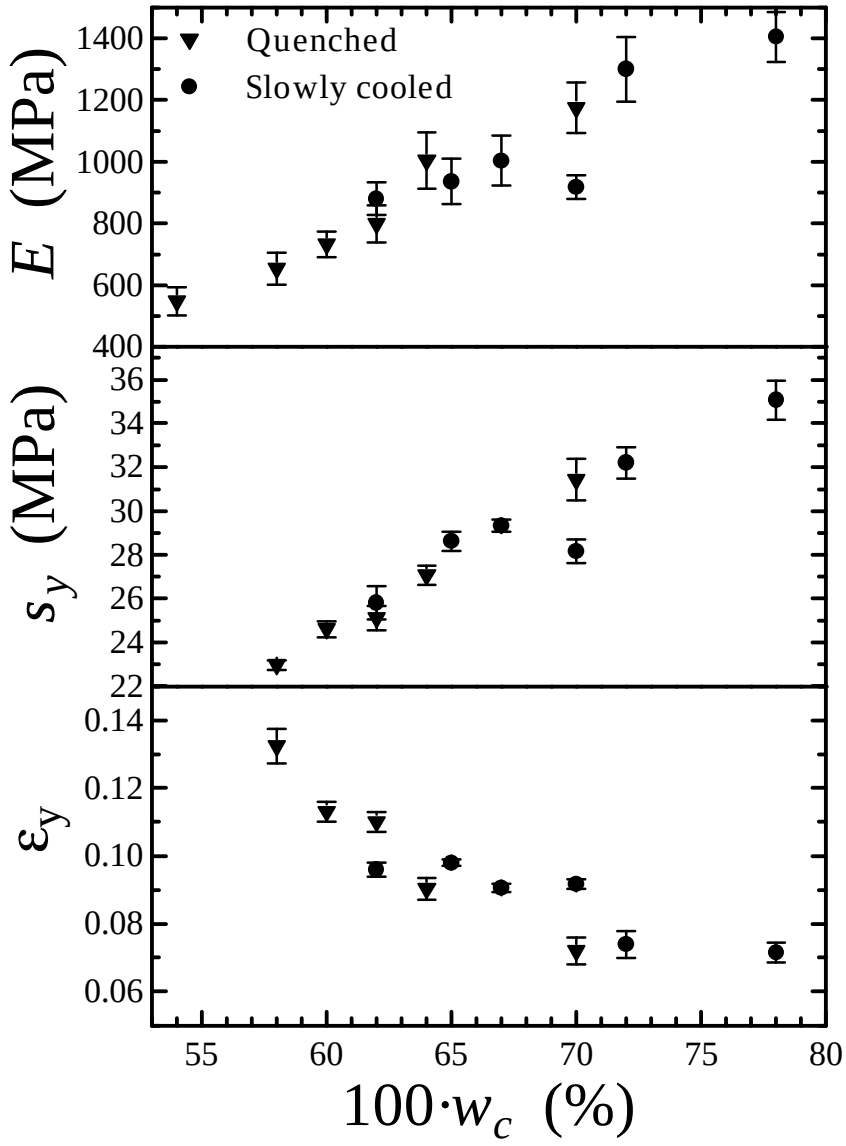

Figure 15. The dependence of Young's modulus, yield stress, and yield strain on percent crystallinity.

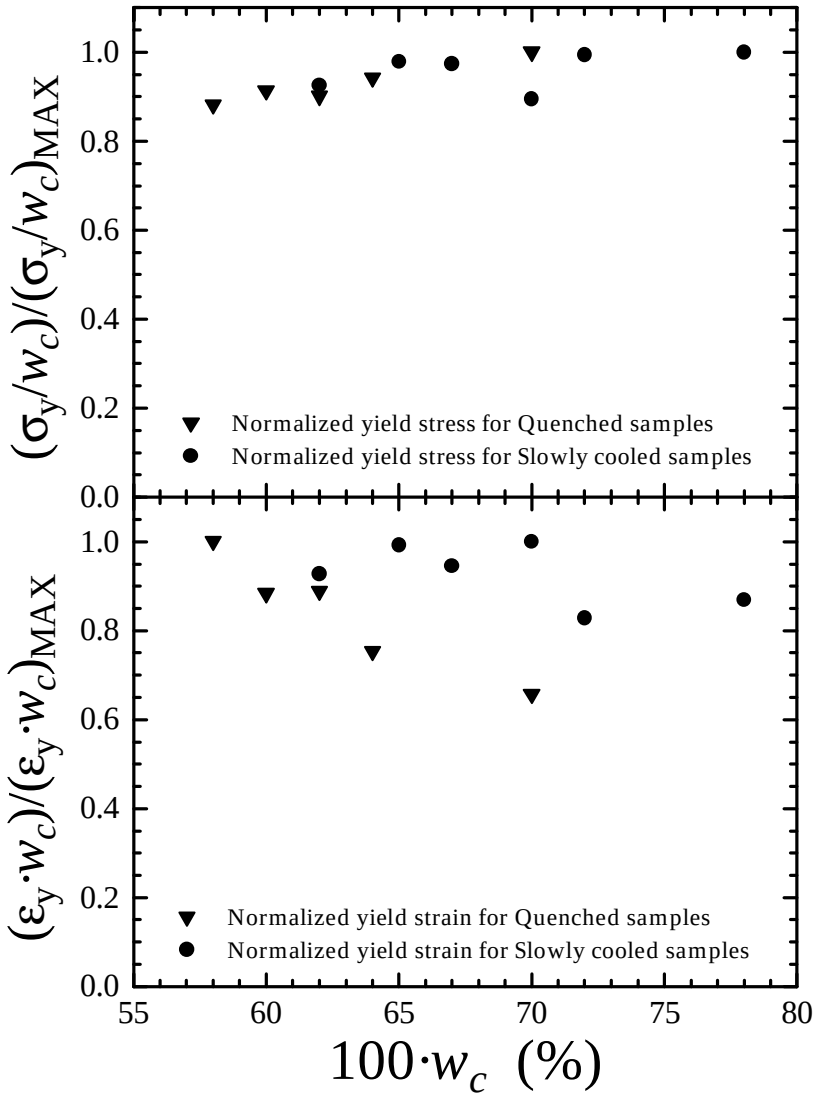

Figure 16. The dependence of normalized (by crystal content) yield stress and yield strain on the percent crystallinity.

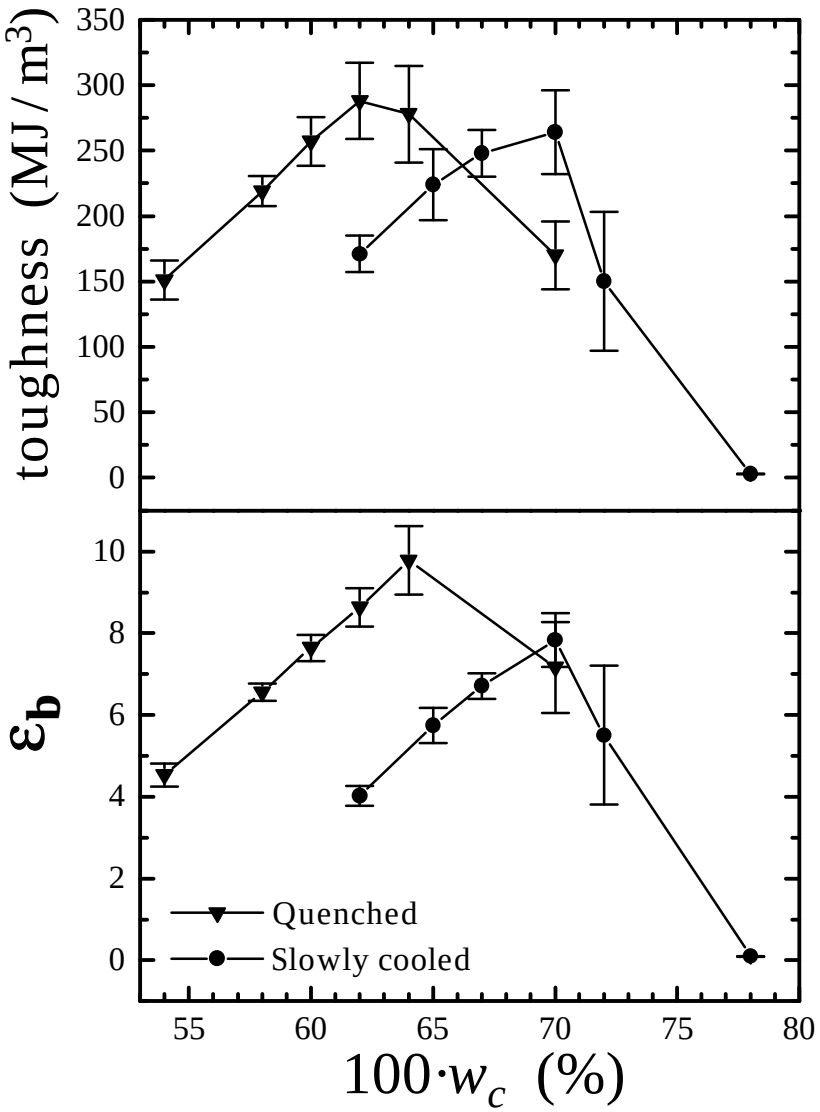

Figure 17. The dependence of toughness and strain at break on percent crystallinity.

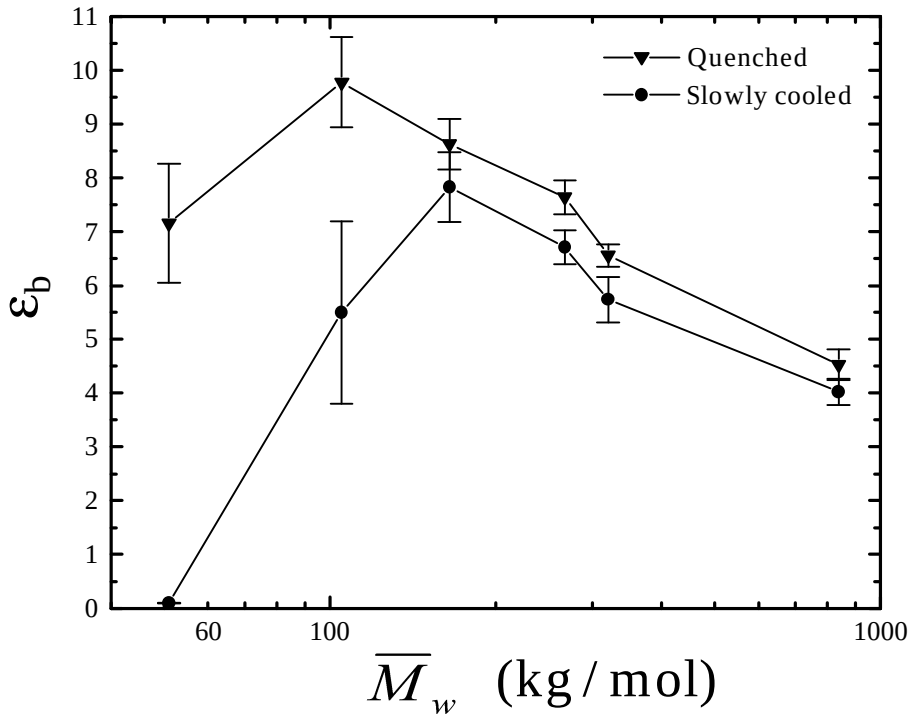

Figure 18. The influence of molecular weight on strain at break.

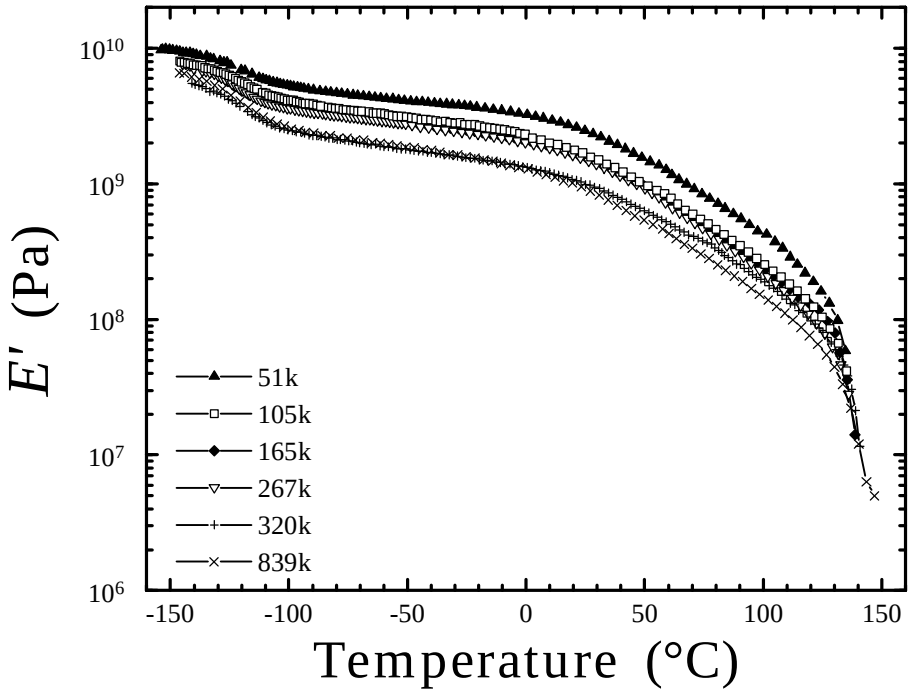

(A)

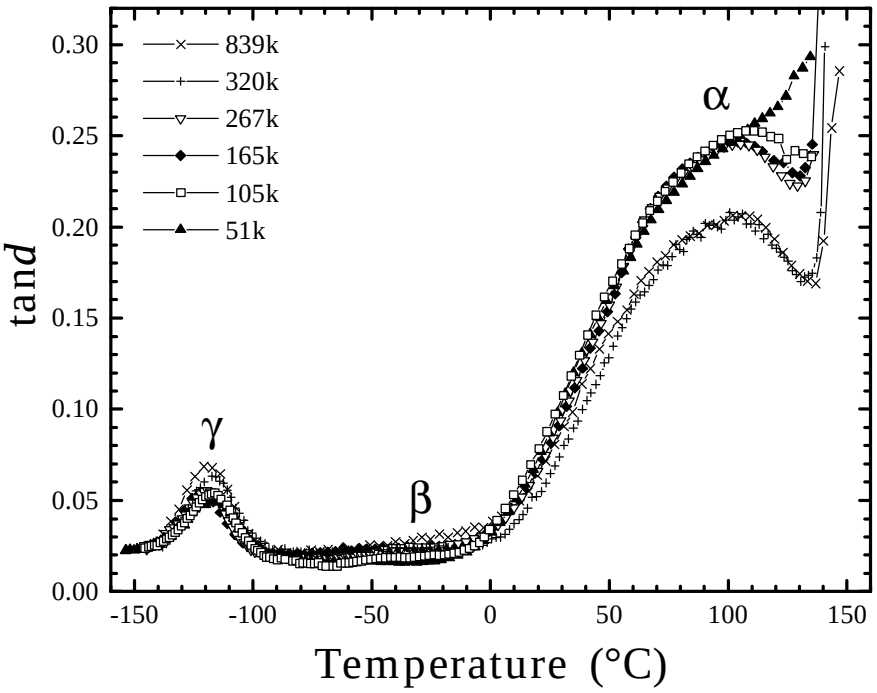

(B)

Figure 19. Dynamic mechanical spectroscopy of the quenched series; (A) storage moduli versus temperature, (B) tan*d* versus temperature.

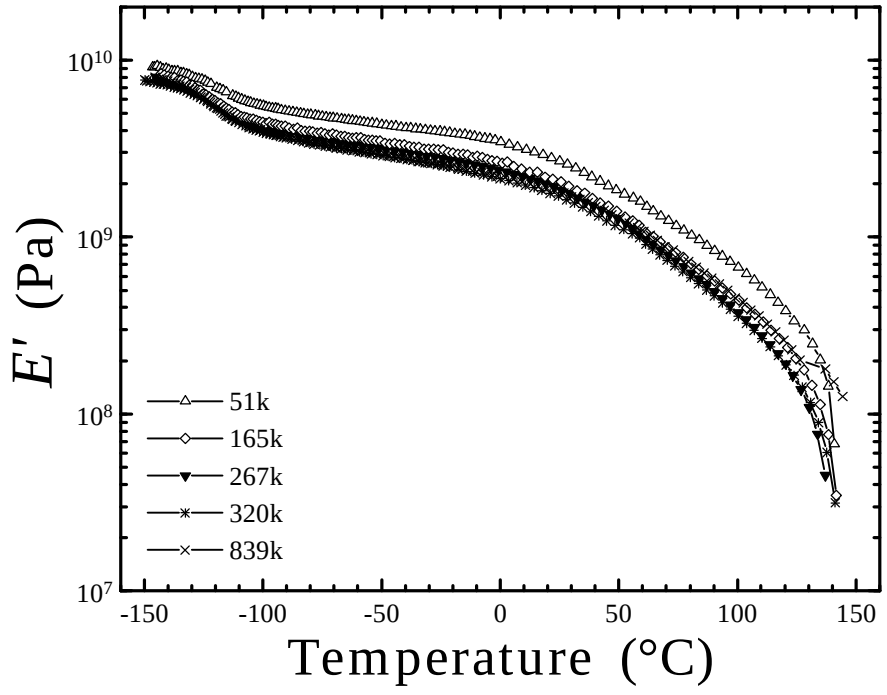

(A)

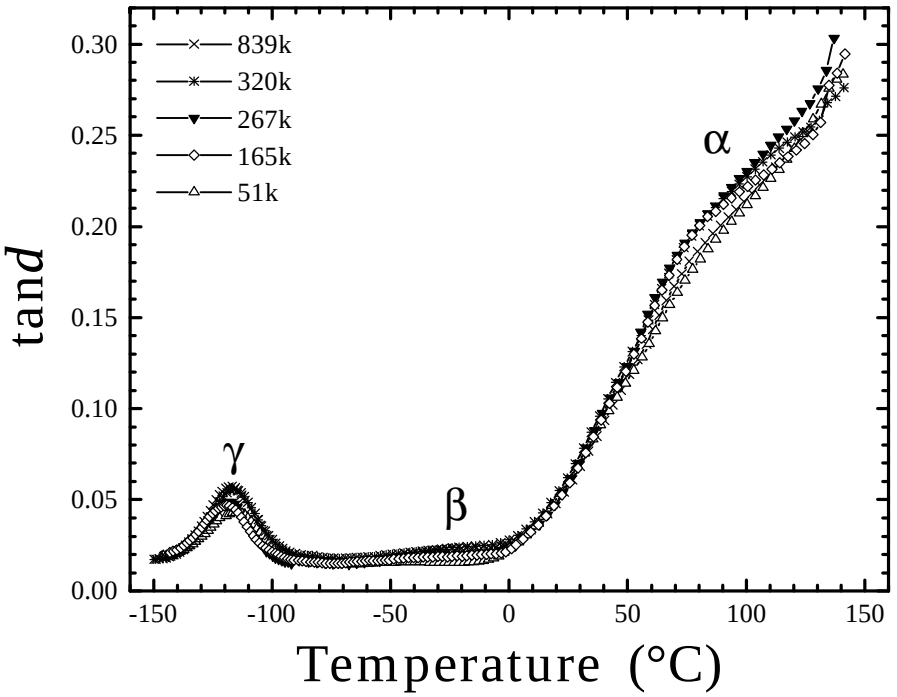

(B)

Figure 20. Dynamic mechanical spectroscopy of the slowly cooled series; (A) storage moduli versus temperature, (B) tan*d* versus temperature.

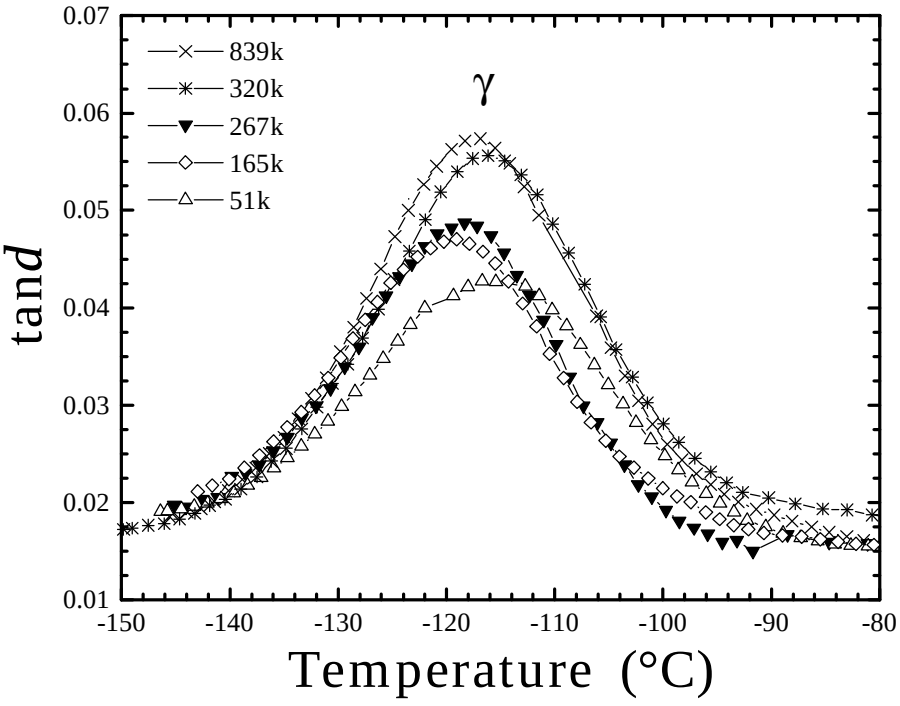

(A)

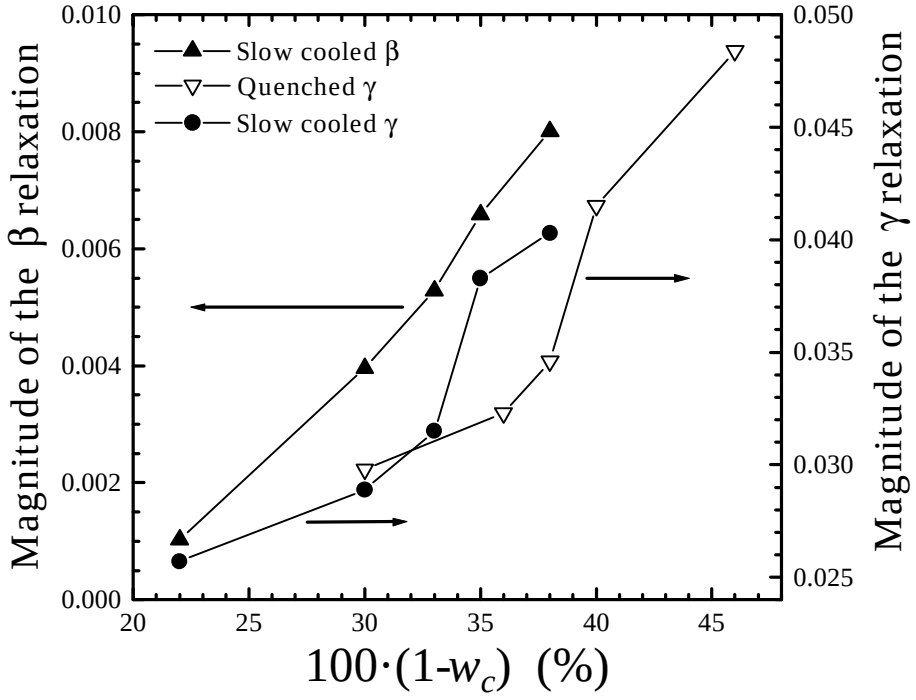

(B)

Figure 21. (A) The loss tangent in the γ–region of the slowly cooled polyethylene series; (B) a plot of the magnitudes of $(\tan d)_{max}$ at the γ and β relaxations versus calculated amorphous content.

Table 1. Molecular weight results from SEC and melt–rheological parameters for the polyethylene series at 230 °C.

$\overline{M}_n$ kg/mol	$\overline{M}_w$ kg/mol	$\overline{M}_w/\overline{M}_n$	Carreau–Yasuda Parameters			E_a kJ/mol
			$h_0\ (Pa\cdot s)$	$t_h\ (s)$	a	
4.1	13	3.24	–*	–*	–*	–*
5.2	14	2.74	6.14	*3.82×10^{-5}* †	*0.422* †	–‡
7.1	26	3.59	26.7	*1.44×10^{-4}* †	*0.602* †	–‡
16	37	2.34	135	*4.00×10^{-8}* †	*0.215* †	–‡
18	51	2.83	364	9.68×10^{-4}	0.565	30.1
35	105	3.05	4200	2.13×10^{-3}	0.333	–‡
45	160	3.54	1.22×10^{4}	0.0195	0.598	–‡
67	165	2.45	1.72×10^{4}	0.0198	0.393	–‡
79	267	3.4	1.44×10^{5}	0.198	0.323	–‡
125	320	2.56	1.01×10^{5}	0.190	0.521	30.3
241	839	3.49	9.81×10^{5}	2.69	0.635	–‡

* *Not measured – insufficient viscosity.*

† *Values poorly determined by the available data (uncertainties much larger than parameter values).*

‡ *Not measured.*

Table 2. Density (r), crystal mass fraction (w_c), and crystal volume fraction (f_c) data for the metallocene catalyzed polyethylene series.

$\overline{M}_w$ kg/mol	Thermal treatment	ρ g/cm^3	w_c (DSC)	w_c (density)	f_c (density)
13	Quenched	0.9714	0.84	0.79	0.76
	Slowly cooled	0.9800	0.87	0.83	0.81
51	Quenched	0.9568	0.72	0.70	0.66
	Slowly cooled	0.9699	0.82	0.78	0.75
105	Quenched	0.9461	0.61	0.64	0.60
	Slowly cooled	0.9604	0.73	0.72	0.69
165	Quenched	0.9432	0.61	0.62	0.58
	Slowly cooled	0.9563	0.73	0.70	0.66
267	Quenched	0.9403	0.56	0.60	0.56
	Slowly cooled	0.9517	0.68	0.67	0.63
320	Quenched	0.9367	0.58	0.58	0.54
	Slowly cooled	0.9484	0.65	0.65	0.61
839	Quenched	0.9302	0.52	0.54	0.49
	Slowly cooled	0.9439	0.62	0.62	0.58

7.6 References

1 S. S. Reddy and S. Sivaram. *Prog. Polym. Sci.*, **20**, 309, (1995).

2 J. Huang and G. L. Rempel. *Prog. Polym. Sci.*, **20**, 459, (1995).

3 Paul J. Flory. Principles of Polymer Chemistry. Cornell University Press, New York, 1953, p. 324.

4 V. K. Gupta, S. Satish, and I. S. Bhardwaj. *J.M.S.–Rev. Macromol. Chem. Phys.*, **C34(3)**, 439, (1994).

5 A. E. Hamielec and J. B. P. Soares. *Prog. Polym. Sci.*, **21**, 651, (1996).

6 W. Kaminsky, H. Sinn, and R. Woldt. *Makromol. Chem., Rapid Commun.*, **4**, 417, (1983).

7 N. Ishihara, M. Kuramoto, and M. Uoi. *Macromolecules*, **21**, 3356, (1988).

8 A. Zambelli, C. Pellecchia, L. Oliva, P. Longo, and A. Grassi. *Makromol. Chem.*, **192**, 223, (1991).

9 W. Spalcek, M. Antberg, V. Dolle, R. Klein, J. Rohrmann, and A. Winter. *New J. Chem.*, **14**, 499, (1990).

10 J. A. Ewen, M. J. Elder, R. I. Jones, S. Curtis, and H. N. Cheng in Catalytic Olefin Polymerization. T. Keii and K Soga, ed., 439, (1990).

11 S. Collins, W. J. Gauthier, D. A. Holden, B. A. Kuntz, N. J. Taylor, and D. G. Ward. *Organometallics*, **10**, 2061, (1991).

12 E. Hauptman, R. M. Waymouth, and J. Ziller. *J. Am. Chem. Soc.* , **117**, 11586, (1995).

13 G. W. Coates and R. M. Waymouth. *Science*, **267**, 217, (1995).

14 G. H. Llinas, S. H. Dong, D. T. Mallin, M. D. Rausch, Y. G. Lin, H. H. Winter, and J. C. W. Chien. *Macromolecules*, **25**, 1242, (1992).

15 H. N. Cheng, G. N. Babu, R. A. Newmark, and J. C. W. Chien. *Macromolecules*, **25**, 6980, (1992).

16 Duane Litteer, Manager, Exxpol® Polyethylene Process R&D, Exxon Chemical Company, Baytown Polymers Center. *Personal communication*. 1 April 1999.

17 J. B. P. Soares and A. E. Hamielec. *Polym. React. Eng.*, **3(2)**, 131, (1995).

18 J. C. W. Chien and D. He. *J. Polym. Sci. Part A: Polym. Chem.*, **29**, 1603, (1991).

19 M. Kaminaka and K. Soga. *Makromol. Chem., Rapid Commun.*, **12**, 367, (1991).

20 F. Garbassi, L. Gila, and A. Proto. *Polymer News*, **19**, 367, (1994).

21 J. Janzen and D. F. Register. Plastics-Racing Into the Future. *Proceedings of the SPE 54th annual Technical Conference (ANTEC '96)*, 2190, (1996).

22 J. Janzen. *Polym. Eng. Sci.*, **32**, 1242, (1992).

23 J. Janzen. *Polym. Eng. Sci.*, **32**, 1255, (1992).

24 B. Crist, C. J. Fisher, and P. R. Howard. *Macromolecules*, **22**, 1709, (1989).

25 M. A. Kennedy, A. J. Peacock, and L. Mandelkern. *Macromolecules*, **27(19)**, 5297, (1994).

26 M. A. Kennedy, A. J. Peacock, M. D. Failla, J. C. Lucas, and L. Mandelkern. *Macromolecules*, **28(5)**, 1407, (1995).

27 A. J. Peacock and L. Mandelkern. *J. Polym. Sci., Part B: Polym. Phys.*, **28(11)**, 1917, (1990).

28 M. D. Failla, J. C. Lucas, and L. Mandelkern. *Macromolecules*, **27(6)**, 1334, (1994).

29 R. G. Alamo, E. K. M. Chan, L. Mandelkern, and I. G. Voigt-Martin. *Macromolecules*, **25(24)**, 6381, (1992).

30 R. Popli and L. Mandelkern. *J. Polym. Sci. Part B: Polym. Phys.*, **25(3)**, 441, (1987).

31 Stephen L. Rosen. Fundamental Principles of Polymeric Materials. 2nd edition, John Wiley and Sons, NY, 1993.

32 M. Varma–Nair and B. Wunderlich. *J. Phys. Chem. Ref. Data*, **20**, 349, (1991).

33 Bernhard Wunderlich. Macromolecular Physics, Vol. 3, *Crystal Melting*. Academic Press, Inc., NY, 1980.

34 Leroy E. Alexander. X-ray Diffraction Methods in Polymer Science. Kreiger Publishing Company, Malabar, Florida, 1969.

35 G. Kanig. *Kolliodzeitschrift*, **251**, 782, (1973). *note: written in German.*

36 G. Kanig. *Prog. Colloid Polym. Sci.*, **57**, 176, (1975). *note: written in German.*

37 W. P. Cox and E. H. Merz, *J. Polym. Sci.*, **28**, 619, (1958).

38 Bird, Armstrong, and Hassager. Dynamics of Polymeric Liquids, Vol.1, Fluid Mechanics. 2nd edition, John Wiley and Sons, NY, 1987.

39 J. Janzen, D. C. Rohlfing, and M. J. Hicks. *J. Rheol.*, in press.

40 A. Pinarbasi, and A. Liakopoulos. *J. Non-Newtonian Fluid Mech.*, **57(2/3)**, 227, (1995).

41 W. W. Graessley. *J. Chem. Phys.*, **47(6)**, 1942, (1967).

42 W. W. Graessley. *Adv. Polym. Sci.*, **16**, (1974). Table 8.1.

43 G. C. Berry and T. G. Fox. *Adv. Polym. Sci.*, **5**, 261, (1968).

44 G. L. Wilkes. *J. Chem. Ed.*, **58**, 880, (1981).

45 W. W. Graessley and S. F. Edwards. *Polymer*, **22**, 1329, (1981).

46 Y. H. Zang and P. J. Carreau. *J. Appl. Polym. Sci.*, **42**, 1965, (1991).

47 R. S. Porter, J. R. Knox, and J. F. Johnson. *Trans. Soc. Rheol.*, **12**, 409, (1968).

48 R. A. Mendelson, W. A. Bowles, and F. L. Finger. *J. Polym. Sci. A-2, Polym. Phys.*, **8**, 105, (1970).

49 K. L. Ngai and D. J. Plazek. *J. Polym. Sci. B: Polym. Phys.*, **23**, 2159, (1985).

50 W. W. Graessley. *Macromolecules*, **15(4)**, 1164, (1982).

51 Charles L. Rohn. Analytical Polymer Rheology. Structure-Processing-Property Relationships. Hanser / Gardner Publications, Inc., Cincinnati, 1995.

52 R. L. Arnett and C. P. Thomas. *J. Phys. Chem.*, **84**, 649, (1980).

53 J. F. Vega, A. Santamaría, A. Muñoz–Escalona, and P. Lafuente. *Macromolecules*, **31**, 3639, (1998).

54 S. H. Wasserman and W. W. Graessley. *Polym. Eng. Sci.*, **36(6)**, 852, (1996).

55 A. Eckstein, J. Suhn, C. Friedrich, R.–D. Maier, J. Sassmannshausen, M. Bochmann, and R. Mülhaupt. *Macromolecules*, **31(4)**, 1335, (1998).

56 A. Eckstein, J. Suhm, C. Friedrich, R. D. Maier, J. Sassmannshausen, M. Bochmann, and R. Mülhaupt. *Macromolecules*. **31(4)**, 1335, (1998).

57 W. M. Whitte, J. C. Randall, and C. H. Leigh. *Chem. Eng. Commun.*, **24**, 139, (1983).

58 Dr. Michael Muhle, Engineering Associate, Exxpol® Technology, Exxon Chemical Company, Baytown Polymers Center. *Personal communication*. April 1, 1999.

59 W. W. Graessley. *J. Polym. Sci. Polym. Phys. Ed.*, **18**, 27, (1980).

60 L. J. Fetters, D. J. Lohse, D. Richter, T. A. Witten, and A. Zirkel. *Macromolecules*, **27(17)**, 4639, (1994).

61 L. J. Fetters, D. J. Lohse, and R. H. Colby. Chapter 24 in Physical Properties of Polymers Handbook. James E. Mark, ed., American Institute of Physics Press, Woodbury, NY, 1996.

62 L. J. Fetters, D. J. Lohse, and W. W. Graessley. *J. Polym. Sci. : Part B: Polym. Phys.*, **37**, 1023, (1999).

63 L. R. G. Treloar. The Physics of Rubber Elasticity. Thrid edition, Clarendon Press, Oxford, 1975.

64 M. Doi and S. F. Edwards. The Theory of Polymer Dynamics. p. 237-8, Clarendon Press, Oxford, 1986.

65 Ralph Colby, Professor of Materials Science and Engineering, Pennsylvania State University. *Personal Communication*. 2 June 1999.

66 J. M. Carrella, W. W. Graessley, and L. J. Fetters. *Macromolecules*, **17**, 2775, (1984).

67 Bernhard Wunderlich. Macromolecular Physics. Vol. 1, *Crystal Structure, Morphology, Defects*. Academic Press, Inc., NY, 1973.

68 Vincent B. F. Mathot, ed. Calorimetry and Thermal Analysis of Polymers. Hanser Publishers, NY, 1994.

69 E. Ergoz, J. G. Fatou, and L. Mandelkern. *Macromolecules*, **5**, 147, (1972).

70 C. J. Stacy and R. L. Arnett. *J. Polym. Sci. A*, **2**, 167, (1964).

71 R. Chiang and P. J. Flory. *J. Am. Chem. Soc.*, **83**, 2057, (1961).

72 J. Rault and E. Robelin–Souffaché. *J. Polym. Sci. Polym. Phys. Ed.*, **27**, 1349, (1989).

73 J. D. Hoffman and R. L. Miller. *Polymer*, **38(13)**, 3151, (1997).

74 D. C. Bassett and A. M. Hodge. *Proc. R. Soc. Lond.*, **A 377**, 25, (1981).

75 D. C. Bassett and A. M. Hodge, and R. H. Olley. *Proc. R. Soc. Lond.*, **A 377**, 39, (1981).

76 D. C. Bassett and A. M. Hodge. *Proc. R. Soc. Lond.*, **A 377**, 61, (1981).

77 D. C. Bassett and A. M. Hodge. *Proc. R. Soc. Lond.*, **A 359**, 121, (1978).

78 M. J. Hill, D. G. Bradshaw, and R. J. Chevili. *Polymer*, **33(4)**, 874, (1992).

79 A. Toda and A. Keller. *Colloid Polym. Sci.*, **271**, 328, (1993).

80 A. Keller. *J. Polym. Sci.*, **17**, 291, (1955).

81 H. D. Keith and F. J. Padden, Jr., *Macromolecules*, **29**, 7776, (1996).

82 H. D. Keith and F. J. Padden, Jr., *J. Polym. Sci.*, **39**, 101, (1959).

83 H. D. Keith and F. J. Padden, Jr., *J. Polym. Sci.*, **39**, 123, (1959).

84 A. Keller. *J. Polym. Sci.*, **39**, 151, (1959).

85 Arthur E. Woodward. Atlas of Polymer Morphology. Hanser Publishers, NY, 1989.

86 I. G. Voigt–Martin and L. Mandelkern. *J. Polym. Sci.: B Polym Phys.*, **22**, 1901, (1984).

87 G. L. Wilkes. "Polymers, Mechanical Behavior", in Encyclopedia of Physical Science and Technology. Vol. 11, Academic Press Inc, 1987.

88 I. M. Ward and D. W. Hadley. Mechanical Properties of Solid Polymers. John Wiley and Sons, 1993.

89 L. Mandelkern, F. L. Smith, M. Failla, M. A. Kennedy, and A. J. Peacock. *J. Polym. Sci. Part B: Polym. Phys.*, **31(4)**, 491, (1993).

90 G. Frink, R. Mülhaupt, and H. H. Brintzinger, eds., Ziegler Catalysts, Recent Scientific Innovations and Technological Improvements. Springer Verlag, 1995.

91 Y. L. Huang and N. Brown. *J. Polym. Sci. B: Polym. Phys.*, **29**, 129, (1991).

92 W. Kaminsky, H. Hahnsen, K. Külper, and R. Wöldt. *US Patent 4,542,199,* 1985.

93 G. Capaccio and I. M. Ward. *Polymer*, **16(4)**, 239, (1975).

94 Y. Mohajer and G. L. Wilkes. *J. Polym. Sci.: Polym. Phys. Ed.*, **20**, 457, (1982).

95 Pierre-Gilles de Gennes. Scaling Concepts in Polymer Physics. Cornell University Press, NY, 1979.

96 N. G. McCrum, B. E. Read, and G. Williams. Anelastic and Dielectric Effects in Polymeric Solids. Dover Publications (reprint), NY, 1991.

97 N. G. McCrum, "Polyethylene: Detailed Interpretation of Mechanical Relaxation in a Crystalline Polymer." in Molecular Basis of Transitions and Relaxations. Edited by Dale J. Meier, Gordon and Breach Science Publishers, NY, 1978, p. 167.

98 M. Takayanagi, "Molecular Motions in Crystalline Polymers." in Molecular Basis of Transitions and Relaxations. Edited by Dale J. Meier, Gordon and Breach Science Publishers, NY, 1978, p. 117.

99 J. D. Hoffman, G. Williams, and E. Passaglia. *J. Polym. Sci: Part C*, **14**, 173, (1966).

100 R. W. Gray and N. G. McCrum. *J. Polym. Sci: Part A–2*, **7**, 1329, (1969).

101 R. H. Boyd. *Polymer*, **26**, 323, (1985).

102 R. H. Boyd. *Polymer*, **26**, 1123, (1985).

103 F. C. Stehling and L. Mandelkern. *Macromolecules,* **3(2)**, 242, (1970).

104 R. Popli, M. Glotin, and L. Mandelkern. *J. Polym. Sci: Polym. Phys Ed.*, **22**, 407, (1984).

105 J. Rault. *J.M.S.–Rev. Macromol. Chem. Phys.*, **C37(2)**, 335, (1997).

106 Y. Ohta and H. Yasuda. *J. Polym. Sci.: Part B, Polym. Phys.*, **32**, 2241, (1994).

107 T. F. Schatzki. *J. Polym. Sci.*, **57**, 496, (1962).

108 T. F. Schatzki. *J. Am. Chem. Soc., Div. Polym. Chem., (Polymer Preprints)*, **6**, 646, (1965).

109 D. E. Kline, J. A. Sauer, and A. E. Woodward. *J. Polym. Sci.*, **22**, 455, (1956).

110 J. W. Cooper and N. G. McCrum. *J. Mater. Sci.*, **7**, 1221, (1972).

111 H. Zhou and G. L. Wilkes. *Macromolecules*, **30**, 2421, (1997).

112 C. P. Buckley and N. G. McCrum. *J. Polym. Sci. A-2*, **9**, 369, (1971).

113 K. M. Sinnott. *J. Appl. Phys.*, **37**, 3385, (1966).

114 M. Takayanagi and T. Matsuo. *J. Macromol. Sci. Phys. B.*, **1**, 407, (1967).

Chapter 8

Supplement to Chapter 7
Metallocene Catalyzed Linear Polyethylene:
Stress–Strain and Dynamic Loss Modulus Data

8.1 Comments

In chapter 7, concerning the behavior of metallocene linear polyethylenes, some of the stress–strain (σ_o–ε) data were left out in the interest of file space. It is included here to emphasize the reproducibility among the ten samples of each condition and the general quality of the data. Also included here are the dynamic loss modulus data for the series.

First consider the σ_o–ε data for the quenched 51 kg/mol material displayed in Figure 1. As was mentioned in chapter 7, this material displayed a peculiar breaking process where a hole developed at one end of the gauge, and hence a distinct break point was not observed for these samples. All specimens of the quenched 51 kg/mol material behaved in this manner, as the data shows. The slowly cooled form of the 51 kg/mol material was quite brittle, as shown in Figure 2, where it broke just after yielding. At the high extreme of molecular weight, the quenched 839 kg/mol material displayed no distinct yield point, as shown in Figure 11, but rather just a knee, followed by immediate strain hardening. All of the intermediate samples behaved in a more typical manner; they all went through a distinct yield point, followed by some amount of

strain hardening, and finally failed. This is shown in Figure 3 through Figure 12. Included in these plots are the statistical values of Young's modulus *E*, yield stress and strain σ_y and ε_y, break stress and strain σ_b and ε_b, and the toughness.

Included in Figure 13 and Figure 14 are the dynamic loss modulus data for the quenched and slowly cooled materials, respectively. This is added here as a supplement to the dynamic mechanical data in chapter 7 which revealed only the storage modulus and tan*d* data for these materials. Notice that the loss modulus in the vicinity of the α-relaxation (≈ 0 to 130 °C range) for the quenched materials in Figure 13 show a dependence of their magnitude on molecular weight. More correctly, the determining variable is the crystal fraction. Since the α-relaxation occurs in the crystalline phase of polyethylene (see chapter 7 for a molecular description), it is expected that the magnitude of the loss modulus in the α region should increase with increasing crystal fraction. This is indeed the observation for the materials in both Figure 13 and Figure 14, where increasing the molecular weight (which corresponds to decreasing the crystal fraction for a given thermal treatment) leads to a decrease in the magnitude of the loss modulus at the peak of the α-relaxation.

Although not observed clearly in the quenched samples, the slowly cooled materials in Figure 14 show a similar relationship between crystal fraction and the magnitude of the γ–relaxation. However, since the γ–relaxation occurs in the amorphous phase exclusively (again a molecular description of this process can be found in chapter 7), the trend is in the opposite direction of that for the α-relaxation. Specifically, increasing molecular weight (which increases the *amorphous* content for the slowly cooled materials of Figure 14), leads to an increase in the magnitude of the loss modulus at the peak of the γ–relaxation.

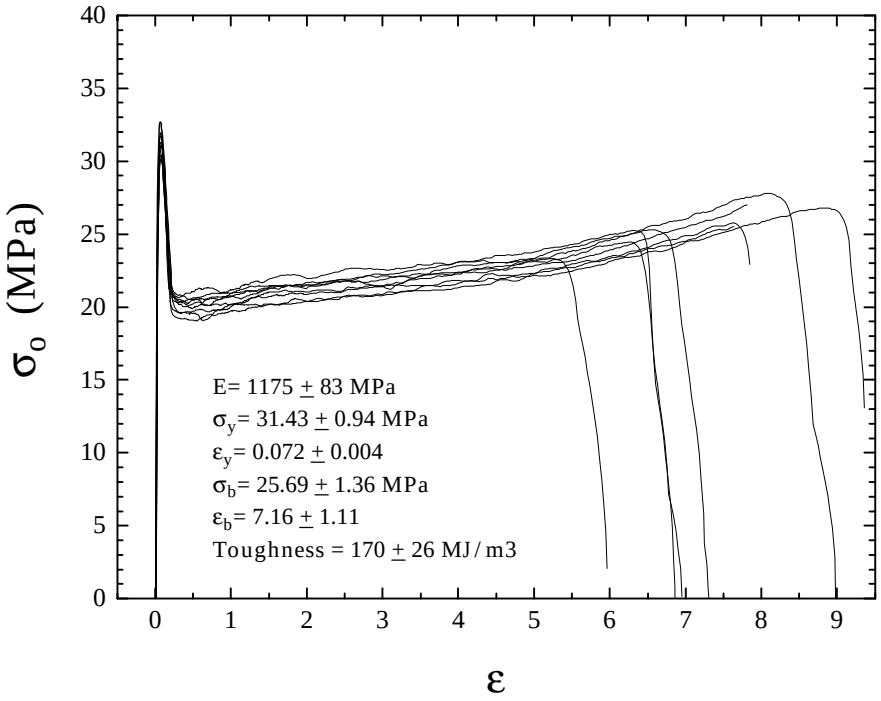

Figure 1. Stress–strain data for all ten specimens of the quenched 51 kg / mol material.

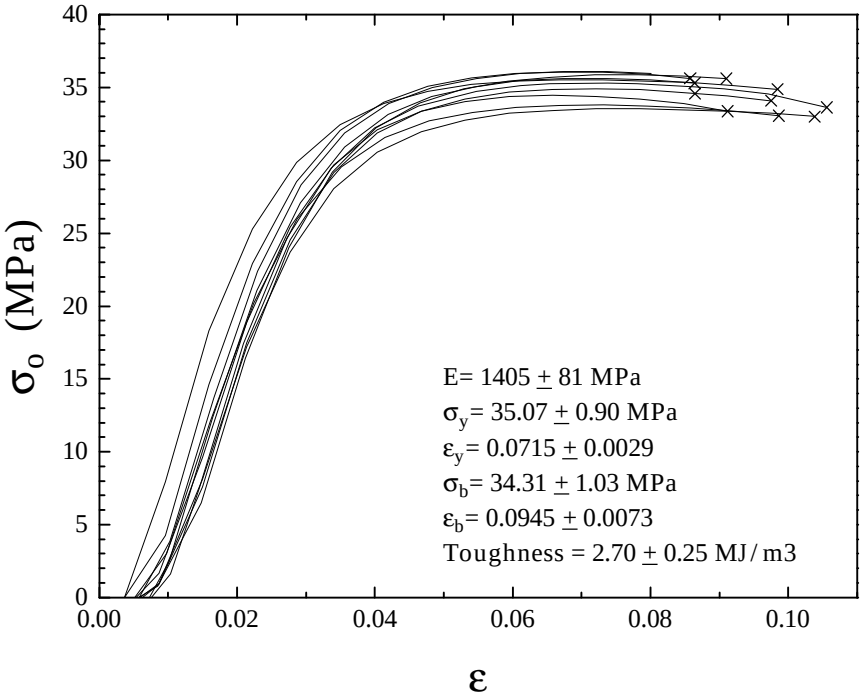

Figure 2. Stress–strain data for all ten specimens of the slowly cooled 51 kg / mol material.

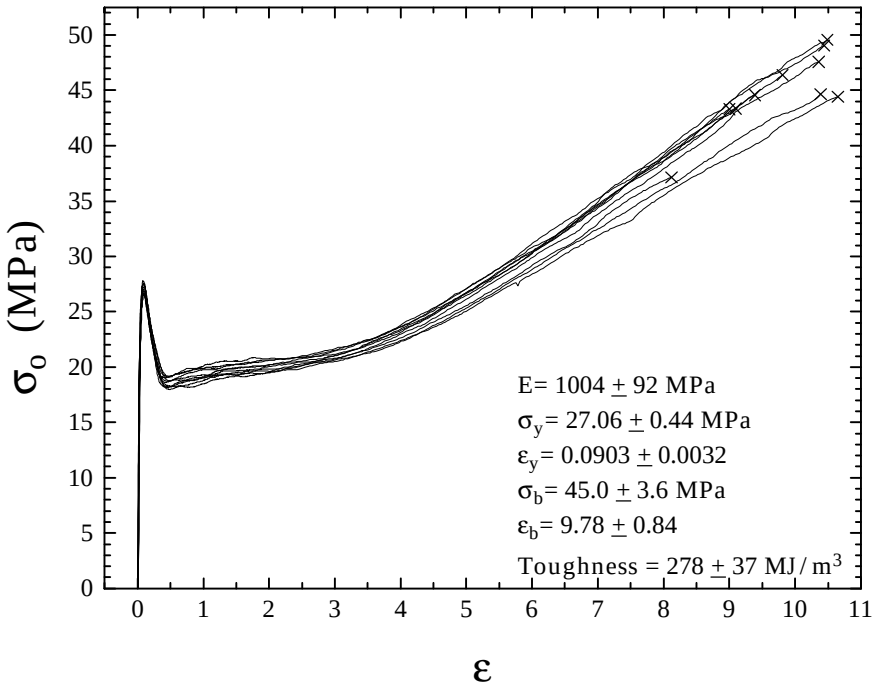

Figure 3. Stress–strain data for all ten specimens of the quenched 105 kg/mol material.

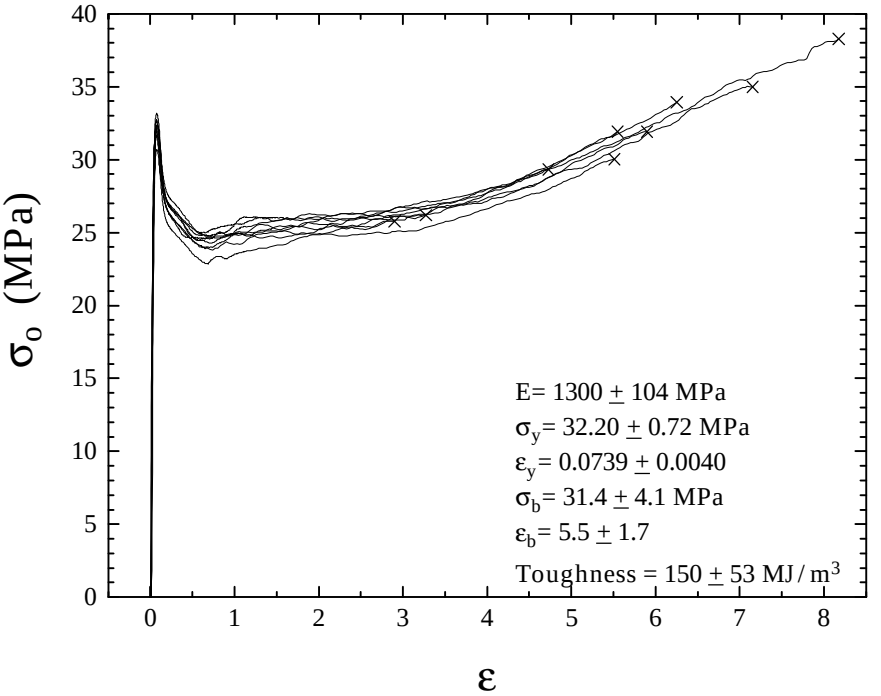

Figure 4. Stress–strain data for all ten specimens of the slowly cooled 105 kg/mol material.

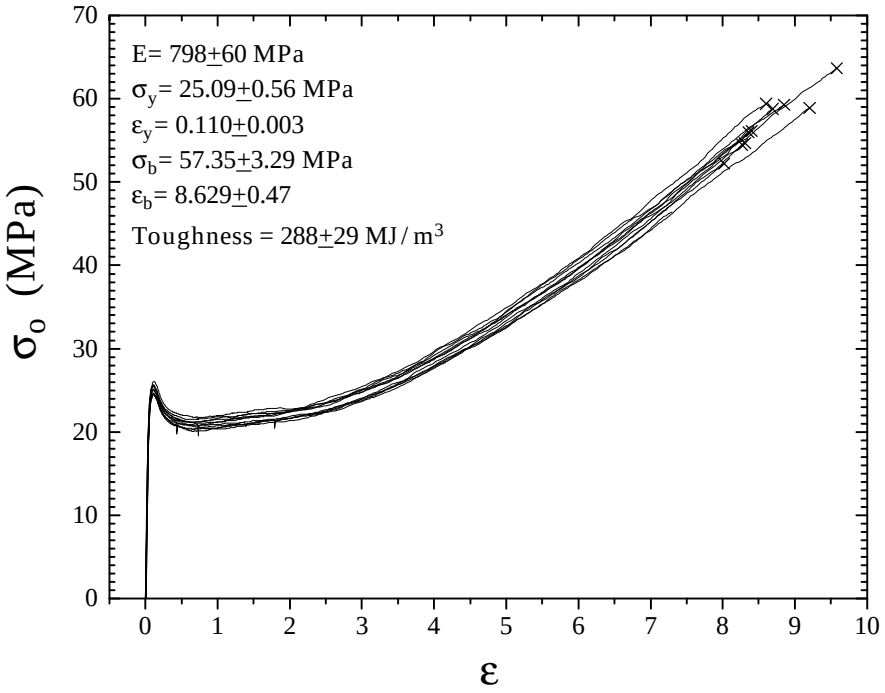

Figure 5. Stress–strain data for all ten specimens of the quenched 165 kg / mol material.

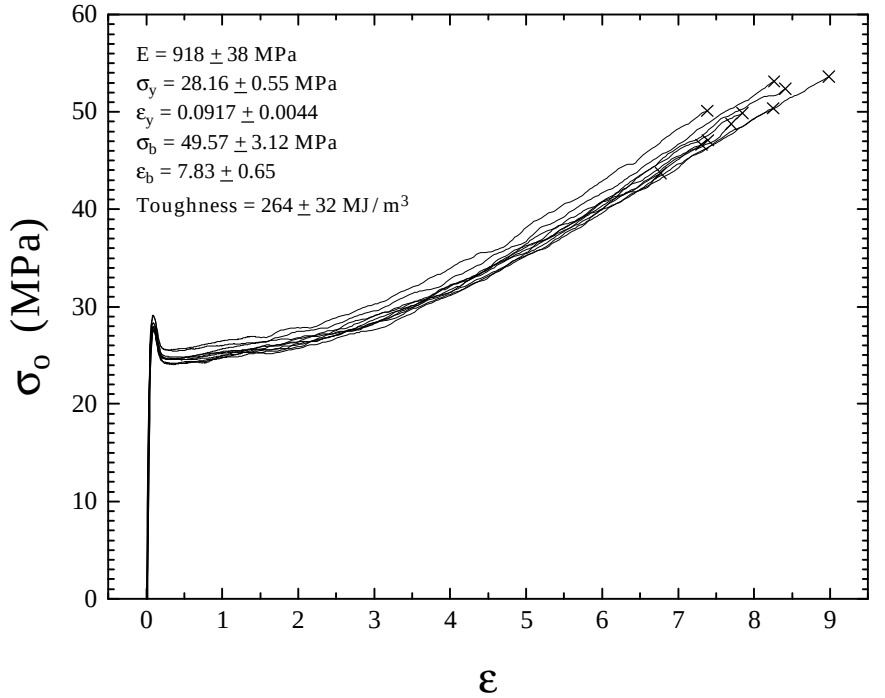

Figure 6. Stress–strain data for all ten specimens of the slowly cooled 165 kg / mol material.

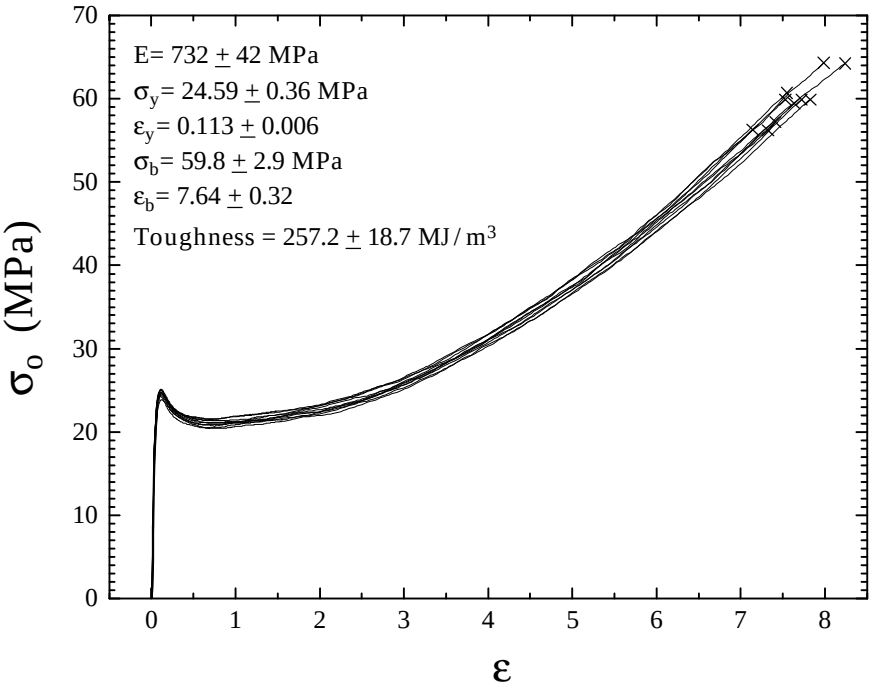

Figure 7. Stress–strain data for all ten specimens of the quenched 267 kg / mol material.

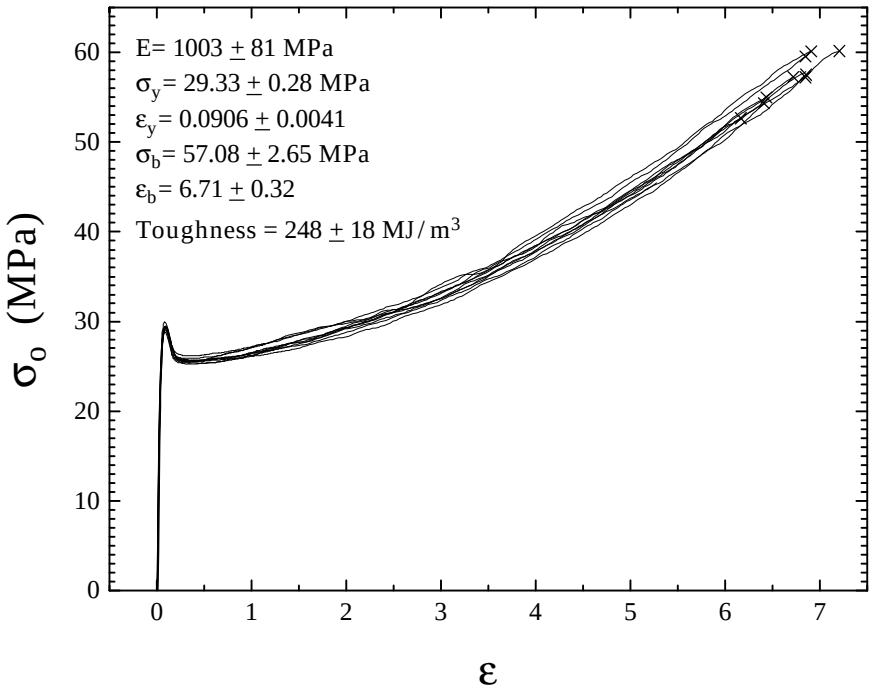

Figure 8. Stress–strain data for all ten specimens of the slowly cooled 267 kg / mol material.

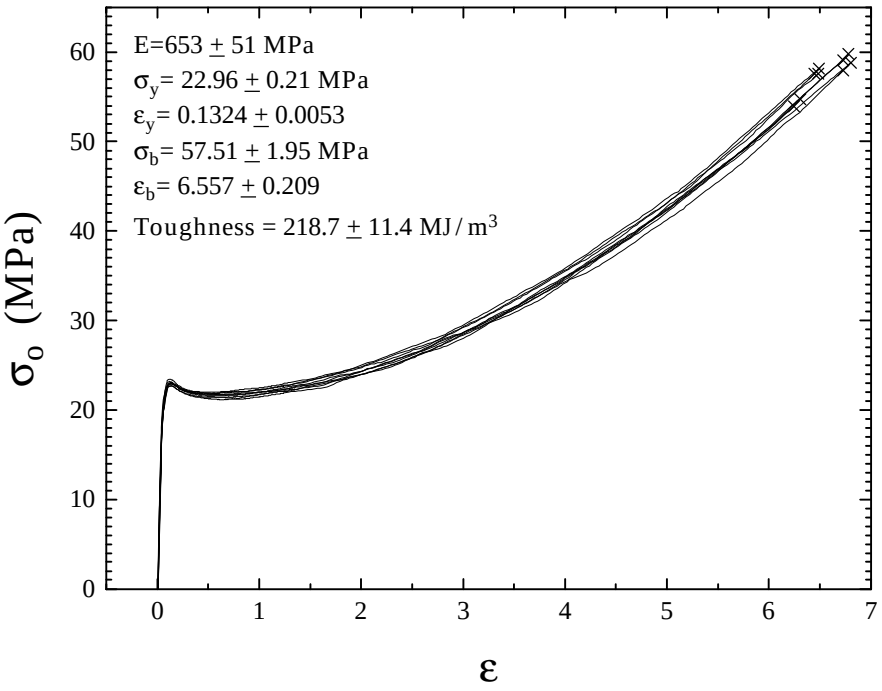

Figure 9. Stress–strain data for all ten specimens of the quenched 320 kg / mol material.

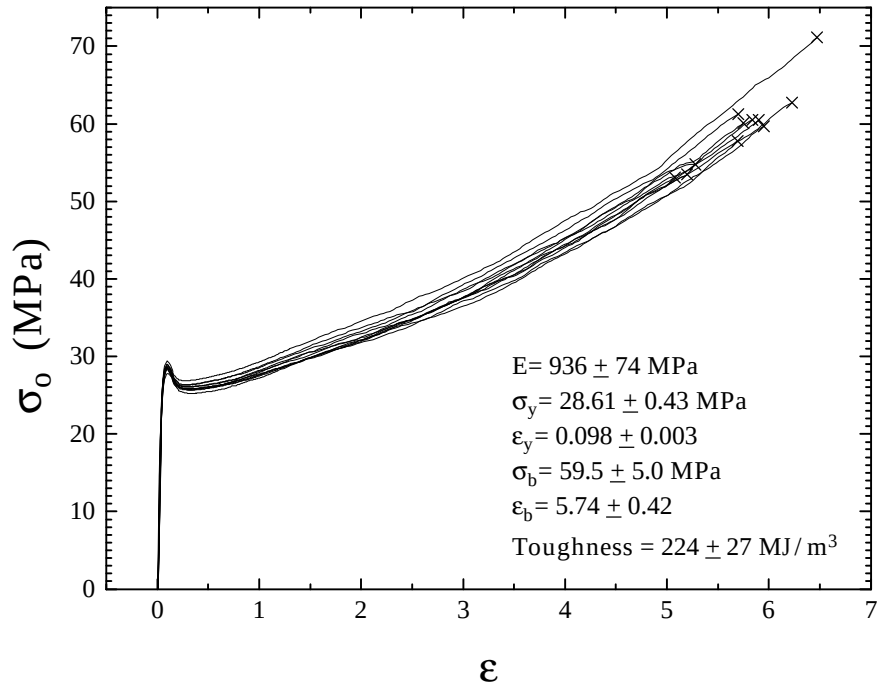

Figure 10. Stress–strain data for all ten specimens of the slowly cooled 320 kg / mol material.

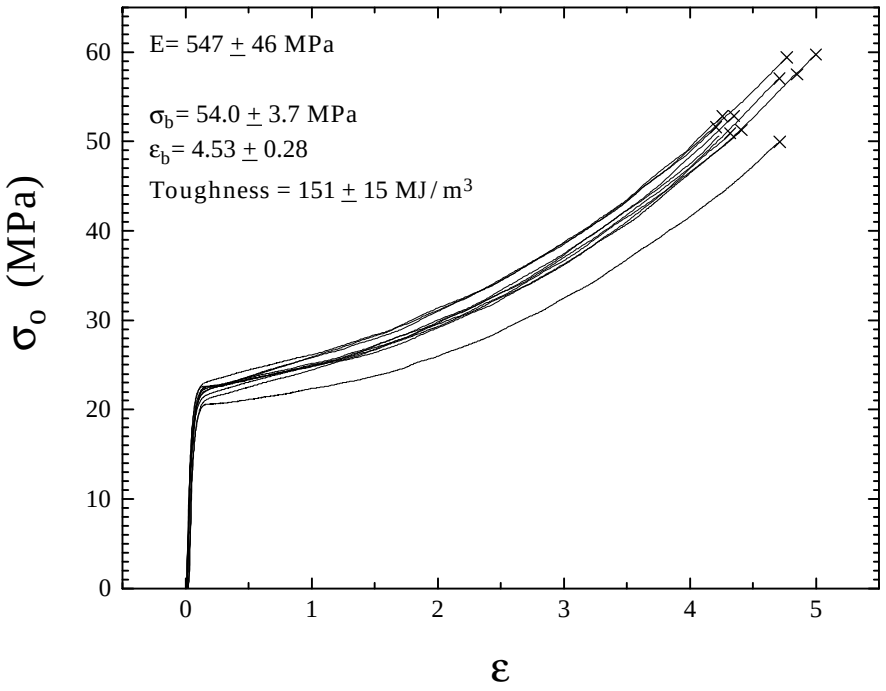

Figure 11. Stress–strain data for all ten specimens of the quenched 839 kg / mol material.

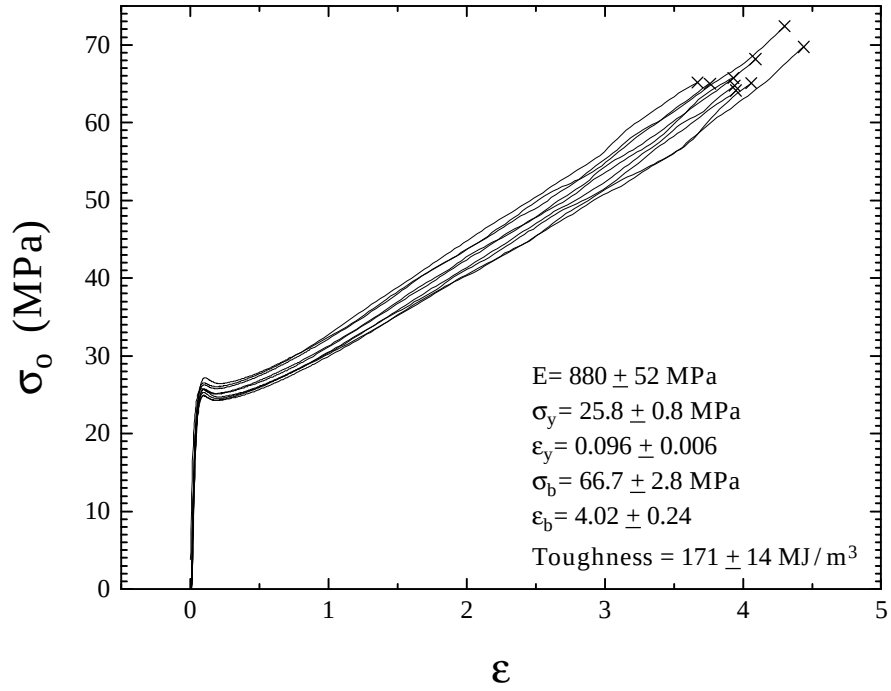

Figure 12. Stress–strain data for all ten specimens of the slowly cooled 839 kg / mol material.

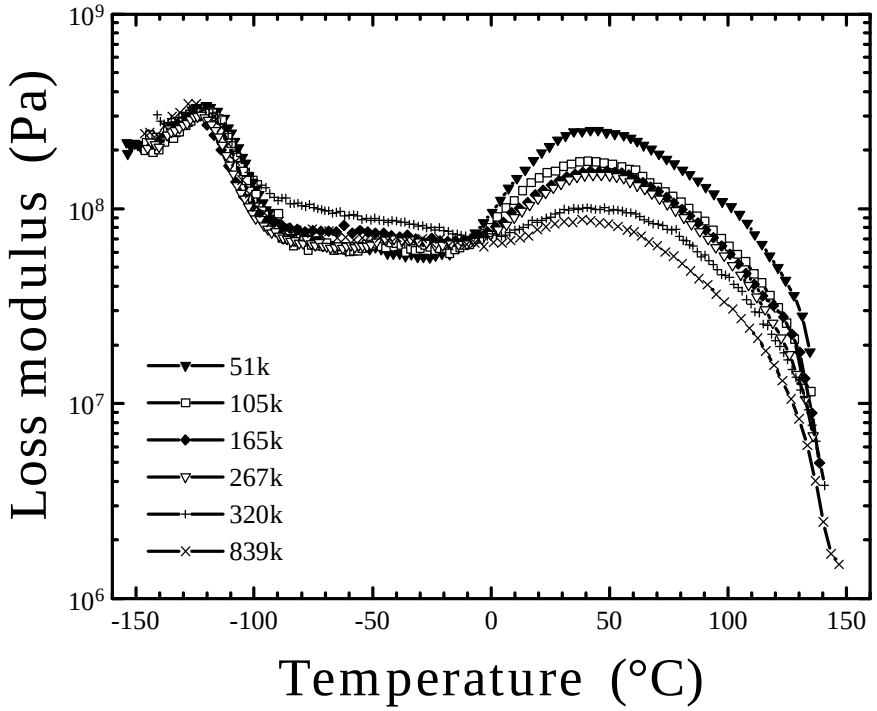

Figure 13. Dynamic loss moduli for the quenched series (1 Hz).

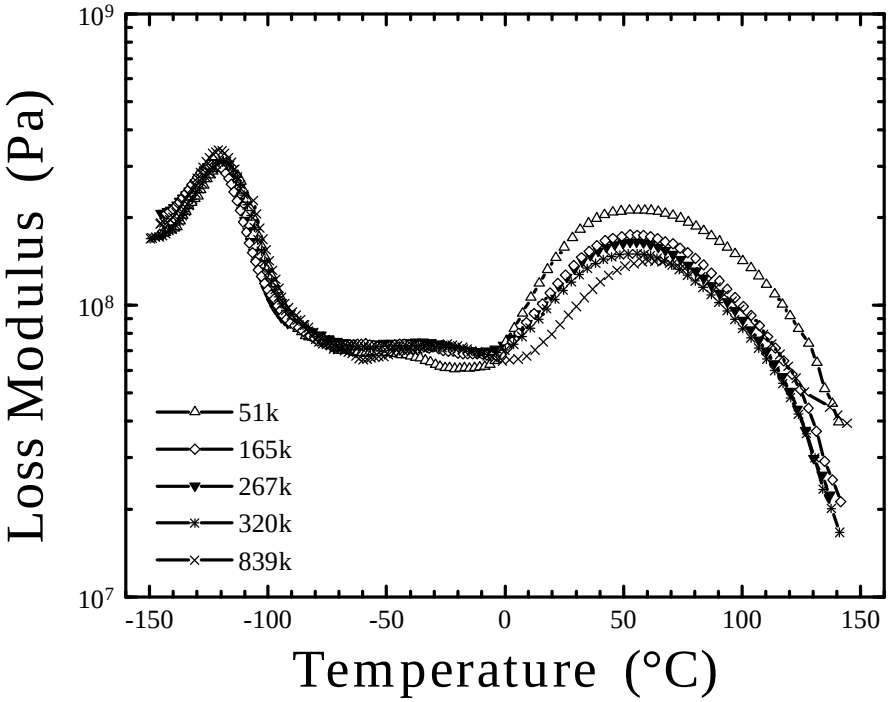

Figure 14. Dynamic loss moduli for the slowly cooled series (1 Hz).

Chapter 9

Recommendations for future work

9.1 JEFFAMINE® based ceramer materials

Since these ceramer materials were allowed to react only at room temperature, the reaction in many cases took a week or so to reach an equilibrium. This extent of reaction can be either increased or realized more rapidly if the films were allowed to cure at an elevated temperature. This would also provide a stronger driving force to eliminate the volatile by–product alcohols. Cure temperatures should remain low enough to avoid degradation of the poly(propylene oxide) component. The resulting network materials may posses a higher glass transition temperature (especially if TMOS is included in the formulation), a higher modulus in the rubbery state, and possibly a lower sol–fraction. Also, these materials should be more stable during storage at room temperature (reaction would not be able to proceed further since they would have been cured at an elevated temperature).

The ceramers could also be synthesized in different solvents – solvents which have varied solvent "quality" or "power" for the PPO oligomers. Poor solvents for PPO would lead to contraction of the chains and good solvents would lead to expansion. Formation of the network oxide would then trap the chains in this conformation (or perhaps a better description would be a restriction of the chain to the total number of

conformations that entropy will allow for this fixed end-to-end distance). The end-to-end distance of the chains would in turn influence the correlation lengths in the final ceramers. Also, depending on whether the chains are stretched or contracted, the mechanical properties of the final materials may be affected.

9.2 ACCLAIM™ based ceramer materials

Similarly to the JEFFAMINE® based ceramers, the ACCLAIM™ based materials might also benefit from curing at elevated temperatures.

When comparing the properties of the JEFFAMINE® versus ACCLAIM™ based ceramers, perhaps additional mechanical measurements would provide further insight into the differences in the network structures. It has been suggested that the JEFFAMINE® oligomers, with their lower functionality, produce poorer networks than the ACCLAIM™ based systems (more dangling ends, etc.). Certain experiments might help to show these differences, such as creep, stress relaxation, and cyclic tensile tests. A more ideal network structure would display less creep and stress relaxation behavior and less mechanical hysteresis than the more imperfect network.

Another interesting variation in structure would be to combine two oligomers of different molecular weights, to produce a "bimodal" network. Some bimodal networks have displayed stress at break and toughness superior to networks composed of their individual components.[1,2] The reason for this apparent synergism is not yet well understood.[3] ACCLAIM™ oligomers similar to the 2200 material used in chapter 4 are available at molecular weights of 4200 and 8200. Also, to the author's knowledge, trimodal networks have not been explored.

9.3 Abrasion resistant coatings

Some preliminary experiments were performed in the lab where our ceramer coatings were applied to painted automotive panels supplied by PPG (not reported). These panels already had several layers on it, among them a primer layer on the metal, a paint layer, and topcoat layer(s). Subsequently, our coating was applied on top to

provide abrasion resistance. Perhaps some of the layers could be eliminated if the ceramer coating were modified to serve the purpose of the lower layers. Specifically, dyes or pigments could be added to the ceramer formulation to generate a colored coating. An obvious choice would be titanium dioxide particles, which are used to produce a white color in some paints. TiO_2 would seem to be an ideal candidate to be incorporated into the network oxide structure of the ceramer coatings, as it is itself an inorganic oxide, and the potential for covalent bonding exists.

9.4 Polymer–clay nanocomposites

Intercalated structures are certainly readily formed between many organic polymers and organoclays, as shown in chapter 6 and in many of the cited references. One idea that has not been explored (to the author's knowledge) is intercalating an ionomer into the clay. Taking this route, the need for an *organically modified* montmorillonite clay might be eliminated. The ionomer should be cationic (such as quaternary amine functionalized) for use with raw or sodium exchanged montmorillonite clay, and a simple ion exchange reaction between the clay and the ionomer should prove sufficient in forming the nanocomposite. The effect of the ionomer type (telechelic, zwitterionic, etc.,) on the final nanocomposite structure formed may be interesting. Generating a nanocomposite by this route may prove to be a good alternative to the usual multi–step process of organically modifying the clay and then blending with polymer. However it should be determined whether the clay provides any significant improvement in the properties compared to the unfilled counterpart, which it certainly may not.

Another aspect which has not been explored is curing epoxy–clay nanocomposites with microwave radiation. Since clays typically transmit microwave radiation, exposure of a reacting epoxy–clay blend would likely produce directional (i.e. somewhat polarized) lines of force around the stacked clay layers. This would heat the clay sheets and any reactants in the vicinity of the clay sheets, particularly intercalated molecules. Such heating would affect the curing kinetics of these molecules. This could influence the final structure of the nanocomposites.

9.5 Metallocene catalyzed linear polyethylene

The number and types of studies that could be explored for this series of polyethylenes are vast. The results found in chapter 7 showed the metallocene polyethylenes to behave similarly to the materials of previous studies. For example, the zero–shear viscosity showed a dependence on $\overline{M}_w^{3.4}$, the lamellar structures followed previously noted trends on molecular weight, etc. The most notable difference between the metallocene catalyzed polyolefins and conventional Ziegler–Natta polyolefins is the ability to produce narrow molecular weight distributions in the former. This variable has a most dramatic effect *not* on the solid–state behavior, but rather on the melt rheological behavior. This is why capillary rheometry is suggested as a tool to further probe the series. The capillary rheometry would provide important insight into the behavior of these materials at industrially significant conditions, i.e. high shear rates as encountered in extrusion. The small amplitude oscillatory rheology experiments shown in chapter 7 are good for providing information about the molecular structure of the materials, but capillary data is necessary to quantitatively provide the behavior in the shear–thinning, power–law region such as that which is encountered in industrial settings. Although the author employed the Cox–Merz rule to the oscillatory shear data in chapter 7, this rule breaks down at high shear rates and must be avoided. Hence capillary measurements are necessary to quantify behavior at high shear rates. It also would be better to perform the rheology tests at a more common temperature employed in industry for linear polyethylene (HDPE), namely 190 °C.

Another related area to probe would be extensional flow. One aspect of this type of flow is the apparent contribution from long chain branching – such branched materials show significant strain hardening in extensional flow when compared to linear analogs. Such experiments could further confirm the author's conclusion of the lack of LCB in this series.

The metallocene catalyzed materials should display the largest variance in behavior compared to conventional Z–N catalyzed systems by these rheological experiments, and would be valuable to the polymer processing industry.

In addition, the morphological structure of the series could be determined as a function of isothermal crystallization temperature. This method is more academic then quenching and slowly cooling the samples. Lower molecular weight species are rejected upon crystallization of the longer molecules, and therefore, the breadth of the molecular weight distribution should play a role in the final morphological structure during slow isothermal crystallization (e.g. at low undercooling). For example, the shorter molecules tend to be found at the boundaries of spherulites. Since the distribution breadth of the metallocene systems is the major distinction from conventional Z–N polyethylenes, this avenue of study might also reveal some distinctions between the two.

The properties (density, crystal content, etc.) and morphological state of the samples could also be probed *after* the tensile deformation tests. The effects of initial structure on final structure could then be determined in addition to the effects of molecular weight and thermal treatment.

9.6 References

1 J. E. Mark. *Adv. Polym. Sci.*, **44**, 1, (1982).

2 J. E. Mark and M. Y. Tang. *J. Polym. Sci.: Polym. Phys. Ed.*, **22**, 1849, (1984).

3 P. R. von Lockette and E. M. Arruda. *Macromolecules*, **32(6)**, 1990, (1999).

Vita: Kurt Jordens

Continuing his education after high school, Kurt attended college at Virginia Tech in pursuit of an engineering degree. After four years of study in the chemical engineering department, he received his B.S. degree in May of 1993. Learning about polymer science as an undergraduate, Kurt decided to enter the chemical engineering Ph.D. program at Virginia Tech under the tutelage of Prof. Garth Wilkes. Lengthy though it was, his graduate education was a pleasant process. Many different research projects exposed him to a broad range of interesting areas in polymer science. Even though he was intrigued by all of his research challenges, polyolefins remained his favorite topic of study. Devoutly committed to polyolefin research, he was determined to find a position in the polyolefin industry. Regarding his future work, he will be moving to Longview, Texas where he will join the Texas Eastman Division of the Eastman Chemical Company in the polyethylene business.